Quantum Nonlinear Optics Using Cold Atomic Ensembles

by

Thibault Peyronel

Submitted to the Department of Physics
in partial fulfillment of the requirements for the degree of

Doctor of Philosophy

at the

MASSACHUSETTS INSTITUTE OF TECHNOLOGY

September 2013

Author .....
Department of Physics
July 29, 2013

Certified by .....
Vladan Vuletić
Professor of Physics
Thesis Supervisor

Accepted by .....
Krishna Rajagopal
Professor, Associate Department Head for Education

Quantum Nonlinear Optics Using Cold Atomic Ensembles

by

Thibault Peyronel

Submitted to the Department of Physics
on July 29, 2013, in partial fulfillment of the
requirements for the degree of
Doctor of Philosophy

Abstract

The fundamental properties of light derive from its constituent particles, photons, which are massless and do no interact with each other. The realization of interactions between photons could enable a wide variety of scientific and engineering applications. In particular, coherent interactions would open the path for the simulation of quantum systems with light. Photon-photon interactions can be mediated by matter, in our case cold atomic ensembles, which provide a nonlinear medium. In conventional nonlinear media, the nonlinearities are negligibly weak at intensities corresponding to single photons and nonlinear optics at the few-photon level is a long-standing goal of optical and quantum science.

In this thesis, we report on two different experimental approaches to create optical media with giant nonlinearities. Both approaches rely on Electromagnetically Induced Transparency, in which photons traveling in the medium are best described as part-matter part-light quantum particles, called polaritons. In our first approach, we achieve low-light nonlinearities by loading ensembles of cold atoms in a hollow-core photonic crystal fiber to enhance the polariton-photon interactions. In our second approach, the photons are coupled to strongly interacting Rydberg atoms, which mediate large interactions between single quanta of light. Moreover, the intrinsic nature of these interactions can be tailored to take on a coherent dispersive form.

Thesis Supervisor: Vladan Vuletić
Title: Professor of Physics

Dedicated to my wife, Sarah.

Acknowledgments

The work presented in this thesis would not have been possible without the decisive help and contributions from a number of exceptional individuals who transformed the six years I spent at MIT into an unforgettable intellectual and human journey.

I am foremost indebted to my supervisor, Prof. Vladan Vuletic, for the generous attention and kind support I received from him over the course of my graduate studies. His incredibly deep understanding of science and his motivation to share it with people around him in a friendly yet highly motivating atmosphere have made me feel very privileged to be part of his research group. His patience to find interest even in the most basic questions, his ability to systematically bring out the meaningful and exciting aspects in a project and his absolute intellectual honesty, as well as his profound comprehension of physics, constitute a invaluable inspiration on how research should be conducted. I could not have asked for a better adviser.

It has also been a fantastic privilege to have Prof. Misha Lukin as a second mentor throughout my PhD work. His vision and charism have been a great source of motivation and inspiration. I have learned an inestimable amount from his highly rigorous yet exhilarating approach to scientific research. I am deeply honored to have profited from his unique insight, as well as his continuous help and encouragements.

I have had the opportunity to learn a tremendous amount from many other wonderful physicists at MIT and in the CUA. Firstly, I am most grateful to Prof. Dan Kleppner and Prof. Ike Chuang for being on my thesis committee. Writing this thesis has reminded me of their key pioneering contributions to modern quantum physics. Prof. Dave Pritchard has been my academic supervisor throughout my stay at MIT, and I would like to thank him for his wise advice and friendly support, as well as the wonderful and instructive times spent sailing with him and his crew. The AMO class taught by Prof. Wolfgang Ketterle and Prof. Ike Chuang has spurred my understanding of atomic physics, and I heavily referred myself to it during my research. Their teaching was a precious addition to the high caliber quantum physics classes by Profs. Jean Dalibard, Phillipe Grangier, Alain Aspect and Michel Brune that I followed during my undergraduate studies at Ecole Polytechnique. I am also grateful to Prof. Wolfgang Ketterle for extending my learning experience by giving me the opportunity to be a teaching assistant.

I will never stress out enough that this work was only made possible by my closest collaborators, who in addition made the long working hours a bliss. During the earlier stages of my PhD, I have learned a tremendous amount from Misho Bajcsy and Dr. Sebastian Hofferberth, who taught me with infinite patience the tools of the trade, and with whom I have developed a great friendship. The projects I carried out during the rest of my PhD were solely enabled by the knowledge they generously passed onto me. Qi-Yu Liang has been an amazing lab partner: her mesmerizing commitment, humility and enthusiasm for learning have been an example to me, and I will never be able to thank her enough for all her dedication. I also feel extremely lucky to have benefited from the presence of Dr. Ofer Firstenberg, whose highly contagious enthusiasm and exciting ideas have been pivotal to this work. Finally, I am grateful to Anton Matzurenko who brought us for part of his undergraduate studies his inspiring talent and friendliness.

Our experimental efforts have been boosted by the unique theoretical expertise of Michael Gullans, Mohammed Hafezi, Dr. Alexey Gorshkov and Prof. Thomas Pohl. I am especially indebted to Michael Gullans and Alexey Gorshkov for the many hours they spent helping us getting an analytical understanding of our measurements and their admirable willingness to confront with small technical details and limitations inherent to our experiment. Their vision provided us with invaluable insight and outlook.

Members of the Vuletic and Lukin groups have been a constant source of advice. Dr. Alexander Zibrov, Marko Cetina, Andrew Grier, Jon Simon, Ian Leroux, Monika Schleier-Smith, Haruka Tanji-Suzuki, Jeff Thompson and Yiwen Li are among the many people who kindly provided us with technical help and contributed to creating an energizing environment. I would also like to thank Joanna Keseberg for all the administrative support.

Finally, I am grateful to my parents, grand-parents, brother, sisters, and new and old friends for their continuous presence and encouragements. Above all, I would like to thank my wife Sarah for her love, her infinite generosity, her unconditional support and the sacrifices she made to allow me to carry out this work with happiness and peace of mind.

Citations to Previously Published Work

The results and theoretical analysis described in Chapter 7 and Appendix C have been published as:

> "Quantum nonlinear optics with single photons enabled by strongly interacting atoms", T. Peyronel, O. Firstenberg, Q.-Y. Liang, S. Hofferberth, A. V. Gorshkov, T. Pohl, M. D. Lukin and V. Vuletic, Nature **488**, 5760 (2012).

Part of the work presented in Chapter 8 and Appendix D has been submitted for publication to Nature, under the title:

> "Attractive Photons in a Quantum Nonlinear Medium", O. Firstenberg*, T. Peyronel*, Q.-Y. Liang, A.V. Gorshkov, M.D. Lukin and V. Vuletic

Large portions of Chapter 3 have appeared in the following publications:

> "Switching and Counting With Atomic Vapors in Photonic-Crystal Fibers", T. Peyronel*, M. Bajcsy*, S. Hofferberth*, V. Balic, M. Hafezi, Q. Liang, A. Zibrov, V. Vuletic, and M. D. Lukin, IEEE Journal of Selected Topics in Quantum Electronics, VOL. 18, NO. 6, (2012)

> "Laser-cooled atoms inside a hollow-core photonic-crystal fiber, M. Bajcsy, S. Hofferberth, T. Peyronel, V. Balic, Q. Liang, A. S. Zibrov, V. Vuletic, and M. D. Lukin, Phys. Rev. A **83**, 063830 (2011).

> "Efficient All-Optical Switching Using Slow Light within a Hollow Fiber", M. Bajcsy, S. Hofferberth, V. Balic, T. Peyronel, M. Hafezi, A. S. Zibrov, V. Vuletic, and M. D. Lukin, Phys. Rev. Lett. **102**, 203902 (2009).

Contents

List of Figures

Chapter 1

Introduction

1.1 Overview

The fundamental properties of light derive from its constituent particles, photons, which are massless and do no interact with each other. At the same time, the realization of interaction between photons could enable a wide variety of scientific and engineering applications. In particular, coherent interactions, akin to those associated with conventional massive particles, would open the path for the simulation of quantum systems with photons. Photon-photon interactions can be mediated by matter, in our case cold atomic ensembles, which provide a nonlinear medium. In conventional nonlinear media, the nonlinearities are negligibly weak at intensities corresponding to single photons and nonlinear optics at the few-photon level is a long-standing goal of optical and quantum science. In this thesis, we report on two different experimental approaches to create optical media with giant nonlinearities. Both approaches rely on Electromagnetically Induced Transparency (EIT) techniques, in which a single photon is coherently mapped onto and retrieved from an ensemble of cold atoms, which offer exquisite control and long coherence times. Under EIT condition, photons traveling in the medium are best described as part-matter part-light quantum particles, called polaritons. In our first approach, we achieve low-light nonlinearities through interactions between the atomic component of the polaritons and photons. This approach requires a large interaction probability between individual photons and atoms: to that purpose, we load ensembles of cold atoms in a hollow-core photonic crystal fiber. In our second approach, the photons are coherently

coupled via EIT to strongly interacting Rydberg atoms, which mediate large photon-photon interactions between single quanta of light. Moreover, the intrinsic nature of these interactions can be tailored to take on a dissipative form or a coherent dispersive one.

This thesis is organized in the following manner. Firstly, we provide some scientific motivation for this work by considering the importance of quantum nonlinear optics for applications in the fields of quantum information science and quantum simulation (present Chapter). In Chapter 2, we review how EIT techniques allow dramatic enhancement of the optical nonlinearities with respect to conventional media. We then turn to the description of our hollow core fiber experiment, which is covered in Chapters 3 and 4. In particular, in Chapter 4, we report on experimental progress towards optical nonlinearities beyond the single-photon single-atom cooperativity. In the remaining part of the thesis, we focus on the results of our Rydberg EIT experiment. Rydberg atoms properties are reviewed in Chapter 5. Our experimental setup is detailed in Chapter 6. In Chapters 7 and 8, we demonstrate single photon nonlinearities using Rydberg EIT, respectively in the dissipative and dispersive regimes. The details of our theoretical analysis are postponed to the Appendix section. EIT is reviewed in Appendix A. Appendix B details our analytical treatment of the stationary light experiments presented in Section 4.2. Quantum nonlinear optics theory for Rydberg EIT is described in Appendix C for the dissipative regime and Appendix D for the dispersive regime.

1.2 Nonlinear Optics in Quantum Information Science.

The rapid developpement of integrated photonics and optoelectronics over the last decades raises the question of the partial replacement of electronic currents by optical waves in computational devices. The motivation stems from the traveling speed of light and the possibility to shape wavepackets with sub-picosecond length, which could increase information transfer and processing rates. A building block for such computers would be photonic transistors, where few control photons would enable or disable the transmission of light in a waveguide. A fundamental obstacle for a foreseeable future is the miniatur-

ization, scalability and bandwidth of these all-optical devices.

Beyond classical computation, the experimental demonstration of entanglement in the early 1980s [1, 2] has generated a tremendous interest in exploiting quantum mechanical properties to improve the transmission and processing of information, a field known as Quantum Information Science [3]. Three particularly enticing directions of research have emerged over the last years. The first one is quantum communication, where information encoded in quantum states (qubits) is exchanged between nodes of a quantum network, where it can be stored and manipulated in a coherent way [4, 5, 6]. In particular, the transmission of information in these networks can be secured by quantum cryptography. Secondly, entangled states can be used to push the boundaries of metrology beyond the Standard Quantum Limit, which sets a limit to the measurement precision due to detection photon shot-noise [7]. Finally, the most awaited application is the realization of a quantum computer, where qubits interact through quantum logic gates to perform computational tasks more efficiently than their classical analogs [3].

Photons are a natural candidate for Quantum Information Science and were initially used to demonstrate entanglement[1, 2]. They are the obvious choice to act as "flying" qubits in quantum communication protocols, given their ability to travel over long distance with little noise and at the speed of light. For quantum computation, photons are one of the alternatives currently being explored, along with ions[8], nuclear magnetic resonance[9], atoms [10, 11], and superconducting qubits[12, 13]. The realization of quantum gates requires the qubits to be initialized and read while being protected from decoherence induced by interactions with the environment. Simultaneously, it requires strong controllable coherent interactions between individual qubits (possibly between different sorts of qubits in hybrid systems). Single photons (for which the qubits states can be encoded as polarization, spatial modes or time bins) offer the advantage to robustly and quickly carry the information between spatially separated gates, and techniques to manipulate and detect light at the single-photon level are well established. Two essential elements still actively pursued are the on-demand, deterministic generation of single photons and the realization of strong coherent interactions at the single photon level. In principle, nonlinear optics can be used to attain these goals. For example, parametric down conversion has proved itself a useful source of single photons in the early stages of

experimental quantum optics. As we will review, intensity sensitive Kerr-type materials exhibiting a third order nonlinear susceptibility can be used to convert coherent pulses into single photon pulses or achieve conditional nonlinear phase-shifts, a fundamental element for quantum gates. Unfortunately optical nonlinearities (both dissipative and dispersive) in traditional media are negligibly weak at intensities corresponding to a single photon. Bright deterministic single photon sources are still an active topic of research, as well as optical nonlinearities at the single photon level. To this day, the most promising paths are cavity Quantum Electro-Dynamics (QED) and Electromagnetically Induced Transparency (EIT). In cavity QED, photons are strongly coupled to a common atom or atomic ensemble by way of a high-finesse optical cavity. In EIT, quantum interferences are harnessed to coherently map photons onto large atomic ensembles, giving rise to partially atomic and partially photonic quasi-particles, called polaritons. The purpose of the work presented in this thesis is the creation of EIT-based strong photon-polariton and polariton-polariton interactions, leading to single-pass optical media with large nonlinear susceptibilities at the few-photon level.

To illustrate the possibilities of Kerr nonlinearities for photonic quantum computation, we consider the canonical C-NOT gate [14, 15]. A C-NOT gate, which flips a target qubit depending on the value of a control qubit can be realized for photons by using a Mach-Zender interferometer, with a Kerr nonlinear medium inserted in one of the arms, as depicted in Fig. 1-1. Here we used a dual-rail qubit repsentation, in which a single photon is shared between two modes a and b, and the two states of the qubit are $|10\rangle_{ab}$ and $|01\rangle_{ab}$. In the absence of phase-shit introduced by the Kerr medium, the status of the control qubit is unchanged as photons in modes a and b will exit the interferometer in modes a'' and b'' respectively. The Kerr-type nonlinear susceptibility $\chi^{(3)}$ generates cross-phase modulation between a photon in mode b' and a photon in mode c, resulting in a phase shift $\phi = \chi^{(3)}L$ for the photon in mode b', and rotates the state at the output of the second beamsplitter. In particular, for a conditional phase shift of π, the output modes are inverted: $a'' = b$ and $b'' = a$, as expected for a C-NOT gate.

The C-NOT gate plays a fundamental role in quantum computation, as any unitary gate between two qubits can be engendered by a C-NOT gate and an ensemble of single qubit rotations. A C-NOT gate between photons can also be implemented with solely

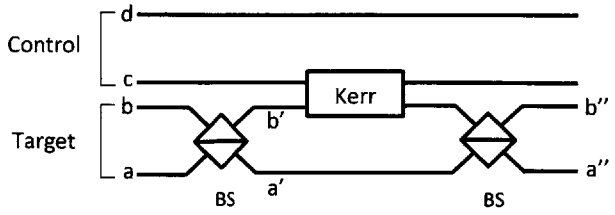

Figure 1-1: **C-NOT gate for photons.** The states of the dual rail qubits are encoded as $|1\rangle = |10\rangle_{ab}$ and $|0\rangle = |01\rangle_{ab}$ for the control qubit and $|1\rangle = |10\rangle_{cd}$ and $|0\rangle = |01\rangle_{cd}$ for the target qubit. The annihilation operators for the different modes follow the relations: $a' = \frac{a+b}{\sqrt{2}}$, $b' = \frac{b-a}{\sqrt{2}}$, $a'' = \frac{a'-b'e^{i\phi}}{\sqrt{2}}$, and $b'' = \frac{a'+b'e^{i\phi}}{\sqrt{2}}$.

linear optical elements, as proposed by Knill, Laflamme and Milburn (KLM) [16] and later demonstrated experimentally [17]. Nevertheless, such a gate is non deterministic as it only performs the C-NOT operation with a finite probability and at least two additional single photons are needed to condition the success of the operation. In theory, the success probability can be increased by using higher number of auxiliary single photons. In practice, the overhead cost in single photons is an issue for scalable quantum computing in the absence of bright on-demand single photon sources. As a consequence, large nonlinear interactions at the single-photon level are still a much needed stepping stone for the optical implementation of quantum information processes.

The C-NOT gate described in figure Fig. 1-1 is closely related to a quantum non-demolition (QND) measurement of photons based on dispersive Kerr effect [18]. The photon number of a signal field in mode c determines the phase of the field in mode b', which can subsequently be detected by interference with the field in mode a'. The quantum non-demolition measurement is enabled by the fact that the Kerr effect affects the phase of the probe beam without modifying the photon number observables of the probe and signal fields. The measurement of the photon number of the signal increases the uncertainty of its conjugate variable, i.e. the phase of the signal field, to satisfy the Heisenberg inequality. In particular, it was demonstrated in [18] that the product of the uncertainties for the photon number and the phase of the signal field after the QND measurement is equal to that of the probe field and can thus satisfy the Heisenberg equality.

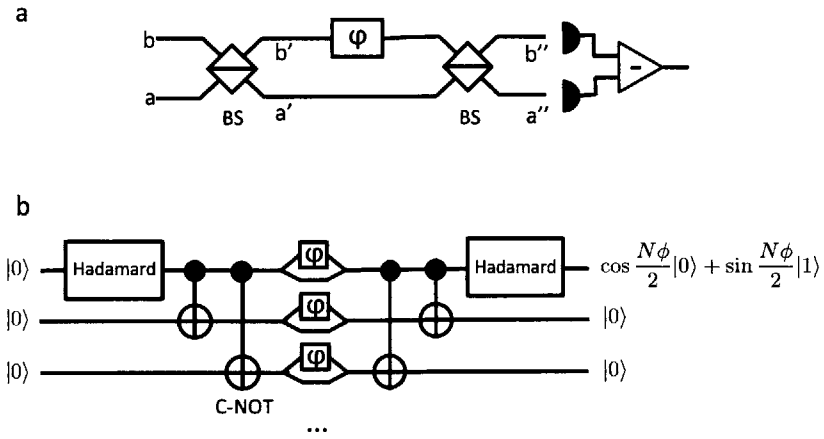

Figure 1-2: **Entanglement enhanced interferometry. a,** Mach-Zender interferometer. The output signal on the balanced photodiode gives a measure of the phase ϕ with an uncertainty set by the Standard Quantum Limit $\Delta\phi$=$1/\sqrt{N}$ for classical input states. **b,** The Heisenberg uncertainty limit $\Delta\phi$=1/N can be reached using entangled states. Here the entanglement between single photons is realized by a series of C-NOT gates.

A crucial property of Kerr nonlinearities is the ability to entangle photons. Photons are a convenient tool for quantum metrology where interferometers measure the phase of electric fields with sub-wavelength accuracy. Typically, interferometers are limited by the standard quantum limit (SQL) which is due to photon shot noise. A typical example is given by the Mach-Zender interferometer (see Fig. 1-2,a). If the qubit is intialized in state $|0\rangle$, the presence of a phase shift ϕ in one of the arms of the interferometer induces a rotation of the qubit to the state: $\cos\frac{\phi}{2}|0\rangle + \sin\frac{\phi}{2}|1\rangle$ (where we have neglected the factors i introduced by the beam splitters and the overall phase for simplicity). The signal P at the output of the balanced photon detectors which subtracts the signal between the two arms of the interferometer is $P = \langle b''^{\dagger}b'' - a''^{\dagger}a''\rangle = \cos\phi$. The corresponding standard deviation is $\Delta P = |\sin\phi|$, and the uncertainty of the phase measurement $\Delta\phi = \Delta P\,|\partial P/\partial\phi|^{-1}$ is 1. By repeating the experiment with N uncorrelated photons, the uncertainty is reduced to the standard quantum limit $\Delta\phi = 1/\sqrt{N}$. The same limit is obtained for a coherent state with average photon number N at the input of the interferometer. However, the fundamental limit imposed by the laws of quantum mechanics is the the Heisenberg limit $\Delta\phi = 1/N$. This limit can be reached by using entangled photons. An example is given in Fig. 1-2,b. A Hadamard gate on the first photonic

qubit followed by a series of C-NOT gates prepares the multi-qubit system in the entangled state :$|0,0,....,0\rangle+|1,1,...,1\rangle$. The phase shift affecting the qubits in state $|1\rangle$ rotates the qubits to $|0,0,....,0\rangle + e^{iN\phi}|1,1,....,1\rangle$, which can then be desentangled into $\left(\cos\frac{N\phi}{2}|0\rangle + \sin\frac{N\phi}{2}|1\rangle\right)\otimes|0,0,...,0\rangle$. The signal $P = \cos N\phi$ still has a standard deviation 1 corresponding to the detection of a single photon, but the sensitivity of the interferometer has been increased by a factor N and the standard deviation $\Delta\phi = 1/N$ reaches the Heisenberg limit. More generally, optical nonlinearities induce light squeezing, which can subsequently be used in interferometry. An example is the squeezing of the photon number by quantum-non demolition measurement introduced previously.

1.3 Highly correlated states of light

A typical example of strongly correlated states is the Tonks-Girardeau gas of impenetrable bosons [19, 20]. In this one-dimensional system, bosons partially acquire fermionic properties due to the repulsive potential which prevents them form occupying the same position, much like the Pauli exclusion principle. Because the particles cannot pass each other for large repulsive interactions, their position is strongly correlated to that of their nearest neighbors. Proposed more than 50 years ago, Tonks-Girardeau gases[21, 22] as well as other highly correlated states, most famously the Mott insulator[23], were observed recently in cold atomic gases loaded into optical lattices.

The possibility to achieve similarly correlated states for photons has been extensively studied in recent years [24] but many-body strongly correlated photonic states have not been observed yet. An advantage over their atomic counterparts is that direct correlation measurements of photons are a standard procedure in quantum optics. The earliest proposals were based on photon blockade [25] in coupled arrays of optical cavities [26, 27, 28]. For strong enough coupling of the photon-atom system, each cavity behaves like an impenetrable particle for other photons, but the realization of such a system is highly challenging experimentally. Tonks-Girardeau type gases of photons were subsequently proposed for one-dimensional geometries, using light with tight confinement in a waveguide [29, 30]. In this work, the cavity induced blockade is replaced by effective nonlinear interactions in the EIT regime between stationary light pulses for which a Bragg grating created by counter-

propagating control fields acts as an effective cavity. The experimental challenge resides in the high optical depth (> 1000) and cooperativity (> 0.1) needed to reach a large effective cavity finesse and a strong photon-photon interaction probability. Cold atoms loaded in the hollow core of an photonic crystal fiber is one of the proposed experimental solutions to meet these conditions and is explored in Chapters 3,4. Other experimental efforts in that direction include cold atoms trapped along tapered fibers [31].

In such a system, the light propagation is governed by a quantum nonlinear Schroedinger equation [32, 30]. The nonlinearities are tunable and result in repulsive or attractive interactions, corresponding respectively to anti-bunching and bunching of light. In the case of an attractive potential, the bunching is due to the excitation of two-photon bound states in the system. In Chapters 7 and 8, we will explore equivalent physics where the strong nonlinearities are introduced by Rydberg blockade instead of stationary light pulses techniques. Interestingly, photonic bound states have also been predicted for other nonlinear one-dimensional system, such as a single scatterer strongly coupled to a photonic waveguide [33, 34]. On a related topic, a nonlinear Kerr medium with group velocity dispersion supports the existence of solitons (see Chapter 2). The existence of quantum solitons, *i.e.* clusters of bound polaritons with well defined energy and photon number has been predicted but never observed due to the low Kerr nonlinearities of conventional optical materials [35].

Finally, as mentioned above, the Rydberg blockade in dense atomic gases is a useful tool to introduce large atomic and photonic interactions and explore the many-body physics of interacting systems. In particular, highly correlated atomic states, Rydberg crystals, have been predicted [36] and observed [37]. These correlations can then be coherently mapped and retrieved on photonic states.

1.4 Cavity QED-based quantum nonlinear optics

As underlined above, large optical nonlinearities are a cornerstone of future photon-based quantum technologies. In particular for quantum information processes and quantum simulation of many-body physics with light, it is necessary for the nonlinearities to be significant at the single-photon level in media which are simultaneously loss-free. In

Chapter 2, we will discuss how optical nonlinearities, traditionally weak in conventional media, can be enhanced in atomic gases by EIT and Rydberg EIT. It is an alternative approach to the field of cavity QED [38], which has been successful a path to mediate strong photon-photon interactions.

The concept of photon blockade was first introduced by considering a medium with third-order EIT-enhanced nonlinearities [39, 40] placed in a high finesse cavity [25]. However, it was rapidly realized that the anharmonic system provided by a single two-level scatterer strongly coupled to an optical resonator was a simpler way to experimentally achieve photon blockade. For such a system, the scatterer-cavity mode system is described by the Jaynes-Cummings Hamitonian. On resonance, the atomic state is dressed by the field in the mode of the cavity, which symmetrically splits the coupled atom-light system in two eigenlevels separated by $2\sqrt{N}g$ where g is the vacuum Rabi frequency of the atom-cavity system and N the number of photons in the cavity mode. The anharmonicity of the system prevents the simultaneous resonance of the system by several photons. One of the most striking application is the ability for the atom-cavity system to act as a photon turnstile, which transmits photons one by one and reflects the others [41]. The strong coupling regime between atom-like scatterers and optical resonators has since then been achieved in various systems and blockade experiments have been performed for atoms evanescently coupled to microtoroidal cavities [42], quantum dots coupled to photonic crystals [43, 44], and superconducting qubits in transmission line resonators [45], among other works. Another spectacular achievement of cavity QED is the realization of conditional phase shifts, paving the way for quantum gates [46, 47, 48].

The main limitations of cavity QED are first the scalability in the context of photonic many-body physics and secondly the necessity to mitigate the high finesse required in the strong coupling regime with the bandwidth of the cavity and the power transmission. In contrast, EIT and Rydberg EIT offer a virtually loss-free (only limited by atomic decoherence) platform for studying mesoscopic numbers of interacting quantum particles of light.

Chapter 2

Nonlinear Optics

2.1 Optical Kerr effect

Optical nonlinearities [49] arise when the polarization density $\vec{P}(\mathbf{r},t)$ of a dielectric medium is not strictly proportional to the electric field $\vec{E}(\mathbf{r},t)$. For a field much smaller in amplitude to the characteristic electric field of the medium (the field binding the nucleus and the electron), the instantaneous polarization of the medium can be expanded in series of the electric field as:

$$\vec{P}(\mathbf{r},t) = \vec{P}^{(1)}(\mathbf{r},t) + \vec{P}^{(2)}(\mathbf{r},t) + \vec{P}^{(3)}(\mathbf{r},t) + ... \tag{2.1}$$

where the n-th order term in the polarization expansion is related to the n-th order nonlinear susceptibility $\chi^{(n)}$ by:

$$P_i(\mathbf{r},t) = \epsilon_0 \int \frac{d\omega_1}{2\pi} ... \int \frac{d\omega_n}{2\pi} \chi^{(n)}_{i,i_1,i_2,...,i_n}(\omega_1,\omega_2,...\omega_n) \times E_{i_1}(\mathbf{r},\omega_1)E_{i_2}(\mathbf{r},\omega_2)...E_{i_n}(\mathbf{r},\omega_n)e^{-i(\omega_1+\omega_2+...+\omega_n)t} \tag{2.2}$$

The indices refer to the spatial coordinate system and $\vec{E}(\mathbf{r},\omega)$ is the Fourier transform of the electric field:

$$\vec{E}(\mathbf{r},\omega) = \int dt \vec{E}(\mathbf{r},t)e^{i\omega t} \tag{2.3}$$

In the Fourier domain, the polarization spectrum is generated by the mixing of the different oscillation frequencies of the electric field:

$$P_i(\mathbf{r},\omega) = \epsilon_0 \int \frac{d\omega_1}{2\pi} ... \int \frac{d\omega_n}{2\pi} \chi^{(n)}_{i,i_1,i_2,...,i_n}(\omega_1,\omega_2,...\omega_n) \times E_{i_1}(\mathbf{r},\omega_1)E_{i_2}(\mathbf{r},\omega_2)...E_{i_n}(\mathbf{r},\omega_n)\delta(\omega-\omega_1-\omega_2-...-\omega_n) \tag{2.4}$$

As a reminder of the δ-function, the notation $\chi^{(n)}(-\omega;\omega_1,\omega_2,...\omega_n)$ with $\omega = \omega_1+\omega_2+...\omega_n$ is generally used. $\chi^{(n)}$ is an (n+1)-th order tensor mixing the different spatial projections of the electric field. For simplicity and without loss of generality for the topics covered here, we can ignore the vectorial character of the electric field and the polarization density, and treat the susceptibility as a scalar field. To first order, the expansion of the polarization with the electric field gives the linear susceptibility of the medium $\chi^{(1)}$, which dominates the answer of the medium in the limit of low power. For centrosymmetric materials, in which the structural properties are invariant by symmetry around a center (including gases and liquids), the second-order susceptibility $\chi^{(2)}$ vanishes. Second-order nonlinear crystals in Optical Parametric Oscillators have played a historical role in quantum optics and are a widely used source of entangled and squeezed light. The third-order susceptibility $\chi^{(3)}$ is thus the lowest order nonlinear correction to the polarization of atomic gases. The generally complex nonlinear susceptibility defined in Eq. 2.2 encompasses the non-instantaneous response of the medium and is simplified when the electric field is restricted to a superposition of quasi-monochromatic waves, with carrier frequencies ω_i and slowly varying envelopes $\mathcal{E}_i(\mathbf{r},t)$ propagating along z with wave vectors $k_i = \omega_i/c$ in vacuum:

$$E(\mathbf{r},t) = \sum_i \mathcal{E}_i(\mathbf{r},t)e^{i(k_i z-\omega_i t)} + c.c. \tag{2.5}$$

In that case, the response of the medium can be considered instantaneous on the scale of the slow-varying envelopes of the field, and the polarization can similarly be expanded as:

$$P^{(n)}(\mathbf{r},t) = \sum_l \mathcal{P}^{(n)}_l(\mathbf{r},t)e^{i(k_l z-\omega_l t)} + c.c. \tag{2.6}$$

where the carrier frequencies ω_l are generated by a combination of the electric field carrier

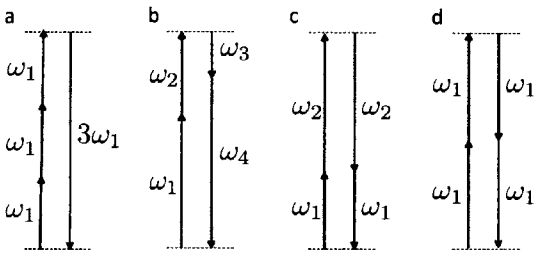

Figure 2-1: **Example of four-photon nonlinear processes.** **a,** Third harmonic generation, described by $\chi^{(3)}(-3\omega_1; -\omega_1, \omega_1, \omega_1)$. **b,** Non degenerate four-wave mixing ($\chi^{(3)}(-\omega_4; -\omega_3, \omega_2, \omega_1)$). **c,** Cross-phase and cross-amplitude modulation ($\chi^{(3)}(-\omega_1; -\omega_2, \omega_2, \omega_1)$). **d,** Optical Kerr effect ($\chi^{(3)}(-\omega_1; -\omega_1, \omega_1, \omega_1)$).

frequencies $\omega_l = \omega_i + \omega_j + ... + \omega_k$. We adopted the convention $\omega_i > 0$ for positive indices and $\omega_{-i} = -\omega_i$ and $\mathcal{E}_{-i} = \mathcal{E}_i{}^*$. The slow varying envelopes are related by:

$$\mathcal{P}_l^{(n)}(\mathbf{r}, t) = \epsilon_0 \chi^{(n)}(-\omega_l; \omega_i, \omega_j, \omega_k) \mathcal{E}_i(\mathbf{r}, t) \mathcal{E}_j(\mathbf{r}, t) ... \mathcal{E}_k(\mathbf{r}, t) \tag{2.7}$$

Third order nonlinearities in atomic media give rise to the rich physics of four-photon processes, most notably third harmonic generation and four-wave mixing, illustrated in Fig. 2-1. In the context of this work, we are interested in two cases of degenerate four-wave mixing. The first one is the optical (self-)Kerr effect, *i.e.* the nonlinear response of the medium to a quasi-monochromatic beam $\mathcal{E}_1$:

$$\chi(-\omega_1; \omega_1) = \chi^{(1)}(-\omega_1; \omega_1) + \chi^{(3)}(-\omega_1; -\omega_1, \omega_1, \omega_1) \left|\mathcal{E}_1\right|^2 \tag{2.8}$$

The second is the optical cross-Kerr effect (also called cross-modulation), in which a field $\mathcal{E}_2$ modifies the optical properties of the medium for a distinguisable field $\mathcal{E}_1$:

$$\chi(-\omega_1; \omega_1) = \chi^{(1)}(-\omega_1; \omega_1) + \chi^{(3)}(-\omega_1; -\omega_2, \omega_2, \omega_1) \left|\mathcal{E}_2\right|^2 \tag{2.9}$$

Optical Kerr media exhibit an intensity-dependent index of refraction $n = n_0 + n_2 I$, a phenomenon analogous to the modification of the index of refraction in dielectric materials proportionally to the square of an applied static electric field, discovered by physicist John Kerr at the end of the 19th century.

2.2 Propagation in dielectric media

2.2.1 Propagation in a nonlinear Kerr medium

This section is a brief reminder about the propagation of an electric field **E** in a dielectric medium. For a medium devoid of free charges and free currents, the Maxwell equations reduce to:

$$\nabla^2\vec{E} - \nabla(\nabla.\vec{E}) - \frac{1}{c^2}\frac{\partial^2\vec{E}}{\partial t^2} = \frac{1}{\epsilon_0 c^2}\frac{\partial^2\vec{P}}{\partial t^2} \tag{2.10}$$

The second term in Eq. 2.10 vanishes for a plane wave and is generally negligible in the slow varying envelope approximation (see for example [49]). Equation 2.10 can be further simplified for fields with slowly varying envelopes. Under the assumptions (which must be valid up to $n = 2$):

$$\begin{aligned}\left|\frac{\partial^n\mathcal{E}_i(z,t)}{\partial t^n}\right| \ll \omega_i\left|\frac{\partial^{n-1}\mathcal{E}_i(z,t)}{\partial t^{n-1}}\right|, \left|\frac{\partial^n\mathcal{E}_i(z,t)}{\partial z^n}\right| \ll k_i\left|\frac{\partial^{n-1}\mathcal{E}_i(z,t)}{\partial z^{n-1}}\right|, \\ \left|\frac{\partial^n\mathcal{P}_i(z,t)}{\partial t^n}\right| \ll \omega_i\left|\frac{\partial^{n-1}\mathcal{P}_i(z,t)}{\partial t^{n-1}}\right|,\end{aligned} \tag{2.11}$$

keeping the lowest order terms in the temporal and spatial derivatives for $\mathcal{E}$ and $\mathcal{P}$ and ignoring rotating terms, the propagation of the slow varying envelopes is given by:

$$\frac{1}{2k_i}\nabla_\perp^2\mathcal{E}_i + \frac{\partial\mathcal{E}_i}{\partial z} + \frac{1}{c}\frac{\partial\mathcal{E}_i}{\partial t} = \frac{ik_i}{2\epsilon_0}\mathcal{P}_i \tag{2.12}$$

We consider a one-dimensional problem in which the amplitude of the field is only dependent on the propagation direction z. We thus neglect the first term of the equation, although we point out that Kerr-type nonlinearities can have dramatic effects on the beam profile such as self-focusing. For a one-dimensional Kerr medium, the slow varying envelope approximation simplifies to (with $j = i$ for the self-Kerr effect):

$$\frac{\partial\mathcal{E}_i}{\partial z} + \frac{1}{c}\frac{\partial\mathcal{E}_i}{\partial t} = \frac{ik_i}{2}\chi_I^{(1)}\mathcal{E}_i + \frac{ik_i}{2}\chi^{(3)}\left|\mathcal{E}_j\right|^2\mathcal{E}_i \tag{2.13}$$

The real part of the susceptibility sets the index of refraction $n_i = 1 + \frac{1}{2}\chi_R^{(1)}(\omega_i)$, and has been factored out of Eq. 2.13 by the transformation: $\mathcal{E}_i \rightarrow \mathcal{E}_i e^{\frac{ik_i}{2}\chi_R^{(1)}z}$. The imaginary part

governs the linear intensity absorption per unit length in the medium: $\alpha = k_i \chi_I^{(1)}$. Kerr nonlineartities induce, in the absence of linear absorption for $\mathcal{E}_j$, a nonlinear phase shift (for an homogeneous medium of length L and monochromatic fields) $\phi_{XPM} = \frac{k_i L}{2} \chi_R^{(3)} |\mathcal{E}_j|^2$ and a nonlinear two-photon absoprtion $\alpha = k_i L \chi_I^{(3)} |\mathcal{E}_j|^2$.

2.2.2 Group velocity, bandwidth and dispersion

In this section, we consider the effect of the frequency dependence of the linear susceptibility for time-varying fields, typically pulses, which are broadened in the frequency domain and sample this dependence in near-resonant systems. The resulting effects, such as bandwidth, reduced group velocity and group velocity dispersion, can play a major role for phenomena with narrow resonances such as EIT. For a linear susceptibility χ, relating the polarization density of the medium and the local electric field according to:

$$\mathcal{P}_1(z, \delta\omega) = \epsilon_0 \chi(\omega_1 + \delta\omega) \mathcal{E}_1(z, \delta\omega) \tag{2.14}$$

where the slow varying envelope $\mathcal{P}_1$ and $\mathcal{E}_1$ are non-zero over a small range of frequencies $\delta\omega = \omega - \omega_1$, the Fourier transform of Eq. 2.12 is:

$$\frac{\partial \mathcal{E}_1}{\partial z} - \frac{i\delta\omega}{c} \mathcal{E}_1(z, \delta\omega) = \frac{ik_1}{2} \chi(\omega_1 + \delta\omega) \mathcal{E}_1(z, \delta\omega) \tag{2.15}$$

and its solution:

$$\mathcal{E}_1(z, \delta\omega) = \mathcal{E}_1(0, \delta\omega) e^{i\left(\frac{\delta\omega}{c} + \frac{k_1}{2}\chi(\omega_1 + \delta\omega)\right)z} \tag{2.16}$$

We can expand the linear susceptibility in series of $\delta\omega$:

$$\chi(\omega_1 + \delta\omega) = \chi(\omega_1) + \chi'(\omega_1)\delta\omega + \frac{1}{2}\chi''(\omega_1)\delta\omega^2 ... \tag{2.17}$$

To further simplify the problem, we nullify the linear effects $\chi(\omega_1) = 0$ (as is ideally the case for EIT).

In time domain, the field is given by the Fourier transform of Eq. 2.16:

$$\mathcal{E}_1(z,t) = \int d(\delta\omega) e^{-i\delta\omega t} \mathcal{E}_1(0,\delta\omega) e^{iz(\frac{1}{c}+\frac{k_1}{2}\chi'_R)\delta\omega} e^{iz\frac{k_1}{4}\chi''\delta\omega^2} \tag{2.18}$$

An initial Gaussian pulse with length τ_p at the input of the medium $E_1(0,t) = \exp\left(\frac{-t^2}{2\tau_p^2}\right)$ has a Fourier transform $E_1(0,\delta\omega) = \sqrt{2\pi\tau_p^2}\exp\left(\frac{-\delta\omega^2\tau_p^2}{2}\right)$:

$$\mathcal{E}_1(z,t) = \sqrt{2\pi\tau_p^2}\int d(\delta\omega) e^{-i\delta\omega(t-(\frac{1}{c}+\frac{k_1}{2}\chi'_R)z)} e^{\frac{-\delta\omega^2}{2}(\tau_p^2+iz\frac{k_1}{2}\chi'')} \tag{2.19}$$

From Eq. 2.19, we can immediately conclude from the substitution $t \rightarrow t - v_g^{-1}z$ that the first derivative of the linear susceptibility sets the group velocity:

$$v_g = \frac{c}{1 + c\frac{k_1}{2}\chi'_R(\omega_1)} \tag{2.20}$$

It is also obvious that the second order derivative affects the pulse width τ_p as the pulse propagates in the medium. The Fourier integration yields:

$$\mathcal{E}_1(z,t) = \left(\frac{\tau_p^4}{\left(\tau_p^2 - \frac{k_1}{2}\chi''_I z\right)\tau^2(z)}\right)^{1/4} \exp\left(-\frac{(t-v_g^{-1}z)^2}{2\tau^2(z)}\right) \tag{2.21}$$

where:

$$\tau^2(z) = \left(\tau_p^2 - \frac{k_1}{2}\chi''_I z\right) + \left(\tau_p^2 - \frac{k_1}{2}\chi''_I z\right)^{-1}\left(\frac{k_1}{2}\chi''_R z\right)^2 \tag{2.22}$$

Up to second order in the expansion of the linear susceptibility, the Gaussian profile of the pulse is conserved with a width $\tau(z)$ increasing as the pulse travels through the medium at group velocity v_g. The broadening of the pulse is caused by two separate effects originating from the second derivative of the susceptibility. The first effect is the bandwidth (for a transmission peak, $\chi''_I < 0$). When an initial short pulse ($\tau_p^2 < \frac{k_1}{2}|\chi''_I| L$) is broader than the bandwidth of the medium in frequency domain, the high frequency components of the slowly varying envelope are absorbed by the medium, erasing the sharp features of the pulse in time domain by dissipation. The second mechanism causing pulse spreading is the group velocity dispersion $\partial v_g/\partial\omega \propto \chi''_R$: the variation in group velocity across the different frequencies composing the wavepacket travel causes the slow varying envelope of the pulse to sprawl dispersively (*i.e.* without losses).

2.2.3 Solitons

Group velocity and bandwidth play an essential role in EIT. An interesting example of higher order contributions of the susceptibility in nonlinear optics is given by the physics of solitons in Kerr media, where dispersion and Kerr nonlinearities (effectively an intensity-dependent group velocity) have counteracting effects and allow the propagation of a "solitary wave" without deformation. The Fourier transform $\mathcal{FT}$ of equation Eq. 2.13 governs the evolution $\mathcal{E}_1(z,\delta\omega)$, similarly to Eq. 2.15, assuming $\chi^{(1)}(\omega_1) = 0$. Here, we included the frequency dependance of the linear susceptibility to second order:

$$\frac{\partial \mathcal{E}_1}{\partial z} - \frac{i\delta\omega}{c}\mathcal{E}_1 = \frac{ik_1}{2}\chi^{(1)'}\delta\omega\mathcal{E}_1 + \frac{ik_1}{4}\chi^{(1)''}\delta\omega^2\mathcal{E}_1 + \frac{ik_1}{2}\mathcal{FT}\left(\chi^{(3)}\left|\mathcal{E}_1(z,t)\right|^2\mathcal{E}_1(z,t)\right) \quad (2.23)$$

Going back to time domain through the inverse Fourier transform, we obtain the propagation equation for $\mathcal{E}_1(z,t)$:

$$\frac{\partial \mathcal{E}_1}{\partial z} + \frac{1}{v_g}\frac{\partial \mathcal{E}_1}{\partial t} = -\frac{ik_1}{4}\chi^{(1)''}\frac{\partial^2 \mathcal{E}_1}{\partial t^2} + \frac{ik_1}{2}\chi^{(3)}\left|\mathcal{E}_1\right|^2\mathcal{E}_1 \quad (2.24)$$

In the coordinates system $(Z = z - v_g t, z)$, the equation takes the form of a nonlinear Schroedinger equation (NLSE) where z plays the role of time and Z the role of space (we assume $\chi''^{(1)}$ and $\chi^{(3)}$ are real, *i.e.* that the susceptibility of the medium is purely dispersive, as is typically the case far off resonance):

$$i\frac{\partial \mathcal{E}_1}{\partial z} = -\frac{1}{2}\left(\frac{\partial v_g}{\partial \omega}\right)_{\omega_1}\frac{\partial^2 \mathcal{E}_1}{\partial Z^2} - \frac{k_1}{2}\chi^{(3)}\left|\mathcal{E}_1\right|^2\mathcal{E}_1 \quad (2.25)$$

The effective mass originates from the group velocity dispersion: $m^{-1} = \partial_\omega v_g(\omega_1)$. A particular solution of the NLSE when m and $\chi^{(3)}$ are of same sign is the temporal soliton [50]:

$$\mathcal{E}(z,Z) = E_s\frac{\exp\left(i\frac{k_1}{4}\chi^{(3)}E_s^2 z\right)}{\cosh(Z/a)} \quad (2.26)$$

where the spatial extent of the soliton a depends on the peak electric field amplitude E_s as:

$$a = \sqrt{\frac{2}{mk_1\chi^{(3)}E_s^2}} \tag{2.27}$$

Optical solitons were first proposed in the 1970s as a mean to increase the digital data rate in fibers limited by pulse spreading[51].

2.3 Nonlinear Lorentz model

The Lorentz model of an elastically bound electron correctly predicts the linear response of the medium for atomic gases[50] and can be used to estimate the strength of the nonlinear susceptibility[49]. The first centro-symmetric correction to the harmonic potential is a quadratic potential $U = -\frac{1}{2}m\omega_0^2 r^2 - \frac{1}{4}mb|\vec{r}|^4$. The equation of motion for the electron becomes:

$$\ddot{\vec{r}} - \Gamma\dot{\vec{r}} + (\omega_0^2 + b|r|^2)\vec{r} = -eE/m \tag{2.28}$$

In absence of the correction term, the damped harmonic response of the system to the drive of the electric field oscillating at ω is the well-know Lorentzian response near resonance ($|\omega - \omega_0| \sim \Gamma \ll \omega_0, \omega$), $\chi^{(1)} = -\frac{\mathcal{N}e^2}{m\epsilon_0}D(\omega)^{-1} \approx \frac{\mathcal{N}e^2}{m\omega_0\epsilon_0}\frac{1}{(\omega-\omega_0)-i\Gamma}$, where:

$$D(\omega) = \omega_0^2 - \omega^2 + i\Gamma\omega. \tag{2.29}$$

For $b \neq 0$ the system can be solved perturbatively. For a superposition of monochromatic fields: $E = \sum_i \mathcal{E}_i e^{i\omega_i t} + \mathcal{E}_{-i}e^{i\omega_{-i}t}$, the polarization is expanded as:

$$r = \frac{\epsilon_0}{\mathcal{N}e}\left(\sum_i \chi^{(1)}(\omega_i)\mathcal{E}_i + \sum_{i,j}\chi^{(2)}(\omega_i+\omega_j)\mathcal{E}_i\mathcal{E}_j + \sum_{i,j,k}\chi^{(3)}(\omega_i+\omega_j+\omega_k)\mathcal{E}_i\mathcal{E}_j\mathcal{E}_k + ...\right) \tag{2.30}$$

Up to third order, the susceptibilities satisfy:

$$-\frac{\mathcal{N}e^2}{m\epsilon_0} = \chi^{(1)}(\omega_i) \times (\omega_0^2 - \omega_i^2 + i\Gamma\omega_i), \tag{2.31}$$

$$0 = \chi^{(2)}(\omega_i + \omega_j) \times (\omega_0^2 - (\omega_i + \omega_j)^2 + i\Gamma(\omega_i + \omega_j)), \tag{2.32}$$

$$0 = \chi^{(3)}(\omega_i + \omega_j + \omega_k) \times [\omega_0^2 - (\omega_i + \omega_j + \omega_k)^2 + i\Gamma(\omega_i + \omega_j + \omega_k)] + \frac{b\epsilon_0^2}{\mathcal{N}^2e^2}\chi^{(1)}(\omega_i)\chi^{(1)}(\omega_j)\chi^{(1)}(\omega_k), \tag{2.33}$$

yielding $\chi^{(2)}(\omega_i + \omega_j) = 0$, as expected from a centrosymmetric material, and the third order nonlinear susceptibility

$$\chi^{(3)}(\omega_i + \omega_j + \omega_k) = b\frac{\mathcal{N}e^4}{m^3\epsilon_0}[D(\omega_i + \omega_j + \omega_k)D(\omega_i)D(\omega_j)D(\omega_k)]^{-1}, \tag{2.34}$$

which simplifies to

$$\chi^{(3)}(\omega) = b\frac{\mathcal{N}e^4}{m^3\epsilon_0}[D(\omega)^3D(-\omega)]^{-1} \tag{2.35}$$

for a Kerr medium. This simple model underlines a crucial limitation for most nonlinear media: the third-oder nonlinear susceptibility is simultaneously resonant with the linear susceptibility. To avoid linear absorption, it is necessary to largely detune the field from the atomic resonance, which results in a large suppression (to the power 4) of the nonlinear susceptibility, and conventional material are strongly dominated by linear effects. The highest values for the nonlinear susceptibility in the strongly detuned regime are achieved for a red-detuned field $\omega \ll \omega_0$, for which $D \approx \omega_0^2$.

We can also extract order of magnitudes for the nonlinear susceptibility from the bound-electron model. An upper-bound for the nonlinear correction b is obtained by comparing the corrective force to the restoring force. For a typical atomic dimension given by the Bohr radius a_0, the perturbation due to the electric field equals the force exerted by the nucleus on the electrons for $b\,a_0^2 \sim \omega_0^2$. Using $D = \omega_0^2$ and an atomic density (for a solid) $\mathcal{N} = a_0^{-3}$, the third order nonlinear susceptibility is limited to:

$$\chi^{(3)} < \frac{e^4}{m^3\epsilon_0}\frac{\omega_0^{-6}}{a_0^5} \sim 10^{-16}\mathrm{V}^{-2}\ \mathrm{m}^2 \tag{2.36}$$

Measured values for conventional materials are summarized in [49]. Most conventional

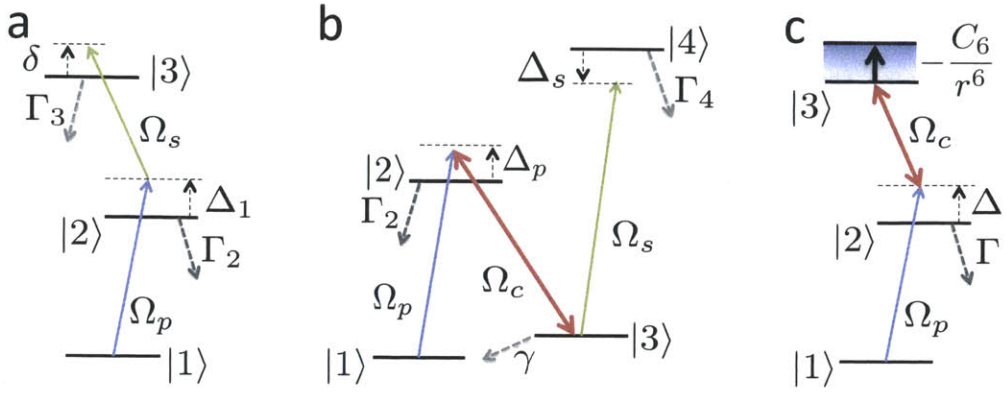

Figure 2-2: **Third-order nonlinearities in multi-level atoms. a,** Cross-modulation in a 3-level atomic system. To avoid strong linear absorption, it is necessary to operate at large detuning Δ_1 with respect to the intermediate state $|2\rangle$, which weakens the nonlinear two-photon absorption or cross-phase modulation. **b,** EIT-based nonlinear optics. Under EIT conditions, the linear susceptibility vanishes while a third-order nonlinear susceptibility is induced by the additional switch field Ω_s. **c,** Rydberg-blockade mediated nonlinear interactions. At large enough probe intensity, the Rydberg level is detuned out of resonance and the effect of the control field is cancelled. The susceptibility of the medium is then given by the bare $|1\rangle \rightarrow |2\rangle$ transmission. (Notations are defined in the text).

materials such as glass, crystals, liquids, gases have a third-order nonlinear susceptibility ranging from 10^{-22} V^{-2} m^2 to 10^{-19} V^{-2} m^2. Certain nano-particles and polymers achieve third-order nonlinear susceptibility up to 10^{-16} V^{-2} m^2. For single photon applications, the proper figure of merit is the product of the nonlinear susceptibility by the bandwidth of the system, which determines the minimum length of a single photon pulse.

2.4 Nonlinear optics in 3-level atoms

In media with narrow and well defined optical resonances, typically atomic gases, the level structure can be exploited to optimize multi-photon resonances and enhance the nonlinear processes. In such systems the susceptibility can be precisely calculated from the Bloch equations (see for example Appendix A), which include decay and decoherence and reduce to a system of linear equations in the steady state regime.

The simplest resonant atomic system exhibiting third-order nonlinearities is an ensemble of 3-level atoms. We consider a ladder-type level scheme where the excited states $|2\rangle$ and $|3\rangle$ have a finite lifetime Γ_2 and Γ_3, and the probe (respectively switch) field couples the $|1\rangle \rightarrow |2\rangle$ (respectively $|2\rangle \rightarrow |3\rangle$) transition with Rabi frequency Ω_p (Ω_s) and detuning Δ_1 ($\Delta_2 = \delta - \Delta_1$) (see Fig. 2-2,a). The Bloch equations in the steady-state regime and under the approximation that the atoms populate principally the ground state yield the susceptibility for the probe field $\tilde{\chi} = \frac{k_1}{2}\chi$ to lowest order in Ω_s as a function of the absorption length of the medium $l_a = \mathcal{N}\sigma_0$ (where σ_0 is the resonant atomic cross-section for the probe field) (see Eq. A.12):

$$\tilde{\chi} \approx \frac{i}{2l_a}\frac{\Gamma_2}{(\Gamma_2 - 2i\Delta_1)}\left(1 - \frac{|\Omega_s|^2}{(\Gamma_3 - 2i\delta)(\Gamma_2 - 2i\Delta_1)}\right) \tag{2.37}$$

The first term in Eq. 2.37 is the characteristic linear Lorentzian absorption profile with peak absorption $OD = \int l_a^{-1} dz$. Due to the large linear absorption, it is necessary to operate at large detuning $\Delta_1 \gg \Gamma_2$ where the intensity attenuation is $OD\Gamma_2^2/(4\Delta_1^2)$ (for a corresponding phase-shift $OD\Gamma_2/(4\Delta_1)$) in the absence of switch field. The second term is the cross-Kerr nonlinearity with the switch beam, which induces two-photon absorption and cross-phase modulation. At large intermediate detuning $\Delta_1 \gg \Gamma_2$ and at two-photon resonance ($\delta = 0$), the presence of the weak Rabi-frequency Ω_s increases the absorption per unit length of the medium by a factor $1 + \Omega_s^2/(\Gamma_2\Gamma_3)$. This expansion is valid in the limit $\Omega_s^2 \ll \Gamma_2\Gamma_3$ for which the nonlinearities are negligible with respect to the linear absorption. The opposite regime, $\Omega_s^2 \gg \Gamma_2\Gamma_3$, corresponds to EIT (see Appendix A).

Cross-phase modulation (XPM) is obtained by introducing a finite two-photon detuning δ to avoid two-photon absorption. For $\Delta_1 \gg \Gamma_2$ and $\delta \gg \Gamma_3$, the switch beam induces a nonlinear phase-shift of the probe beam $OD\frac{\Gamma_2}{16\Delta_1^2\delta}|\Omega_s|^2$. The nonlinear phase-shift is strongly weakened by the large detuning from the intermediate state Δ_1 and is negligible at the low light intensities provided by few photon pulses. The physical interpretation for the cross phase modulation in the limit of large switch field detuning is simply that the Stark effect of the switch field detunes the intermediate level $|2\rangle$ by an amount $|\Omega_s|^2/4(\delta - \Delta_1)$, which modifies the linear response to $OD\Gamma_2/[4(\Delta_1 + |\Omega_s|^2/4(\delta - \Delta_1)] \sim OD\frac{\Gamma_2}{(4\Delta_1)}(1 - \frac{|\Omega_s|^2}{4\delta\Delta_1})$ for $\delta \gg \Delta_1$. Finally, another figure of merit for the cross-phase modulation is the ratio $\Omega_s^2/(\Gamma_2\delta)$ between the absorption (here mainly linear) and the nonlinear phase-shift.

Two-photon absorption and cross-phase modulation in atomic ensembles illustrate the dominance of linear effects on nonlinear processes in resonant multi-level systems. The necessary large detunings has so far prevented the observation of nonlinear phase-shifts larger than a few tenths of milliradians per photon [52].

2.5 EIT-enhanced nonlinear optics

As described in Appendix A, a strong coherent control field meeting the two photon resonance condition cancels the linear absorption and phase shift of an ensemble of three-level atoms. One of the most remarkable properties of EIT is the persistence of third order nonlinearities even as the linear susceptibility vanishes, as pointed out by Imamoglu, Harris and coworkers in the 1990s[39, 40, 53, 54]. As a result, under EIT conditions, four-wave mixing occur in the absence of linear absorption and phase-shift (see [55] and references therein). This starkly contrasts with traditional media where the nonlinearities amount to a negligible fraction of the linear effects at low probe power. Here, we focus on cross-Kerr type nonlinearities between a probe field and a switch field (of Rabi frequency Ω_s) in a N-type level scheme [40, 53, 54, 56]. The switch field couples the ground state carrying the spin coherence $|3\rangle$ to a fast-decaying state $|4\rangle$ (see Fig. 2-2,b). The extra ground-state decoherence introduced by this coupling modifies the propagation properties for the probe field, otherwise traveling without loss under EIT conditions. The susceptibility of the medium (derived from the Bloch equations) is:

$$\tilde{\chi} = \frac{i}{2l_a}\frac{\Gamma_2\gamma}{\gamma(\Gamma_2 - 2i\Delta_s) + |\Omega_c|^2} \times \left(1 + \frac{|\Omega_c|^2}{\gamma(\Gamma_4 - 2i\Delta_s)(\gamma(\Gamma_2 - 2i\Delta_p) + |\Omega_c|^2)}|\Omega_s|^2\right) \tag{2.38}$$

where we assumed that the probe and control field match the two-photon resonance with the $|1\rangle \rightarrow |3\rangle$ transition. Γ_2 is the decay rate of the intermediate excited state $|2\rangle$, Γ_4 the decay rate of the state $|4\rangle$ and γ the decoherence between ground states $|1\rangle$ and $|2\rangle$. In Eq. 2.38, the linear EIT susceptibility is modified by a correction term corresponding to the cross-Kerr nonlinear susceptibility.

We first turn to all-optical switching for the resonant case $\Delta_p = \Delta_s = 0$. The residual linear absorption of the medium $OD\gamma/\gamma_{EIT}$ (where $\gamma_{EIT} = \Omega_s^2/\Gamma_2$) is amplified by the switch-induced decoherence $\gamma \rightarrow \gamma + \Omega_c^2/\Gamma_4$, resulting in a nonlinear absorption $OD\Omega_s^2/(\Gamma_4\gamma_{EIT})$. The nonlinear effects are strongly enhanced as the EIT linewidth γ_{EIT} is narrowed. The EIT linewidth is only limited by the decoherence rate γ due to the linear absorption, and in the limit of small decoherence rates $\gamma \ll \Gamma_2$ can be made much narrower than the excited state linewidth. A figure of merit for all-optical switching is the ratio between nonlinear and linear absorption: $\Omega_s^2/(\Gamma_4\gamma)$, which is improved by a factor Γ_2/γ with respect to the 3-level system introduced in the previous section.

EIT-enhanced XPM are obtained by detuning the switch field away from resonance. In the limit $\Delta_3 \gg \Gamma_4$, the XPM phase-shift is $OD\Omega_s^2/(\gamma_{EIT}\Delta_3)$. The ratio between the nonlinear phase shift and the absorption in the medium is Δ_3/Γ_4. In contrast to conventional XPM in a 3-level medium, this number does not depend on the switch field intensity. For a given Ω_s, the EIT linewidth will determine the nonlinear phase-shift whose upper bound $OD\Omega_s^2/(\gamma\Gamma_4)$ can be made arbitrarily large in the absence of decoherence. Experimentally, low decoherence rates are limited by the 2-photon laser linewidth, Doppler broadening, atomic collisions, inhomogeneous magnetic shifts or trapping potentials. It is possible to compensate for these effect to obtain coherence time of a few seconds [57] using specific clock transitions and compensation for inhomogeneous trapping shifts. With conventional lasers used in atomic physics and spectroscopy based frequency locks, the typical laser linewidths are on the order of 100 kHz, and are generally the limiting dephasing factor in cold dilute gases, setting the typical EIT linewidth γ_{EIT} to a few MHz, on the order of the excited states atomic linewidths.

The photon-photon interaction can be characterized by the magnitude of the Kerr effect obtained for bandwidth limited pulses containing a single photon. A pulse acquires a group delay $\tau_d = OD/\gamma_{EIT}$ in the medium. The switch pulse is not slowed down by the medium, and covers the delay time of the probe pulse when its length τ_s equals the probe pulse delay (in the large OD limit where the probe pulse is entirely stored in the medium). The Rabi frequency of a single photon switch pulse is then:

$$\Omega_s^2 \cong \frac{\sigma_s}{A}\frac{\Gamma_4}{\tau_s} \cong \frac{1}{OD}\frac{\sigma_s}{A}\gamma_{EIT}\Gamma_4 \tag{2.39}$$

in terms of the atomic cross-section for the switch field $\sigma_s = |\mu_{34}|^2 \frac{2\omega_s}{c\epsilon_0 \hbar \Gamma_4}$ (μ_{34} is the dipole matrix element for the switch transition), and the transverse area of the switch beam A. We used the energy of a single photon pulse $\hbar\omega_s = \int_V \epsilon_0 E^2 \approx \epsilon_0 c\tau_s A E^2$. As a consequence, typical quantum nonlinear effects, such as conditional absorption and phase-shift, are on the order of the cooperativity:

$$\eta = \frac{\sigma_s}{A}, \tag{2.40}$$

which is the probability for a photon to be scattered by a single atom. In the polariton picture (see Chapter A), a probe photon traveling in the medium is mapped onto an coherently shared atomic excitation carried by an atom in state $|3\rangle$. The photon-photon interaction will thus be consequent if the switch photon has a large interaction probability with the atom on which the spin coherence is imprinted.

As a consequence, optical nonlinearities are only achieved at the single-photon level for a strong transverse light confinement over the extent of the medium. The resonant atomic cross section is, for the strongest transition between magnetic sub-levels, $\sigma_0 = \frac{3}{2\pi}\lambda^2$ and large nonlinearities require transverse light confinement to better than a wavelength. In Chapter 3, we describe an experiment where cold atoms are loaded into a hollow-core fiber, giving a cooperativity $\eta \sim 0.5$ over the extent of the medium and which displays nonlinearities for a few-hundred photons.

It is nevertheless possible to beat the cooperativity limit by modifying the group velocity of the switch pulse[58]. For a matched group velocity with the probe field, the switch pulse width can be reduced to its bandwidth limited value $\tau_p = \tau_d/\sqrt{OD}$: the photon-photon interaction then scale as $\sqrt{OD}\eta$. An even stronger enhancement is offered by Stationary Light Pulse techniques [59, 60], for which the nonlinearities scale linearly with OD. Experimental progress towards the implementation of these ideas is reported in Chapter 4.

2.6 Rydberg EIT

The properties of Rydberg atoms are described in Chapter 5. The two main characteristics that distinguish them from the low lying excited states are the long lifetime (typically ~ 100 μs for the $100S_{1/2}$ state of ^{87}Rb including room-temperature blackbody radiation)

and their large dipole moment. The large dipole moment results in long range Van der Waals interaction which can shift the Rydberg levels by several tens of MHz for atoms located at distances as large as 10 μm. This concept leads to the so-called dipole blockade, which prevents simultaneous optical excitation of several atoms in a certain volume (see Chapter 5). Due to their long-lived states, Rydberg levels can be used as a metastable state to enable EIT in an otherwise opaque medium. If a strong control-field is resonant with an (intermediate) excited- to Rydberg- state transition, a single probe photon coupling the atomic population in its ground state to the intermediate excited state will propagate in the medium under the form of a dark state polariton (see Appendix A). The dipole-dipole interaction strongly modifies the properties of the medium for multi-photon states propagating simultaneously by tuning the Rydberg of level far out of resonance, effectively cancelling the effect of the control field for most of the photons.

The dipole-dipole interaction is described by the interaction Hamiltonian:

$$\hat{H}_{int} = \hbar \sum_{i,j=1;i\neq j}^{N} V_{ij}\hat{\sigma}_{33}^{i}\hat{\sigma}_{33}^{j} \tag{2.41}$$

where $\hbar V_{ij} = -C_6/\left|\vec{r}_i - \vec{r}_j\right|^6$ is the Van der Waals interaction between two atoms located at $\vec{r}_i$ and $\vec{r}_j$. The blockade introduces correlations between the atoms, which are mapped onto the polarization of the medium. The nonlinear susceptibility of the medium in the low density limit can be derived from a mean-field approach[61]. For $\Delta_1 = \Delta_2 = 0$, the polarization of the medium is given by [61]:

$$\tilde{\chi}(\mathbf{r}) = i\frac{1}{2l_a}\frac{\gamma\Gamma_2}{\gamma\Gamma_2 + \left|\Omega_c\right|^2} - \frac{1}{2l_a}\Gamma\rho\frac{\Omega_p(\mathbf{r})\Omega_c^4}{\left(\Omega_c^2 - \gamma\Gamma\right)\left|\Omega_c^2 + \gamma\Gamma\right|^2}\int d\mathbf{r}'\frac{2\left|\Omega_p(\mathbf{r}')\right|^2\frac{C_6}{|\mathbf{r}-\mathbf{r}'|^6}}{\Omega_c^2 + \gamma\Gamma + i\Gamma\frac{C_6}{|\mathbf{r}-\mathbf{r}'|^6}} \tag{2.42}$$

The first term, dominant at low probe intensity, describes the EIT. The finite decoherence rate γ creates negligible absorption in the medium in the limit $\gamma_{EIT} \gg \gamma$. The second term describes the third order non-linearity introduced by the Rydberg blockade. In the limit where $\gamma_{EIT} \gg \gamma$ and $\Omega_p(\mathbf{r}') = \Omega_p(\mathbf{r}')$ (i.e. for nonlinear effects weak enough not to create strong correlations in the probe light), the integral can be expressed as a function of the blockade radius $r_b = \left|2C_6\Gamma/\Omega^2\right|^{1/6}$:

$$\int d\mathbf{r}' \frac{2\left|\Omega_p(\mathbf{r}')\right|^2 \frac{C_6}{|\mathbf{r}-\mathbf{r}'|^6}}{\Omega^2+\gamma\Gamma+i\Gamma\frac{C_6}{|\mathbf{r}-\mathbf{r}'|^6}} \cong \frac{|\Omega_p|^2}{\Gamma}\frac{\mathrm{sgn}(C_6)-i}{3}\pi^2 {r_b}^3 \tag{2.43}$$

and the nonlinear susceptibility of the Rydberg medium in the low saturation regime is:

$$\tilde{\chi} = \frac{\pi}{2}(i-\mathrm{sgn}(C_6))\frac{1}{2l_a}\frac{4}{3}\pi {r_b}^3\rho\frac{|\Omega_p|^2}{\Omega_c^2} \tag{2.44}$$

To within a factor $\pi/2$, the imaginary nonlinear susceptibility is the product of the 2-level ($|1\rangle \rightarrow |2\rangle$) linear response $\tilde{\chi}_{12} = i(2l_a)^{-1}$, the average number of atoms per blockade volume $N_B = \frac{4}{3}\pi {r_b}^3\rho$ and the fraction of the atomic population in the Rydberg state under EIT conditions, Ω_p^2/Ω_s^2. At probe intensities corresponding to a number of Rydberg atoms per Rydberg blockade approaching one ($N_B\Omega_p^2/\Omega_c^2 \sim 1$), the susceptibility becomes that of a 2-level medium due to the cancellation of the control field by the large detuning of the Rydberg states. Rydberg EIT simultaneously provides low linear absorption and large non-linearities. In contrast to EIT enhanced nonlinearities introduced in the previous section, the ratio between the nonlinear and linear absorption can be made arbitrarily high by increasing the atomic density of the medium. To characterize the strength of the nonlinearity at the single-photon level, we again consider a bandwidth-limited single photon pulse of duration $\tau_p \sim \sqrt{OD}\gamma_{EIT}^{-1}$. The nonlinear effects in the medium are on the order of $N_B\eta$ where η is the single-photon single-atom cooperativity. The medium can be described in terms of super-atoms, made of N_b atoms comprised in a single Rydberg volume, with a cross-section $N_b\sigma_0$ (see Chapter 5). In the limit where the transverse profile A is smaller than r_b^2, the order of magnitude of the single-photon nonlinearities is given by the optical depth over a blockade length of the medium, $OD_B = \rho\sigma_0 r_b$.

Dispersive nonlinearities are obtained by introducing a large detuning Δ of the probe and control field from the intermediate transition while maintaining the two-photon resonance,. The idealized response of the medium in the large blockade fraction regime ($N_B\Omega_p^2/\Omega_c^2 \sim 1$) is that of an ensemble of an off-resonant ensemble of two-level atoms with absorption $\sim OD\Gamma^2/(4\Delta^2)$ and phase-shift $\sim OD\Gamma/(4\Delta)$, enabling non-dissipative interactions at large detunings $\Delta \gg \Gamma$. Formally, this result is obtained upon the substitution $\Gamma \rightarrow \Gamma - 2i\Delta$ and expansion to lowest order in Γ/Δ of the integral in Eq. 2.43:

$$\tilde{\chi} = \frac{\pi}{2}\frac{1}{2l_a}\left(\frac{\Gamma}{\Delta} + i\frac{\Gamma^2}{4\Delta^2}\right) \cdot \frac{4}{3}\pi {r_B}^3 \rho \frac{|\Omega_p|^2}{\Omega_c^2} \tag{2.45}$$

where the off-resonant blockade radius is $r_B = \left(4\left|C_6\Delta\right|/\Omega_c^2\right)^{\frac{1}{6}}$ [62].

As expected, to within a constant of order unity, the response of the system is the product of the two-level linear response and the number of Rydberg excitation per blockade volume. The mean-field approach used in the susceptibility calculation is valid in the limit where the number of Rydberg atoms per blockade volume is much smaller than one, for example for atomic gases with low atomic density [63, 64]. At higher densities, nonlinear effects between few photons introduce strong correlations in the probe field. Experimental results in the high density limit as well as a full quantum analysis are carried out in Chapters 7,8 and Appendices C,D.

Chapter 3

Few-photon nonlinear optics using cold atoms in a hollow-core fiber.

3.1 Overview

The implementation of few-photon nonlinear optics has until now only been feasible in the context of cavity quantum electrodynamics (QED) when single quantum emitters, such as neutral atoms or quantum dots, are placed inside narrow-band, high-finesse cavities. In these systems, the original nonlinearities of the optical medium created by the single emitter are amplified by the cavity finesse to the point where they can be controlled by the field of a single photon. Over the last decade, several experiments have demonstrated nonlinear optical phenomena with single intracavity photons [41, 65, 43, 42]. However, the large nonlinearities achievable in these cavity-based systems come at the price of technological complexity, limitations imposed by cavity bandwidth, and often times substantial losses at the input and output of the cavity. The work presented here uses an alternative approach, which is based on coupling single emitters or ensembles of emitters to a propagating light field confined to an area comparable to the diffraction limit. Such tight confinement can be achieved either in free space by focusing the light beam with a large numerical aperture lens [66] or under conditions provided by a photonic waveguide. In particular, systems based on hollow core photonic crystal fibers [67], hollow antiresonant reflecting waveguides (ARROWs) [68], optical nanofibers [69], optical nanocavities [70] and nanostructure plasmonic waveguides allowing subdiffraction propagation have all

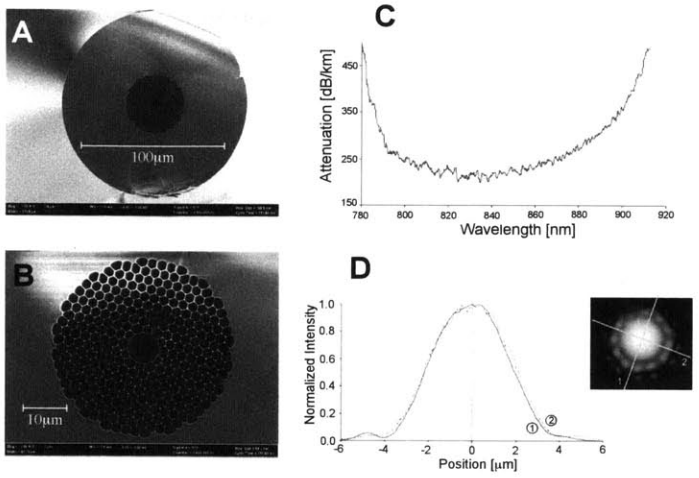

Figure 3-1: **Photonic Crystal Fiber.** (A) Scanning electron microscope (SEM) image of a cross section of the hollow-core photonic-crystal fiber from Blaze Photonics used in the experiment (model *HC-800-02*). (B) Detail of the photonic crystal region of the fiber with the hollow core in the center. Manufacturer's specifications of (C) losses of guided mode propagating in the fiber as a function of wavelength and (D) near field intensity distribution of the guided mode.

been actively explored in the last few years.

Hollow core photonic crystal fibers (PCFs, also known as photonic bandgap fibers), that guide light through interference [71] instead of total internal reflection [72], are now available off the shelf and can be integrated with conventional optical fibers [73]. When filled with molecular gas, these fibers have shown significant enhancements in the efficiency of processes such as stimulated Raman scattering [74] and four-wave mixing [75]. Recently, both room-temperature and ultra-cold atoms have successfully been loaded into PCFs [76, 77, 78] and observations of electromagnetically induced transparency with less than a micro-Watt control field have been reported for the case of room temperature atoms [76].

Here, we review our experiments that demonstrate the strong coupling between light and laser-cooled atoms inside the hollow core PCF and allow us to implement all-optical switching controlled with light pulses containing as few as several hundred photons and few atoms detection.

The atoms are first laser-cooled and collected in a free-space magneto-optical trap and then transferred into a 30mm long piece of hollow-core fiber (Fig. 3-1) with a procedure detailed in the following section. Once inside the fiber core, the cold atoms are confined

in a red detuned dipole trap [79]. The trap is created with an off-resonant beam guided by the fiber, and it prevents the atoms from colliding with the fiber wall. We probe the atoms, which form an approximately 1cm long cloud inside the fiber core, by monitoring the transmission of very-low-power ($\sim 1\,\mathrm{pW}$) probe beams that can be coupled into the fiber piece from either of its ends. After the probe beams emerge from the fiber, they are collimated by the coupling lenses and then passed through a series of optical filters that separate the probe photons from other light beams coupled into the fiber during the experiments. Finally, the probes are coupled into single-mode fibers connected to single-photon counters. The use of single-mode fibers provides spatial filtering that ensures that only photons propagating in the guided mode of the PCF are detected. When the frequency of the probe laser is scanned over an atomic resonance, we observe in the transmitted signal an approximately Lorentzian absorption line-shape from the atoms present inside the fiber:

$$T = \exp\left(-\frac{OD}{1+4(\frac{\Delta_p}{\Gamma})^2}\right), \tag{3.1}$$

where Γ is the linewidth of the excited atomic state and Δ_p is the detuning of the probe laser from resonance. The optical depth OD is a figure of merit for the strength of the observed absorption. In general, OD depends on the atomic density integrated along the fiber, and the strength of the considered atomic transition. Since the atoms are confined within the optical trap created by the guided light inside the fiber, the radial extent of the atomic cloud is smaller than the beam area of the single-mode probe light beam propagating through the fiber. To get an accurate relation between optical depth and atomic density inside the fiber, we have to take into account the atoms' radial distribution in the probe beam. In particular, an atom at the edge of a beam experiences a smaller electric field and therefore absorbs less light than an atom on the beam's axis. Assuming a Gaussian beam with waist w_o and a radially symmetric atomic density $n(r,z)$, the expression for optical depth on resonance is

$$OD_{fiber} = \frac{2}{\pi w_o^2}\int_{L_{cloud}} 2\pi \int_0^{r_{core}} n(z,r) c_{CG}^2 \sigma_o e^{-\frac{2r^2}{w_o^2}} r dr dz \tag{3.2}$$

where $\sigma_o = \frac{3\lambda^2}{2\pi}$ is the maximal atomic cross-section, and c_{CG} is the Clebsch-Gordon coefficient for the specific atomic transition being used. In general, (3.2) reduces to a

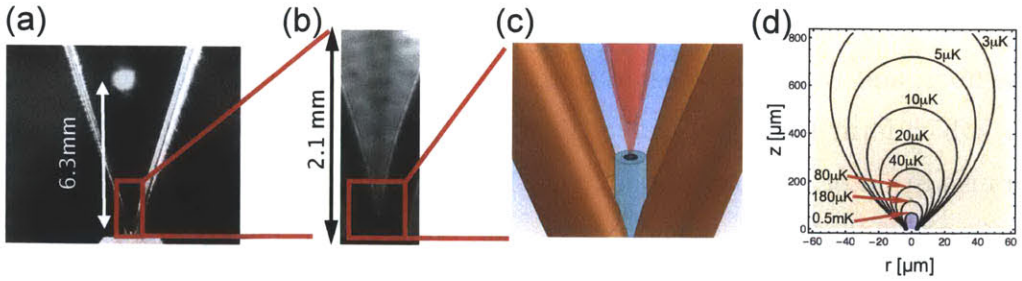

Figure 3-2: **Loading procedure into the hollow core fiber.** (a) Atoms collected in a MOT above the fiber. (b) Absorption image of the atoms in the magnetic-funnel area above the fiber. (c) Once near the fiber tip, the atoms are transferred into a red-detuned dipole trap inside the fiber. (d) Contour plot of the dipole trap potential above the fiber tip resulting from the diverging beam emerging from the fiber tip (located at the origin). The contour labels correspond to a 10 mK deep trap inside the fiber resulting from ~25 mW of 802 nm trap light inside the fiber.

simple expression that shows that OD is proportional to the number of atoms N_{at} inside the fiber:

$$OD_{fiber} = \eta\, N_{at}\, \frac{2c_{CG}^2\sigma_o}{\pi w_0^2}. \tag{3.3}$$

The prefactor η is given by the radial distribution of atoms in the fiber-confined cloud. The highest value of η corresponds to all atoms being localized on the axis of the fiber, in which case $\eta = 2$. In the case of a Gaussian radial density distribution $n(r) = n_0 e^{-\frac{r^2}{2x_0^2}}$, $\eta = \frac{2(w_0/2)^2}{x_0^2+(w_0/2)^2}$. The optical depth of the atomic cloud inside the fiber is thus determined by the number and temperature of atoms inside the fiber. In particular, higher atomic temperatures lead to more axially delocalized cloud (increased x_0), which in turn results in decreased OD. Assuming an atomic temperature $T \sim 1\,\mathrm{mK}$ and using the measured beam waist of guided light inside the fiber $w_0 = 1.9 \pm 0.2\,\mu\mathrm{m}$, ~ 100 atoms inside the fiber create an optically dense medium ($OD = 1$) when probed at the transition with the highest Clebsch-Gordon coefficient.

3.2 Loading procedure

The starting point of our fiber loading procedure is a standard six-beam magneto-optical trap (MOT) located approximately 6 mm above the upper tip of the fiber piece (Fig. 3-

2a). The required light fields are provided by three crossed retro-reflected beams with one-inch diameter, while the magnetic field is realized by the two circular coils inside the vacuum chamber operated in an anti-Helmholtz configuration. During a $\sim$ 1 s loading phase we collect about 10^7 ^{87}Rb atoms at a temperature of $\sim 100\,\mu$K in the MOT from the room-temperature rubidium vapor produced inside the vacuum chamber by a heated dispenser. Following this step, the magnetic fields are ramped up over a period of 40 ms to compress the cloud, the frequency of the trapping beams is moved from the initial 15 MHz off-resonance to 50-60 MHz detuning, and their power is reduced by a factor of ~ 4. Finally, the magnetic fields are shut off, and the atomic cloud is allowed to slowly expand for 10 ms in the optical molasses of the intersecting beams as it undergoes polarization gradient cooling. This last cooling step lowers the cloud temperature to $\sim 40\ \mu$K.

After the laser-cooling stage, we transfer the atoms downwards into the vicinity of the fiber tip (Fig. 3-2b, c) from where they are loaded into the fiber. Over the course of the experiment, we have implemented different procedures for this transfer, which are described in the following.

The original transfer procedure conceptualized during the design of the experiment is based on magnetic guiding of the atoms. In this procedure, after the initial cooling stages in the MOT and optical molasses are completed, the atoms are optically pumped into the $|F = 2, m_F = 2\rangle$ state and then transferred into a magnetic quadrupole trap formed by the same coils which provide the MOT field. This trap is then adiabatically shifted towards the fiber tip by adding a vertically-oriented homogeneous offset field, which displaces the zero-field center of the quadrupole trap. In addition, current in the magnetic funnel wires is turned on, creating a transverse quadrupole field, in which the gradient increases with decreasing distance from the upper fiber tip. At the fiber tip this transverse gradient reaches $\sim 6\,$kG/cm, resulting in strong radial compression of the magnetic trap (Fig. 3-2b). The complete transfer of the magnetic trap towards the fiber takes place over the course of 45 ms. This brings the atoms within a few hundred micrometers of the fiber tip. During the transfer stage, the fiber-guided dipole trap is turned on, so that when the atoms start approaching the fiber face, they are captured by the expanding beam of the dipole trap and pulled into the hollow core of the PCF(Fig. 3-2c, d). At the end of the transfer, all magnetic fields are shut off and the atoms are probed. With this method

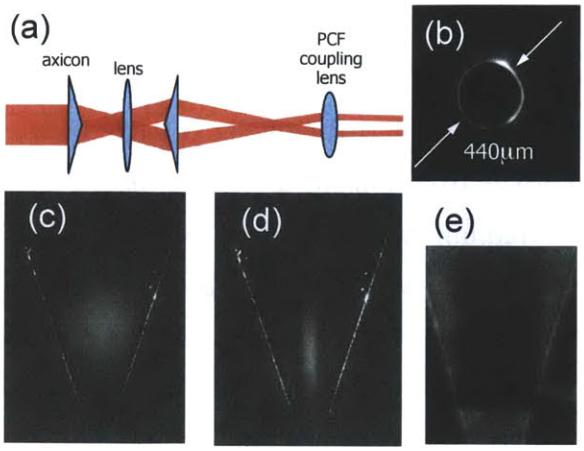

Figure 3-3: **Hollow beam atomic waveguide.** (a) Schematics of the optics used for the hollow beam generation. (b) CCD image of the hollow beam intensity distribution about 1 mm above the fiber face. (c) Fluorescence image of the freely expanding atomic cloud 20 ms after its release from the optical molasses. (d) Fluorescence image of the atomic cloud guided by the blue detuned hollow beam 20 ms after the optical molasses beams are turned off. (e) Absorption image of the atoms collected in the hollow beam guide $\sim$ 1 mm above the fiber tip. Here, the hollow beam is intersected by a blue detuned Gaussian beam focused by a cylindrical lens into a sheet.

we observe the loading of up to $\sim 10^4$ atoms into the fiber, equivalent to a maximum $OD \sim 50$.

While this procedure loads atoms into the fiber reliably, it turns out to have significant drawbacks. When current is pulsed through the funnel wires, the resulting heat pulse causes the fiber tip to shake slightly. Additionally, the cumulative heat of the repeated experimental cycles causes drifts in the overall fiber coupling efficiency. This requires the system to run for about two hours before the fiber position stabilizes and after that the funnel needs to be cycled constantly to maintain the steady-state temperature of the fiber mount.

The problems associated with the pulsed currents required for the magnetic transfer led us to the development of an all-optical transfer method. Instead of capturing the initial MOT in a magnetic trap we confine it transversally by an optical guiding potential. This atomic guide is based on a hollow-beam blue-detuned dipole trap. The hollow beam is generated using a combination of lenses and axicons (conical lenses) sketched out in Fig. 3-3a. This setup allows us to generate a vertical hollow beam that is close to collimated

both in diameter and wall thickness in the region between the MOT site and $\sim$ 1 mm above the fiber tip (Fig 3-3b). The idea behind this particular lens combination is to turn "inside out" an axicon-generated quasi-Bessel beam, which leads to an excellent suppression of light in the hollow part of the resulting beam. One practical constraint in our implementation of this optical guide is that it has to pass through the $f = 20\,\text{mm}$ collimation lense above the fiber. Consequently, the other optical elements, located outside the vacuum chamber, have to be matched to this lens. This leads to a combination of optics consisting of two 175° axicons (Greyhawk Optics) and a 75 cm focal-length lens between them. Fine tuning of the hollow beam shape is done by adjusting the collimation of the input Gaussian beam.

The atom-guiding performance of the blue-detuned hollow beam generated with this setup can be seen in Fig. 3-3 c, d and e. The hollow beam with $P \approx 40$ mW and $\lambda \approx 780.20$ nm is turned on at the end of the atom cooling stage, and the atoms are then allowed to free-fall towards the fiber. Comparing the fluorescence images of the freely expanding MOT (Fig. 3-3 c) and the optically confined cloud (Fig. 3-3 d) shows how the hollow guide increases the atomic density in the area above the fiber tip, by preventing atoms from escaping from this region. On the other hand, it can be seen that the cloud still expands freely in the vertical direction. To also decrease the size of the atomic cloud in this direction, we add a blue-detuned light sheet perpendicular to the fiber $\sim 1\,\text{mm}$ above the fiber tip. This closes off the optical trap in the vertical direction, creating a cup-like potential together with the hollow guide, in which the atoms are collected close to the upper fiber tip (Fig. 3-3e). Once the atoms have accumulated in this cup, the light sheet is turned off and the atoms again fall freely towards the fiber where they are captured by the in-fiber dipole trap. With this method we load $\sim 3 \times 10^4$ atoms into the fiber, which results in a maximum $OD \sim 180$.

It is interesting to note that we can also load atoms into the fiber by simply releasing the MOT and letting the atoms fall completely unrestricted. In this case, we observe up to $\sim$ 5000 atoms in the fiber, which is the same order of magnitude as the results achieved by the other transfer methods. This is due to the fact that all our transfer methods are adiabatic, i.e. there is no additional cooling of the atoms after the optical molasses stage. Consequently, any transverse compression of the atomic cloud will result in an increase

of its temperature, which in turn reduces the chance of individual atoms being loaded into the fiber dipole trap. In particular, most of the transverse compression happens in the last $< 100\,\mu$m above the fiber, where the potential from the fiber guided dipole trap becomes significant (Fig. 3-2d). Only a fraction of the atoms passes through this area into the fiber. The majority has too much kinetic energy which results in trajectories that do not end inside the fiber, but instead lead the atoms back upwards, anagolous to the angular momentum barrier in a magnetic bottle trap. To increase the number of atoms passing this barrier, optical cooling during this final compression stage is required. In our current setup, the magnetic funnel wires block the optical access to this region, which prevents us from implementing this improvement.

3.3 Atoms inside the fiber

After the end of the transfer stage, we wait $\sim$5 ms before we perform the actual in-fiber experiments, which allows the captured atoms to move into the fiber, and atoms remaining above the fiber to expand sufficiently to not cause any residual absorption. Additionally, if magnetic guiding is used in the transfer process, this step gives the transient magnetic fields time to vanish. Typically, the duration of the actual experiments ranges from 100 to 400 μs. The whole cooling, trapping, and data collection cycle is repeated every 1.5 s. For the probe transmission scans such as those shown in Fig. 3-4, each data point corresponds to a single run of the experiment (or multiple runs in the case of data averaging). Between these runs, the frequency of the probe laser is changed, and a new atomic sample is prepared in the fiber.

For the dipole trap inside the fiber we couple $P = 25$ mW of light with wavelength $\lambda = 802$ nm into the fiber. This provides a trap depth of ~ 10 mK inside the fiber, while the detuning from the rubidium lines is sufficient to allow for easy optical filtering and negligible residual heating during the experiments.

Absorption profiles associated with atomic resonance lines are the signature of interaction between atoms and light guided through the PCF. The dipole trap introduces a power-dependent, radially varying AC-Stark shift [79], which results in broadening and a frequency shift of the absorption profile. For actual experiments, we usually want to

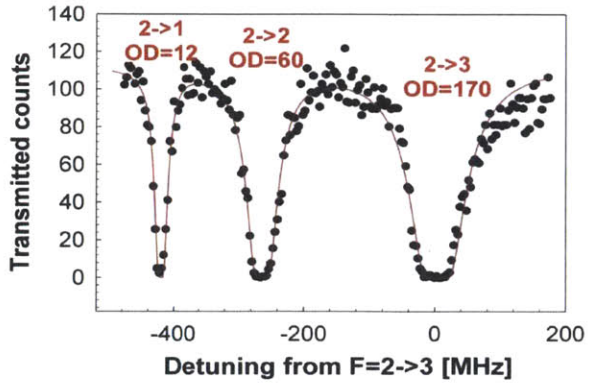

Figure 3-4: **In-fiber optical depth.** Frequency scan over the D_2 line of ^{87}Rb for $\sim$ 26000 atoms loaded inside the fiber. The atoms are optically pumped into the $F = 2$ state and then probed with linearly polarized light over the three transitions accessible from this state, $F = 2 \rightarrow F' = 1$ (left), $F = 2 \rightarrow F' = 2$ (middle), and $F = 2 \rightarrow F' = 3$ (right). The different observed optical depths agree well with a number of loaded atoms of $N_{at} \sim 30000$ when the relative strengths of these transitions are taken into account.

avoid this broadening of the atomic transition. To achieve this, we apply a synchronous square-wave modulation of the dipole trap and the probe beam with opposite phase at a rate much higher than the trapping frequency. This results in a time-averaged trapping potential that is still sufficiently deep to confine the atoms inside the fiber. On the other hand, during the off-times of the dipole trap, we can perform optical experiments with the atoms exhibiting their field-free atomic structure. When using this technique and scanning the probe laser over a particular hyperfine transition, we observe a narrowed absorption profile. The shape of this resonance is completely determined by the natural line profile of the transition (Equation 3.1). There is solely homogeneous broadening due to the large optical depth. The exact frequency of the trap light modulation is adapted based on the experiments performed. Slower modulation increases the off-times of the trap light, providing more time for individual experiments. Comparing the observed OD for different modulation frequencies shows that the slowest modulation we can use before we observe loss of atoms is $\sim 300\,\mathrm{kHz}$.

Figure 3-4 shows a typical absorption scan when the atoms are initially prepared in the $F = 2$ hyperfine ground state and the probe laser is scanned over the $D2$ transition while the dipole trap is turned off. The maximum optical depth $OD \sim 180$ is observed

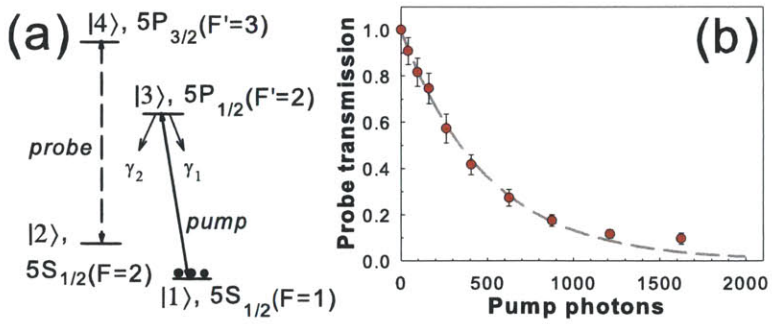

Figure 3-5: **Cooperativity calibration.** Calibration of the cooperativity η in the fiber by comparing the number of photons absorbed from the pump beam to the absorption on the probe transition, based on the knowledge of the branching ratios. 500 pump photons are sufficient to create an optical depth of 1 on the probe transition. Fitting an exponential (dashed line) to the measured data (red dots) yields $\eta \approx 0.42$.

on the $F = 2 \rightarrow F' = 3$ cycling transition when we use the all-optical loading procedure. While this number grows monotonically with the number of atoms loaded, we cannot straightforwardly extract how many atoms are inside the fiber from the measured OD. To measure this quantity N_{at} we perform a nonlinear saturation measurement based on incoherent population transfer in our mesoscopic atomic ensemble. The transmission of a probe beam coupled to a cycling atomic transition, $|2\rangle \rightarrow |4\rangle$, is controlled via an additional pump beam transferring atoms from an auxiliary state $|1\rangle$ into $|2\rangle$ (Fig. 3-5a). Initially, the state $|2\rangle$ is not populated and the system is transparent for the probe beam. The incident pump beam, resonant with the $|1\rangle \rightarrow |3\rangle$ transition, is fully absorbed by the optically dense atom cloud, thereby transferring atoms into the $|2\rangle$ state, where they then affect the propagation of the probe beam. As demonstrated in Fig. 3-5,b, we achieve a 50% reduction of the probe transmission with only 300 pump photons. This corresponds to ~ 150 atoms being transferred into the $|2\rangle$ state, which yields the desired proportionality constant between optical depth on the considered transition and number of atoms inside the fiber. From this number we can calculate this conversion factor for any atomic transition by comparing its strength to the reference cycling transition.

From the absorption scans we cannot infer with absolute certainty that the atoms are inside the fiber. Atoms trapped in some local potential minimum just outside the fiber would create an almost identical absorption signal. Such a minimum could form due to

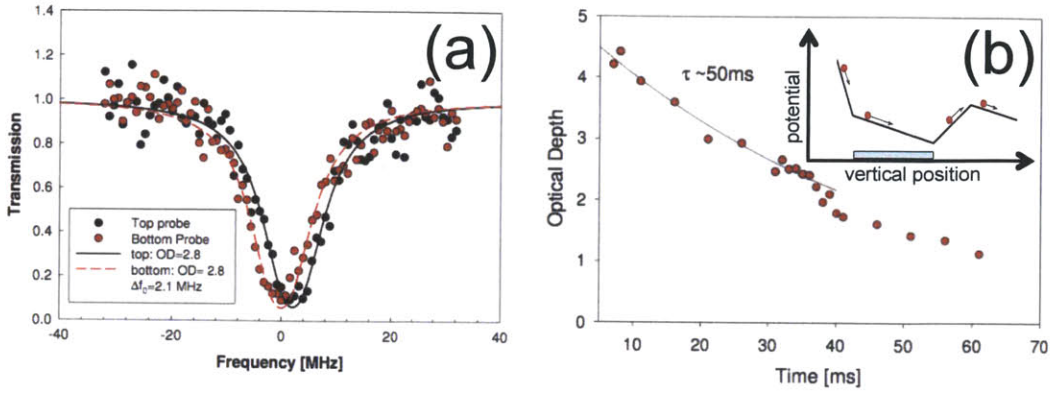

Figure 3-6: **Atoms inside the fiber.** (a) Doppler shift of the falling atom cloud observed by using two probes propagating through the fiber in opposite directions. (b) Lifetime of the atoms inside the fiber. Inset: A qualitative sketch of the potential along the fiber axis experienced by the atoms as they load into the fiber-guided dipole trap.

stray trap light at the fiber tip if the fiber is not cleaved properly, for example. Due to the magnetic funnel wires surrounding the fiber, we cannot obtain a direct image of the atoms inside or right above the fiber, which would let us determine their position exactly. For the number of atoms we load into the fiber, detection of atoms exiting at the lower end is challenging, as we would need to detect very few atoms at relatively high temperature ($\sim$ 1 mK) in free space. While this can be accomplished, e. g., by using an image intensified CCD camera [80] or a channel electron multiplier [77], we instead confirm that the atoms are loading into the fiber core by measuring their vertical velocity over an extended period of time. For this, we deploy two probes propagating in opposite directions through the fiber simultaneously. The observed absorption profiles show a distinct difference between the frequency centers of the two profiles (Fig. 3-6,a) after the atoms are loaded into the dipole trap. This frequency difference is the result of the Doppler shift caused by the vertical motion of the atomic cloud. In the case shown in figure 3-6,a, the observed shift corresponds to the cloud moving downwards with velocity 0.82 m/s. This shift can be observed for times exceeding 30 ms, which means the atoms have to be moving downward inside the fiber.

Additionally, we can control the velocity of the atoms inside the fiber in two ways. In the first way, we can simply change the depth of the fiber-guided dipole trap, which modifies the kinetic energy picked up by the atoms when they are loaded into this trap.

The second way is based on coupling into the fiber an additional weak ($\sim 1nW$) nearly-resonant red-detuned upward or downward propagating 'push' beam, which allows us to alter the overall velocity as well as the direction of movement of the atomic cloud inside the fiber. The light pressure from this beam – depending on the beam's direction, intensity, and duration – can speed up, slow down, stop, or reverse the direction of the movement of the atoms inside the fiber, as observable from the Doppler shift between top- and bottom-coupled probes.

The knowledge of the atomic velocities allows us to estimate the cloud length. In general, during the loading procedures the atoms arrive at the upper tip of the fiber with velocities of ~ 0.35 m/s over time intervals ~ 10 ms. Once they fall into the dipole trap potential, their velocity will reach up to ~ 1.4 m/s, depending on the depth of the dipole trap inside the fiber. Consequently, during the ~ 10 ms when the atoms are entering the fiber, the front edge of the atomic cloud is moving at ~ 1.4 m/s, while its rear edge is moving at ~ 0.35 m/s. Based on this, we can estimate the minimum length of the atomic cloud inside the fiber to be ~ 1 cm.

3.4 Atom lifetime in the fiber

Once inside the fiber, the atoms are confined by the red detuned dipole trap only in the radial direction, while in the vertical direction they experience a free fall until they reach the lower end of the fiber. An example of the measured optical depth of the falling atomic cloud as a function of time is plotted in figure 3-6b. Here, the zero on the time axis corresponds to the instant when the optical depth in the fiber is the largest. In this measurement, each point on the graph corresponds to a newly loaded atomic cloud for which the dipole trap was kept on continuously until the point in time when the OD was measured using the modulation described above. The 'kink' in the data near 40 ms corresponds to the free-falling atoms reaching the lower end of the fiber. Up to this point the atoms decay out of the dipole trap exponentially with a time constant of ~ 40 ms. We explain the data after the 'kink' as part of the atomic cloud leaving the fiber and part of the cloud reflecting back from the potential change associated with the dipole-trap beam being coupled into the lower end of the fiber.

Due to the small size of the hollow core, the possibility that attractive forces from the core wall cancel the dipole trap potential has to be considered. However, comparing the attractive Casimir-Polder potential C_4/r_{wall}^4 created by the fiber wall, with the nominal value of $C_4 = 8.2 \times 10^{-56}$ J m^4 [81, 82], with the dipole trap potential shows that attractive forces become dominant only for distances less than ~ 100 nm and that the reduction of total depth of the optical trap is negligible. Therefore, for a fiber with a 7 μm diameter core, the shape or depth of a red-detuned dipole trap potential in the central area is not noticeably affected by the nearby walls.

As the atoms move inside the fiber, they are lost from the dipole trap mostly through two mechanisms. The first and more obvious one is caused by collisions with the background gas present due to imperfect vacuum within the PCF core. While the vacuum pressure is 10^{-9} torr or less within the general volume of our vacuum chamber, the small diameter of the fiber core and the associated pumping speeds should result in a significantly higher background gas pressure inside the fiber. Considering the expansion of a room temperature gas in a one-dimensional tube with diameter 7 μm, we can estimate that the pressure inside the fiber reaches 10^{-6} torr after about one day of pumping, while getting down to 10^{-8} torr takes a little more than a month. This model neglects possible outgasing from the fiber walls, which will increase the obtainable steady-state pressure. From our observations, background gas collisions inside the fiber are not the main limitation on our observed lifetimes. Instead, we identify a second mechanism leading to faster atom loss, which originates from the presence of higher-order guided modes propagating through the PCF. These modes are present in all single-mode fibers, as their excitation during beam coupling from free space into fiber is virtually inevitable. However, these modes propagate with losses significantly larger than those of the fundamental mode and generally die away when propagating through fiber pieces longer than ~ 1 m. For a short piece of fiber, like the one used in the experiment, the losses of the higher order modes will not be sufficient to suppress them. These higher-order spatial modes interfere with the fundamental mode and create a transverse as well as longitudinal variation of the dipole trap potential. Since this is an interference effect, even small amounts of power propagating in higher modes can lead to a significant modulation of the original potential. These potential variations couple the longitudinal velocity of the atoms, which is quite large

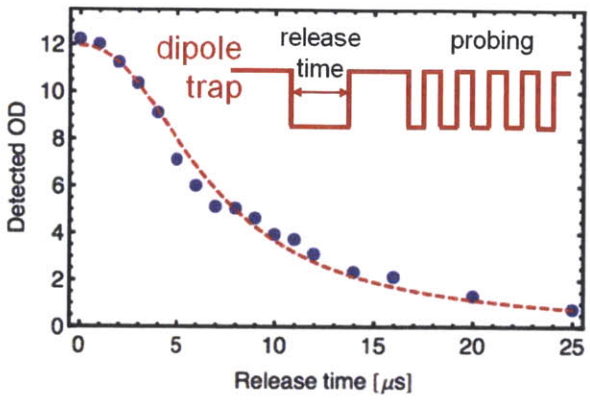

Figure 3-7: **Temperature estimate from a TOF measurement.** (a) The time sequence diagram: After the atoms are released from the trap and then recaptured, the trap is modulated for the *OD* measurement. (b) Optical depth of the recaptured cloud as a function of the release time. The dashed red line represents a fit based on the Gaussian cloud expansion model.

as the atoms gain kinetic energy from falling into the dipole trap potential (Fig. 3-6b, inset), to the radial motion of the atoms. This coupling heats the atoms in the transverse direction and ejects them from the dipole trap. As a result, we have observed a decay constant of the atoms inside the fiber ranging from 100 ms down to 10 ms depending on position and the velocity of the atomic cloud inside the fiber. In particular, we observe the longest lifetimes when the atoms are comletely stopped inside the fiber, while we register a reduction of lifetime when the atoms move both up or down inside the fiber.

The tight confinement of the fiber-guided dipole trap will increase the temperature of the atoms compared to the initial $40\,\mu$K outside the fiber. To estimate the temperature of the atoms inside the fiber, we perform a time of flight (TOF) measurement. We shut off the dipole trap and let the cloud expand, then turn the trap on again to recapture atoms that have not collided with the wall (Fig. 3-7a). After this, we modulate the dipole trap in the usual manner and measure the optical depth of the recaptured atoms. Assuming a Gaussian distribution of the atoms in the radial direction $n(r) \sim e^{-(r/r_o)^2}$, the optical depth of the recaptured cloud as a function of the release time τ_r is given by

$$OD(\tau_r) \approx OD_0 \left(1 - \exp \left[\frac{-\left(\frac{R_{core}}{r_o}\right)^2}{1 + \left(\frac{v_o}{r_o}\right)^2 \tau_r^2} \right] \right) \tag{3.4}$$

where $v_o = \sqrt{2k_B T_r/m_{Rb}}$ and R_{core} is the radius of the PCF core. We extract the temperature of the cloud by fitting (3.4) to a set of release and recapture data with $A = (R_{core}/r_o)^2$ and $B = (v_o/r_o)^2$ as the fit parameters, as shown in Fig. 3-7b. The fit to this data set yields $T_r \approx 1.6$ mK and $r_o \approx 2.2$ μm. Using the measured temperature $T \sim 1\,\mathrm{mK}$, cloud length $L = 1\,\mathrm{cm}$, $\omega_\perp = (2\pi)50$ kHz, we obtain $\rho_{fiber} = 10^{-7}$, which is identical to the original peak phase space density in the MOT, showing that our transfer is adiabatic. The essence of our current loading implementation is that we rely on capturing the lower tail of the Maxwell-Boltzmann velocity distribution of the atoms by the fiber-coupled dipole trap. Currently, the atoms in this tail are brought into the capture radius of the fiber trap. This is the philosophy behind both the magnetic funnel and the hollow-beam guide. To increase the loading efficiency, and thereby the number of loaded atoms, by an order of magnitude or more, one has to take a different approach, i.e. one has to increase the phase space density of the atomic cloud by additional cooling of the atoms before or during the transfer into the fiber. In the most extreme case this means loading a Bose-Einstein condensate into the fiber. This was successfully demonstrated in [78], but this leads to a severe decrease in the repetition rate of the experiment in addition to a somewhat increased technical complexity of the apparatus. An alternative approach is optical cooling of the atomic cloud in the vicinity of the fiber tip once the atomic cloud has been significantly compressed. In our current setup, the magnetic-funnel wires block the optical access for implementing this scheme. Since our current loading scheme does not rely on these wires anymore, they can be removed, allowing the fiber tip to be easily optically accessible.

3.5 All-optical switching

To demonstrate Electromagnetically Induced Transparency (EIT), we first prepare the atoms in the $F = 1$ ground state, and then probe the medium with a linearly polarized probe tuned to the D1 $F = 1 \rightarrow F' = 1$ transition. In the absence of the control beam, the medium is completely opaque at resonance (Fig. 3-8C, black data points). In contrast, when a co-propagating control field resonant with the $F = 2 \rightarrow F' = 1$ transition is added, the atomic ensemble becomes transparent near the probe resonance (Fig. 3-8C,

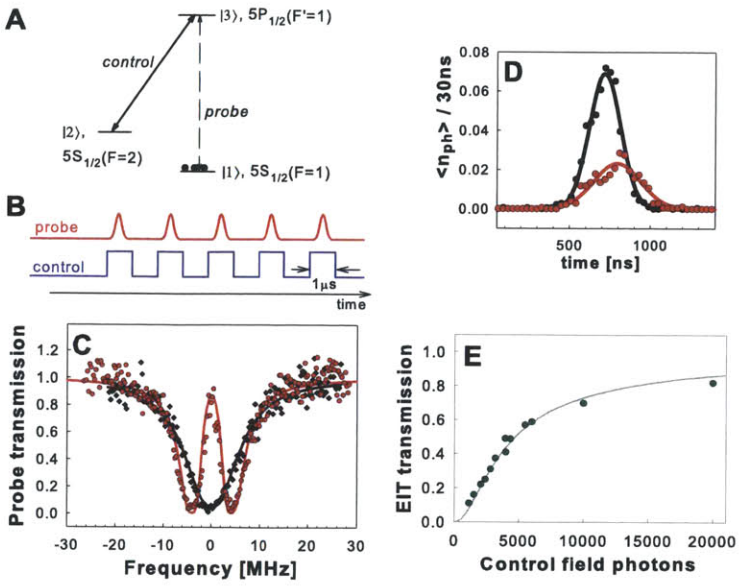

Figure 3-8: **In-fiber EIT.** (A) The atomic level scheme and the corresponding hyperfine states of ^{87}Rb used in the EIT demonstration. (B) Both probe and control field are broken into a set of ~ 100 synchronized pulses sent through the fiber during the off-times of the dipole trap. (C) Transmission of the probe light through the fiber as a function of detuning from resonance in the presence of the control field (red data). The black data show probe transmission without the control field. (D) Individual probe pulse shape and delay. Here, $\langle n_{ph} \rangle$ represents the average number of photons detected in a 30 ns time bin. The reference pulse (black) is obtained without the presence of atoms inside the fiber. The red pulse is delayed due to the group velocity reduction in the atomic medium under EIT conditions. (E) Observed transmission of the probe pulses on resonance as a function of average number of photons in the 1 μs control field pulse.

red data points). Figure 3-8D shows the individual pulse shape and its transmission and delay due to reduced group velocity v_g inside the atomic medium. For a probe pulse of half-width $t_p \sim 150$ ns we observe a group delay t_d approaching 100 ns, corresponding to reduction of group velocity to $v_g \approx 3$ km/s. Finally, Fig. 3-8E shows the resonant probe transmission as a function of the average number of photons contained in each control field pulse. Due to the tight confinement of light provided by the PCF, control pulses containing $\sim 10^4$ photons are sufficient to achieve almost complete transparency of an otherwise opaque system.

An efficient nonlinear optical switch can be realized by adding to the EIT Λ-system a switch field coupling the state $|2\rangle$ to an excited state $|4\rangle$ (Fig. 3-9A), as proposed by

Harris and Yamamoto [53] (see Chapter 2). In this scheme, the switching photons interact with atomic spins within the slow dark-state polariton, causing a simultaneous absorption of a probe and a switch photon [83, 56, 84].

In our experiment, an additional switching field resonant with the $F = 2 \rightarrow F' = 3$ transition of the D2 line of rubidium^{87} (Fig. 3-9A, B) controls the transmission through the EIT medium. As shown in Figure 3-9C, in the absence of the switching field (red data), we observe high transmission of the probe beam on resonance due to EIT. When the switch field is turned on, this transmission is reduced. The strength of the reduction depends on the switch field intensity, which, for a fixed switch pulse length, is determined by the number of photons contained in the switch pulse (Fig. 3-9D). Experimentally, we observe best switching results for switch pulses of length $t_s \approx t_p + t_d$. We find a 50% reduction of the initial transmission for a total number of ~ 700 switch photons per pulse. Figure 3-9E presents the truth table of our switch. In the case of no probe pulse (0/0 and 0/1 settings of the switch) only background noise from the control field is detected, which is orders of magnitude smaller than the single photon per probe pulse.

We now turn to the detailed analysis of the nonlinear behavior of our atomic medium. In the case when the resonant control and switching pulses are longer than the weak probe pulse, the effect of the atomic medium on such probe pulses with carrier frequency ω_p is given by $\mathcal{E}_{\text{out}}(t) = \frac{1}{\sqrt{2\pi}} \int \mathrm{d}\omega\, \mathcal{E}_{\text{in}}(\omega)\, e^{i\tilde{\chi}(\omega)}\, e^{-\imath\omega t}$, where $\mathcal{E}_{\text{in}}(\omega)$ is the Fourier transform of the slowly varying envelope $\mathcal{E}_{in}(t)$ of the probe pulse. The frequency dependent atomic nonlinear susceptibility $\tilde{\chi}(\omega)$ is given by [40, 53]

$$\tilde{\chi}(\omega) = \frac{OD}{2} \frac{\gamma_{13}\left(|\Omega_s|^2 - 4\delta_{12}\delta_{24}\right)}{\delta_{24}\left(4\delta_{12}\delta_{13} - |\Omega_c|^2\right) - \delta_{13}|\Omega_s|^2}. \tag{3.5}$$

Here, $\Omega_{s,c} = \frac{\mu_{s,c}E_{s,c}}{\hbar}$ are the Rabi frequencies of the switch and control fields, with $\mu_{s,c}$ being the respective dipole matrix elements. The complex detunings δ_{ij} are defined as $\delta_{ij} = \delta_p + \imath\gamma_{ij}$, with γ_{ij} being the dephasing rates between levels i, j, while $\delta_p = \omega_p + \omega - \omega_{13}$, where ω_{13} is the frequency of the $|1\rangle \rightarrow |3\rangle$ transition. The number of input and output photons is given by $N_{in,out} = \int \mathrm{d}t\, |\mathcal{E}_{\text{in,out}}(t)|^2$. In what follows, we consider input pulses with Gaussian envelope $\mathcal{E}_{\text{in}}(t) \sim e^{-\frac{t^2}{2t_p^2}}$, in which case the transmission through our atomic

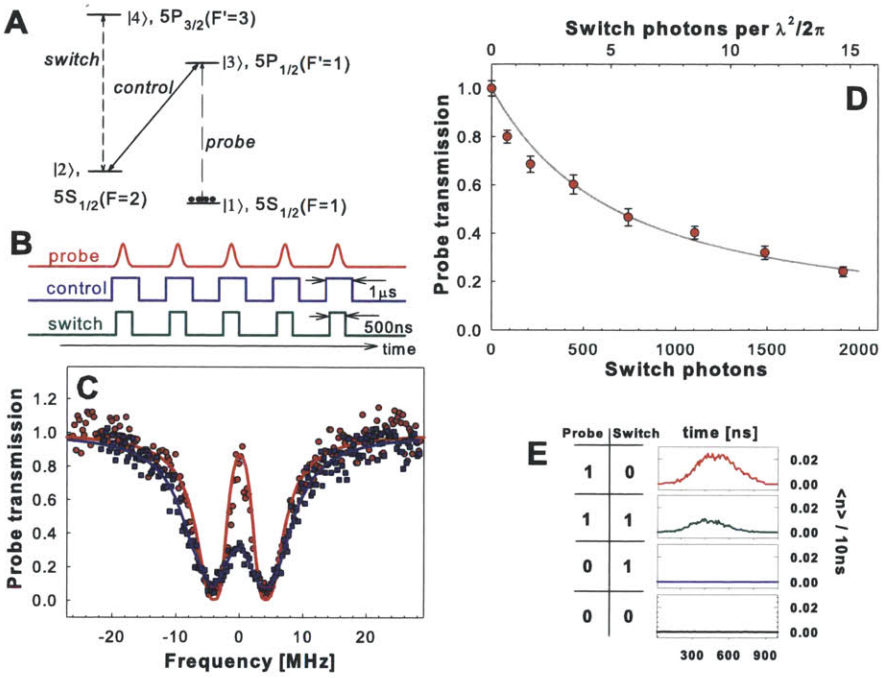

Figure 3-9: **All-optical switching.** (A) The atomic level scheme with corresponding hyperfine states of rubidium^{87} used in the experiment. (B) Probe, control and switch fields are broken into a set of $\sim$ 100 synchronized pulses sent through the fiber during the off-times of the dipole trap. (C) Probe transmission through the fiber without (red) and with (blue) the switch field present. Solid lines are fits of Eq. 3.6. (D) Observed transmission versus average number of switch photons per pulse. The solid grey line is the prediction based on equation Eq. 3.6. The transmission is normalized to the EIT transmission in the absence of the switch photons. (E) Truth table of the switch, showing the detected photons in the output port of the switch system as a function of the presence of the probe and switch field pulses. Data are presented for probe pulses containing on average $\sim$ 2 photons and with $\sim 1/e$ attenuation of transmission in the presence of the switch photons.

medium is

$$T(\omega_p, OD) = \frac{N_{out}}{N_{in}} = \frac{t_p}{\sqrt{\pi}} \int \mathrm{d}\omega \, e^{-t_p^2\omega^2} \, e^{-2\,\mathrm{Im}\tilde{\chi}(\omega)}. \tag{3.6}$$

By fitting expression (3.6) to the absorption profiles shown in figures 3-8C and 3-9C, we extract the control and switch Rabi frequencies, optical depth and ground state decoherence rate. We next use these parameters to compare our observed EIT and coherent switch data to the theoretical prediction. The solid line in Fig. 3-8D shows the calculated EIT transmission as a function of control pulse photons, while the solid line in Fig. 3-9D shows the on-resonance attenuation of the probe pulse as a function of the number of switch photons. In both cases, we find excellent agreement between our experimental data and the theoretical model. However, for the relevant case of a resonant probe field, the transmission of the probe pulse can be approximated by

$$T = \frac{\exp\left(-N_s \left(\frac{\mu_s}{\mu_p}\right)^2 \frac{3}{\pi} \frac{\lambda^2}{A} \frac{t_d}{t_p + t_d}\right)}{\sqrt{1 + \frac{16 t_d^2}{OD\, t_p^2}}}. \tag{3.7}$$

Here, N_s is the number of switch photons, we assumed that the Rabi frequency of the control field is much larger than that of the switching field, the decay rate of state $|3\rangle$ is approximately the same as of state $|4\rangle$, and we used $t_d = L/v_g \approx \frac{OD\gamma_{13}}{|\Omega_c|^2}$, with L being the length of the medium.

For the investigated case of a relatively weak probe transition and resulting $OD \approx 3$, the delay time is small ($t_d \sim t_p$) and the probe pulse is never fully stored inside the medium. If the OD is increased (either by improving the atom loading efficiency or using a stronger probe transition), $t_d \gg t_p$ and the whole probe pulse is contained inside the medium as a dark state polariton in a mostly atomic form. In this case, it follows from equation (3.7) that $N_s \sim \frac{A}{\lambda^2}$ switch photons attenuate the probe pulse by a factor of $1/e$.

Improvements to the switching efficiency can be obtained by increasing the effective interaction time between the switch and probe photons. Since the switching mechanism is based on a simultaneous absorption of a switch and a probe photon, the electric field envelopes of switch pulse and of the probe pulse have to overlap inside the atomic medium. To maintain this overlap despite the large mismatch between the propagation velocities of the two pulses, the switching pulse has to stay on during the whole time t_d the probe

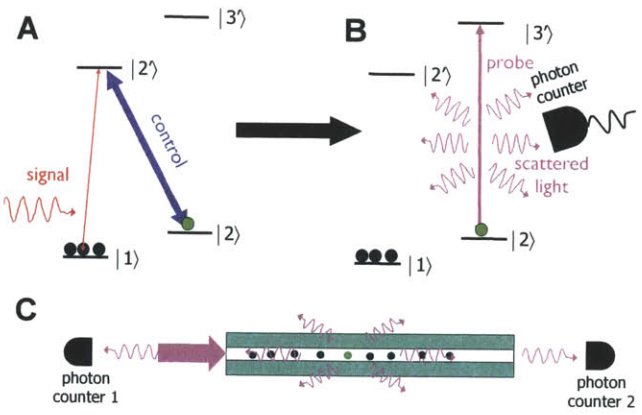

Figure 3-10: **Photon counter.** (A) Photons are coherently stored in an atomic ensemble as dark state polaritons and each photon results in a single collective excitation. (B) The ensemble is then probed with a detection laser on a cycling transition, which allows scattering of multiple photons by a single excitation. (C) When the atomic ensemble is confined inside a holow-core PCF, the scattered photons are collected and guided by the hollow fiber and detected with a photon counter. Alternatively, the presence of collective excitations can be detected by measuring the transmission of the fiber.

pulse is propagating in the medium. This in turn leads to an inefficient performance of the switch, as most of the area of the switching pulse will end up not overlapping with the probe pulse. Consequently, most of the switch photons needed to create a long switching pulse of required field intensity will go to waste. One way to counteract this inefficiency is to match the group velocities of the probe and switching pulses during their propagation through the atomic ensemble [58] (which increases the efficiency by a factor $\sqrt{OD}$ per switch photon). Alternatively, the efficiency of this switching scheme can potentially be further improved by using stationary-pulse techniques [85]. In this case, a standing wave control field from two counter-propagating beams forms an EIT Bragg grating in which the probe pulse can be completely stopped with non-vanishing photonic component. In that case, the probability of interaction between two single photons scales linearly with OD [60]. Experimental progress towards the implementation of these enhanced nonlinearities in our hollow-core fiber experiment are presented in Chapter 4.

3.6 Single photon detection

In addition to all-optical switching, our system can be used to implement an efficient photon counting scheme proposed in Ref. [86] and [87]. This scheme combines photon storage (Fig. 3-10A)[88, 89] with spin-flipped atom interrogation via a cycling transition as illustrated in Fig.3-10B. Practical limitations in realistic atomic systems arise from experimental imperfections that can transfer the atom into state $|1\rangle$ with non-zero probability during the interrogation stage. This restricts the number of photons that can be scattered from the stored excitation, which in turn requires the scattered light to be collected with certain minimum efficiency. Implementing the photon-counting scheme with an atomic ensemble confined inside a hollow-core fiber could potentially provide the necessary efficiency boost due to collection and guiding of the scattered photons by the fiber (Fig. 3-10C). A necessary step on such implementation is the detection of single atoms inside the hollow-core fiber as this would indicate the capability of the system to detect and resolve single photons stored in atomic ensembles. Here we present initial experimental results of our work in this area.

When detecting small number of atoms inside the hollow fiber, the number of photons detected by the photon counter in Fig. 3-10 is given by

$$N_{det} = N_{sig} M_{cycl} \alpha, \tag{3.8}$$

where N_{sig} is the number of atoms inside fiber, M_{cycl} is the average number of photons that can be scattered by a single atom before the atom is lost by a transfer to state $|1\rangle$ or by being heated out of the trap, and α the overall detection efficiency of the scattered photons. This relation also works for the case of photon counting with N_{sig} being the number of photons stored in the atomic ensemble. α is the product of our atom-fiber cooperativity and of the detection efficiency for photons in the guided mode of the fiber. The atom-fiber cooperativity for an atom located at the center of the fiber (ie the probability for the atom to absorb a single photon in the mode of the fiber) is (3.3) 1.8% (we use linear-polarized light on the cycling $|5S_{1/2}, F = 2\rangle \rightarrow |5P_{3/2}, F = 3\rangle$ transition, because of the polarization properties of the PCF). From the optical theorem, it is equivalent to the probability for an atom inside the fiber to scatter a photon in one of the directions of

the guided mode of the fiber [90]. We measure a cooperativity of 0.38% by comparing the transmission and back-scattering of resonant light out of the PCF for ensembles of $\sim$ 100 atoms. This value is in excellent agreement with the one measured using incoherent population transfer. Although this number is compatible with a gaussian distribution with temperature 1.6mK, more detailed probing of the resonant transitions inside the dipole trap point towards the fact that a significant fraction of the atoms seem to have a radially elliptical trajectory and do not contribute highly to the atom-fiber cooperativity (Fig. 3-12A). This agrees with classical single-particle trajectories for atoms rolling down a bottleneck-type potential created by the dipole trap at the entrance of the fiber and starting off-center with some initial azimuthal velocity. Densities in the fiber are too low for the atomic ensemble to rethermalize. Combining the atom-fiber cooperativity with the quantum efficiency of our photon counters and coupling losses, our current setup is limited to $\alpha \sim 10^{-3}$.

The total number of photons M_{cycl} which an atom can scatter is limited by the off-resonant scattering to another state, especially inside the PCF where the clean circular polarization required for the $|5S_{1/2}, F = 2, mF = 2\rangle \rightarrow |5P_{3/2}, F = 3, mF = 3\rangle$ transition is not achievable because of birefringence and multimode effects. For the purpose of atoms counting, the loss of atoms to the $|5S_{1/2}, F = 1\rangle$ state can be counteracted by periodic optical pumping. Another limiting factor to M_{cycl} is the lifetime of the atoms in the modulated dipole trap. The probing occurs during the off times of a modulated dipole trap as it is not possible to filter out dipole trap photons well enough to detect the low light level signal emanating from a few atoms. The lifetime in the modulated dipole trap is reduced to 4 ms at 1 MHz modulation rate due to parametric heating. Other heating mechanisms contribute to reducing the lifetime. If the atoms are probed uni-directionally in the fiber, the photon recoil accelerates the atoms, with two important consequences: the probe light is Doppler-shifted out of resonance, and the atoms rapidly escape the trap. We attribute the second effect to the mixing of the longitudinal and radial external degrees of freedom due to corrugations in the confining potential created by interference with the surface modes propagating at the core-cladding interface [91]. A clear signature of the longitudinal acceleration is the Doppler shift of the atoms and the effect can be counterbalanced by alternating probing phases with in-fiber longitudinal

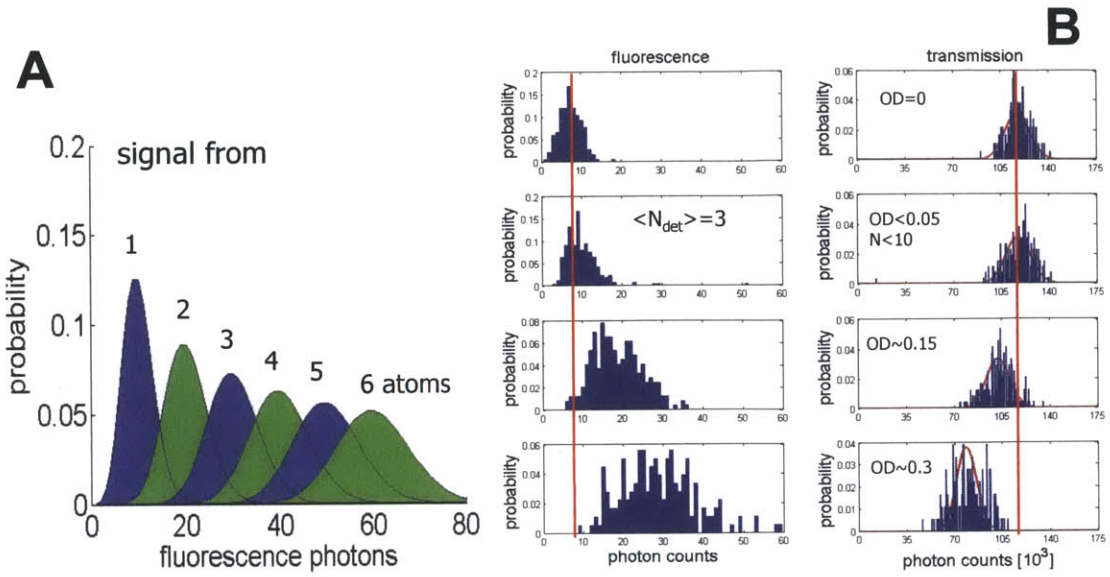

Figure 3-11: **Few-atom detection.** (A) Effects of the photon shot noise on the atom number resolution for $\alpha M_{cycl} = 10$. (B) Collected fluorescence and measured transmission from fiber-confined atomic ensembles of various optical depths. For the probed transition, ~ 200 atoms result in $OD \approx 1$. As little as 30 atoms are clearly detected by fluorescence and transmission. For smaller ensembles, the average fluorescence signal is not significant enough with respect to the variance of the noise.

red-detuned molasses. Each scattering event also contributes one photon-recoil energy to the thermal energy of the atoms, due to the randomness of the emission process. The molasses can compensate the heating in the longitudinal direction. In the radial directions, the trap depth of ~ 10 mK corresponds to $\sim 10^5$ times the thermal energy gained per scattering event. In the absence of any other heating mechanism and using a resonant probe at saturation intensity, M_{cycl} is restricted by the lifetime of the atoms in the modulated dipole trap to $\sim 10^4$.

The atom number (and eventually photon number) resolution in this system is limited by the shot noise of detected photons, and we get from equation (3.8) that the uncertainty in measured photon number would be

$$\Delta N_{sig} = \frac{N_{det}^{\frac{1}{2}}}{\alpha M_{cycl}} = \left(\frac{N_{sig}}{\alpha M_{cycl}}\right)^{\frac{1}{2}} \tag{3.9}$$

Figure 3-11,A plots the probabilities of detecting a particular number of photons for

various number of atoms present in the fiber. For the parameters of our system, we see that the resolution of atom number becomes more difficult as the atom number increases over just a few.

Fig. 3-11,B shows our initial experimental results. Here, we observed the fluorescence (photon counter 1 in Fig. 3-10,C) and transmission (photon counter 2 in Fig. 3-10,C) of atoms loaded into the fiber and probed on the cycling transition. The data is compared with the signal obtained from an empty fiber. We were able to detect as few as ~ 10 atoms using the scattered light, when the atoms could not be observed in the transmission signal anymore. However, atoms disappear from the dipole trap after scattering only ~ 350 photons/atom. This value is independent of density, excluding light assisted collisions. It is also independent of trap depth, which excludes the simple heating meachanisms described above. We attribute this effect to the non-pefectly linear polarization of the dipole trap, especially in the presence of surface modes. For a perfectly circular polarization, the dipole trap acts as a fictitious magnetic field and two successive Zeeman sub-levels are shifted (for $|5S_{1/2}, F = 1\rangle$) by $\sim 40MHz$ for our parameters. At each turn on of the dipole trap, the probe has reshuffled the population between the Zeeman sub-levels. These energy fluctuations increase the thermal energy of the atoms by the Zeeman splitting at each cycle of the dipole trap. A few percent of circularly polarized light is enough to account for the atoms escaping the trap in the absence of radial cooling (the heating in the longitudinal direction is reduced by the optical molasses). Fig. 3-12,B describes a way to cool the atoms without radial access by adding a weak blue-detuned (a few GHz to the $|5S_{1/2}, F = 2\rangle \rightarrow |5P_{1/2}, F = 1\rangle$ transition) and a weak repumper beam close to the free space resonance. For each depicted cycle, the atoms cool by an energy corresponding to the peak energy difference between the Stark-shifted hyperfine states. Fig. 3-12,C displays preliminary results of this cooling method inside the PCF. After a few ms of cooling, the absorption in the dipole trap indicates that the atoms have radially cooled to the bottom of the trap. Some losses occur during the process and we are currently working on improving this effect.

While the system in its current form is not suitable for photon number detection, its weak spots can be fixed in the future. In particular, improvement of the atom-fiber cooperativity by an order of magnitude would allow robust photon number resolution.

This could be achieved by in part by additional cooling and increased confinement of the atoms inside the fiber, but most directly by using a hollow waveguide with smaller diameter of the guided mode, such as the one demonstrated in Ref. [92].

With the fiber acting as a guide for both photons and atoms, the photons can interact with an optically dense atomic ensemble without being limited by diffraction. This makes the system an excellent candidate for nonlinear optics at very low light levels [93], while the large optical depth achievable in this system makes it ideally suited for the implementation of schemes for enhancing optical nonlinearities and creating effective photon-photon interactions [60, 94, 29, 95, 96]. Finally, while the experiments discussed here were performed in a vacuum chamber containing a piece of hollow-core PCF, recent developments in design and fabrication of integrated hollow optical waveguides [97, 98] open the possibilities for developing this system into a scalable on-chip architecture.

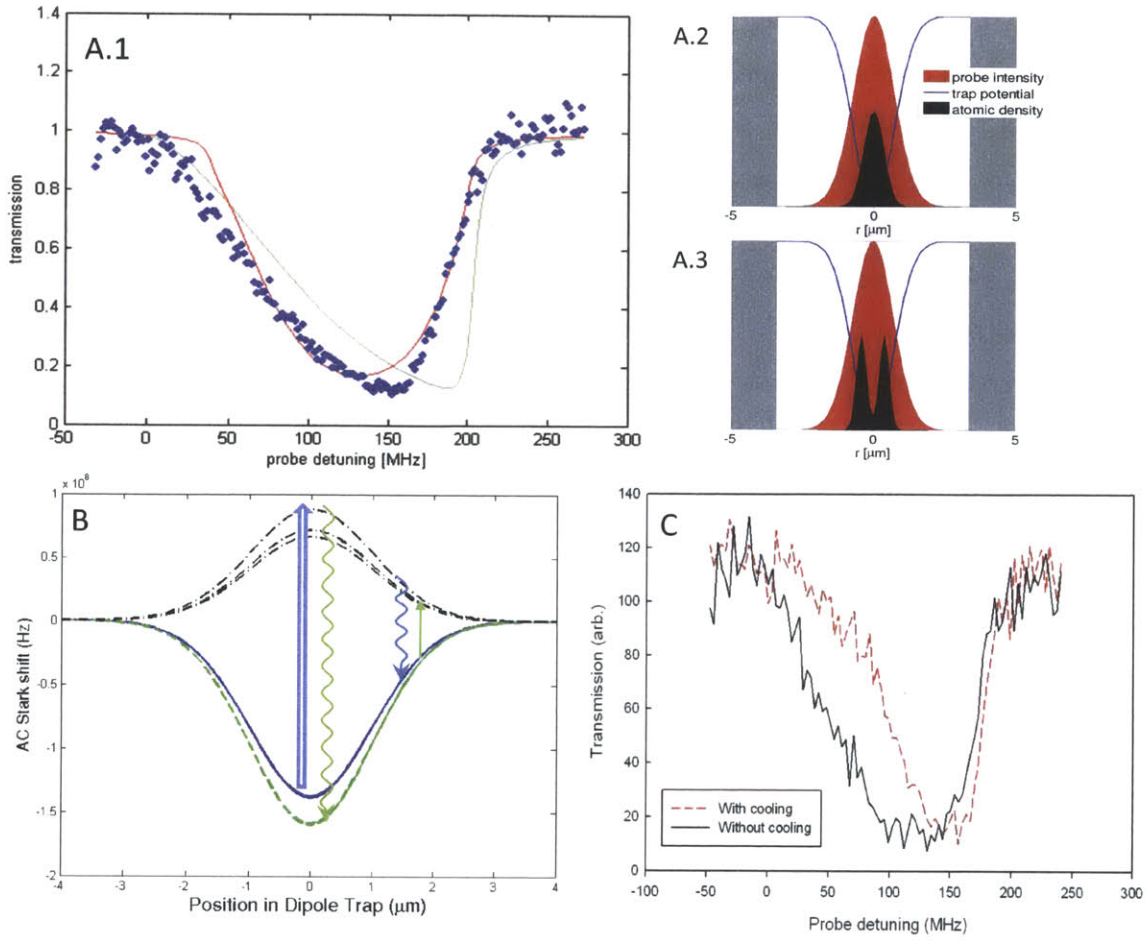

Figure 3-12: **In-fiber cooling.** (A.1) Probe absorption in the continuous dipole trap (blue dots). The data shows a stronger ressemblance to the expected curves for a ring-like distribution (red, A.3) than for a thermalized cloud (green, A.2). (B) In-fiber cooling can be implemented by adding a blue detuned beam to our dipole trap. The AC Stark shift along the radial axis of the dipole trap is plotted for the different Zeeman sub-levels of the $|5S_{1/2}, F = 1\rangle$(continuous, blue), $|5S_{1/2}, F = 2\rangle$(dashed, green) and $|5P_{1/2}, F = 2\rangle$(dash-point, black) states in the presence of a 25 μW beam, blue-detuned by 8 GHz from the $|5S_{1/2}, F = 1\rangle \rightarrow |5P_{1/2}, F = 2\rangle$ transition. At the center of the trap, the blue-detuned light preferentially scatters the atoms out of $|F = 1\rangle$. When the atoms spontaneously decay back to $|F = 2\rangle$, their energy is reduced by the difference in Stark-shift between the two hyperfine ground states. A low-power repumper recycles the atoms back into $|F = 1\rangle$ away from the center of the trap, at a position where the level-shift difference is lesser. (C) Probe absorption in the dipole trap with (black,continuous) and without (red, dashed) $\sim$ 1 ms of the cooling scheme described in (B). In the presence of cooling, the blue-shifted absorption is due to the atoms being radially cooled to the bottom of the trap, although we simultaneously observe atoms loss out of the trap.

Chapter 4

Beyond the cooperativity limit for nonlinear optics with cold atoms inside hollow core fibers

4.1 Double Slow Light

As described in Chapter 2, EIT is a powerful technique to obtain nonlinear effects dominating the linear absorption and phase-shift. In its most simple implementation [40, 53], it is nevertheless limited by the single-photon single-atom cooperativity and efficient nonlinearities at very low light level require transverse confinement on the order of a wavelength over an extended medium of large *OD*. It was proposed in [58] that significant enhancement of the nonlinearities can be achieved if the group velocity of the switch pulse is matched to that of the slowly propagating probe pulse. A simple way to understand this enhancement is to consider the propagation of a bandwidth limited pulse of duration τ_p undergoing EIT in the presence of a (low power) switch beam in a configuration described by Fig. 4-2,a. In the absence of switch beam, the probe pulse group velocity v_g is strongly reduced. Provided that the spectral profile of the pulse fits inside the EIT bandwidth, the width of the pulse envelope is compressed by a factor v_g/c and the peak electric field amplitude is conserved in the absence of ground state decoherence (see Appendix A). This

compression of the pulse is explained by the slowing down of the front of the pulse while the tail of the pulse still moves at group velocity outside the medium. The missing energy of the pulse is coherently stored in the control field and the spin-wave. As the probe pulse reaches the end of the medium, it expands back to its original shape. For a high OD, the group delay τ_d can be larger than the minimum length of a bandwidth-limited pulse τ_p:

$$\tau_d = \frac{OD}{\gamma_{EIT}} \cong \sqrt{OD}\tau_p \tag{4.1}$$

In the implementation of [53] described in Chapter 3, the group velocity of the switch pulse is the vacuum speed of light. As a consequence, the probe pulse fully compressed in the medium only experiences the amplitude of the electric field of the switch pulse for a duration τ_p after wich the pulses do not overlap anymore. In contrast, if the switch pulse also propagates under EIT condition with matched group velocity, simultaneous pulses will overlap throughout the medium for a duration $\tau_d \sim \sqrt{OD}\tau_p$. Because the peak value of the switch electric field is not attenuated, the effect of the nonlinearities will be increased by a factor $\sim \sqrt{OD}$. Alternatively, a long switch pulse of width τ_d covering the delay time of the probe pulse in the medium will have the same effect as a slowed switch pulse of extent τ_p with same peak intensity, although the latter contains $\sqrt{OD}$ times less photons.

For continuous fields, the enhancement of the photon-photon interaction probability by $\sqrt{OD}$ can be understood as a multiplication of the chances for photons to pass each other as they travel in the medium. In comparison, for a non-slowed switch, switch photons are never absorbed by the medium and pass the target probe polariton once, giving a photon-photon interaction limited by the single atom-single photon cooperativity, i.e. the ratio between the cross section of the corresponding atomic transition σ_s and the area of the switch beam A.

For slow switch photons, the interaction probability $\sim \sqrt{OD}\sigma_s/A$ is greatly enhanced for systems combining large optical depth and strong converse confinement over the extent of the medium, such as cold atomic clouds inside hollow core fiber. For our experimental setup, the cooperativity $\eta \leq 0.005$ will only enable nonlinear optics at the quantum level for extremely large optical depths ($OD \geq 40000$) but the intermediate optical depth can in principle be used to improve on our classical switching results presented in Chapter 3.

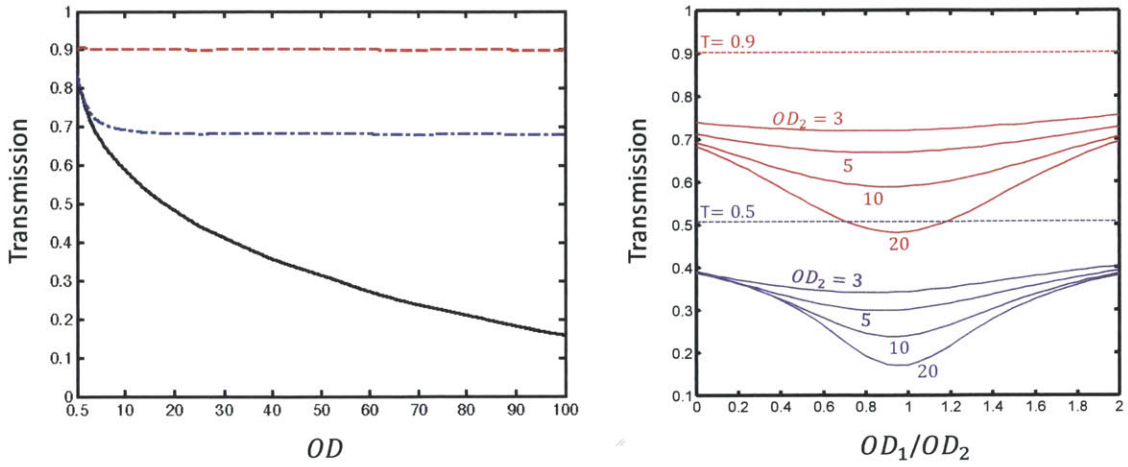

Figure 4-1: **Nonlinearities enhancement by double slow light. a,** Probe transmission in the absence of switch field (red dashed line), for a switch field with speed of light group velocity (dot-dashed blue line) and for a matched group velocity (black line) achieved by two independent EIT schemes for the probe and switch fields with equal optical depth OD. The switch field peak Rabi frequency is 1 MHz. At large OD, the probe pulse is entirely compressed in the medium and the switching efficiency is limited by the single photon-single atom cooperativity for a non-slowed switch. In contrast, for a matched group velocity of the switch field, the nonlinearities are enhanced by the large OD. The lines are the solution to the Maxwell-Bloch equations in the absence of decoherence. For each value of OD, the control frequency is adjusted to obtain a transmission in the absence of switch field of 0.9 for the probe Gaussian pulse with a standard deviation of 100 ns (setting the bandwidth of the experiment). **b,** Transmission of the probe pulse for various values of the probe optical depth OD_2 as a function of the ration between the switch optical depth OD_1 and OD_2, for two different values of the transmission in absence of switch (0.9 for the red curves, 0.5 for the purple curves). At large OD, the enhancement of the nonlinear interactions is maximized around $OD_1 = OD_2$. For lower values of the control field, giving larger group delay and lower transmission, the relative switching effect is enhanced by the longer interaction time.

The scaling with $\sqrt{OD}$ of the enhancement of the nonlinearities is only valid in the limit where the pulses are entirely stored in the medium. For resonant control fields, the EIT peak defines an approximately Gaussian transparency window for the probe intensity $T_p(\Delta_p) = \mathrm{Exp}(-\Delta_p^2/2B^2)$ (in the absence of ground state decoherence) where Δ_p is the probe detuning, $B = \gamma_{EIT}/\sqrt{8OD}$ is the bandwidth of the system and $\gamma_{EIT}/ = \Omega_c^2/\Gamma$ the EIT linewidth set by the control field Rabi frequency Ω_c and the lifetime of the excited

state Γ. The delay $\tau_d = OD/\gamma_{EIT}$ will be larger than a bandwidth limited pulse for $OD \geq 10$ as confirmed numerically and experimentally.

We numerically solve the time-dependent Bloch equation and propagations equation in the SVEA using a homogeneous medium and in the absence of dephasing rate between the ground states (other than the broadening introduced the time dependance of the pulses). Using simultaneously incoming Gaussian field envelopes with a standard deviation of 100 ns for the probe and switch pulses (corresponding to a two-photon broadening on the order of the observed dephasing rate $\gamma \sim$1MHz), and a peak switch Rabi frequency of 1 MHz, we calculate the energy transmission of the pulses. As displayed in Fig. 4-1, in the limit of low OD, the pulse does not fit entirely inside the medium, and the effect of the group velocity reduction of the switch field is not significant. As the OD increases, the effect of the non-slowed switch saturates as it reaches the cooperativity limit. In contrast, the nonlinearities are increased for $OD \geq 10$ by the matched optical depths for the probe and switch EIT schemes (see also Fig. 4-2). As the OD increases, the transmission of the pulse is decreased by the narrowing bandwidth. This effect is compensated for by increasing the control field to allow direct comparison of the nonlinearities enhancement at fixed transmission in the absence of switch field. The result of the simulations presented in Fig. 4-1 neglect decoherence effect, which are expected to reduce the nonlinearities enhancement. The existence of a dephasing rate γ between the ground states sets a lower limit to the EIT linewidth and prevents arbitrarily long delays in the medium. The dephasing rate also limits the nonlinearities by reducing the ratio $\tau_d/\tau_p \sim |\chi'_R| / \sqrt{\chi''_I}$ to (to first order in $\gamma/\Gamma, \gamma/\gamma_{EIT}$):

$$\frac{\tau_d}{\tau_p} = \sqrt{\frac{OD}{8}} \left(1 - \frac{1}{2}\left(\frac{\gamma}{\Gamma} + \frac{\gamma}{\gamma_{EIT}}\right)\right) \tag{4.2}$$

The original proposal for slow interacting pulses [58] resorts to two different species of atoms to simultaneously implement EIT on the probe and switch fields. Both species need to be simultaneously cooled and have a resonant transition in common. It is unclear which atomic elements would fulfill these criteria. Here we demonstrate a scheme to implement double slow light in a single atomic species, shown in Fig. 4-2. To the best of our knowledge, this is the only possible level scheme implementing [58] on the D1-line of ^{87}Rb. This scheme relies on balancing the atomic population between the ($F =$

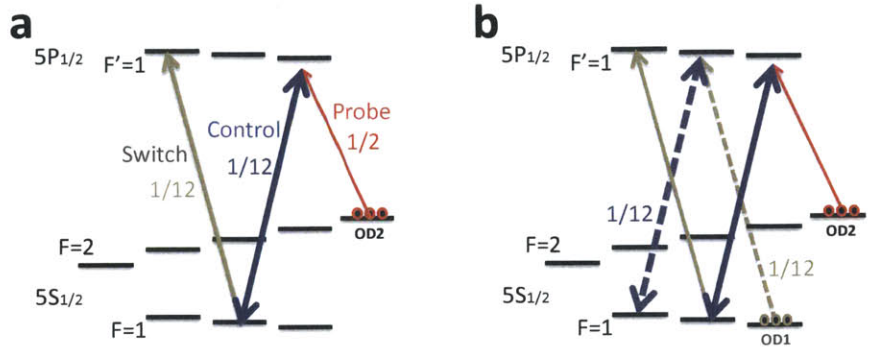

Figure 4-2: **Double EIT scheme. a,** Level scheme for the implementation of the Harris-Yamamoto all-optical switch[53] on the ^{87}Rb D1-line (including Clebsch-Gordan coefficients and schematic Zeeman shift). **b,** Harris-Yamamoto configuration with reduced switch group velocity. The balance of optical depth on the switch and probe transitions is tuned by optical pumping into the $|g_2\rangle = |F = 2, m_F = 2\rangle$ and $|g_1\rangle = |F = 1, m_F = 1\rangle$ levels. In particular, the nonlinear enhancement is measured by comparison of the cases $OD_2 = OD_1 = OD$ and $OD_2 = OD$, $OD_1 = 0$.

$1, m_F = 1)$, and $(F = 2, m_F = 2)$ magnetic sub-levels of the ground state $5S_{1/2}$ of ^{87}Rb by optical pumping. The probe, respectively switch, field is σ^--polarized and couples $(F = 2, m_F = 2)$, respectively $(F = 1, m_{F'} = 1)$, to the $(F' = 1, m_{F'} = 1)$, respectively $(F' = 1, m_{F'} = 0)$, magnetic level of the $5P_{1/2}$ state. σ^+-polarized light on the F=1 to F'=1 transition acts as a control field for both the probe and switch light, with equal Clebsch-Gordan coefficients. The interaction is mediated by the decoherence induced on the $(F = 1, m_F = 0)$ level of the probe EIT scheme due its resonant coupling by the switch field to $(F' = 1, m_{F'} = 1)$. We are here using the D1-line of ^{87}Rb (J=1/2) because the corresponding wavelength of 795nm is further away from the edge of the hollow core fiber bandgap, resulting in better defined polarization of the light in the fiber than on the D2-line for circularly polarized light. The birefringence of the fiber as well as multimode propagation with different polarizations constitute a strong technical limitation. The polarization optics are set to optimize the circular polarization at the top entrance of the fiber, close to which the atoms are mainly located during the experimental probing time.

To maintain the optical pumping, it is necessary to impose a magnetic field along the quantization axis (which is chosen along the propagation direction in the fiber), to

avoid mixing by stray magnetic fields orthogonal to the quantization axis. To maximize the optical switching at low light power, we tune the switch field to resonance with the magnetically shifted atomic transition, and correspondingly adjust the control field and probe field to satisfy the two-photon resonance (see Fig. 4-2). As a consequence, the probe and switch EIT operate at small (compared to the linewidth) one-photon detuning, which has no consequence in the absence of strong decoherence. Finally, by reducing the number of atoms loaded in the fiber and fully pumping them to the $(F = 2, m_F = 2)$ level, we can directly measure the enhancement of the nonlinearities with respect to a switch field with speed of light group velocity. Because of the difference in Clebsch-Gordan coefficients, the group velocity are matched for a strongly imbalanced distribution of atoms corresponding to $OD_2 = OD_1 = OD/7$, which puts high balanced optical depths out of reach for our current loading mechanism.

As described in Chapter 3, the atoms are free-falling inside the hollow core of the photonic crystal fiber, and are initially loaded using a blue detuned hollow guide outside the fiber and a red-detuned dipole trap coupled into the fiber. At the time of this experiment, the maximal optical depth achievable with a cycle rate of 1 s was $OD = 50$, corresponding to an optical depth of 25 on the probe transition. In general, we observed over the years a slow decay of the loading efficiency into the fiber. Coating of the fiber tip and inner walls by ^{87}Rb atoms which are desorbed and limit the lifetime in the fiber possibly explain this decay [99], as well as a reduction of the getters flux. After the initial loading period, the atoms are optically pumped into $|g_1\rangle = |F = 1, m_F = 1\rangle$ and $|g_2\rangle = |F = 2, m_F = 2\rangle$ by a combination of laser fields with σ^+ polarization on the $F = 1 \rightarrow F' = 1$ and $F = 2 \rightarrow F' = 2$ transitions of the D1 line. Their intensity ratio and polarization purity determines the balance between the two populations. In particular, larger scattering rates for the $F = 2 \rightarrow F' = 2$ transition favors the population of $|g_1\rangle$ as the remaining σ^- component of the pump light transfers atoms out of $|g_2\rangle$. The exact ratio between the pumping fields is fine-tuned by directly matching the group delays for the probe $(\tau_{d,p})$ and switch $(\tau_{d,s})$ fields. This procedure also corrects for the change in group velocity of the probe pulse induced by the switch field. To measure the enhancement of the nonlinearities, we compare the case $\tau_{d,p} = \tau_{d,s} = \tau_d$ to the case $\tau_{d,p} = \tau_d, \tau_{d,s} = 0$. For the latter, all the atoms are pumped into $|g_2\rangle$ by increasing the intensity of the $F = 1 \rightarrow F' = 1$

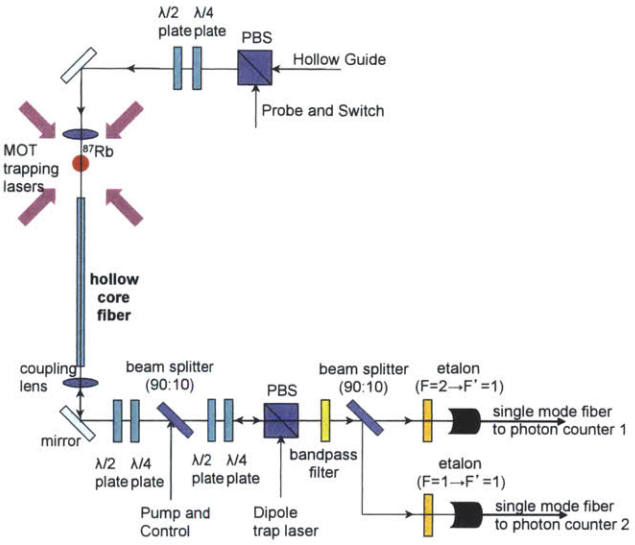

Figure 4-3: **Setup for double slow light experiments.** ^{87}Rb atoms are loaded from a MOT into the core of the HCF using a hollow blue detuned guide outside the fiber and a red-detuned 802nm dipole trap inside the fiber. The probe and switch pulses are counter-propagating with the control field to minimized the amount of control field light on the single photon detectors. Three sets of polarization optics comprising one half-waveplate and one-quarter waveplate are used to independently set the polarizations of the probe and switch fields, the pump and control fields, and the dipole trap. The polarization for the probe and switch fields are optimized by taking transmission spectra in large bias magnetic fields along the z-axis. The control and pump fields are optimized using EIT spectra. In both cases, the settings of the waveplates corresponds to circularly polarized light at the top of the fiber, where most atoms are likely located during our probing sequence. The observed polarization rotation, change in ellipticity and loss of degree of polarization over the length of the piece of fiber severely limit the quality and the robustness of the optical pumping. The last set of waveplates imposes the polarization of the dipole trap in the fiber and the amount of probe and switch signal transmitted to the single-photon counter after the polarizing beam splitter (PBS) merging the dipole trap. For our fiber, the setting of the waveplates corresponding to the best probe signal transmission does not correspond to the optimal (linear) dipole trap polarization for the atoms loading into the fiber. Finally, the probe and switch signal are dected by single-photon detectors. The (stronger) switch signal is filtered out from the probe signal by two consecutive etalons. The transmission of the switch pulses is simultaneously monitored by sampling a small ($\sim 10\%$) amount of the signal and filtering out the probe signal with an etalon.

pumping beam and decreasing the intensity of the $F = 2 \rightarrow F' = 2$ pumping beam. Finally, the loading time of the MOT can be used to adjust the total number of atoms

inside the fiber.

We estimate that $\sim$ 80% of the atoms are initially pumped into the states $|g_1\rangle$ and $|g_2\rangle$. This fraction is lower than what is typically achievable in free space and is probably due to the observed change in polarization of the pumping light as it travels in the fiber. For the same reason, the strong control field intensity quickly destroys the quality of the optical pumping by removing atoms from $|g_1\rangle$. To counteract this effect, it is necessary to alternate probing sequences with longer pumping sequences, which limits the number of repetitions per cycle time to about 50. We verify that the loss of OD_1 during one pulse propagation in the medium is on the order of ten percent by measuring the remaining atomic population in $F = 1$ after a few successive repetitions. Importantly, the reshuffling of the atomic population by the control beam has the same signature as an enhancement of the optical nonlinearities because it reduces the probe transmission by increasing the atomic population in $F = 2$. Furthermore, the partial absorption of the switch beam due to decoherence also contributes to this effect. The lack of robustness of the optical pumping due to the birefringent and multimode character of the fiber is a severe limitation for the observation of the few percent nonlinear enhancement expected in our OD regime.

At the output of the fiber, the outgoing switch and probe pulses are separately recorded using a set of etalons and two single photon counters. For each cycle, reference probe, switch and control pulses are accurately measured for the empty fiber after the dipole trap has been turned off for 10 ms in order to eliminate slow drifts of the coupling efficiency in the hollow core fiber and of the etalons transmission. We also determine the amount of control and switch field light leaking through the etalon on the probe detector. The time-resolved control field and switch noise is subsequently substracted from the probe pulse and the transmission is calculated.

We first demonstrate our ability to match group delays for the probe and switch pulses using the optical pumping techniques described above. Pulses with Gaussian envelope with a standard deviation of 85 ns are created with acousto-optical modulators. The pulses are sent simultaneously into the medium and the delays are measured at powers corresponding to a few photons per pulse. For the low optical depth achievable simultaneously on the probe and switch transition $OD_2 \leq 4$ and because of typical dephasing between the ground states $\sim$ 1 MHz, significant delays with respect to the pulse length are

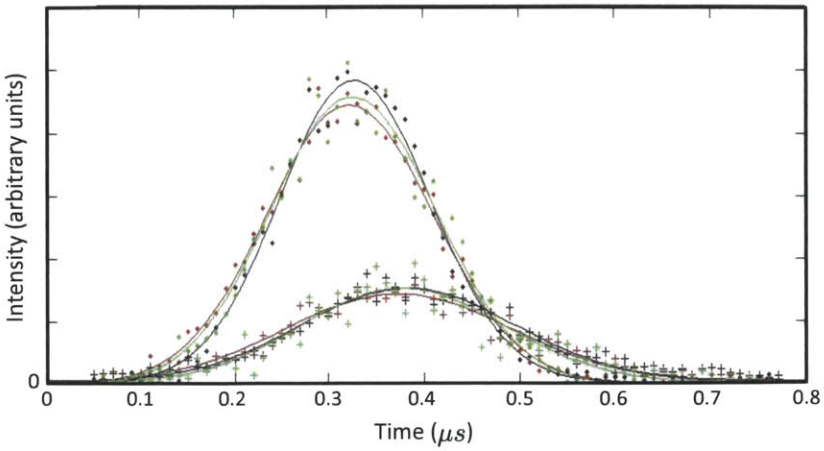

Figure 4-4: **Probe and switch group delays.** Incoming (dot) and outgoing(+) pulses for the probe and switch field and corresponding Gaussian fits (line). The pulses are measured for two configurations corresponding to Fig. 4-2.a and Fig. 4-2.b. Enhanced nonlinearities are expected when the group delays for the probe (red) and switch (black) pulses are matched by distributing the atoms in $|g_2\rangle$ ans $|g_1\rangle$. For direct comparison, we also measure the nonlinearities when no atoms are left in $|g_1\rangle$ and the overall number of atoms is reduced to obtain an identical probe delay (green). In that case, the outgoing switch pulse is equal to the incoming one.

not achievable simultaneously with large transmission. Given the scaling of the nonlinearities with the group delay in the medium, the constant control field intensity is chosen to achieve group delays of 50 ns. It corresponds to a transmission of 0.4 and a broadening of the pulses by a factor 1.5 (See Fig. 4-4). By fine tuning of the optical pumping intensities and the MOT loading time, we are able to equalize the group delays of the probe light and the switch light, as well as the probe light in absence of switch delay, within a few percent of the pulse duration.

We then measure the relative probe transmission with and without switching pulses for different switch pulse energies. After the initial pumping, the dipole trap is modulated with a 1 μs half period. The main experimental sequence consists of 50 repetitions of alternating probe pulses with and without switch field, separated by optical pumping pulses. After noise substraction, the switching efficiency plotted in Fig. 4-5 is defined as the difference between the pulse transmission with and without switch pulse, normalized to the transmission in the absence of switch field. To compare the photon-photon interaction

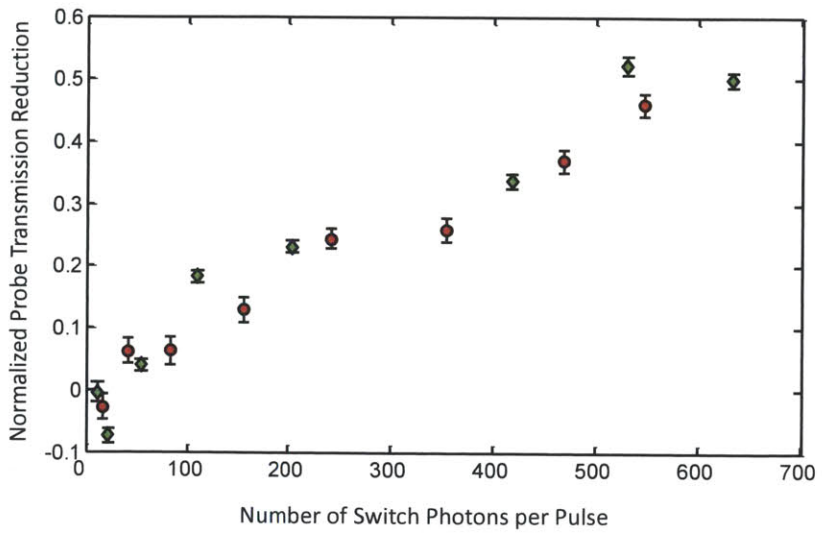

Figure 4-5: **Double slow light switching efficiency.** Difference in probe transmission with and without switch pulses, normalized to the transmission in absence of switch field. Red circles correspond to the case where the group velocities of the probe and switch pulses are matched. Green diamonds correspond to an identical group delay for the probe but no group delay for the switch and serves as a reference. The error-bars correspond to the shot-noise. The number of switch photons is rescaled in the double slow light case to compensate for the absorption of the switch photons. Measurements are carried out for $OD_2 = 4$. In this regime, no visible enhancement of the nonlinearities is expected (see Fig. 4-1).

enhancement, we compensate for the important absorption for slow switch pulses by rescaling the number of switch photons per pulse. Assuming an exponential decay of the intensity over the length of the medium, we rescale the number of switch photons per pulse to its average value inside the medium $(N_{in} - N_{out})/\ln(N_{in}/N_{out})$ where N_{in} and N_{out} refer to the input and output numbers of switch photons.

In spite of this rescaling, we do not observe any enhancement of the photon-photon interaction within our measurement noise, as expected from our numerical simulations carried out for a medium free of decoherence. We nevertheless demonstrate group velocity matching in the hollow-core fiber and were able to observe nonlinear effects for less than 100 switch photons per pulse after carefully accounting for the noise. This holds some promise for future experiments, provided that fiber with better polarization properties are used and higher number of atoms can be loaded in the fiber. It will also be necessary

to use PCFs with sub-wavelength transverse mode dimensions to reach single-photon nonlinearities, although the atoms loading might be affected. A three-fold enhancement of the nonlinearities by double slow light was recently demonstrated in [100] using an M-level scheme with optical depths of 50-100 in a MOT.

4.2 Stationary Light Pulses in cold atomic media

Zero-velocity dark-state polaritons with non-vanishing photonic compononent in atomic media, so-called stationary light pulses, have attracted intense attention in recent years because of the possibility of creating strong optical nonlinearities on the few-photons level. Here, we present a comprehensive experimental study of stationary light in cold atoms at large optical depth inside a hollow core photonic crystal fiber. We observe qualitative changes of the stationary light compared to room-temperature atoms and show that these effects are due to higher-order coherences relevant for cold atoms. We investigate how the required features of stationary light for proposed enhancements of optical nonlinearities can be recovered in cold atoms and demonstrate a distributed Bragg reflector made of a few thousands atoms.

Controlled localization and storage of photonic pulses allows for novel approaches to manipulating of light via enhanced nonlinear optical processes. Electromagnetically induced transparency in an ensemble of Λ-type three-level atoms can be used to reduce the group velocity of propagating light pulses and to reversibly map propagating light pulses into stationary spin excitations in atomic media [55]. A special type of stored pulses, so called stationary light, is of particular interest, because here, the combined atom-photon excitation inside the medium retains a non-vanishing photonic component, even when it is completely stopped inside the medium [59, 85]. This enables enhancement of optical nonlinearities by increasing solely the optical density of the medium [60]. The basic idea of stationary light is to illuminate the atomic medium with two counter-propagating control fields instead of the single, usually co-propagating control field in normal EIT. Since the two control fields form a standing wave intensity pattern, this results in a periodic modulation of the EIT conditions inside the atomic medium, similar to the periodic refractive index change in a distributed Bragg reflector. Stored photons released inside this medium

can undergo multiple Bragg-reflections and thus remain trapped inside the medium. Conceptually, this is similar to the electric field build-up in an optical cavity, which results in strong enhancement of the confined light with e.g. atoms inside the resonator. Similarly, if the stationary light is confined inside a nonlinear medium, the multiple reflections result in strongly increased interaction times, enhancing effective photon-photon interactions. This key concept is at the heart of many proposed applications of stationary light inside nonlinear media, such as Bose-Einstein condensation of stationary light polaritons [94], crystalization of a strongly interacting one-dimensional photon gas [29], simulating Dirac dynamics with photons [95], and creating effective magnetic fields for photons [96]. The existence of stationary light pulses has been demonstrated in room-temperature atomic vapor cells [85]. Following these experiments, it has been realized that some care must be taken when transfering the concept of stationary light to ultracold atoms. An essential assumption of the original theoretical description of stationary light is the secular approximation in which spatial modulations of the ground-state coherence of the Λ-type atoms with wave numbers on the order of the optical fields and its harmonics are neglected [59, 101]. While this is a very good approximation in warm gases, where atomic motion leads to a fast dephasing of fast spatial oscillations, it fails however for cold gases where the atoms are almost stationary on the typical timescale of experiments [102, 103, 104]. This has recently been confirmed by experiment [105], where the absence of stationary light under resonant conditions inside a laser-cooled atomic vapor was demonstrated. In this section, we study stationary light inside a one-dimensional cold atom medium, taking advantage of the large optical depth, up to $OD = 85$. For this we utilize optically trapped atoms inside the hollow core of a photonic crystal fiber (see Chapter 3). This system provides the combined advantages of an enhanced single atom-single photon interaction probability and a large OD, a key requisite to observe strong non-linearities on a few-photon level [93]. We study the effects of periodically varying EIT control fields inside the fiber and use our observations to develop a solid theoretical treatment of stationary light pulses in cold atoms.

We start by loading $N \sim 2 \times 10^4$ atoms inside our 3 cm long hollow core photonic crystal fiber with methods described in Chapter 3, where they are guided by a red-detuned dipole trap. We detect these atoms by sending very weak pulses of probe light

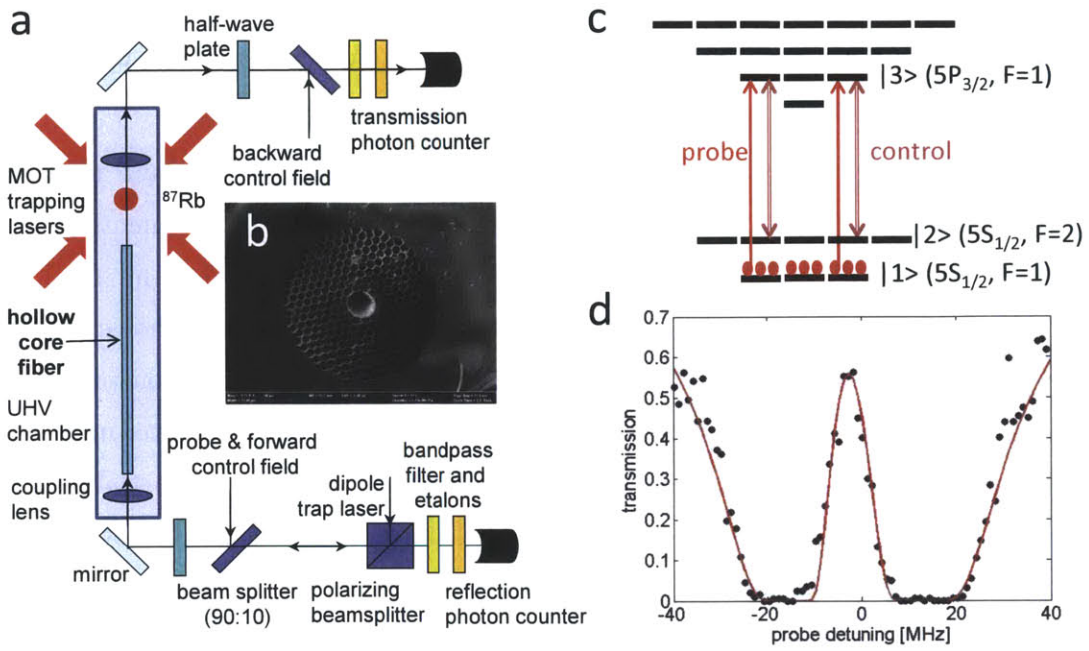

Figure 4-6: **Experimental setup for stationary light pulses inside a hollow-core fiber. a,** Schematics of the experimental setup. After guiding the atoms into a hollow-core photonic bandgap fiber with a red-detuned dipole trap, the medium is probed in the presence of co- and counter-propagating control fields, and the transmitted and reflected probe photons are detected with single photon detectors. **b,** SEM image of the hollow core fiber. **c,** Implementation of the EIT Λ-scheme on the hyperfine states of the Rubidium D2-transition. Since the atoms are distributed randomly over the Zeeman-sublevels, the system is made up of two identical, independent Λ-schemes that result in exactly the same EIT transmission. This level-scheme minimizes the strong rotation and change in ellipticity observed for nonlinearly polarized fields. **d,** Observation of induced transparency at $OD = 45$. While the control field is on single-photon resonance for this scan, we observe a shift of the transmission peak by a few MHz to the blue. This is caused by the AC-Stark shift induced on level $|2\rangle$ by the control field coupling off-resonantly to $5P_{3/2}$ hyperfine states. This effect is included in our analysis.

through the fiber (Figure 4-6,a,b). As defined previously, the important figure of merit is the optical depth $OD = N\,(\sigma_0/A)$, where N is the number of atoms in the fiber, σ_0 is the atomic absorption cross section for the probed transition, and A is the area of the fiber guided mode. Since the atoms experience a strong spatially dependent AC-Stark shift due to the trapping light, resulting in a shifting and inhomogeneous broadening of the observed absorption lines, we modulate the dipole trap at a frequency (1 MHz) much faster than the oscillation frequency of the trap (50 kHz). We perform a series of 100

pulsed experiments on one sample in the off-times of the dipole trap before completely releasing all the atoms and restarting the loading cycle. When using this technique, we observe a maximum $OD \sim 180$ on the $F = 2 \rightarrow F' = 3$ cycling transition.

Despite this very large optical depth, the fiber medium can be made transparent by EIT. Figure 4-6,c shows the 3-level Λ-system we use in the experiments described here. On the chosen probe transition $F = 1 \rightarrow F' = 1$ of the Rubidium D2 line the maximum optical depth we can achieve is $OD = 85$. Our particular choice of parallel linear polarization for probe and control field is based on the polarization properties of the hollow-core fiber. Because this fiber type by design is not polarization maintaining, we observe polarization rotation and change in ellipticity, as well as a partial loss of the Stokes degree of polarization of the outgoing light, attributed to the multimode character of the short piece of fiber and the excitation of surface modes propagating with different polarizations. Nevertheless, transverse pressure on the fiber create two main axes. Light polarized along these main axes experiences little polarization change when travelling through the fiber. This is important for our experiments, as we rely on two counter-propagating control fields interfering to form a standing wave inside the fiber. A typical EIT transmission scan at $OD \sim 45$ is shown in Fig. 4-6,d. Due to the tight confinement of light inside the hollow core fiber, very low control field power (10 nW) is sufficient to achieve $> 80\%$ transmission on two-photon resonance. We observe similar EIT spectra for co- and counter-propagating control fields (the atoms are sufficiently cold for Doppler-shifts to be negligible).

To turn this EIT configuration into stationary light inside the fiber, we turn on both control fields simultaneously, such that they form a standing wave pattern of control field intensity with spacing $\lambda/2 = 390\,\text{nm}$. We then study the response of the medium in the frequency domain by measuring the transmission and reflection spectra of an incoming probe beam. We can infer the possibility for stationary light inside the medium from unique features in the observed spectra. In particular, the key feature pointing towards the ability to confine light inside the medium is the observation of a strong Bragg-reflection peak, accompanyied by a bandgap in the transmission spectrum, *i.e.* a frequency range over which any transmission through the system is strongly suppressed.

Before turning to experimental results, we briefly review the theory for stationary

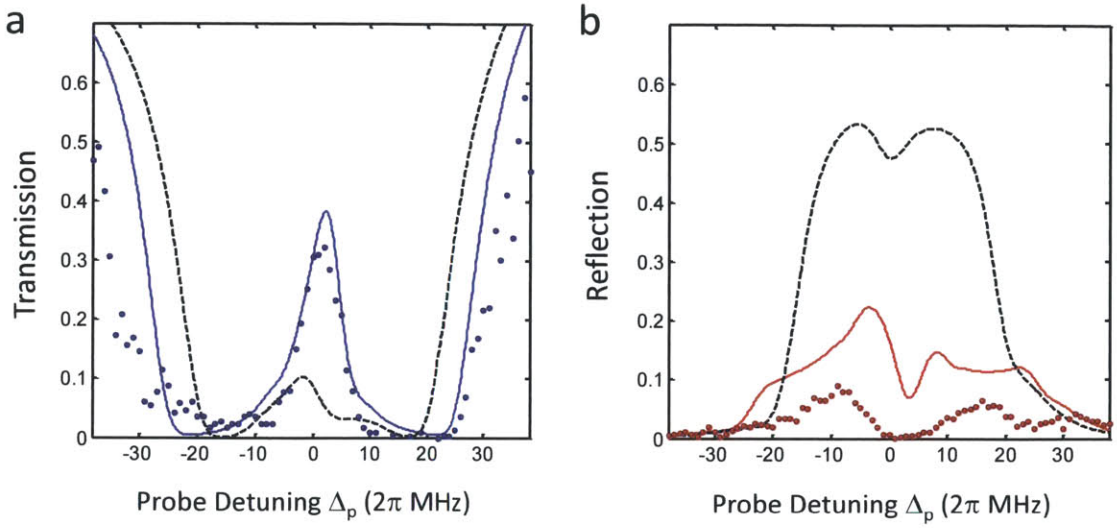

Figure 4-7: **Absence of optical bandgap on resonance.** Measured transmission (**a**) and reflection (**b**) for resonant control fields (Δ_+=Δ_-=0). The expected reflection peak vanishes, as predicted by our analytical model (solid curves). 0-th order predictions, pertaining to room-temperature atomic vapors are plotted for identical parameters (black dashed lines). The analysis takes into account a 10% power imbalance between the co-and counter-propagating control fields. All the parameters are within 20% of the values independently extracted from EIT fits for free-running control fields. The measured reflection is rescaled by a factor 1/3.5 (see text).

light, including the effects of a finite detuning between the two control fields and finite pulse duration. We first decompose the probe field into two slowly varying components $\mathcal{E}_+$ (forward propagating) and $\mathcal{E}_-$ (backward propagating) and introduce coarse-grained, slowly varying collective atomic operators $\hat{\mathcal{P}}$, $\hat{\mathcal{S}}$, $\hat{\mathcal{C}}$ pertaining respectively to the $|1\rangle \rightarrow |2\rangle$, $|1\rangle \rightarrow |3\rangle$ and $|3\rangle \rightarrow |2\rangle$ coherences (see Appendix B). The atom-photon interaction Hamiltonian in the rotating frame is given by (Eq. B.1):

$$\hat{H}_I = -\frac{\hbar}{2}\int_L dz\sqrt{n}\left[g\left(e^{ik_p z}\hat{\mathcal{E}}_+(z,t)+e^{-ik_p z}\hat{\mathcal{E}}_-(z,t)\right)\hat{\mathcal{P}}^\dagger(z,t)\right] - \frac{\hbar}{2}\int_L dz\sqrt{n}\left[\left(\Omega_+ e^{i(k_c+\Delta k_+)z-i\Delta t}+\Omega_- e^{-i(k_c+\Delta k_-)z+i\Delta t}\right)\hat{\mathcal{C}}^\dagger(z,t)\right]+\text{h.c.} \tag{4.3}$$

where g is the single atom-probe field coupling constant, L is the length of the medium,

$\Omega_\pm$ are the rabi frequencies and $\Delta_\pm = \Delta_c \pm \Delta$ the detunings for the forward (+) and backward (-) propagating control fields (Δ_c is the average detuning between the forward and backward control fields). In what follows we neglect the terms $\Delta k_\pm z = \pm\Delta \cdot z/c$ because, for the experimentally relevant detunings, they correspond to negligible phase shifts over the length of the medium. The counter propagating control fields have the effect of coupling different spatial Fourier components of the atomic polarization, which allows $\mathcal{E}_+$ to be backscattered into $\mathcal{E}_-$ through a four photon process. Therefore, it is convenient to expand the polarization in its Fourier harmonics $\hat{\mathcal{P}} = \sum_m \hat{\mathcal{P}}^{(m)} e^{im(k_c z - \Delta t)}$, $\hat{\mathcal{S}} = \sum_m \hat{\mathcal{S}}^{(m)} e^{im(k_c z - \Delta t)}$. The higher order Fourier components of the polarization drive an electric field at the corresponding frequency, but these fields do not satisfy the phase matching condition and, as a result, are strongly suppressed. Since we are primarily interested in the case of weak signal fields corresponding to a few photons, we can expand $\hat{\mathcal{P}}^{(\pm 1)}$ to first order in $\mathcal{E}_\pm$. We obtain a set of Langevin-Maxwell equations for the atomic coherences and the probe fields, given, in the Fourier domain and for steady states by (see Appendix B):

$$\pm c\partial_z \hat{\mathcal{E}}_\pm(z,0) = ic(\Delta k)\hat{\mathcal{E}}_\pm(z,0) + i\frac{g_p}{2}\hat{\mathcal{P}}^{(\pm 1)}(z,\mp\Delta) \tag{4.4}$$

$$\begin{aligned} 0 &= -\left(\frac{\Gamma}{2} \mp i\Delta - i\Delta_p\right)\hat{\mathcal{P}}^{(\pm 1)}(z,0) + \frac{i}{2}\Omega_\pm \hat{\mathcal{S}}^{(0)}(z,0) \\ &\quad + \frac{i}{2}\Omega_\mp \hat{\mathcal{S}}^{(\pm 2)}(z,0) + \frac{ig_p}{2}\hat{\mathcal{E}}_\pm(z,\pm\Delta) \end{aligned} \tag{4.5}$$

$$\begin{aligned} 0 &= -\left(\frac{\Gamma}{2} - im\Delta - i\Delta_p\right)\hat{\mathcal{P}}^{(m)}(z,0) \\ &\quad + \frac{i}{2}\Omega_+ \hat{\mathcal{S}}^{(m-1)}(z,0) + \frac{i}{2}\Omega_- \hat{\mathcal{S}}^{(m+1)}(z,0) \end{aligned} \tag{4.6}$$

$$\begin{aligned} 0 &= -\left(\frac{\gamma}{2} - im\Delta - i\delta\right)\hat{\mathcal{S}}^{(m)}(z,0) \\ &\quad + \frac{i}{2}\Omega_+^* \hat{\mathcal{P}}^{(m+1)}(z,0) + \frac{i}{2}\Omega_-^* \hat{\mathcal{P}}^{(m-1)}(z,0) \end{aligned} \tag{4.7}$$

where $g_p = \sqrt{n}g$ is the collective probe coupling, Γ is the decay rate of the excited state and γ is the Raman decoherence rate, Δ_p the probe detuning, δ the two-photon detuning and $\Delta k = k_p - k_c$ the phase mismatch. After taking the average values for the operators

(i.e. the classical envelopes of the fields), we can invert Eqs. 4.5-4.7 to find the frequency dependent susceptibility, which allows us to integrate Eq. 4.4 in z to obtain the reflection, transmission and absorption through the medium.

We first investigate the simple case of on-resonant control fields of equal power. The observed transmission and reflection spectra are shown in Fig. 4-7,a and b. Unlike the results obtained in hot atoms [85], we observe almost no reflection on two-photon resonance as well as the absence of a transmission band gap. This is equivalent to the observation of non-stationary pulses inside the medium obtained before in cold vapor experiments [105], confirming that the simple picture of stationary light does not hold in cold atoms. This also is apparent in the visible qualitative discrepancy between our measured spectra and the 0th-order calculations (back dashed lines in Fig. 4-7). Agreement between theory (solid colored lines, for which all the parameters of the model are measured independently) and experiment can only be obtained by including higher order coherences, in which case the theory reproduces the qualitative changes observed in the experiment. For our experiment, there is a large experimental uncertainty in the normalization of the observed reflection. We observe a factor ~ 10 larger magnitude of the reflection peak depending if the experiment is carried out with an input probe coupled at the top of the fiber or an input probe coupled at the lower facet of the fiber. We attribute this effect to a defect or impurity close to the bottom end of the fiber, resulting in a loss factor η_F for the probe fields propagating past it. The atoms are probed when they are near the top entrance of the fiber. According to this model, upon renormalization by the transmission in the absence of atoms, the reflection is overestimated by a factor η_F for an input beam from top and underestimated by a factor η_F for an input beam from the bottom. As a consequence, using $\eta_F^2 = 12$, we rescale all the reflection spectra, taken with a top incoming beam, by a factor 3.5 and notice that it gives reasonable qualitative agreement with our model.

These findings lead to the question of the existence of stationary light in cold atoms. One solution to recover stationary light is to use a double-Λ scheme instead of the simple 3-level system [106], so that no higher-order coherence terms coupling forward and backward propagating probe fields can form at all. While this greatly simplifies the theoretical approach, it may be relatively complicated to implement experimentally. An alternative

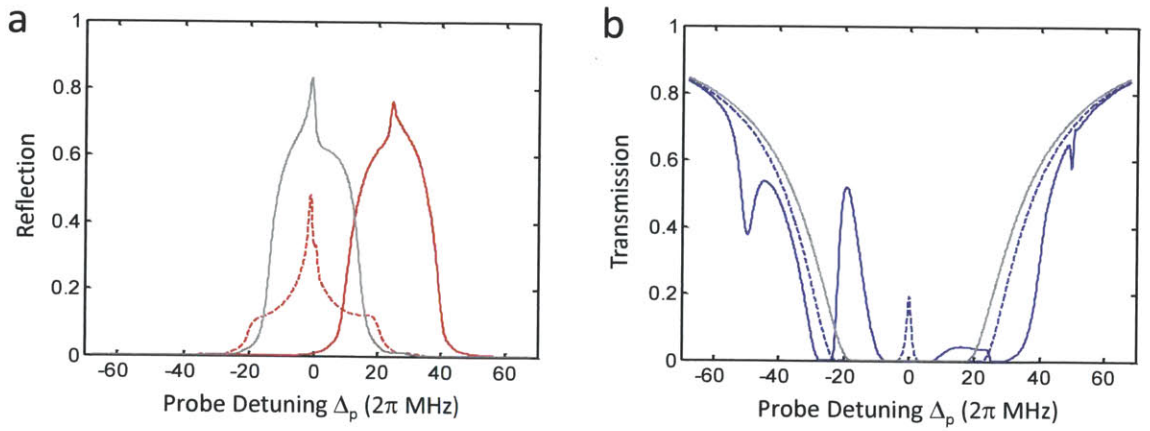

Figure 4-8: **Stationary Light Pulses in hot and cold atomic vapors. a**, Reflection and **b**, transmission for $OD = 80$, in the absence of decoherence. For room-temperature atoms, the large displacement of the atoms on the length scale of the imprinted spin-wave grating ($\sim \lambda$) and on the timescale of the EIT process ($\sim \Omega^2/\Gamma$) is well described by the 0th order theory (grey lines), where the higher spatial harmonics of the spin-wave are neglected. As a result, a large optical bandgap replaces the EIT transmission peak and is accompanied by a broad reflection peak. In contrast, for cold atoms, it is necessary to include higher spatial Fourier components of the spin-wave. The inclusion of the faster oscillating spatial components of the spin-wave significantly reduces bandgap (dotted lines, see also Fig. 4-7). The hot atoms behavior can be recovered by introducing a detuning between the control fields, creating a running control-field standing wave (colored sold lines). In that case, the reflection exhibits a broad reflection peak almost identical to the one expected for room-temperature atoms, centered on resonance with the co-propagating control field. The parameters are $\Omega_+ = \Omega_- = 20$ MHz and $\Delta_+ = \Delta_- = 20$ MHz for the detuned case.

solution that has been proposed are "'two-color"' control fields, i.e. the introduction of a (small) relative detuning between the two control fields [107, 105]. In this case, the two fields form a "'moving"' standing wave, i.e. the nodes and anti-nodes of the control field move along the medium with the beatnote frequency of the two beams. As visible in equations Eqs. 4.7, 4.6, the detuning creates dephasing at rates $\propto m\Delta$ between the higher harmonic of the atomic coherence, resulting in a washing out of the higher order coherence terms. As visible from the theoretical predictions in Fig. 4-8, the reflection feature obtained by detuning symmetrically the control fields from the resonance ressembles strongly that of the resonant case, albeit shifted by an amount corresponding

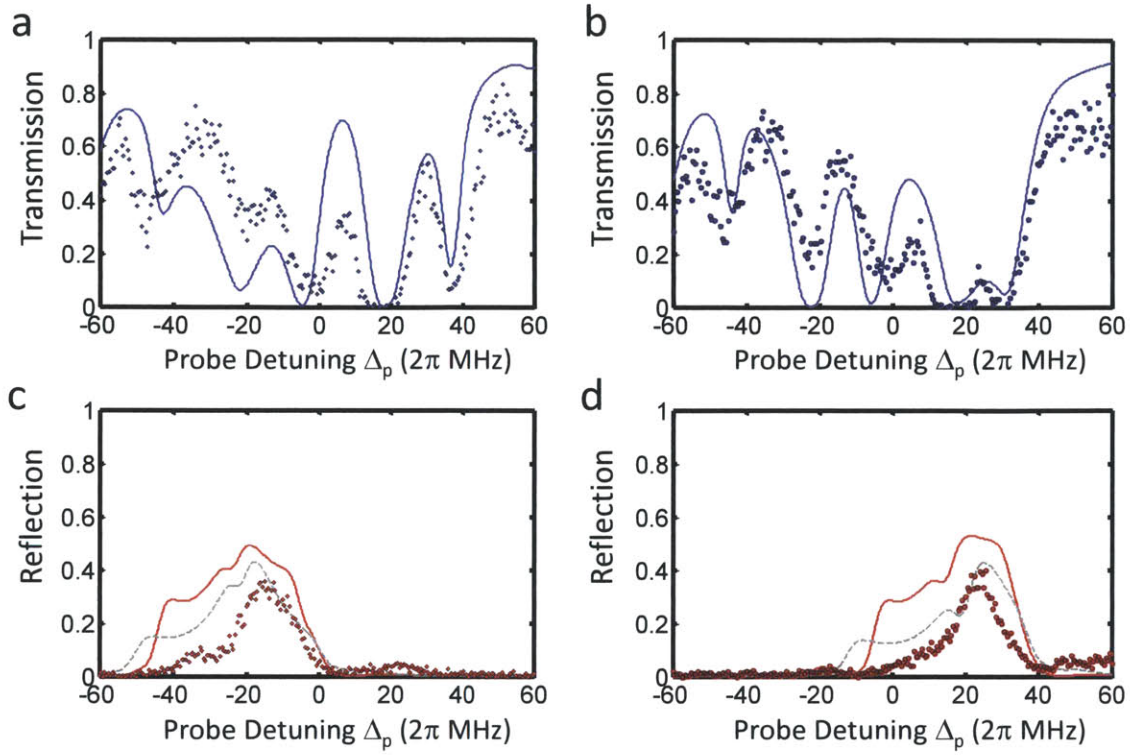

Figure 4-9: **Spectra for a moving-wave control field.** Measured transmission (**a,b**) and reflection (**c,d**) for detuned control fields (**a,c**: Δ_+=-Δ_-=-20 MHz; **b,d**: Δ_+=-Δ_-=20 MHz). Here, the optical depth is OD=20 and the control fields Rabi frequency $\sim$ 30MHz. The transmission spectrum exhibits a complex multi-peak structure arising from the higher order coherence terms in the spin-wave, accompanied by a reflection peak close to resonance with the co-propagating control field. We observe good qualitative agreement between the measured reflection peak, the theoretical prediction including higher order of the spin-wave and the 0-th order theory (grey dashed lines). We also observe good qualitative agreement between our theoretical prediction and the transmission spectrum. The discrepancy between the measured data and our model is likely caused by many technical imperfections in our hollow-core fiber experiment, such as polarization rotation and ellipticity of the light, multimode character of the beams and attenuation of the fields along the fiber.

to the detuning of the forward control beam.

This has been studied at low optical densities in dilute vapor of cold atoms, where strong damping of the higher order terms was observed for small relative detunings on the order of the probe transition linewidth (6 MHz) [105]. In our investigation at significantly larger OD, we find that much larger detunings are required to reproduce the qualitative

aspects of the 0th-order calculation. In Figure Fig. 4-9 we show transmission and reflection spectra for the case of $OD = 20$ and detunings of $\Delta_c = 0, \Delta = 20$ MHz. Only when we increase the relative detuning to this large value on the order of the control frequency do we observe a significant reflection peak at two-photon resonance with the forward control field, accompanied by a frequency range of suppressed transmission. The running lattice creates dephasing on the order of the wavelength over a timescale $\sim 1/\Delta$, effectively washing out the higher order coherences when this timescale is smaller than the inverse EIT bandwidth, $\sim \Delta/\Omega_c^2$. The effect of the detuning is similar to the atomic motion as can be seen by the fact that both the full theory (solid color lines) as well as the 0th order calculation (grey dashed lines) predict this reflection peak. Other features, such as extra peaks in the transmission spectrum, are qualitatively reproduced only by the full theory, while the 0th order theory fails to predict them completely. Based on our observations and the full calculations, the criterium for the required relative detuning between the control fields to observe stationary light is that it is larger than the control field Rabi frequencies. This might limit the applicability of this solution in the case of very large OD (> 1000) and control field Rabi frequencies ($> 100\,\text{MHz}$) envisioned in some of the proposed applications of stationary light [59, 29].

Finally, we explore the possibility to create distributed Bragg gratings by taking advantage of the multi-level atomic structure. The ground state $|2\rangle$ is off-resonantly coupled by the standing wave control field to the hyperfine levels $F = 2$ and 3 (see Fig. 4-6), inducing a periodical level-shift with a periodicity $\lambda_c/2$ given by that of the control lattice. Here, we neglect the effect of the control field on the other levels due to the large energy separation of the hyperfine ground states. At large control fields detuning ($\Delta_c \gg \Gamma$), close to two-photon resonance ($\delta = 0$), the probe samples a periodical medium consisting of alternating layers with different index of refraction and transmission. Experimentally, the control fields are blue-detuned from the $|2\rangle \rightarrow |3\rangle$ transition and have the same frequency ($\Delta = 0$). We denote Δ_L the Stark shift at an anti-node of the control field lattice (which equals four times the level-shift generated be a single control field, due to constructive interference between the control fields) and take the effect of the periodic shift into account by making the substitution $\delta \rightarrow \delta - \frac{\Delta_L}{2}(1 + \cos(2k_c z))$ in (4.7). The equation for the spin-wave harmonics becomes:

$$0 = -\left(\frac{\gamma}{2} - i\delta + i\frac{\Delta_L}{2}\right)\hat{\mathcal{S}}^{(m)} - i\frac{\Delta_L}{4}\left(\hat{\mathcal{S}}^{(m+2)} + \hat{\mathcal{S}}^{(m-2)}\right) + \frac{i}{2}\Omega_+^*\hat{\mathcal{P}}^{(m+1)} + \frac{i}{2}\Omega_-^*\hat{\mathcal{P}}^{(m-1)} \quad (4.8)$$

On top of the average Stark shift $\Delta_L/2$, the grating also induces direct coupling between the even harmonics of the spin-wave. The theoretical predictions are displayed in Fig. 4-10,a, where the transmission and reflection spectra are plotted for equal parameters in the presence and absence of coupling to a fourth excited level responsible for the periodic phase-shift. The modulation of the level-shift clearly induces a large reflection peak associated with an opaque optical bandgap. We verify that theses prediction are in excellent agreement with our theoretical predictions, as displayed in Fig. 4-10,b, where the reflection was scaled by the same factor $\eta_F = 3.5$. In particular we observe a large reflection peak ($> 70\%$) associated with a large optical bandgap. All the parameters in the theoretical model (solid lines) are independently measured from EIT fits, showing excellent qualitative agreement between our model and observations. Note that a running lattice creates a moving periodic Stark-shift in the case $\Delta \neq 0$ and has been included in the theoretical model displayed Fig. 4-9.

In this case, the system can be seen as a dynamically controllable mirror, made out of few thousand atoms, which may be useful for creating dynamic cavities [108, 109] or for all-optical routing of probe pulses [110]. In conclusion, we have presented the first experimental investigation of stationary light in a cold-atom system with large optical depth. Comparison to the full theory of stationary light in a Λ-system sheds new light on how this phenomenon has to be treated theoretically in the case of cold atoms. This understanding will be essential for the application of stationary light to the enhancement of optical nonlinearities [60, 106, 29, 95, 96], which was recently demonstrated in [111].

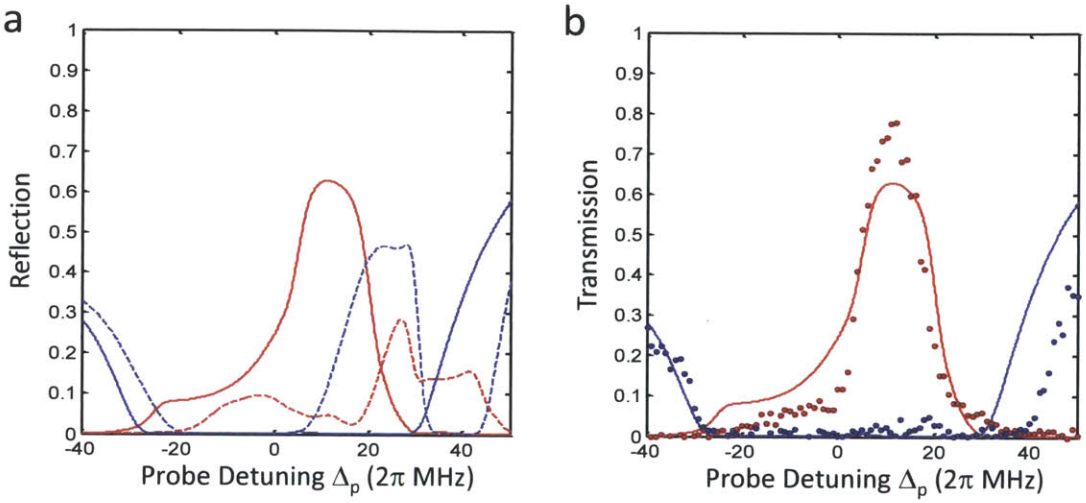

Figure 4-10: **Atomic Bragg grating.** **a**, Expected transmission (blue) and reflection (red) for similarly detuned control fields ($\Delta_+ = \Delta_-$=32 MHz) of equal power ($\Omega_+ = \Omega_- =$ 12 MHz), for a Λ-type 3-level system (dashed) and in the presence of a fourth atomic level inducing periodical level-shift of the ground state $|2\rangle$ by the standing-wave control field (see also Fig. A-1,b), at an optical depth $OD = 75$. The periodical Stark shift induces a modulation of the index of refraction, and the probe field is strongly reflected from the Bragg-type medium. **b**, Measured transmission (blue circles) and reflection (red circles) for the same parameters, showing a large reflection accompanied by a large extinction of the transmission over and extended bandgap. The solid lines correspond to our numerical prediction, for which all the parameters have been extracted from free-running control field EIT spectra.

.

Chapter 5

Properties of Rydberg Atoms

5.1 Atomic structure

Rydberg atoms are named after Johannes Rydberg, who generalized John Balmer's spectroscopic observations in hydrogen atoms to propose an empirical scaling law for the spectral line series of alkali atoms in 1889:

$$\frac{1}{\lambda} = -\frac{\lambda_0^{-1}}{(n-\delta)^2} \tag{5.1}$$

where n was the ordering of the line in the series, δ a constant for a given series and λ_0 an empirical constant for all alkali species. In 1913, Niels Bohr quantum theory of the atom showed that the spectral lines of hydrogen atoms correspond to transitions between the electronic energy levels given by:

$$E_n = -hc\frac{R_\infty}{n^2} \tag{5.2}$$

with the Rydberg constant:

$$R_\infty = \frac{m_e e^4}{8\epsilon_0^2 h^3 c} = 1.0973731568525(73) \times 10^7 \mathrm{m}^{-1} \tag{5.3}$$

The approximation of an infinite nucleus mass is corrected by substituting an element specific Rydberg constant $R = R_\infty(\mu/m_e)$, incorporating the reduced mass $\mu = \frac{m_e m_N}{m_e+m_N}$ for the electron (m_e) and nucleus (m_N) masses. Alkali atoms in highly excited states are

well described by a hydrogenoid model where a single valence electron is interacting with a positively charged effective nucleus comprising Z protons shielded by $Z-1$ neighboring electrons. The overlap between the electron wavefunction and the nucleus introduces a small deviation from the point-like hydrogenoid atom, characterized by the quantum defect $\delta_{n,l,J}$, which depends on the azimuthal quantum number l and the total angular momentum quantum number J. The energy of the (n,l,J) level with respect to the ground state is given by:

$$\Delta E_{n,l,J} = E_I - \frac{R}{(n-\delta_{n,l,J})^2} = E_I - \frac{R}{n^{*2}} \tag{5.4}$$

where E_I is the ionization limit. Here we are particularly interested in the low l states which can be optically accessed from the ground state by a one- ($l=1$) or two- photon($l=0,2$) transition. The quantum defect arises from the penetration of the valence electron into the finite size atomic core and the resulting modification of its interaction with the core electrons and the nucleus. The quantum defect decreases with the orbital angular momentum l as l^{-5}[112]. At higher l, the orbital is becoming more circular and the penetration of the electron in the core and the core polarization are reduced. The electronic wavefunction then ressembles that of a classical Bohr orbit [113].

A useful list of references for spectroscopic measurements of the quantum defect for the different alkali atoms is given in [114]. For Rubidium, millimeter-wave spectroscopy [115], and two-photon spectroscopy [116, 117] show excellent agreement for the extracted quantum defect. The latter reference also provides the absolute ionization energy by using a calibrated frequency comb. The results for the level of interests in the framework of this thesis are summarized in Table 5.1.

Two successive high lying levels have an energy difference $2R/n^{*3}$. For $n=100$, this difference is ~ 7 GHz and the level structure is still easily resolvable with MHz linewidth lasers commonly used in atomic physics. The fine structure splitting similarly scales as $1/n^{*3}$ and is $\sim$10 MHz for $n=100$.

For Rydberg atoms, the hyperfine structure arising from the interaction of the nucleus spin with the electron angular momentum is generally negligible. The hyperfine splitting is measured to be 1.5 MHz [115] for the $30S_{1/2}$ state and scales as n^{*-3}[114]. As a consequence, it is expected to be on the order of a few tens of kHz for $n=100$, which is

	$nS_{1/2}$	$nP_{1/2}$	$nP_{3/2}$	$nD_{3/2}$	$nD_{5/2}$
$E_I(5S_{1/2}, F=1)$	33 690.946 44 cm^{-1} 1 010.029 164 6 (2π) THz				
$R(^{87}Rb)$	109 736.623 243 cm^{-1} 3289.821 194 66 (2π) THz				
δ_0 δ_2	3.131 180 7(8) 0.178 7(2)	2.654 884 9(1) 0.290 0(6)	2.641 673 7(1) 0.295 0(7)	1.348 094 8(11) -0.605 4(4)	1.346 462 2(11) -0.594 0(4)

Table 5.1: ^{87}Rb spectroscopy values for the Rydberg states accessible from the $5S_{1/2}$ ground state by one- and two-photon transitions. For a given n, l, J level, the quantum defect is given by the Rydberg-Ritz expansion: $\delta_{n,l,J} = \delta_0 + \frac{\delta_2}{(n-\delta_2)^2} + ...$ The energy levels are given by Eq. 5.4. The quantum defect and ionization energy values are taken from [117].

not resolvable with our lasers. The hyperfine quantum numbers (F, m_F) cease to be good quantum numbers in magnetic fields as low as a few mG and we will restrict ourselves for the Rydberg levels to the fine structure description (n, l, J, m_J) where m_J is the projection of the total electronic angular momentum along the quantization axis.

5.2 Wavefunctions and dipole matrix elements.

The electronic wavefunctions of Rydberg atoms are crucial for the calculation of many of their properties, such as their lifetime and the dipole-dipole interactions. To a good approximation, the general scaling properties can be retrieved from the hydrogenic wavefunctions:

$$\psi_{n,l,m}(r,\theta,\phi) = R_{n,l}(r)Y_l^m(\theta,\phi), \tag{5.5}$$

separated in an angular dependance described by the spherical harmonics $Y_l^m(\theta,\phi)$ and a radial dependance $R_{n,l}(r)$ obeying the Schroedinger equation for a Coulombian interaction potential:

$$\left[-\frac{\hbar^2}{2\mu}\frac{1}{r}\frac{d^2}{dr^2}r + \frac{\hbar^2 l(l+1)}{2\mu}\frac{1}{r^2} - \frac{e^2}{4\pi\epsilon_0}\frac{1}{r}\right] R_{n,l}(r) = -\frac{R}{n^2}R_{n,l}(r) \tag{5.6}$$

All Rydberg atoms properties stem from the large electron-nucleus separation. Using the radial probability density of the hydrogen wavefunctions, the average electron-nucleus separation $\langle r\rangle = \int_0^\infty dr R_{n,l}^2(r)r^3$ is:

$$\langle r\rangle = \frac{3}{2}a_0(n^2 - \frac{l(l+1)}{3}) \tag{5.7}$$

More precise values of the fine structure wavefunctions:

$$\psi_{n,l,J,m_J}(r,\theta,\phi) = R_{n,l,J}(r) \sum_{m_l,m_s} \langle l,s;m_l,m_s|l,s;J,m_J\rangle Y_l^m(\theta,\phi) \tag{5.8}$$

(where $\langle l,s;m_l,m_s|l,s;J,m_J\rangle$ are the Clebsch-Gordan coefficients for the addition of the orbital angular momentum l and electronic spin $s = 1/2$, with respective quantum numbers m_l and m_s for their projection onto the quantization axis verifying $m_l + m_s = m_J$) including effects of the core on the radial wavefunction[118, 119, 120] can be derived from the knowledge of the quantum defect by application of the quantum defect theory [121, 119] or by numerical integration of the radial Schroedinger equation (in atomic units) [118]:

$$\begin{aligned} -\frac{1}{n^{*2}} R_{n,l,J}(r) = &\left[-\frac{1}{r}\frac{d^2}{dr^2} + \frac{l(l+1)}{2r^2}\right] R_{n,l,J}(r) \\ &+ \left[\alpha^2 \frac{J(J+1) - l(l+1) - s(s+1)}{2r^3} + V(r)\right] R_{n,l,J}(r), \end{aligned} \tag{5.9}$$

where we included the spin-orbit coupling. It is generally sufficient to consider a modified potential taking into account the polarizability of the nucleus $\alpha_0 = 9.023$ a.u. (for ^{87}Rb):

$$V(r) = -\frac{2}{r} - \frac{\alpha_0}{2r^4}, \tag{5.10}$$

although more complex potentials exist to model the core penetration by the electron [122].

The dipole matrix elements are related to the radial integral $\langle R_{n,l,J}|r|R_{n',l',J'}\rangle = \int_0^\infty dr R_{n,l,J}(r) R_{n',l',J'}(r) r^3$ by:

$$\begin{aligned} \langle n,l,J,m_J|r_q|n',l',J',m_J'\rangle = &\langle R_{n,l,J}|r|R_{n',l',J'}\rangle \sqrt{\mathrm{Max}(l,l')}(l-l')(-1)^{2J'+l+s+m_J} \\ &\times \sqrt{2J+1}\sqrt{2J'+1} \begin{pmatrix} J' & 1 & J \\ m_J' & q & -m_J \end{pmatrix} \begin{Bmatrix} l & l' & 1 \\ J' & J & s \end{Bmatrix} \end{aligned} \tag{5.11}$$

where the Wigner-3j and -6j coefficients enforce the selection rules $|l - l'| = 1, |J - J'| \leq$

1, and $m_J = m'_J + q$ and the index $q = \{-1, 0, 1\}$ refers to the polarizations $\{\frac{1}{\sqrt{2}}(\mathbf{e}_x - i\mathbf{e}_y), \mathbf{e}_z, -\frac{1}{\sqrt{2}}(\mathbf{e}_x + i\mathbf{e}_y)\}$.

The integration of the radial matrix elements $\langle R_{n,l,J}|r|R_{n',l',J'}\rangle$ generally requires the knowledge of the Rydberg wavefunctions. Nevertheless, the observable r in the radial integral strongly weighs the region of the wavefunction located further away from the nucleus. In this region, the electronic wavefunction is well described by the hydrogen wavefunctions and the quantum defect and a good approximation in the calculation of the radial matrix element consists in using solutions to the Coulomb potential over the region $[r_1, \infty]$ where $r_1 \sim a_0$ is the core size.

$$\langle R_{n,l,J}|r|R_{n',l',J'}\rangle \approx \int_{r_1}^{\infty} r^3 R^{Coul.}_{n,l,J}(r) R^{Coul.}_{n',l',J'}(r) dr \tag{5.12}$$

The above approximation becomes better at large l, as the penetration of the core by the valence electron is reduced due to the circular orbit.

We first turn to the coupling between low-lying states and highly excited states. For these transitions, in the limit $n' \gg n, l'$ the dipole matrix elements scale as [123, 119]:

$$\langle R_{n,l,J}|r|R_{n',l',J'}\rangle \sim a_0 n'^{*-\frac{3}{2}} \tag{5.13}$$

For low excited state, $rR_{n,l,J}(r)$ is only significant in a region smaller than the core size, and the scaling law 5.13 reflects the amplitude of the Rydberg wavefunction at $r = 0$: $|\psi_{n',l'}(0)|^2 \propto n^{-3}$. This scaling sets an experimental challenge as it limits the coupling rate to the Rydberg state and for example the possibility to detect them optically. In contrast, the dipole coupling between neighboring Rydberg levels (in the microwave domain) increases rapidly with n as:

$$\langle R_{n,l,J}|r|R_{n',l',J'}\rangle = \frac{3}{2} a_0 n_c^2 \mathcal{G}(n^* - n'^*) \tag{5.14}$$

where $n_c = (\frac{2n^* n^{*'}}{n^* + n'^*})$, and for $l \ll n$, $\mathcal{G}(n^* - n'^*)$ is a universal function independent of the species and is numerically evaluated and tabulated in [124]. In particular, $\mathcal{G}(0) = 1$. The relation 5.14 stems from the fact that the wavefunction of highly excited states oscillate approximately independently of l, and the radial integral differs little from $\langle r\rangle$ when $n \approx n'$. For circular states, the quantum defect becomes negligible and the radial dipole

matrix element between states $|n,l\rangle$ and states $|n,l+1\rangle$ is $\frac{3}{2}a_0n^2$ [125]. This gigantic coupling with microwave photons is a cornerstone of microwave cavity QED [38].

5.3 Rydberg states lifetime

An atom in Rydberg state $|n,l\rangle$ spontaneously decays to neighboring Rydberg and lower lying states. The spontaneous decay rate to a particular level $|n',l'\rangle$ is given by Einstein's A coefficients, after summation over the degenerate final states and average over the initial states:

$$\Gamma_{n,l\rightarrow n',l'} = \frac{4}{3}\alpha\frac{\omega^3}{c^2}\frac{\mathrm{Max}(l,l')}{2l+1}\left|\langle R_{n,l,J}|r|R_{n',l',J'}\rangle\right|^2 \tag{5.15}$$

where $\hbar\omega = E_{n,l} - E'_{n',l'}$ is the energy difference between the involved levels.The natural lifetime $\tau_{n,l}$ is obtained by incoherently summing over all the possible decay channels allowed by dipole transition rules and satisfying $E_{n,l} > E'_{n',l'}$:

$$\frac{1}{\tau_{n,l}} = \Gamma_{nl} = \sum_{n',l'}\Gamma_{nl\rightarrow n'l'} \tag{5.16}$$

For Rydberg states, spontaneous emission rates towards low-lying states are dominated by the transitions with the highest energy difference, typically to the state $5P$ for the nS and nD states of ^{87}Rb, which subsequently decay rapidly to the ground state $5S$. By replacing the ionization energy by ω in Eq. 5.15, we deduce that these rates are on the order of $\frac{\alpha^4 c}{a_0}n^{*-3}$. The scaling with n originates from the dipole matrix coupling (see Eq. 5.13). Spontaneous emission also happens towards neighbouring Rydberg states with a rate on the order of $\frac{\alpha^4 c}{a_0}n^{*-5}$. There, the level proximity $\omega \propto n^{*-3}$ counterbalances the large coupling coefficients $\propto n^{*2}$. As a consequence, for low l states, the lifetime of the Rydberg state is dominated by the decay to the low-lying states and scales as n^{*3}. The situation differs for circular states (with high azimuthal quantum number l), as transition towards low-lying states are forbidden by conservation of the photon angular momentum $\Delta l = \pm 1$. These states have an extended lifetimes scaling as n^{*5}.

Numerical calculations and experimental measurements of the lifetime are well reproduced by a simple scaling law [126]:

$$\tau = \tau' n^{*\kappa}. \tag{5.17}$$

The parameters τ' ~1-3 ns and $\kappa = 3 \pm 0.1$ measured in [127] for the S,P and D states of ^{87}Rb, are in good agreement with the simple interpretation given above.

5.4 Effect of the blackbody radiation on the lifetime

Due to the large value of the electric dipole matrix between neighboring Rydberg atoms and the large wavelength of the corresponding transitions, Rydberg states are highly sensitive to blackbody radiations, which stimulate atomic excitations with resonant energy $\hbar\omega = E_{n,l} - E_{n',l'}$ proportionally to the average number of blackbody photons per mode $\bar{N}_\omega = (e^{\frac{\hbar\omega}{kT}} - 1)^{-1}$. The blackbody decay rate of the level n, l, Γ_{nl}^{bb} is given by [128]:

$$g_l \Gamma_{nl}^{bb} = \sum_{E'<E} g_l \bar{N}_\omega \Gamma_{nl \to n'l'} + \sum_{E'>E} g_{l'} \bar{N}_\omega \Gamma_{nl \to n'l'} \tag{5.18}$$

In contrast to the spontaneous lifetime, the blackbody radiation induces stimulated excitation to levels n', l' with both higher and lower energies. $g_l = 2l+1$ is the degeneracy of the corresponding level. Each term of the sum in Eq. 5.18 is proportional to the product of the blackbody radiation energy spectral density $\frac{8\pi\hbar\omega^3}{c^3}(e^{\frac{\hbar\omega}{kT}} - 1)^{-1}$ and the square of the radial matrix dipole element: $|\langle R_{n,l,J}|r|R_{n',l',J'}\rangle|^2$.

At room temperature, the energy spectral density is peaked at $\nu \sim 18$ THz. For larger frequencies (corresponding to transitions between high and low-lying states), the black body stimulated emission decreases rapidly and is rightfully neglected. Blackbody stimulated absorption and emission between Rydberg states benefits from the slowly decaying tail of the blackbody energy spectral density at low frequencies, $\propto \nu^2$, in coincidence with large coupling strengths. The blackbody radiation stimulates transitions either to neighbouring Rydberg states, to lower intermediate states or to the ionization limit. The dominant contribution is the stimulated emission between neighboring states [129]. As a consequence, in the presence of blackbody radiation, the atomic population diffuses through the neighboring Rydberg states. The blackbody radiation induced lifetime increases for higher states a n^{*2}, due to the n^{*-6} scaling of the energy spectral density and

the n^{*2} scaling of the dipole matrix element. An approximate expression can be derived for the blackbody radiation induced decay rate [128]:

$$\tau_{BB}^{-1} = \frac{4\alpha^3 k_B T}{3\hbar n^{*2}} \tag{5.19}$$

The blackbody radiation decreases the lifetime τ' from the spontaneous lifetime τ to:

$$\frac{1}{\tau'} = \frac{1}{\tau} + \frac{1}{\tau_{BB}} \tag{5.20}$$

For ^{87}Rb, lifetimes at room temperature are measured in [127] and are shown to be in excellent agreement with the model described in Eqs. 5.17,5.19,5.20.

5.5 Stark effect

Due to the large average distance between the valence electron and the core, Rydberg atoms are easily polarized by a static electric field $\vec{F}$. The interaction between the electric field and the dipole operator $\hat{\vec{\mu}}$ is governed by the interaction Hamiltonian:

$$\hat{V} = -\hat{\vec{\mu}} \cdot \vec{F} \tag{5.21}$$

The so-called Stark map, describing the eigenstates of the system in arbitrary high fields, require the knowledge of the dipole matrix elements $\langle n, l, J, m_J | z | n', l', J', m'_J \rangle$ (for a constant electric field aligned along z) to diagonalize the interaction matrix in the $|n, l, j, m_j\rangle$ basis. The methods for the calculation of the Stark maps are detailed in [118]. For Stark shifts small compared to the level separations, the $|n, l, J, m_J\rangle$ states are not significantly mixed by the electric field and second-order perturbation theory (for non degenerate states) yields a quadratic Sark shift. The partially mixed levels are, to first order:

$$|n, l, J, m_J\rangle_F = |n, l, J, m_J\rangle - eF \sum_{n', l', J', m'_J} \frac{\langle n', l', J', m'_J | z | n, l, J, m_J \rangle}{E_{n,l,J} - E_{n',l',J'}} |n', l', J', m'_J\rangle \tag{5.22}$$

The electric field induces a finite permanent average dipole moment:

$$\langle \mu_z \rangle = \frac{1}{2}\alpha_p F = -e^2 F \sum_{n',l',J',m'_J} \frac{|\langle n',l',J',m'_J|z|n,l,J,m_J\rangle|^2}{E_{n,l,J} - E_{n',l',J'}} \tag{5.23}$$

The scalar polarizability α_p is dominated by the interaction between the nearest Rydberg levels, which are simultaneously favored the strong dipole coupling ($\propto n^{*2}$) and decreasing energy difference ($\propto n^{*-3}$). As a consequence, the scalar polarizability of Rydberg states scales very favorably with the primary quantum number: $\alpha_p \propto n^{*7}$. The polarizability of the $nS_{1/2}$ states of ^{85}Rb was measured over the range $n = 15$ to $n = 80$ [130] and is indeed dominated by an n^{*7} dependance at large n :

$$\alpha = 5.53(13) \times 10^{-11} n^{*7} + 2.202(28) \times 10^{-9} n^{*6} \ \text{[MHz/(V/cm}^{-1})^2] \tag{5.24}$$

Due to this gigantic polarizability, atoms are very sensitive to stray electric fields and static charges, and experimental precautions have to be taken in the presence of nearby insulating surfaces.

5.6 Field ionization

Field ionization is used to selectively ionize atoms in specific Rydberg states and efficienty detect them using channeltrons. This technique is crucial to many Rydberg atoms experiments [131, 132] as the optical detection of atoms in Rydberg states is impaired by the weak coupling to the ground states. To a very good approximation, the electric field values necessary to ionize Rydberg atoms are given by a classical model: the electric field sufficiently distorts the core potential to lower the resulting potential barrier below the unperturbed energy of the state, $-R/n^{*2}$. Using the Coulombian approximation for the interaction with the atomic core, the total electronic potential long the z direction

$$V(z) = -\frac{1}{4\pi\epsilon_0}\frac{e^2}{|z|} + eFz \tag{5.25}$$

admits a local maximum at $z = -\sqrt{4\pi\epsilon_0 e/F}$, lowering the potential barrier to $-2e^{3/2}\sqrt{F}/4\pi\epsilon_0$. In this classical approximation, where tunneling, Stark shift and level mixing[133] are neglected, the ionization treshhold field for the state n is:

$$F_{ion} = \frac{1}{n^{*4}} 3.2 \times 10^8 \ [\mathrm{V/cm^{-1}}] \tag{5.26}$$

and the predicted values typically fall within 20% of the measured ionization thresholds.

.

5.7 AC Stark shift and optical trapping

In this section, we are interested in the level-shift induced on Rydberg levels by fields with wavelengths much shorter than the Rydberg energy separations, typically corresponding to optical frequencies used for dipole trapping of ground states atoms. The perturbative level-shift of the state $\{n, l, m\}$ induced by an AC electric field of amplitude E, angular frequency ω and polarization e_q is, to lowest order:

$$\Delta E_{n,l} = \frac{e^2 E^2}{4\hbar} \sum_{n',l',m'} |\langle n, l, m | r_q | n', l', m' \rangle|^2 \left(\frac{1}{\omega_{n,l,n',l'} - \omega} + \frac{1}{\omega_{n,l,n',l'} + \omega} \right) \tag{5.27}$$

where $\hbar\omega_{n,l,n',l'} = E_{n,l} - E_{n',l'}$ is relative energy of the levels coupled by dipole coupling (and can be positive or negative). For low-lying levels, for which the energy differences correspond to optical frequencies, the level-shift is well detemined by the few transitions closest to resonance with the electric field angular frequency. For Rydberg atoms, the situation differs as there are a finite number of off-resonant transitions to lower-lying states with weak coupling and an infinite number of largely off-resonant ($|\omega_{n,l,n',l'}| \ll \omega$) transitions to Rydberg states with large coupling elements. In that case, it is possible to expand the formula above to lowest order in $|\omega_{n,l,n',l'}| / \omega$:

$$\Delta E_{n,l} = -\frac{e^2 E^2}{2\hbar\omega} \sum_{n',l',m'} |\langle n, l, m | r_q | n', l', m' \rangle|^2 \omega_{n,l,n',l'} \tag{5.28}$$

In many cold atoms experiments, atoms are trapped at the maximum intensity region of high power fields red-detuned from the ground state to first excited transition. Eq. 5.28 assumes that couplings between the Rydberg level n, l and a finite number of low-lying states n', l' with energy $\omega_{n,l,n',l'} \sim \omega$ have a negligible contribution to the sum due to the

weak scaling of the dipole matrix element. This approximation does not hold for strong near-resonant fields coupling the Rydberg levels to the low-lying states [134, 135]. The terms of the sum in Eq. 5.28 are proportional to the oscillator strength:

$$f_{n,l,n',l'} = -\frac{2m_e}{\hbar^2} \sum_{m'} |\langle n,l,m|r_q|n',l',m'\rangle|^2 \, \omega_{n,l,n',l'} \tag{5.29}$$

which obeys the Thomas-Reiche-Kuhn rule: $\sum_{n',l'} f_{n,l,n',l'} = 1$. As a consequence,

$$\Delta E_{n,l} = \frac{e^2 E^2}{4 m_e \omega^2} \tag{5.30}$$

The energy shift correspond to the so-called ponderomotive energy of a free electron vibrating in the electromagnetic field: $E^2/2\omega^2$ is the average value of the vector potential $\vec{A}$ and the level-shift is the average value of the quadratic term in the free-particle Hamiltonian $\frac{1}{2m_e}(\vec{p} + e\vec{A})^2$ (the oscillating terms averaging out to 0 over time). Numerically, a 1064 nm field with an intensity of 100 kW/cm^2 will induce a level shift of 2.5 MHz (of the same order of magnitude as the ground state shift for ^{87}Rb).

In a far-off resonant trap, all Rydberg levels are shifted by the same amount and the level-shift is positive, independently of the wavelength of the field. As a consequence, Rydberg atoms can be trapped at a minimum of the light field intensity, for example in optical lattices [136, 137]. Nevertheless, ground states atoms are trapped at the field intensity maximum of red-detuned dipole traps, preventing simultaneous trapping of ground states and Rydberg atoms [137]. Blue detuned traps can in principle be used to match the level-shift of the ground states and Rydberg states using specific wavelengths [120]. Furthermore, the large extension of the average Rydberg atom extension compared to the typical lattice dimension induces a strong dependance of the trapping potential on the sublevels (j, m_j)[138].

Another possible limitation to the combined use of Rydberg states and optical traps is the induced photo-ionization of the Rydberg states[134, 139]. Photo-ionization is also expected to play a role in dark traps, such as ponderomotive lattices, due to the extent of the Rydberg atom compared to the lattice size. The calculations in [134, 139] predict a photo-ioization lifetime increasing with n^* and the wavelength of the trapping light. Nevertheless, for $n = 100$, the photoionization time for a 5W, 1064 nm trap focused to 50

μm is expected to be much larger than the natural lifetime of the state.

Simultaneous trapping of ground- and Rydberg-states can be achieved by taking advantage of the mutli-level structure of low lying states, as recently demonstrated in [135]. In that experiment, the lattice is blue detuned tens of MHz from the transition between the Rydberg state of interest and a low-lying excited states to create a trapping lattice for both ground states and Rydberg states. Moreover, the parameters for the lattice can be chosen to achieve a magical trap, which detunes the ground and Rydberg states by the same amount. Such a magic trap conveniently eliminates inhomogeneous broadening of the two-photon resonance.

5.8 Dipole-dipole interactions

Due to their gigantic dipole moment $\propto n^{*2}ea_0$, Rydberg atoms interact strongly through the dipole-dipole interaction, acting as microscopic antennas sensitive to each other radiated field. The dipole-dipole interaction is described by the Hamiltonian:

$$\hat{V} = \frac{e^2}{4\pi\epsilon_0}\frac{1}{R^3}\left(\hat{\mathbf{r}}_1\cdot\hat{\mathbf{r}}_2 - \frac{3(\hat{\mathbf{r}}_1\cdot\mathbf{R})(\mathbf{R}\cdot\hat{\mathbf{r}}_2)}{R^2}\right), \tag{5.31}$$

valid for dipole separations $R = |\mathbf{R}|$ larger than the dipole size $\langle r_1\rangle, \langle r_2\rangle$. For the peak densities $\mathcal{N} = 10^{12}$ cm^{-3} used in our experiments, the mean atomic distance is not significantly larger than the average orbit radius of the Rydberg states. Nevertheless, the critical length scale of the problem is the Rydberg blockade length which is determined by long range interactions between atoms typically separated by $R \sim 10$ μm, and the exact nature of the short range interactions is irrelevant for the physics we are exploring in the context of this thesis. As a consequence, $\mathbf{R}$ is treated as a classical vector and not an operator.

The interaction term $\hat{V}$ couples the two-atom state $|n,l,J,m_J\rangle|n',l',J',m'_J\rangle$ to all states $|n'',l'',J'',m''_J\rangle|n''',l''',J''',m'''_J\rangle$ allowed by dipole transition. Assuming again the long range approximation $\langle r_1\rangle, \langle r_2\rangle \ll R$, the interaction can be treated in the framework of non-degenrate second order perturbation theory. Here we restrict ourselves to interaction between two atoms in the same Rydberg state. The interaction induced level shift

corresponds to the Van der Waals potential:

$$\Delta E_{n,l,J,m_J} = -\hbar \frac{C_6}{R^6} \tag{5.32}$$

The C_6 coefficients is calculated from the dipole matrix elements and the energy levels:

$$C_6 = -\frac{1}{4\pi\epsilon_0 \hbar} \sum_{|e'\rangle} \sum_{|e''\rangle} \frac{\left| \sum_{q=\pm 1} \mu'_q \mu''_{-q} + 2\mu'_0 \mu''_0 \right|^2}{2E - E' - E''} \tag{5.33}$$

(for the quantization axis aligned with $\mathbf{R}$). To simplify Eq. 5.33, we used the notations $|e\rangle = |n, l, J, m_J\rangle$ (respectively $|e'\rangle = |n', l', J', m'_J\rangle$, ...) for the level associated with the unperturbed energy E (respectively E', ...) and $\mu'_q = e\langle e|r_q|e'\rangle$, $\mu''_q = e\langle e|r_q|e''\rangle$. The calculation of the C_6 coefficient is generally nontrivial as it involves a large number of state pairs and require the exact knowledge of the unperturbed levels and of the dipole matrix elements [140, 141, 142].

The main contribution in the double sum of Eq. 5.33 comes from the level pairs $|e'\rangle, |e''\rangle$ with the average energy closest to the energy of the level $|e\rangle$: $E \sim (E' + E'')/2$. For example, for the $100S_{1/2}$ states, the main contribution comes from the dipole coupling to the $(99P_J, 100P_J)$ pairs of states, followed by $(98P_J, 101P_J)$. For the $nS_{1/2}$ states, the energy difference with the closest level pairs $((n-1)P_j, nP_j)$ is always positive and the Van der Waals interaction is repulsive. For the nD_J states, the interaction becomes attractive for $n > 43$ as the energy difference to the closest level pair changes sign.

The C_6 coefficient is highly enhanced for higher Rydberg states by the combined scaling of the energy defect to the nearest states $\propto n^{*-3}$ and the dipole matrix elements $\propto n^{*2}$, resulting in the scaling law $C_6 \propto n^{*11}$. This scaling was confirmed by[141], where the C_6 coefficients were numerically evaluated (albeit without the fine structure) and fitted, for the $nS_{1/2}$ states of ^{87}Rb:

$$C_6 = n^{11}(11.97 - 0.8486n + 3.385 \times 10^{-3} n^2) \text{ a.u.} \tag{5.34}$$

Note that for states with azimuthal quantum number $l > 0$, the interaction depends on the m_j levels considered due to the spherical asymmetry of the magnetic sub-levels. In addition, an external static electric field mixes states of different parities and gives

Rydberg states	$46S_{1/2} - 46S_{1/2}$	$77S_{1/2} - 77S_{1/2}$	$100S_{1/2} - 100S_{1/2}$
$C_6[(2\pi)\text{GHz}\cdot\mu\text{m}^6]$	-5.6	-2.7×10^3	-56.4×10^3
$r_B(\mu\text{m})$	3	9	15

Table 5.2: C_6 coefficients (from Eq. 5.33,[141]) and corresponding blockade radius for an excitation linewidth $\gamma = 2\pi \times 10\text{MHz}$.

the atom a permanent dipole moment in the laboratory frame. As a consequence, the interaction depends on the orientation of the electric field and becomes anisotropic[142].

The $1/R^6$ interaction potential resulting from the perturbative approach is only valid at large distances R, where the coupling elements $V_{2r}^{r',r''} = \langle r|\langle r|V|r'\rangle|r''\rangle \propto \frac{1}{R^3}\mu'\mu''$ are smaller than the pairs energy difference $\Delta_{2r}^{r',r''} = 2E - E' - E''$ and in the absence of degenerate state pairs such that $\Delta_{2r}^{r',r''} = 0$. The latter case corresponds to the so-called Förster resonances[143]. Förster resonances can be engineered by tuning the atomic level structure with electric fields [144]. In that case, it is necessary to diagonalize the interaction matrix for the subspace $|r\rangle|r\rangle, |r'\rangle|r''\rangle$. The eigenenergies of the system $\{|r\rangle|r\rangle, |r'\rangle|r''\rangle\}$ are proportional to $1/R^3$, which correspond to the resonant dipole-dipole interaction:

$$\frac{\Delta_{2r}^{r',r''}}{2} \pm \frac{\sqrt{\Delta_{2r}^{r',r''2} + V_{2r}^{r',r''2}}}{2} \sim \frac{C_3}{R^3} \tag{5.35}$$

The resonant dipole-dipole interaction also dominates the short range interactions even in the absence of Förster resonance. As stated before, for our typical experimental densities and Rydberg states used, neighboring atoms interact through the resonant dipole-dipole interactions. Nevertheless, the relevant length scale is set by the long range interactions which define the blockade radius. For distances smaller than the blockade radius, the levels are largely by the interaction, and the exact form of the interaction is irrelevant given that the induced detuning is much larger than the excitation linewidth. In the remaining part of this work, we simplify the exact interaction potential to the $1/R^6$ long-range Van der Waals interaction for all R.

5.9 Rydberg blockade

The Rydberg blockade happens when the level-shift induced by the dipole-dipole interaction prevents the simultaneous (typically optical) excitation of several atoms to the Rydberg states, i.e. when the doubly excited Rydberg state is tuned out of resonance by an amount larger than the linewidth of the excitation [145, 146, 120, 147]. For one-photon transitions, or two photon transitions far detuned from the intermediate virtual state, the excitation linewidth γ_{exc} is a convolution of the the Rydberg state lifetime and the laser linewidth. The Rydberg blockade radius is defined as the distance at which the Van der Waals induced level-shift becomes larger than half the interaction linewidth:

$$r_B = \left(\frac{2\,|C_6|}{\gamma_{exc.}}\right)^{1/6} \tag{5.36}$$

The underlying principle for the experiments we are describing is that at most one atom can be excited per Rydberg blockade volume at a given time. For a given excitation linewidth, the Rydberg blockade grows as $n^{*11/6}$. In cold atomic systems, where linewidths are in the MHz range, typical blockade radii are on the order of 10 μm. Precise examples are given in Table 5.2.

Numerous experiments have explored the Rydberg blockade in cold atomic systems over the past few years. The most straightforward demonstration of the blockade between two individual Rydberg atoms was reported in [148, 149], where single atoms are loaded in two dipole micro-traps separated by a few μm. In this configuration, the transfer to the Rydberg state of one of the atoms by a π-pulse strongly inhibits Rabi oscillations between the ground- and Rydberg- states for the other atom.

The blockade mechanism in large atomic ensembles gives rise to rich cooperative mechanisms. For a blockade radius larger than the interatomic distance, readily achieved in cold dilute gases, each blockaded volume contains a mesoscopic number of atoms N_a. Under optical excitation, assuming that the extent of the excitation beam is larger than the blockade radius and that the electric field couples equally to all the atoms, the N_a atoms within a blockade volume, initially in the ground state $|g\rangle$, collectively share at most a

single Rydberg excitation $|r\rangle$. The collectively excited state is:

$$|1_r\rangle = \frac{1}{\sqrt{N_a}} \sum_{j=1}^{N_a} |g_1, g_2, ...r_j, ...g_{N_a}\rangle \tag{5.37}$$

It is equivalent to the first superradiant state of the Dicke ladder for an atomic ensemble in a cavity. The next collective excited state $\frac{1}{\sqrt{N_a(N_a-1)}} \sum_{i,j=1;i>j}^{N} |g_1, g_2, ., r_i, ..r_j, ...g_N\rangle$ is tuned out of resonance from the interaction by the Van-der-Waals interaction. As a consequence, the ensemble of N atoms comprised in the blockade volume behaves as a 2-level "super-atom"[147], with a ground state $|0_r\rangle = \sum_{j=1}^{N_a} |g_1, g_2, ...g_N\rangle$ and an excited state $|1_r\rangle$. The dipole matrix element is enhanced by a factor $\sqrt{N_a}$ compared to that of a single atom:

$$\langle 0_r|e \sum_{j=1}^{N_a} r_q^{(j)}|1_r\rangle = \sqrt{N_a}\langle g|er_q|r\rangle \tag{5.38}$$

A continuous excitation field induces Rabi flopping of the super-atom between states $|0_r\rangle$ and $|1_r\rangle$ with a $\sqrt{N_a}$ enhancement of the Rabi frequency with respect to the non-interacting case. At the beginning of the excitation, the number of Rydberg atoms in the blockade volume grows at the same rate $N_a\Omega^2t^2$ as would non-interacting atoms but it saturates when that number approaches one, corresponding to a Rabi half-period $t \sim (\sqrt{N_a}\Omega)^{-1}$. The super-atom thus has an enhanced cross-section $N_a\sigma_0$ (σ_0 is the resonant single-atom cross-section). This strongly enhanced cross-section at high density provides a single-photon absorption probability close to unity, a key requirement for quantum optical nonlinearities (see Chapter 2).

The blockade-induced saturation of the Rydberg excitations density in atomic clouds has been observed in several experiments over the last decade, [150, 151, 152, 153]. In these experiments, Rydberg atoms were optically excited using one and two-photon transitions, and the saturation of the number of Rydberg atoms is measured by field ionization subsequent detection by microchannel plate detectors. The cooperative enhancement of the Rabi oscillation, a clear signature of the coherent collective behavior, has recently been reported in [154] (it had been previously directly observed for two atoms [148] and indirectly for large ensembles [152]).

The Rydberg blockade was initially proposed in the context of quantum gates between individual neutral atoms [145, 146], as implemented in [148, 149]. Subsequent theoretical efforts on quantum information processes based on Rydberg blockade, including its extension to atomic ensembles and quantum optics, are reviewed in [120].

5.10 Rydberg EIT

In this section, we focus on the applications of the Rydberg blockade to quantum optics. By coherently coupling photons to Rydberg states, it is possible to map the correlations emerging from the atomic interaction onto the photonic field. A direct application is the realization of single photon sources [155], based on the directional retrieval of Rydberg excitations in high density atomic medium with an excitation volume smaller than the blockade sphere. As the spin-wave imprinted in the medium by the write beams carries at most one excitation, the retrieved pulses exhibit a large suppression of two photon probability. For such a scheme, the directional photon retrieval is limited by the optical depth in the blockade volume.

A closely related phenomenon is the Rydberg blockade of photons propagating under Electromagnetically Induced Transparency (EIT) conditions. It was first pointed out in [156] that ladder-type EIT schemes where Rydberg act as the second long-lived state generate strong coherent interactions between photons. Under Rydberg EIT conditions, a single photon pulse entering the medium is adiabatically transformed into a dark-state polariton, which can essentially be pictured as a Rydberg excitation traveling with reduced group velocity and collectively shared by all the atoms within the volume of the compressed pulse. Due to the Rydberg blockade, at most one polariton can exist per blockade volume. The blockade radius

$$r_b = \left(2\left|C_6\right|/\gamma_{EIT}\right)^{1/6} \tag{5.39}$$

is the distance at which the transmission properties of the medium are strongly modified due to the interaction induced detuning of the Rydberg state by an amount larger than

the EIT linewidth

$$\gamma_{EIT} = \frac{\Omega_c^2}{|\Gamma - 2i\Delta|} \tag{5.40}$$

Here Ω_c is the Rabi frequency of the control field, Δ the detuning from the intermediate excited state and Γ the decay rate of the intermediate state.

For two or more polaritons within a blockade volume containing a Rybderg excitation, the effect of the control field is effectively cancelled and the probe photons interact with an ensemble of two-level atoms (the two levels being the ground state and the intermediate excited state). Depending on the detuning Δ from the intermediate level, the difference between the 3-level and the 2-level susceptibility resides mainly in a change of transmission on resonance ($\Delta \sim 0$) or a change of index of refraction at large detuning ($|\Delta| \gg \Gamma$), generating respectively dissipative and dispersive interactions between photons.

Rydberg EIT and the associated nonlinear effects were first demonstrated in the group of C.S. Adams [63] and were subsequently theoretically and numerically investigated in the low density and low excitation limit [61, 157]. The peak atomic densities reported in [63], where experiments are carried out in a compressed magneto-optical trap, are 1.2×10^{10} cm^{-3}, corresponding to an optical depth per blockade volume $OD_B \leq 0.1$ for a blockade radius $\sim$10 μm. Dispersive blockade-induced optical nonlinearities were also recently reported in the low-density limit [64].

In Chapters 6, 7, 8, we present an experimental realization of Rydberg EIT in a density regime where the effective interactions are significant enough at the single photon level to imprint strong correlations on the probe field.

5.11 Summary of properties of Rybderg atoms

Quantity	Scaling law	^{87}Rb, $100S_{1/2}$	Ref.
Ionization Energy E_n	$-R\,n^{*-2}$	350 (2π) GHz	[116],[117]
Level Spacing $E_{n+1} - E_n$	$R\,n^{*-3}$	7.1 (2π) GHz	[117],[115]
Average orbit $\langle r \rangle$	$a_0\,n^{*2}$	0.75 μm	Eq. 5.7
Radial dipole matrix element $\langle R_{n,l}\|er\|R_{n',l'}\rangle$ (to low-lying state)	$e\,a_0\,n^{*-3/2}$	To 5P state: $4.5\,e\,a_0 n^{*-3/2}$	[158]
Radial dipole matrix element $\langle R_{n,l}\|er\|R_{n',l'}\rangle$(to close Rydberg state)	$e\,a_0\,n^{*2}$	-	
Spontaneous lifetime τ	$\frac{a_0}{\alpha^4 c} n^{*3}$	1.5 ms	[127]
Blackbody lifetime τ_{BB}	$\frac{\hbar}{\alpha^3 k_B T} n^{*2}$	0.5 ms	[129],[127]
Scalar polarizability α_p	$a_0^3\,n^{*7}$	6.2 GHz/(V/cm^{-1})	[130]
C_6 coefficient C_6	$R\,a_0^6\,n^{*11}$	-56 (2π) THz μm^6	[141]

Table 5.3: Summary of the scaling laws for Rydberg atoms. As detailed in the previous sections of this chapter, these quantities have simple power laws with the primary quantum number n^* (corrected for the quantum defect) and the order of magnitude of the corresponding quantities can be derived from the scaling laws presented in the table (note that factors of order 1 are neglected). The values for the $100S_{1/2}$ states are calculated using the references in the last column.

Chapter 6

Experimental setup for Rydberg blockade induced nonlinear optics

6.1 Requirements

In this section, we detail the requirements necessary for the observation of quantum nonlinearities at the single photon level using Rydberg Electromagnetically Induced Transparency (EIT) [62, 159]. In Rydberg EIT, the control field can be tuned on resonance to obtain dissipative interactions (the corresponding results are described in Chapter 7) or out of resonance from the intermediate short-lived state, leading to dispersive interactions between photons (described in Chapter 8). We first turn towards the requirements for dissipative nonlinearitites, for which the control field is tuned close to resonance with the intermediate to Rydberg state transition. In this case, the Rydberg blockade is given by (see Eqs. 5.39,5.40):

$$r_b = \left(\frac{2\,|C_6|\,\Gamma}{\Omega_c^2}\right)^{1/6} \tag{6.1}$$

Ultimately, the blockade radius is limited by the residual decoherence which sets a lower limit on the control field Rabi frequency. Strong dissipative interactions happen at the single photon level, if the atomic density is high enough to obtain a large absorption probability per blockade volume. This condition is satisfied if the resonant absorption length in the medium $l_a(z) = (\rho(z)\sigma_0)^{-1}$, related to the total optical depth by $OD =$

$\int dz\,(l_a(z))^{-1}$, is significantly smaller than the blockade radius r_b. In that case, the optical depth per blockade radius OD_B fulfills the condition:

$$OD_B = \frac{r_b}{l_a} \gg 1. \tag{6.2}$$

For a medium of length r_b, it also corresponds to the requirement for compressing a bandwidth limited pulse in the medium, guaranteeing interaction between single-photon pulses.

At large detuning of the control field, $|\Delta| \gg \Gamma$, the probe absorption in the absence of control field decreases as $OD(\Gamma^2/4\Delta^2)$ and the dissipative interactions induced by the Rydberg blockade are suppressed. In that regime, the linewidth is narrowed and is given by the AC-Stark shift induced by the control field on the Rydberg level $\sim \Omega_c^2/\Delta$ (see Appendix A). The blockade radius becomes

$$r_B = \left(\frac{4\,|\Delta C_6|}{\Omega_c^2}\right)^{1/6}. \tag{6.3}$$

When the probe field frequency satisfies the two-photon resonance condition, at low probe rate, the EIT cancels the phase-shift imprinted by the index of refraction. In contrast, several polaritons propagating simultaneously experience the off-resonant index of refraction of the ground- to intermediate-state transition, $\propto \Gamma/\Delta$. Ideally, for applications to quantum information science, the atomic density of the medium should be large enough to produce a conditional phase-shift ϕ_B on the order of π per blockade volume:

$$\phi_B = \frac{2r_B}{l_a}\frac{\Gamma}{4\Delta} = OD_B\frac{\Gamma}{2\Delta} \sim \pi \tag{6.4}$$

As an ideal gate needs to be operated in the regime $|\Delta| \gg \Gamma$ to minimized losses, the density conditions for dispersive interactions are more stringent than for dissipative interactions (note that due to the r^{-6} scaling of the Van der Waals interactions, the ratio between the off-resonant and resonant blockade radius increases only slowly as $(\Delta/\Gamma)^{1/6}$).

Besides large atomic densities, the transverse confinement of the probe photons to within a blockade radius is a key requirement to prevent simultaneous propagations of non-interacting photons and observe single photon nonlinearities in the intensity correlation

function of the transmitted light. In that regime, the interaction dynamics between the photons can be considered unidimensional. This condition is satisfied by focusing the probe to a beam waist

$$w_0 \ll r_b \tag{6.5}$$

over a distance comparable to r_b.

Beyond two-body effects, many-body interactions can create highly correlated states of light, for example by retrieval of crystallized Rydberg excitations [36]. Rydberg crystals were recently imaged for a two-dimensional ultra-cold gas in an optical lattice [37] and indirectly probed for a one-dimensional system [160]. In both cases, the crystal were spontaneously excited, although the coherent preparation of a crystal with a definite number of excitation is in principle achievable by using a chirped pulses which maintains the light on resonance with the Rydberg state as its energy shifts with the number of Rydberg excitation in the cloud [36]. The adiabaticity of the process ensures that the atoms are prepared in the ground state of the system, corresponding to an equal distance between the Rydberg excitations. The spatial correlations of the crystal can then be mapped onto temporal correlations of a light field by photon retrieval of the Rydberg atoms. Due to the collective character of the Rydberg excitations, the retrieval of the photons is preferentially directional at large atomic densities and would constitute a source of highly correlated trains of single photons.

Obviously, the observation of these highy correlated states of light requires a one-dimensional medium of length L longer than the blockade radius and simultaneously a high optical depth per blockade radius $OD_B \gg 1$. In general, such a medium will also enhance two-body interactions due to the increased interaction length for co-propagating photons. For such a medium, it is nevertheless important to take bandwidth effects into consideration. In general, the Rydberg blockade induces atomic correlations on the order of the blockade radius. These correlations can only be coherently transferred to photonic states with high efficiency if $OD_B \gg 1$, and without deformation if the extent of the spin-wave correlations $\sim r_b$ is larger than the extent of a compressed bandwidth-limited pulse, $v_g \tau_p \sim L/\sqrt{OD}$. As a consequence, the maximum number of correlated photons N_c sustained by the system is limited to:

$$N_c \sim \frac{L}{r_b} \ll \sqrt{OD} \tag{6.6}$$

This conditions also sets a lower bound on the necessary density for the retrieval of many-body correlated states of N_c photons, using $OD_B \sim OD/N_c$:

$$N_c \ll \sqrt{OD} \ll OD_B \tag{6.7}$$

These conditions are technically hard to achieve for $N_c \geq 3$.

6.2 Overview of the experimental setup

As detailed in the previous section, the two crucial requirements for achieving optical quantum nonlinearities based on Rydberg EIT are a quasi-one dimensional medium defined by the transverse mode of the probe beam, $\sigma_\perp, r_b \gg w_0$ (where $\sigma_\perp$ is the transverse extent of the medium) and an atomic ensemble of density $\rho > (\sigma_0 r_b)^{-1}$ where σ_0 is the resonant atomic cross-section for the probe field (equal to $3\lambda^2/(2\pi)$ for the cycling transition between streched states). The minimal Rydberg blockade radius is limited by the necessity for the EIT linewidth to overcome the decoherence rate between the ground- and Rydberg-states. Typical numbers are given in Table 5.2. For a blockade radius of 5 μm, OD_B reaches unity for an atomic density $\rho = 0.7 \times 10^{12}$ cm^{-3}.

Such densities can be achieved by loading atoms into a focused far-off resonant dipole trap (FORT) with longitudinal confinement, such as a crossed dipole trap or a single beam lattice. In principle, the maximum atomic density does not depend on the exact trap geometry. As a consequence, we favored a geometry for which $OD \gg OD_B$, i.e. an elongated cloud along the probe light propagation, with an aspect ration limited by the condition $\sigma_\perp > w_0$. There are several advantages for this geometry, compared for example to an interaction volume reduced to a single blockade volume[155, 161]. First, for co-propagating photons, the interaction time between the photons is increased and the effects of the nonlinearities (for example the emergence of a photon bound state as described in Chapter 8) are enhanced. For counter-propagating pulses, a large total OD ensures that both pulses fit entirely in the medium simultaneously and are thus forced

to interact. Finally, many-body effects leading to the coherent preparation of highly correlated states of light, such as Rydberg crystallization, require a medium of length $L > r_b$.

To that end, we load the atoms in a crossed-dipole trap. The trap is formed by two orthogonally polarized beams with waists w_t=50 μm intersecting at an angle of 32°. The centerpiece of our experiment and the essential components inside the vacuum chamber are depicted in Fig. 6-1.

6.3 Vacuum chamber

The vacuum chamber was custom-built and assembled following the guidelines in [162]. It provides optical access for the MOT cooling beams, the probe beam along the optical access and the elongated cross dipole trap as well as large viewports at the top and bottom for high resolution imaging, and enough volume for electric field plates, a channeltron and Rb dispensers. The procedures for ultra-high vacuum assembly are standard, and we here report on a few specific points of interest. Regarding the cleaning process, the first observation is that gaskets should not be cleaned with sonication as it irremediably damages them, either due to the pitting during the sonication process or due to the formation of oxidation layers. In general, gaskets should be used directly from the manufacturer. Similarly, sensitive components of the vacuum assembly, such as optical components, viewports and feedthroughs, should not undergo sonication. The channeltron was cleaned with solvent in the presence of sonication. Kapton insulated wires should not be cleaned with acetone or sonicated. An oxide remover (Caswell Pickle#4) was used for the copper parts who were subsequently stored in a sealed container.

The chamber was assembled directly on the optical table and evacuated using a turbo-pump backed by a rotary vane pump (Varian DS102) separated from the turbo-pump by a valve and a micro-maze fore-line trap (MMA-102-2QF) to avoid back-flow of oil and organic components in the turbo-pump. Kwik-flanges were used for all connections after the exhaust of the turbo-pump. The exhaust of the rotary pump was connected to Welch oil mist eliminator. A mass spectrum analyzer (SRS, RGA200) was inserted between the valve to the vacuum chamber and the turbo-pump to measure the partial pressure

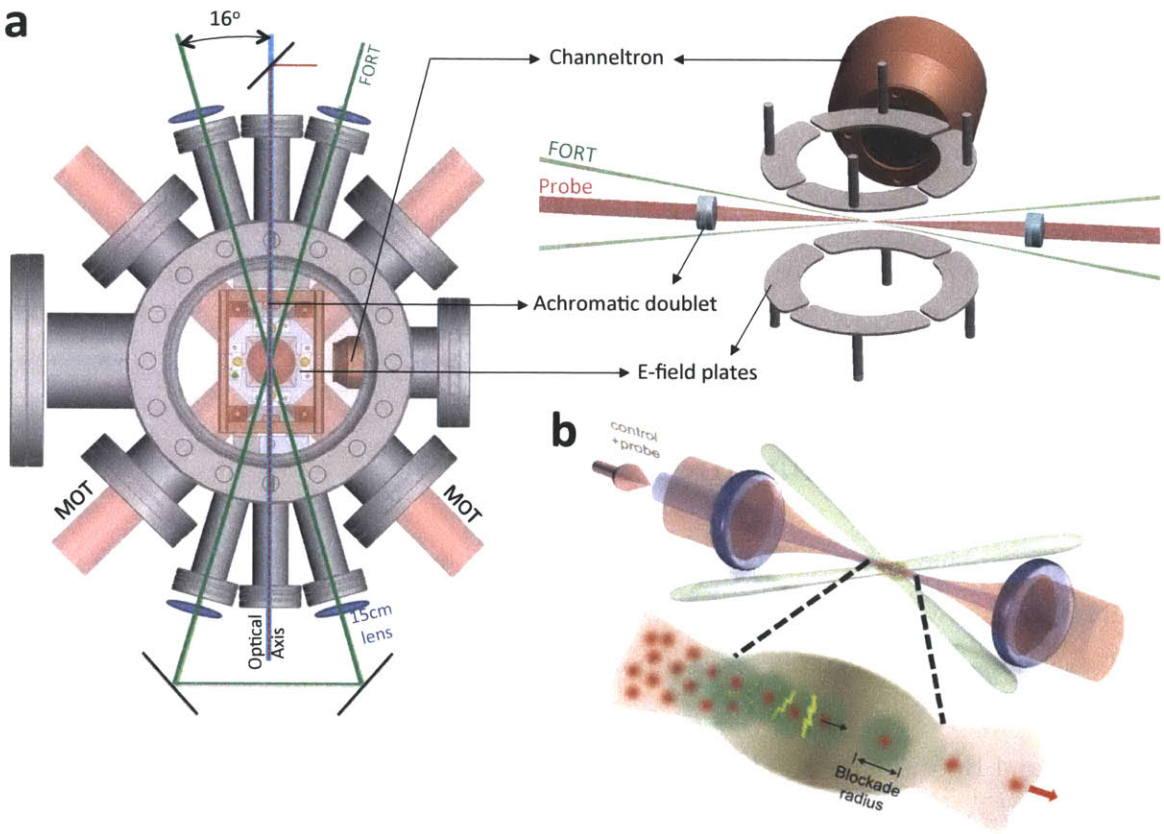

Figure 6-1: **Rydberg EIT setup.** **a,** Top view of the central part of the vacuum chamber (left) and 3D view of the essential component inside the vacuum chamber (right) illustrating the laser arrangement. The atoms are loaded in a crossed dipole trap, with two beams intersecting with an angle of 32°. The trap beams are focused to a waist of 50 μm with 15 cm lenses located outside the vacuum chamber. Inside the chamber, two 3 cm achromatic doublet lenses define the optical axis along the longitudinal extent of the cigar-shaped cloud and focus the probe and control beam at the center of the cloud . The lenses are held in a copper structure, to which eight electric field plates in an octopole configuration are attached through electrically insulating components. A channeltron shielded by a Faraday cage detects ions in the chamber. Four viewports in the horizontal planes are used for the trapping and repumping beams of the MOT, as well as two large 4.5 inch windows at the top and bottom of the chamber. All windows were anti-reflection coated for the appropriate wavelength. **b,** Artist rendition of the setup, illustrating the dissipative nonlinear interactions between Rydberg polaritons taking place in a dense cloud of trapped cold atoms with length of approximately 10 blockade radiuses. The interaction is enforced by confining the transverse extent of the probe beam to less than a bockade radius.

from the background gas. During the evacuation, the background pressure was strongly dominated by hydrogen degassing from the steel of the chamber. N_2, H_2O, and CO_2 also contribute to the background pressure at the beginning of the evacuation. An ion pump (Varian, VacIon Plus 20, Ion Diode, 20 L/S), a Ti-Sublimation pump (Varian, TSP controller 929-0022) and an Ion Gauge (Varian, UHV-24) are permanently attached to the vacuum chambered.

During the evacuation, the chamber was heated to 180°C using heating tape . The limiting temperature for our assembly is the cement used for the achromatic doublet lenses (NOA61 from Norland). The nominal damage value is 125°C, but no visible damages or change in transmission were observed after baking a replacement lens to 215°C. However, the cement changed color and became brittle after heating to 240°C. The lenses are glued inside a copper block with a close fit to guarantee alignment, using vacuum temperature compatible glue Epo-Tek ND353. This glue has the advantage of sustaining high baking temperature (200°C). It also has a large thermal expansion coefficient (260×10^{-6}/°C above the glass transition occurring at 90°C and 54×10^{-6}/°C below the glass transition), compared to copper (17×10^{-6}/°C). Below the glass transition, it is extremely stiff and adhesive. During a first bake of the vacuum chamber, one of the lens presented cracked, likely due to the expansion of the glue. For the second bake, the chamber was only heated to 125°C and the lens is held in place with a springy piece of stainless steel.

The four Rubidium dispensers (SAES Getters, RB/NF/4.8/17 FT 10+10) were degased for hydrogen during the bake by increasing current by 0.1 A steps up to 3 A (waiting for the pressure to stabilize for every step). We then ran 30 seconds pulses up to 5 A until the pressure was affected by less tan 20%. After the evacuation process, we measure a pressure of less than 2×10^{-9} Torr using the ion pump current as a gauge and of 1.0×10^{-9} Torrs (with gas factor 1.0) using the ion gauge. The background pressure rises to $\sim 2 \times 10^{-9}$ Torr when the dispensers are continuously ran at 3 A (from the reading of the ion pump current).

6.4 Probe and control field setup

The probe beam is focused to a $1/e^2$ waist $w_0 = 4.5$ μm by a confocal arrangement of achromatic doublet lenses with focal length 30 mm and diameter 6.25 mm (Edmund Optics, NT49-308). The aperture angle (i.e. the ratio between the focal length and the radius of the lens) is chosen to mitigate the focus size of the probe beam and the acuteness of the FORT arms angle, which sets the elongation of the cloud along the optical axis . Furthermore, is has been observed that static charges on lenses with working distances smaller than 1 cm generate visible level-shifts of the Rydberg levels unless their surface is grounded with a transparent metallic coating [163]. Our lenses are not coated and are mounted in a copper structure, screwed to two plates soldered to the vacuum chamber.

The 780 nm probe light expands from the fiber tip with a Gaussian waist of 2.8 μm (measured in the far field with a knife edge). It is collimated by a 18.4 mm aspheric lens (Thorlabs C280TME). After the 30 mm achromatic doublet, we measured a probe waist $w_0 = 4.5$ μm (also inferred from a knife edge measurement in the far-field). The corresponding Rayleigh range is $z_R = 81.5$ μm. In this configuration, the lens operates close to its diffraction limit $\lambda/(2\ \text{N.A.}) = 3.75$ μm. Over the length of the cloud, the waist average (weighted by the atomic density) is 4.9 μm.

The control field is produced by a Toptica TA-SHG Pro system consisting of an external cavity diode laser (ECDL) operating around 960nm, a 1W tapered amplifier and a frequency-doubling crystal in a circulating cavity. The tuning range of the laser, from 479 nm to 488 nm couples the ^{87}Rb $5P_{3/2}$ state to Rydberg states with primary quantum numbers between $n \sim 20$ and the ionization limit. After passing through an Acousto-Optic Modulator (AOM), the control light is guided by a polarization maintaining optical fiber to the experiment table. There, it expands from a 2.3 μm waist at the output of the fiber and is collimated by an 4.5 mm lens, focusing the beam to a 15 μm waist at the position of the atomic cloud. Note that there is a trade-off between the requirements for an homogeneous control field intensity over the extent of the probe beam and the high power necessary for strong coupling to high lying Rydberg states. The control field power entering the vacuum chamber is limited to 100mW (corresponding to 250 mW at the output of the doubling cavity).

The probe and control beams are overlapped before passing through the chamber,

and split after, by a set of dichroic mirrors (Thorlabs DMLP567). The exact alignement (for co-propagating probe and control beams) is achieved by aligning the beams on a CCD camera at the center of the chamber (as imaged by the combination of the 30 mm achromatic doublet and a 30 cm lens) and far outside the chamber. For the counter-propagating case, a co-propagating beam serves as a reference.

At the output of the chamber, the probe beam is filtered from the control field by the dichroic mirror and interference filters (SEMROCK, LL01-780), coupled into single mode fibers and measured by single photon detectors (PerkinElmer, SPCM-AQR-13-FC,with a deadtime of 40ns). The detection efficiency is typically 0.25 (0.5 due to filtering and coupling and 0.5 due to the quantum efficiency of the detectors). The single photon pulses are recorded by a counter (National Instruments card) or time-tagged with a time-resolved counter (SensL, HRMTime, 4 channels, 28 ns resolution time).

6.5 Dipole trap configuration

In recent years, in conjunction with novel cooling techniques such has polarization gradient cooling [164], degenerate Raman sideband cooling [165], gray molasses [166] and evaporative cooling[167], dipole traps have been key to many crucial developements, such as all-optical BEC [168, 169] and degenerate Fermi gases [170], optical lattices [171]. Dipole traps are extensively reviewed in [79].

For our experiment, the trapping light is produced at a wavelength of $\lambda_t = 1064$ nm by Nd:Yag laser (NP Photonics, FLM-50-1-1064.175-1) seeding a fiber amplifier (Nufern, SFA-PM1064-10W-2), with a 50 kHz linewidth. After passage through a high power accousto-optical modulator (IntraAction), the trap power is 5W. The beams are focused and recollimated from outside the chamber by 15 cm lenses (Thorlabs, LA1433) after passing through a 10/3 times magnifying telescope. The waist (measured outside the chamber) is 50 ± 2 μm and the beam exhibits a small amount of astigmatism (giving approximately a 1 mm difference in the position of the horizontal and vertical focus). After a first path through the vacuum chamber, the dipole trap is re-collimated, sent through a half-waveplate and focused back in the chamber, crossing the first arm with an angle $\theta = 32°$ at the center of the chamber (see Fig. 6-1). The incoming light is

linearly polarized, with a polarization vector orthogonal to the horizontal trap plane . For an on-axis half-waveplate, the retro-reflected beam creates a lattice with periodicity $d = \lambda_t/(2\cos(\theta/2))$ along the optical axis. For the work presented here, we fully destroy the interferences by rotating the linear polarization of the second beam by $\pi/2$. As a result, the reduced longitudinal trapping frequencies attenuate the parametric heating of the atoms under modulation of the trap. In this configuration, the trapping frequency are $\omega_z = 2\pi \times 315$ Hz longitudinally, and $\omega_y = 2\pi \times 1.10$ kHz and $\omega_x = 2\pi \times 1.14$ kHz transversally (horizontally and vertically respectively) and the peak trap depth is $\sim$300 μK. The polarization of the dipole trap is linear and orthogonal to the propagation direction of the reflected beam. In that case, the ground state shift is independent of the particular magnetic level and is given by:

$$\Delta U(r) = \frac{\pi c^2 \Gamma}{2}\left(\frac{2}{\omega_{D2}^3(\omega-\omega_{D2})} + \frac{1}{\omega_{D1}^3(\omega-\omega_{D1})}\right) I(r) \tag{6.8}$$

where $I(r)$ is the sum of the intensities of the two arms of the dipole trap. The peak frequency shift in the ground state is $2\pi \times 7$ MHz (equivalently 336 μK). The level-shift of the excited state at the center of the trap depends on the particular magnetic sub-level.

6.6 Loading procedure

The atoms are initially cooled in a Magneto-Optical Trap (MOT) with 1 inch diameter beams. The loading of the MOT is generally described by a simple rate equation:

$$\dot{N} = R_{MOT} - \Gamma_M N \tag{6.9}$$

where R_{MOT} is the loading rate, *i.e.* the number of atoms entering the trapping region per unit of time with low enough velocity to be captured and Γ_M^{-1} is the lifetime of the atoms in the MOT, typically limited by collision with background atoms or hotter ^{87}Rb atoms. From this simple model, the number of atoms in the MOT saturates with a time constant Γ_M^{-1} to $N_{MOT} = R_{MOT}/\Gamma_M$. For our experiment, the lifetime Γ_M^{-1} is 13s and the atoms are loaded from the getters flux. We also notice that both Γ_M and R increase with the current getters and that $R_{MOT} \propto \Gamma_M^2$. In principle, if the background collisions

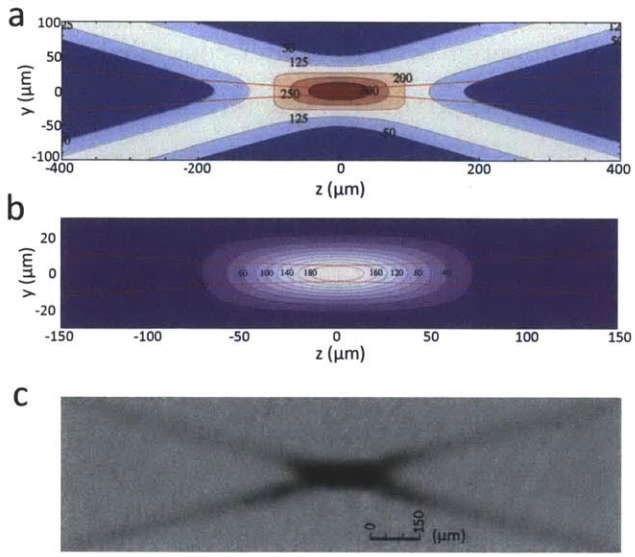

Figure 6-2: **Dipole trap. a,** Countour plots of the trapping depth in the horizontal plane in μK for a power of 5 W per beam. The maximal trap depth is 336 μK. **b,** Contour plots for the density in 10^{10} atoms cm^{-3} for a peak density $\mathcal{N} = 2 \times 10^{12}$ atoms cm^{-3} at a temperature of 40 μK. Contours are plotted for $\mathcal{N} = 2 \times 10^{11}$ to 1.8×10^{12} cm^{-3}, by increments of 2×10^{11} cm^{-3}. The red lines delimit the waist of the probe, focused to 4.5 μm. **c,** Absorption image of the atoms in the crossed dipole trap after 0.1 ms of expansion time.

are dominated by the partial pressure of Rubidium, R_{MOT} should increase linearly with Γ_M as the getter current increases. If the background pressure is dominated by another species, Γ_M is independent of the getters current. For our experiment, R_{MOT} increases as Γ_M^2, suggesting that the background pressure is not strongly dominated by Rubidium or that the getters have higher hydrogen degassing rates at larger operating temperature.

The MOT magnetic field is generated by two coils in anti-Helmholtz configuration located outside the chamber. The coils are wound with 0.1 inch sided square copper wire around a hollow cylinder of radius 3.175 inches, water-cooled and partially cut to avoid eddy currents. The coils count 100 turns, provide a gradient of .97 Gauss/cm/A, and have a resistance of 1 Ohm each. They are mounted in parrallel with transient voltage suppressors (TVS 1.5KE100CA) to damp inductive spikes during fast turn-on and -off of

the magnetic fields. Both coils are mounted in series with a high current solid state relay (Crydom D1D80) and powered by a computer-controlled current supply. The turn-off time of the field from the peak gradient value (40 G/cm) is shorter than 500 μs.

We use a short cycle time of 330 ms, with a MOT duty cycle of $\sim$ 60%, allowing partial recapture of the atoms. At the beginning of the cycle, the trapping light (consisting of $\sim$ 1.5 inches collimated beam cut to a 1 inch diameter for more homegeneous profile, with a power of 30mW per beam) is red detuned by 14 MHz from the D_2-line $F = 2 \rightarrow F' = 3$ cycling transition in presence of a 10 G cm^{-1} magnetic field gradient. After 230 ms, $\sim 10^6$ atoms are loaded in the MOT. The atomic ensemble is compressed [172] by ramping up the magnetic field gradient to 35 G/cm in 10 ms followed by a 50 ms plateau. At the beginning of the compression, the MOT trapping light intensity is halved and the repump power reduced to an intensity of $\sim$ 10 μW cm^{-2}. As a result, the density is increased by a factor 1.5 (the two-fold volume decrease seems to be accompanied by a loss of 25% of the atoms). From absorption imaging , we measure a peak density in the compressed MOT of 3×10^{10} atoms cm^{-3} although this number assumes the largest resonant cross-section and perfect optical pumping to the stretched state by the imaging beam. As a consequence, the imaged densities are to be taken as a lower limit. The MOT magnetic field is suddenly (in less than a ms) shut-off for 18 ms of molasses cooling. During the molasses phase, the MOT light is detuned by an additional 55 MHz. From time-of-flight imaging, we assess a temperature of 35 μK after optimization of the cancellation of stray magnetic fields [173] by three pairs of bias coils, located outside the chamber. The difference between the measured longitudinal and transverse temperatures is generally less than 10%.

The dipole trap is turned on to full power at the beginning of the compression. The loss and loading mechanisms at play are extensively described in [174]. A crucial step to reach high atomic densities in the trap is the reduced repumper intensity $\sim$ 10 μW cm^{-2} during the compression and molasses cooling. At low repumper intensities, the atoms populate mainly the $F = 1$ hyperfine state, where they experience a smaller scattering by the MOT trapping beam than in the $F = 2$ state. The MOT light scattering induces two type of interactions between the atoms [175]. Firstly, light-assisted collisions, i.e. collisions between ground-state and excited atoms in which part of the excited atom energy is converted into kinetic energy, are detailed in [176]. Secondly, radiative trapping of the

light, i.e. reabsorption of the photons scattererd from a specific atom by the surrounding atoms, mediate an effective repulsive force between atoms. As a consequence, the loading in the dipole trap is optimized for an experimentally determined value of the repumping power which mitigate theses effect with the cooling and trapping provided by the MOT beams. At the end of the molasses phase, the repumper is shut off 2.5 ms before the MOT trapping beam and the atomic population is optically pumped in the $F = 1$ ground state. We then proceed to optical pumping to the $F = 2, m_F = 2$ state (see section 6.9).

We use time-of-flight absorption imaging to determine the temperature and the in-trap extent of the atomic cloud. The imaging is done along the vertical direction in the presence of a few Gauss of vertical magnetic field, using a 1:1 imaging system and circularly polarized imaging light for expansion times ranging from 50 μs to 5 ms. The atoms temperature in the trap at the end of the molasses phase is $40 \pm 5\mu$K and the cloud has a Gaussian profile with longitudinal and transverse (horizontal) r.m.s. sizes $\sigma_z \cong 36\mu$m and $\sigma_\perp \cong 10\mu$m. After 4 ms of expansion time, we measure 5×10^4 atoms, corresponding to a peak density of $\mathcal{N}_{Abs} \cong 0.8 \times 10^{12}$ atoms cm^{-3}. By changing the loading time of the MOT, we vary the number of atoms loaded in the trap. We observe a saturation of the peak density to $\mathcal{N}_{Abs}$ for 2×10^4 atoms loaded in the trap. The values for the number of loaded atoms and density we obtain by absorption imaging are a factor 2 to 3 smaller than the values we obtain by measurement of the longitudinal OD after careful optical pumping, for which we infer a peak density $\mathcal{N} = 2 \times 10^{12}$ atoms cm^{-3}. The discrepancy is likely due to the imperfect pumping from the imaging beam as our measurement assumes the maximal atomic cross-section. The saturation of the density in the trap is possibly due to two-body hyperfine state changing collisions, evaporative cooling and three body losses which reduce the lifetime of the atoms in the trap [79].

When monitoring the atoms in the trap, we observe a rapid loss over a few tens of ms, followed by a slower exponential decay with a timescale of 950 ms (see Fig. 6-3). The initial loss is due to collisions between trapped atoms. The remaining number of atoms decrease further if the trap height is lowered. This behavior is characteristic of evaporation and inelastic collisions, during which some atoms acquire a fraction of the trap depth in kinetic energy [176]. Ground state changing collision for the atoms in the $F = 2$ ground state can also eject atoms out of the trap (although this process should be

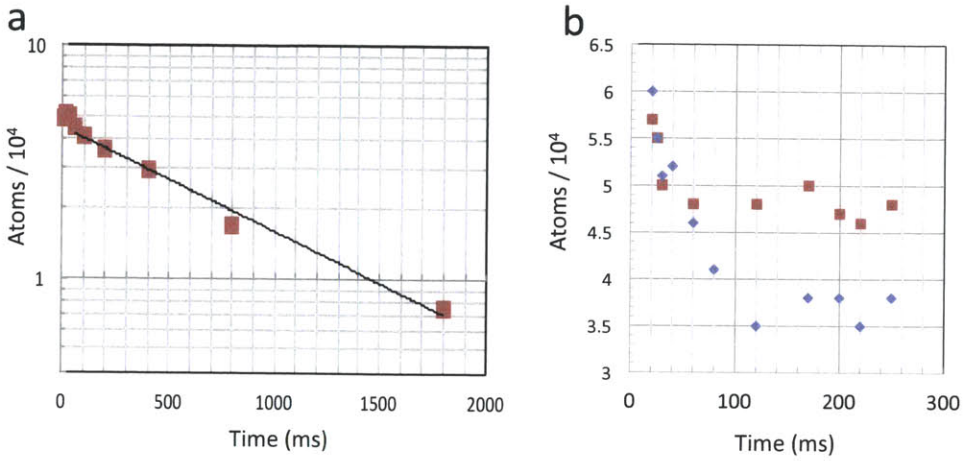

Figure 6-3: **Lifetime in the Dipole Trap. a,** Number of atoms in the trap as a function of time, over a timescale of 2 s. The number of atoms is measured by absorption imaging after the trap shut-off. An exponential fit to the data measured after the first 100 ms yields a lifetime of 950 ms. **b,** Number of atoms in the trap for a power per beam of 5 W (red squares) and a 2.5 W (blue dots). Inelastic collisions reduce the density during the first 100 ms, followed by the background pressure decay rate visible in **a**.

independent of the trap power as the hyperfine splitting of the ground state $\sim$1.4 mK is larger than our maximal trap depth). The departure of the hotter atoms from the trap leads to evaporative cooling and a decrease in temperature from 55 μK to 30 μK. The long lifetime $\sim$ 1 s after initial evaporation is due to collisions with the background gas and is typical of a pressure of $\sim$ 2 Torr [79].

The finite temperature of the atoms in the trap is responsible for inhomogeneous broadening of the excitation linewidths. The EIT is mainly affected by the broadening of the two-photon transition between the ground- and Rydberg states. For ground states atoms, the difference in level-shift for atoms at the center of the trap and 1-σ away for an harmonic trap is $\frac{1}{2}k_BT \sim 350$ kHz. The peak Rydberg state ponderomotive shift is 3 MHz, contributing an approximate inhomogeneous broadening of 150 kHz. Note that the inhomogeneous Stark shift mainly plays a role along the optical axis, as $w_0 < \sigma_\perp$. For our experiment, the total two-photon broadening caused by the inhomogeneous Stark shift

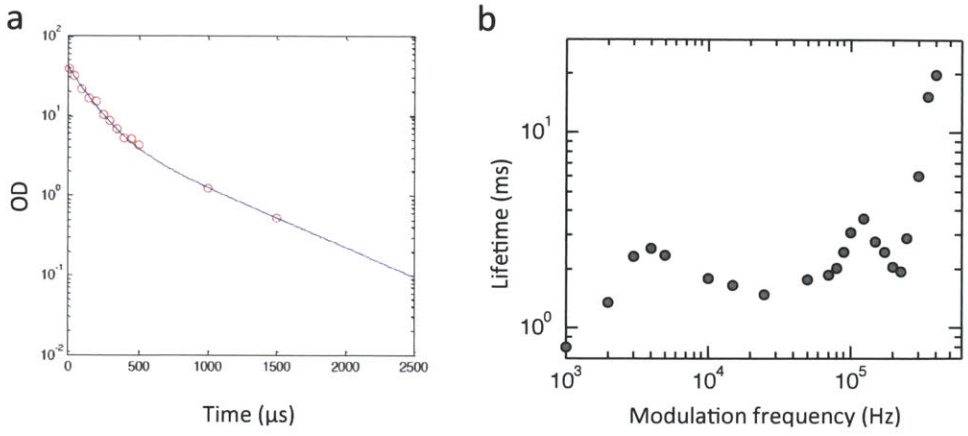

Figure 6-4: **Atom loss during the measurement. a,** Optical Depth *OD* as a function of time during the free expansion of the beam after the dipole trap shut-off. The blue line is a guide to the eye. Measurements in expanding clouds are limited to 100 μs. **b,** Lifetime of the atoms in a modulated trap as a function of the trap square-wave modulation frequency. Here, a frequency of 100 kHz corresponds to a period of 10 μs.

$\sim$ 500 kHz dominates the other broadening mechanisms, typically the two-photon laser linewidth (250 kHz) and the Doppler effect (250 kHz for co-propagating probe and control fields, 50 kHz for the counter-propagating case). As a consequence, EIT experiments áre carried out after the shut-off of the dipole trap in an expanding cloud (during 100 μs) or during the off-time of a modulated trap (typically modulated at an angular frequency $\sim$ 100 kHz much larger than the trapping frequency). For a modulated trap, the *OD* is reduced due to the average half-trapping potential but the measurement time is extended to 2 ms when the interferences between the beams of the dipole trap are carefully cancelled to avoid the creation of a lattice with large trapping frequencies. A higher limit for the modulation trap frequency is set by the group delay in the medium.

The positioning of the elongated cloud along the optical axis is crucial to our experiment. The alignment of the cloud in the horizontal plane is done by using the probe beam as a "push" beam with typical powers of a few hundreds of μW and blue detuned by 100 MHz from the $F = 2 \rightarrow F = 3$ transition. The atoms are expelled from the higher intensity region of the probe beam, an effect clearly visible by imaging absorption (see Fig. 6-5,a). The longitudinal positioning of the cloud along the optical axis is sensitive

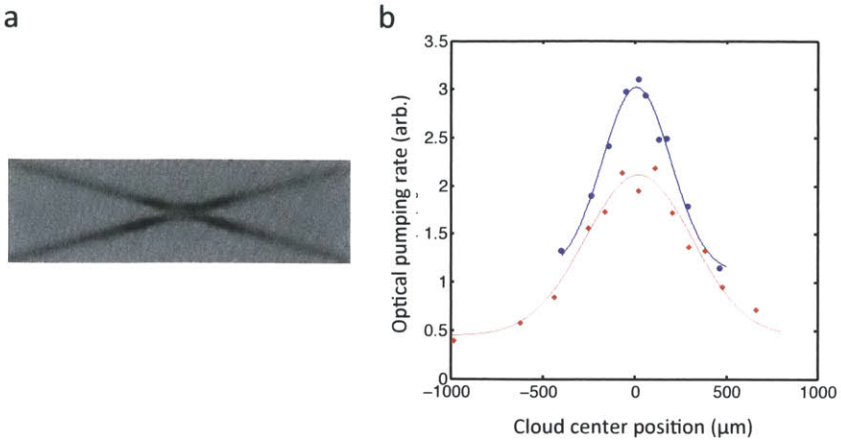

Figure 6-5: **Alignement procedure of the dipole trap. a,** Expulsion of the atoms by a blue-detuned probe field. The clearly delimited maximal intensity probe region is used for the initial alignment of the trap (see Fig. 6-2,c for comparison).**b,** Depumping rates as a function of the central position of the atomic cloud for atoms in a compressed MOT (red diamonds) and a dipole trap (blue dots). The initial atomic population on the probe transition is removed by off-resonant scattering. The depopulation rate is extracted from the intermediate slope of s-shaped transmission curves and exhibits a clear peak when the cloud is positioned at the focus. The positions of the cloud are measured by absorption imaging. The lines are Gaussian fits.

to the probe beam intensity. At powers close to saturation intensity, the probe light $F = 2 \rightarrow F = 3$ induces off-resonant depumping of the atoms out of the $F = 2$ hyperfine ground state. As a function of probing time, the transmission follows an s-shaped saturation curve as the initial opacity of the cloud is reduced by the off-resonant depumping. The depumping rate, proportional to the intermediate slope of the s-curve, depends on the intensity of the probe beam and is maximal when the center of the cloud is located at the focus. By varying the position of the dipole trap along the optical axis, we scan the probe beam intensity as evidenced in Fig. 6-5,b. As a function of the position, the depumping rate follows a bell curve with a HMHW on the order of the Rayleigh range of the probe beam. The fit uncertainty of the center of the bell-curve is typically $\pm$ 20 μm.

6.7 Diagnostic tools

6.7.1 Field-ionization

Rydbergs atoms are easily ionized by static electric fields as low as a few V cm^{-1} for states with principal quantum number $n \geq 100$ (see Chapter 5). Field-ionization is a widely used technique for Rydberg atom experiments, and has been instrumental to the remarkable developments of micro-wave Cavity QED [132] and to the demonstration of the Rydberg blockade in cold atomic ensembles[150, 151, 152, 153, 143]. Recently, microscopic ionization electrodes in combination with a spatially resolved multiple channel plate have been use to image the spatial correlations of a cold Rydberg gas [177]. In contrast, Ryberg atoms are difficult to detect optically due to the low electric dipole coupling to ground states. The electrodes design is identical to that of the Pfau's group (Stuttgart)[158]. It consists of two concentric rings offseted from the horizontal plane (see Fig. 6-1). Each ring is divided into four plates which are individually addressable and allow for a large variety of electric field configurations. The 1 inch vertical spacing between the plates and inner diameter of the ring provides optical acces for the MOT beams. The large aspect ratio of the plates (13 mm wide and 0.5 mm thick) increase homogeneity of the produced fields. The plates are equivalent to an octopole cuboid with dimensions 15:15:14 mm (see [158, 178]). The electrodes are machined out of stainless steel. They were rounded off and polished to avoid electrical breakdowns in the chamber. The electro-polishing was done in a solution of phosphoric and sulfuric acids [158], at a current of 5 A for one minute. The plates are attached to the central copper structure with ceramic (MACOR) screws and 1 mm MACOR spacers. Using barrel connectors, they are connected to a high voltage feedthrough by 1.7mm thick Kapton coated wires. The barrel connectors and insulating elements are recessed beyond the field plates to shield the atoms from stray electric fields created by static charges. The voltage on the field plates can be controlled with a high voltage switch (Behlke, HTS 61-03-GSM). The turn-on and -off time of the high voltage depends on the exact capacitive load of the plates and the cables, and has been demonstrated to be on the order of a few tens of ns in similar setups [158].

Ions are detected with a channeltron electron multiplier (Burle, Magnum 5901 Channeltron). A positive ion is accelarated towards the entrance of the channeltron, which is

maintained at negative high voltage of -2 kV. Upon collision with the walls of a secondary emission material, it releases an electron which is accelerated towards the grounded end of a spiral-shaped funnel, creating a cascade of electrons collected as a current pulse at the output of the channeltron. Typically, a single ion creates a short 10 ns pulse of 10^6 electrons (equivalent to approximately a 10 mV negative pulse across a 50 Ohm resistor). The output of the channeltron is connected to an RF amplifier (ZFL-1000LN) after a bias-T guiding charges accumulating at the output of the channeltron to the ground to avoid damaging static voltages at the input of the amplifier. The resulting negative pulses have an amplitude of 800 mV. The ionization of background atoms creates a measured 800 Hz dark count rate.

The atoms are shielded from the channeltron by Faraday cage. The entrance of the cage is made of a copper mesh with 85% open area. A negative voltage of a few Volts in conjuction with the proper field configuration from the electrodes can be applied to the cage to directionally guide the ions towards the entrance of the cage, before they are accelerated towards the large negative voltage at the channeltron input.

6.7.2 Absorption imaging

Our current absorption imaging system consists of an imaging beam with circular polarization overlapped with the vertical MOT beam and an achromatic doublet lens with a focal length of 10 cm (Thorlabs AC508-100). The MOT beam is propagating at a small angle with the vertical optical axis, and is reflected by a 6 mm diameter mirror positioned in the focal plane of the imaging lens (see Fig. 6-6). It is then collimated and retro-reflected with an orthogonal circular polarization. The small mirror has little impact on the quality of the imaging, as it is located far from the image focal plane of the lens, which works at infinite conjugation ratio. A 10 cm plano-convex lens focuses the beam on a CCD camera (Unibrain 501b). The imaging light is generated by the MOT laser and resonant with the $F = 2 \rightarrow F' = 3$ cycling transition. The MOT repumper is used to pump the atoms into the $F = 2$ hyperfine ground state. The atoms are imaged in a vertical magnetic field of 3 Gauss, provided by the bias coils. The imaging light optically pump the atoms in the $(F = 2, m_F = 2)$ magnetic sub-level, which provides the highest cross-section for the circularly-polarized imaging light.

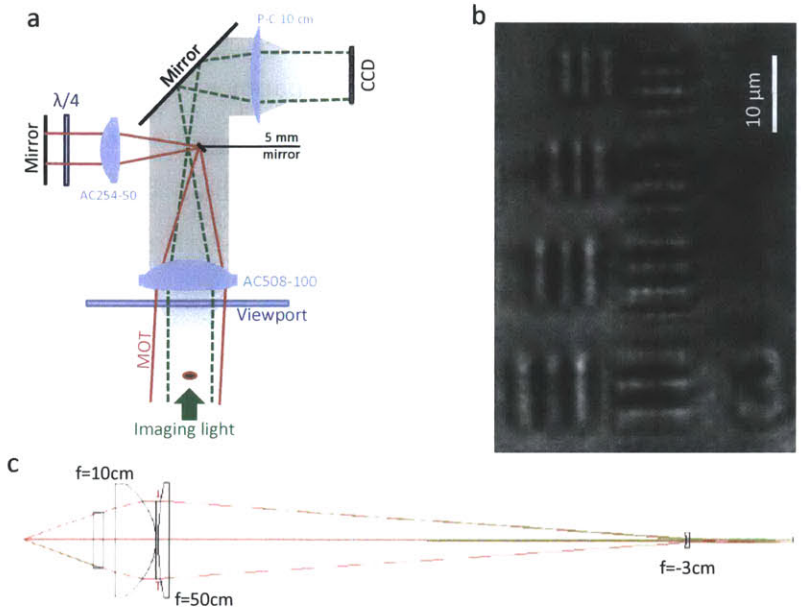

Figure 6-6: **Imaging setup**. **a,** Schematic representation of the current absorption imaging system. The imaging and MOT trapping light overlap at a small angle. The MOT beam is retro-reflected by means of a small 6 mm mirror. A plano-convex lens sets the 1:1 magnification. **b,** Absorption image with coherent light of a resolution target for the high resolution imaging system shown in **c**. The displayed scale shows distances in the object focal plane. The objective provides a resolution smaller than 2 μm. **c,** Schematics for the high resolution telephoto objective for single Rydberg atoms imaging. The 3-lens teleobjective consists in a large numerical aperture 10 cm aspheric lens, a 50 cm plano-convex lens and a diverging -3 cm plano-concave lens. The objective is located outside the viewports (included in the picture).

6.7.3 High resolution imaging of individual Rydberg atoms

Recently, the Rydberg blockade was proposed as a way to image single Rydberg excitations in dense atomic clouds [179, 180]. In these proposals, Rydberg atoms create opaque regions for a probe beam traveling under Rydberg EIT conditions orthogonally to the imaging plane. For imaging systems with a resolution smaller than the blockade radius, individual Rydberg excitations can be resolved to within the blockade area and provide insight into many-body phenomena, such as Rydberg crystallization [36, 180]. The specific Rydberg state used as part of the EIT scheme for the imaging beam $|r'\rangle$ needs to be different from the state of the Rydberg atom $|r\rangle$ to be imaged. A limitation to this proposal is the

interaction between the imaging photons themselves due to Rydberg blockade: the rate of incoming photons per transverse blockade area must be larger than the inverse delay per blockade radius in order to allow for full transparency outside the blockaded areas. Ideally, the levels $|r\rangle$ and $|r'\rangle$ along with the control fields can set the separation between the stationary Rydberg excitations (r_b) to be be larger than the blockade radius for the interaction of the Rydberg excitations with the probe polaritons, (r_b') and the blockade radius between probe polaritons (r_b'')[179]:

$$r_b \geq r_b' \gg r_b'', l_a \tag{6.10}$$

Taking advantage of the large optical depth per blockade length r_b, it is possible to measure the spatial correlations with a resolution r_b''. Assuming a pixel size equal to r_b'' after magnification and a cloud of transvers size on the order of r_b, the rate of probe photons per pixel in a non-blockaded region is $R_{pix.} \approx \gamma_{EIT}\, l_a/r_b$, corresponding to one photon per group delay through a blockade radius. To minimize the shot-noise and increase the rate of imaging photons, the control field can be strongly intensified without large reduction of the blockade radius due to the scaling of the blockade radius as ${\gamma_{EIT}}^{-1/6}$, although the limited control field power typically available will constitute a technical limitation. Finally, the imaging time is limited by a displacement of the Rydberg excitation by blockade radius and by the lifetime of the Rydberg excitation (both on the order of $\sim 100\mu$s assuming a temperature of 40 μK and a blockade radius of 10 μm).

The experimental requirements for individual Rydberg excitations imaging are an imaging system with μm optical resolution and high detection efficiency. High efficiency cameras offer quantum efficiency at 780 nm between 30% and up to 95% (using deep depletion CCDs). The CCD pixel sizes are on the order of 10 μm and require imaging systems with 10 times magnification for the resolution limit to be set by the optical system diffraction and aberrations. The CCD noise include dark currents (typically smaller than 1 electron per pixel per second and thus negligible for sub-ms exposure time) and read out noise. The latter noise corresponds to the uncertainty of the number of electrons retrieved per pixel and is independent of the number of photons impacting the pixel during the exposure time. The readout noise is typically of 10 e^- and is a fundamental constraint for low light imaging with less than a few tens of photons per pixel per exposure. Low

photon number per pixel imaging requires Electron-Multiplying CCD, in which individual photons trigger an avalanche of electrons instead of a single charge.

The optical resolution of our experiment is limited by the viewports which provide a numerical aperture $N.A. = 0.72$. The numerical aperture sets a lower limit to the resolution, which is in addition affected by geometric aberrations such as spherical aberrations from the glass windows, astigmatism and coma for off-axis objects. In addition to a resolution smaller than the blockade radius, the requirements for the imaging system are a field of view and a depth of view respectively larger than the longitudinal and transverse extents of the cloud. We designed a 3-lens telephoto objective depicted in Fig. 6-6. The light gathering lens is a large aspheric lens (ThorLabs, AL100100-B) with a 10 cm focal length and nominal $N.A. = 0.48$, offering a diffraction-limited resolution given by the Rayleigh criterion: $r = 0.61\frac{\lambda}{N.A.} = 1.0$ μm. The rest of the objective consists in a 50 cm plano-convex lens (Ross Optical, A100-100LPX) followed by a diverging -3 cm plano-concave lens (ThorLabs, LC1060) to adjust the magnification. Ray tracing simulation using ZEMAX and including idealized viewports were carried out for on- and off-axis point sources and for different magnifications ranging from 10-fold to 40-fold. The results are thoroughly described in [181]. For an on-axis point source, the simulations predict an Airy disk of radius 28 μm (due to diffraction) and an r.m.s. distribution of 28 μm (from the ray tracing, i.e. the geometric aberrations) in the image plane for a 20-fold magnification magnification, giving a resolution on the order of 1.5 μm.

The objective was built and tested outside the chamber using a test target (Thorlabs, 1951 USAF), as well as a viewport similar to that used in the chamber and a CCD camera with 4.65 μm pixel size (Unibrain 501b Fire-i Camera), using coherent 780nm light. Results for a 19-fold magnification are shown in Fig. 6-6 and the objective clearly resolves features with less than 2.5 μm separation, much smaller than our typical Rydberg blockade radius $r_b \geq 10$ μm. This objective has not yet been integrated to our experiment.

6.8 Laser system

At the exception of the dipole trap and the control field, all the lasers address the 780 nm D2 transition ($5S_{1/2} \rightarrow 5P_{3/2}$) of ^{87}Rb. An external cavity diode laser (ECDL) is

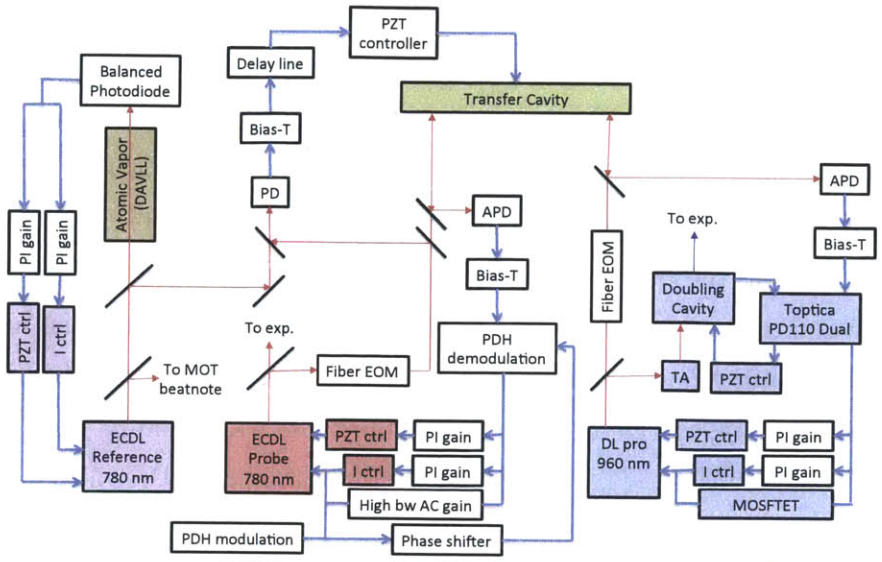

Figure 6-7: **Laser locking diagram.** A reference laser locked to DAVLL spectroscopy serves as a reference for the MOT light. The probe ECDL and control frequency lasers are locked to transfer cavity, which is itself stabilized by the reference laser (see text for a more detailed description). 'PD':photodiode, 'APD': avalanche photodiode, 'ctrl': controller, 'bw': bandwidth, 'exp': experiment, 'TA': tapered amplifier. The other abbreviations are defined in the text.

locked to the ^{85}Rb $(F = 3 \rightarrow F' = 3)(F = 3 \rightarrow F' = 4)$ crossover line of a Dichroic-Atomic-Vapor Laser Lock (DAVLL) setup and serves as a spectroscopic reference for the MOT trapping light (generated by an ECDL followed by a 500 mW Tapered Amplifier) near resonant with the $F = 2 \rightarrow F' = 3$ transition and for the MOT repumper laser (DFB Laser, Eagleyard). These lasers are locked to the reference using a frequency offset lock. The error signal is created by sending the optical beatnote with the reference laser measured by a high bandwidth photodiode (Hamamatsu) through a delay line circuit after being mixed down with a computer controlled Voltage Controlled Oscillator (VCO). The MOT laser also provides the absorption imaging light. Part of the MOT repumper light is sent through a fiber Electro-Optic Modulator (EOM), producing a superposition of light resonant with the $F = 1 \rightarrow F' = 2$ and $F = 2 \rightarrow F' = 2$ used for optical Zeeman pumping.

The probe light is generated by a separate 780 nm ECDL. The laser is locked to a high finesse cavity, which is also used to stabilize the control field. The confocal cavity has a measured finesse of 10^5 and is mounted vertically in a temperature controlled chamber. The probe laser and control field seed laser (at a wavelength of $\sim$ 960 nm) are coupled into the cavity with orthogonal polarizations and are locked with a Pound Driver Hall (PDH) technique [182]. The current of the lasers is modulated to create 20MHz sidebands. When the main carrier frequency is resonant with the cavity, the sidebands are reflected from the cavity and interfere with the carrier field leaking out of the cavity. A frequency shift of the laser is immediately reproduced on the sidebands, whereas the field leaking out of the cavity is delayed due to the travel time inside the cavity, creating a phase sensitive intereference between the reflected sidebands and the averaged value of the main carrier. The cavity reflection in frequency space is given by:

$$\mathcal{R}(\omega) = \frac{r \cdot \exp(i\frac{\omega}{\Delta_{FSR}}) - 1}{1 - r^2 \exp(i\frac{\omega}{\Delta_{FSR}})} \tag{6.11}$$

where r is the reflection coefficient of the mirrors and $\Delta_{FSR} = \frac{c}{2L}$ is the free spectral range of the cavity, related to the cavity linewidth $\Delta\nu$ and the finesse $\mathcal{F} = \frac{\pi}{1-r^2}$ by $\Delta_{FSR} = \mathcal{F}\Delta\nu$. The optical power of the incoming field is denoted $P = e^{i\omega_t}(P_0 + P_1 e^{i\Omega t} + P_1 e^{-i\Omega t})$, where P_0 and P_1 are respectively the carrier and sideband powers. For a laser frequency near-resonant with the cavity: $\omega = \delta\omega + (2\pi k\Delta_{FSR})$ (k is an integer), the carrier electric field has an amplitude $\mathcal{F}(\delta\omega)\sqrt{P_0} \simeq i\frac{\delta\omega}{\pi\Delta\nu}\sqrt{P_0}$. For sidebands with modulation $\Omega \gg \Delta\nu$, the sideband are fully reflected from the cavity, contributing an electric field $[\mathcal{F}(\delta\omega + \Omega)e^{i\Omega_t} + \mathcal{F}(\delta\omega - \Omega)e^{-i\Omega_t}]\sqrt{P_1} \simeq -2i\sin(\Omega t)\sqrt{P_1}$. The amplitude of the signal from the photodiode oscillating at frequency Ω,

$$P_{PD} = 4\sqrt{P_0 P_1}\frac{\delta\omega}{\pi\Delta\nu}\sin(\Omega t) + ... \tag{6.12}$$

is directly proportional to the frequency shift $\delta\omega$ over the narrow range of the cavity linewidth. The DC component of the signal is filtered by a high bandwidth bias-T (Picosecond, 5530B) and the signal is demodulated by the sideband modulation with an adjustable phase shift to compensate for line delay. The full experimental error signal, $\propto -2\sqrt{P_0 P_1}\mathrm{Im}[\mathcal{F}(\omega)]$ [182] is shown in Fig. 6-8,d.

For the probe laser, the error signal is fed into a feedback circuit consisting of three loops. Firstly a slow integrator loop with a bandwidth of a few tens of Hz apply a feedback to the ECDL Piezzo-transducer (PZT) controller to adjust against slow drifts. A second intermediate proportional-integral (PI) gain loop returns to the current controller. The small amount of proportional gain is used to increase the phase at 100 kHz and avoid the zero-phase crossing of unity gain (see Fig. 6-8,a,b). Finally, Fig. 6-8 also displays the gain of the fast feedback loop, which is AC-coupled to the current pins of the laser diode. This feedback loop, shown in Fig. 6-8,c, consists in a flat gain rolled down around 600 kHz, followed by two phase compensators to oppose the phase retardation at 150 kHz and 1 MHz. The total open-loop gain has a zero-crossing close to 1 MHz. Our design also avoids gain crossing at 180 phase between the two feedback circuits. The initial instantaneous laser linewidth (2.7 MHz, FWHM measured over 20 μs) is narrowed by a factor 14 to 200 kHZ (measured from the r.m.s. of the error signal).

The seed laser of the control field (Toptica, DL Pro, 960 nm) is also locked to the transfer cavity with a PDH technique. A high bandwidth ($>$ 10 MHz) MOSFET, built in the enclosure of the laser is used to narrow the laser linewidth to 100 kHz from an initial linewidth $\sim$ 1 MHz. The PDH sidebands are also used to lock the doubling cavity to the laser with a built-in PDH feedback loop.

To have full independent control of the frequency of the lasers with respect to the transfer cavity, the probe and control lasers are first sent through an EOM and the first order sideband are locked to the transfer cavity. By tuning the frequency of the EOMs (who operate over a range larger than the FSR of the transfer cavity), it is possible to independently address all possible frequencies without changing the cavity length. The EOM frequency is generated by a synthesizer (PTS, 3200) controlled by an FPGA. TTL signals to the FPGA trigger fast frequency jumps of the laser, (typically less than 5 μs for a few MHz), enabled by the rapid switching time of the frequency synthesizer. This useful feature allows to measure entire transmission spectra during a single repetition of the experiment, which is convenient for example to align the dipole trap.

Finally, the transfer cavity length needs to be stabilized against slow drifts in temperature and index of refraction. One of the mirror is mounted on a PZT. The first order sideband used to lock the probe laser to the cavity is mixed with the reference laser locked

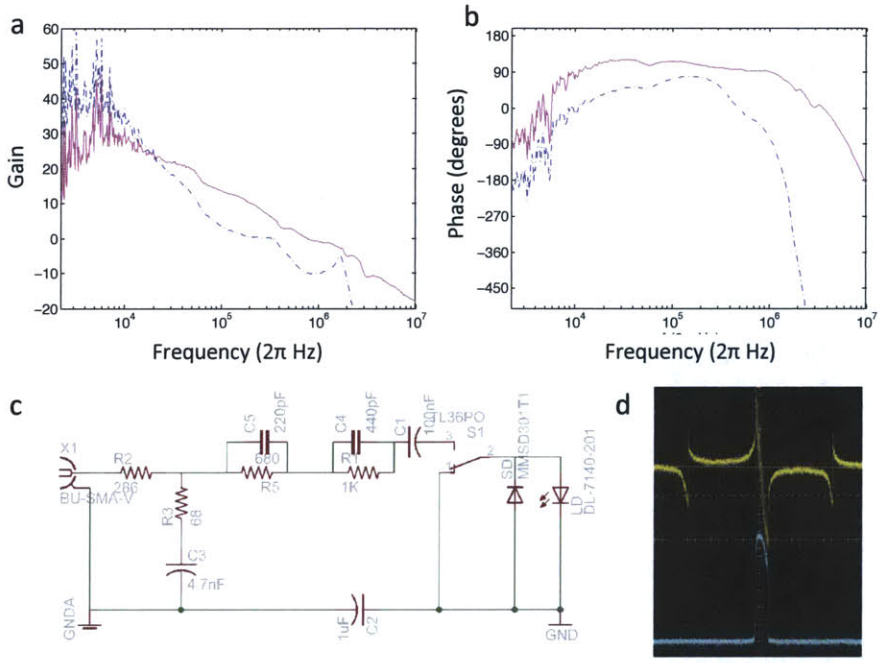

Figure 6-8: **Probe laser lock. a,b,** Open-loop gain (**a**) and corresponding phase (**b**) of the intermediate (dashed, blue) and fast (full, pink) feedback gain of the PDH laser lock for the probe laser. The fast loop is AC-coupled to the laser diode, and extends the feedback up to 1 MHz with the proper phase retardation. The zero-crossing of the intermediate gain is limited to 100kHz due to the rapid dephasing in the 100 kHz regime. **c**, Feedback gain of the high-bandwidth loop. Two capacitors (C1 and C2) AC-couple the signal to the laser diode (LD) and a surge protection diode (SD). The initial filter (R2,R3,C3) consists of a proportional gain rolled down at 600 kHz. Two phase compensators are inserted, operating at 1 MHz (R5, C5) and 150 kHz (R1, C4). **d**, Pound-Driver-Hall error signal (yellow) and probe transmission through the transfer cavity (blue). The broadening of the central slope and the transmission linewidth is due to the active fast feedback-loop.

to the DAVLL spectroscopy. The resulting beatnote is fed via a slow (< 100 Hz) feedback loop to the cavity PZT to compensate for long term drifts of the cavity. Note that this extra feedback loop can broaden the linewidth of the probe and control lasers, who are tightly locked to the cavity. From EIT fits, after subtraction of the Doppler effect, we observe a 2-photon linewidth of 250 kHz, in good agreement with the laser linewidth measured in the absence of feedback on the transfer cavity PZT. Ultrastable cavities with zero thermal expansion coefficient in vacuum chambers (available from Stable Laser Systems) are an alternative solution often used in cold Rydberg experiments where very

narrow linewidth are required, for example for two-photon excitations far detuned from the intermediate level [183].

6.9 Rydberg EIT level scheme

In this section, we describe experimental techniques to implement Rydberg EIT in the cold atomic ensemble loaded in the trap. We use a wavemeter (Advantest Q8326) and the Rydberg levels spectroscopic data detailed in Chapter 5 to initially tune the control field within $\sim$ 1 GHz from the actual resonance. A more accurate value is measured by shining the control field in a continuous MOT (in the absence of probe field) and monitoring the fluorescence. The presence of the control field perturbates the MOT by removing atoms from the $F = 2 \rightarrow F' = 3$ cycling transition and we observe a decrease in fluorescence close to resonance for control field intensities equal to a few percent of the saturation intensity of the excited- to Rydberg-state transition. A typical scan around the $43D$ levels of ^{87}Rb is shown on Fig. 6-9,a. The $\sim$ 50MHz broad lines are split in a double peak structure corresponding to one- and two-photon excitations to the Rydberg state. The one-photon excitation path is the absorption of a control field photon from the $5P_{3/2}, F' = 3$ level and the two-photon excitation consists in the absorption of a control field photon and a MOT trapping light photon from the $F = 2$ ground state. The one- and two-photon excitations occur for control field frequencies respectively red-detuned and blue-detuned from the unperturbed resonance, as measured by EIT with a low power probe. This detuning is caused by the AC Stark shift of the ground and excited states due to the MOT trapping light.

Our EIT level scheme involves transitions between stretched states, i.e. magnetic levels with maximal projection of the total angular momentum along the quantization axis. The level scheme is depicted in Fig. 6-9,b. The σ_+-polarized probe couples the $|5S_{1/2}, F = 2, m_F = 2\rangle$ and $|5P_{3/2}, F = 3, m_F = 3\rangle$ states. In accordance with the selection rules, a control field with circular polarization possibly couples the $|5P_{3/2}, F = 3, m_F = 3\rangle$ state to the $|m_J = 3/2 \pm 1, m_I = 3/2\rangle$ sub-levels of the $nS_{1/2}$, $nD_{3/2}$, $nD_{5/2}$ Rydberg states, where m_J and m_I are the projection of the total electronic angular momentum and nuclear spin. As described in Chapter 5, the hyperfine splitting is not resolved for

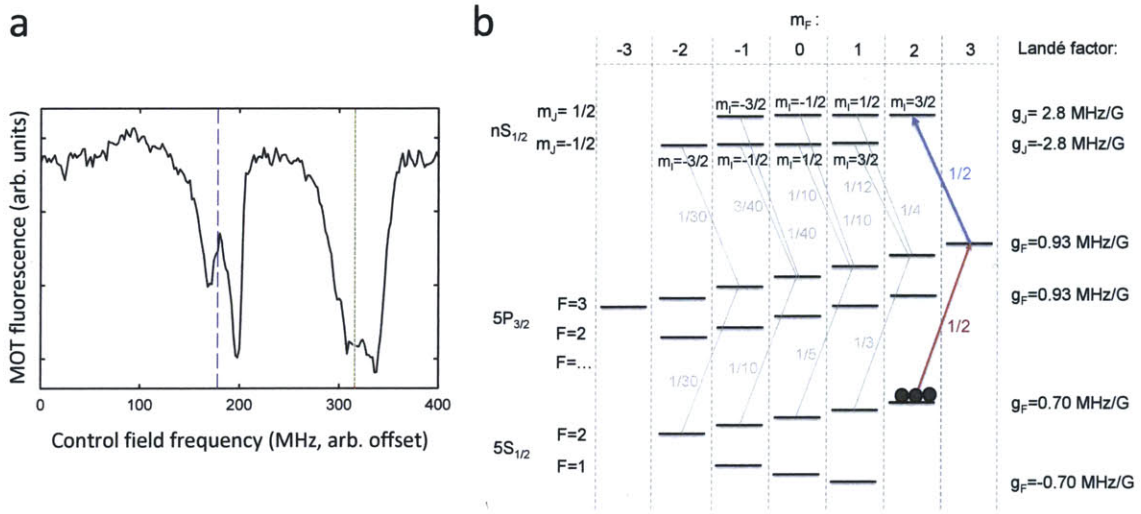

Figure 6-9: **Spectroscopy and EIT scheme. a,** Rydberg spectroscopy of the 44D levels. The MOT fluorescence is continuously monitored while the $\sim$ 480 nm light is scanned. The exact transitions, measured by EIT, are marked for the $44D_{3/2}$ (dashed blue) and $44D_{5/2}$ (dotted green) levels. **b,** Level structure, including all states involved in EIT and optical pumping. The level-shifts in the magnetic field are represented, as well as the Clebsch-Gordan coefficients on the EIT transition and the Lande factors. For Rydberg states, the hypefine structure in unresolved, and the levels are described in the fine structure (J, m_J) (see Chapter 5).

Rydberg states and the electronic and nuclear spins are effectively decoupled. Due to the anisotropy in the presence of stray-electric fields and repulsive character of the dipole-dipole interaction, we restrict our experiments to the $nS_{1/2}$ states. The σ^- polarized control field couples the intermediate excited state to the $|nS_{1/2}, m_J = 1/2, m_I = 3/2\rangle$ states. This level scheme combines two advantages. First, the control field resonantly couples to a single Rydberg sub-level, even with imperfect polarization. Secondly, the dipole matrix elements are maximized for transitions between stretched states, which yields high OD and increase the control Rabi frequency upper limit. The Clebsch-Gordan coefficients are given in Fig. 6-9,b, expressed as multiples of the reduced dipole matrix element $\langle J = 1/2||er||J = 3/2\rangle$ (see [158, 184] for the relation to the radial integral introduced in Chapter 5).

After the molasses phase, we proceed to optically pump the atoms from the $F = 1$ hyperfine state into the $(F = 2, m_F = 2)$ magnetic sub-level. The optical pumping is carried out in the dipole trap and in the presence of a 3.6 Gauss magnetic field along the optical axis. The magnetic field imposes the quantization axis by lifting the degeneracy between the magnetic sub-levels and overcomes the mixing between sub-levels due to stray magnetic fields. A σ^+-polarized beam counter-propagating with the probe provides the light for dark state pumping. The beam is collimated between the probe lenses to achieve homogeneous pumping over the extent of the cloud. The light emanates from the same DFB laser as the MOT repumper, and is modulated with a fiber-coupled EOM (EO Space, PM-0K5-20-PFA-PFA-780) tuned close to resonance with the ^{87}Rb ground state hyperfine splitting to generate a superposition of fields resonant with both the $F = 1 \rightarrow F' = 2$ and $F = 2 \rightarrow F' = 2$ transitions. We evaluate the quality of the optical pumping from transmission spectra after the dipole trap turn-off for σ^+- and σ^--polarized probe light, which respectively correspond to the strongest and weakest Clebsch-Gordan coefficients between $F = 2$ and $F' = 3$ magnetic sublevels. The low OD for the σ^--polarized probe make its transmission spectrum particularly sensitive to the quality of the optical pumping. We achieve a pumping purity of 90% of the atoms in the $F = 2, m_F = 2$ state, as measured from absorption spectra, for a pumping duration of 11 ms, a total optical power of 70μW and a red detuning of the $F = 2 \rightarrow F' = 2$ of 25 MHz. The red-detuning increase the scattering rate for low m_F states in the presence of the magnetic field and the value of the optimal detuning is linked to the beam intensity. For a modulated trap, the scattering of the trapping light tends to equally redistribute the atoms between the different mF states for a linearly polarized trap [79], although this effect is negligible at the few ms timescale of the experiment, given the dipole trap scattering rate on the order of a Hz. After optical pumping, we routinely obtain $OD \sim 50$ in an expanding cloud (averaged over 100 μs) and $OD \sim 25$ in a modulated dipole trap (averaged over 4 ms).

Chapter 7

Quantum Nonlinear Optics enabled by Ryberg EIT

7.1 Concept and setup summary

In this Chapter, we report on the realization of an optical medium nonlinear at the level of individual quanta of light. The medium strongly absorbs photon pairs while remaining transparent to single photons. The quantum nonlinearity is obtained using Rydberg electromagnetically induced transparency (EIT)[63]: slowly propagating photons[185, 186, 55] are coherently coupled to strongly interacting atomic Rydberg states[150, 151, 187, 153, 188, 149, 148] in a cold, dense atomic gas. The experimental demonstration of an extraordinary optical material exhibiting strong two-photon attenuation in combination with single-photon transmission is the central result of this work. In contrast to successful approaches based on high-finesse optical cavities to enhance the atom-photon interaction probability[42, 41, 65, 47, 44, 189], our present method is cavity-free and is based on mapping photons onto atomic states with strong interactions[62, 190, 61, 63].

The central idea is illustrated in Fig. 7-1, where a quantum probe field incident onto a cold atomic gas is coupled to high-lying Rydberg levels (see Chapter 5) by means of a second, stronger laser field (control field). For a single incident probe photon, the control field induces a transparency window in the otherwise opaque medium via EIT, and the probe photon travels at much reduced speed in the form of a coupled excitation of light and matter (Rydberg polariton). However, in stark contrast to conventional EIT[55], if

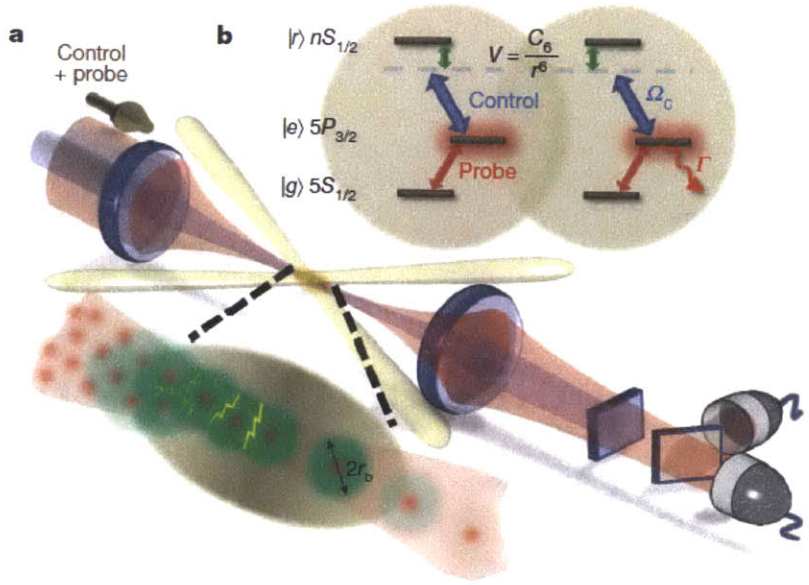

Figure 7-1: **Interaction between slow photons mediated by Rydberg blockade. a, b,** An elongated ensemble of laser-cooled rubidium atoms is prepared in a crossed optical-dipole trap. Co-propagating control and probe fields couple the ground-state $|g\rangle$ to a high-lying Rydberg state $|r\rangle$ via a short-lived excited state $|e\rangle$. Under EIT conditions, the probe photons slowly propagate in the medium as Rydberg polaritons. The Rydberg-Rydberg atom interaction $V(r) = C_6/r^6$ shifts the Rydberg levels out of resonance and blocks simultaneous Rydberg excitation if the interaction exceeds half the EIT-associated linewidth $\gamma_{\mathrm{EIT}}/2$. As a result, two Rydberg polaritons cannot both propagate when they are closer than the blockade radius $r_b = (2C_6/\gamma_{\mathrm{EIT}})^{1/6}$, set by $V(r_b) = \gamma_{\mathrm{EIT}}/2$.

two probe photons are incident onto the Rydberg EIT medium, the strong interaction between two Rydberg atoms tunes the EIT transition out of resonance, thereby destroying the EIT and leading to absorption[191, 192, 190, 62, 61]. The quantum nonlinearity can be viewed as a photon-photon blockade mechanism that prevents the transmission of any multi-photon state. It arises from the Rydberg excitation blockade[146], which precludes the simultaneous excitation of two Rydberg atoms that are separated by less than a blockade radius r_b (see Fig. 7-1). During the optical excitation, an incident single photon is converted, under the EIT conditions, into a Rydberg polariton inside the medium. However, due to the Rydberg blockade, a second polariton cannot travel within a blockade radius from the first one, and EIT is destroyed. Accordingly if the second photon approaches the single Rydberg polariton, it will be significantly attenuated, provided

that r_b exceeds the resonant attenuation length of the medium in the absence of EIT, $l_a = (\mathcal{N}\sigma_0)^{-1}$, where $\mathcal{N}$ is the peak atomic density and σ_0 the absorption cross-section. This simple physical picture implies that, in the regime where the blockade radius exceeds the absorption length, $r_b \gtrsim l_a$, two photons in a tightly focused beam not only cannot pass through each other[62], and as we show in a detailed theoretical analysis below, cannot co-propagate simultaneously inside the medium. Using Rydberg states with principal quantum numbers $46 \leq n \leq 100$, we can realize blockade radii r_b between 3 μm and 13 μm, while for our highest atomic densities of $\mathcal{N} = 2 \times 10^{12}$ cm^{-3}, the attenuation length l_a is below 2μm. The optical medium then acts as a quantum nonlinear absorption filter, converting incident laser light into non-classical light composed of single-photon pulses. Giant optical nonlinearities using Rydberg EIT[190, 62, 61] have been observed in a classical, multi-photon regime[63]. Very recently, the Rydberg blockade in a dense, mesoscopic atomic ensemble has been used to implement a deterministic single-photon source[155].

To observe the photon-photon blockade, several key requirements must be fulfilled. First, to eliminate Doppler broadening, the atoms should be cold so that they move by less than an optical wavelength on the microsecond time scale of the experiment. Second, the atomic cloud should be sufficiently dense such that the blockade condition $r_b \gtrsim l_a$ is fulfilled. Finally, the system should be one-dimensional, *i.e.* the transverse size of the probe beam should be smaller than the blockade radius in order to prevent polaritons from traveling side by side. We fulfill these conditions by trapping a laser-cooled atomic ensemble and focusing the probe beam to a Gaussian waist $w_0 = 4.5\mu\text{m} < r_b$.

The experimental setup is detailed in Chapter 6. To summarize, we prepare a laser-cooled ^{87}Rb ensemble containing up to $N = 10^5$ atoms in a far-detuned optical dipole trap, formed by two orthogonally polarized beams with waists $w_t = 50\mu$m intersecting at an angle of 32°. The atoms are optically pumped into the state $|g\rangle = |5S_{1/2}, F = 2, m_F = 2\rangle$ in the presence of a 3.6 G magnetic field along the quantization axis defined by the propagation direction of the probe and control beams along the long axis of the cloud. The probe beam on the $|g\rangle \rightarrow |e\rangle = |5P_{3/2}, F = 3, m_F = 3\rangle$ transition and the control beam on the $|e\rangle \rightarrow |r\rangle = |nS_{1/2}, J = \frac{1}{2}, m_J = \frac{1}{2}\rangle$ transition with waist $w_c = 12.5\mu$m are oppositely circularly polarized. To avoid inhomogeneous light-shift broadening of the

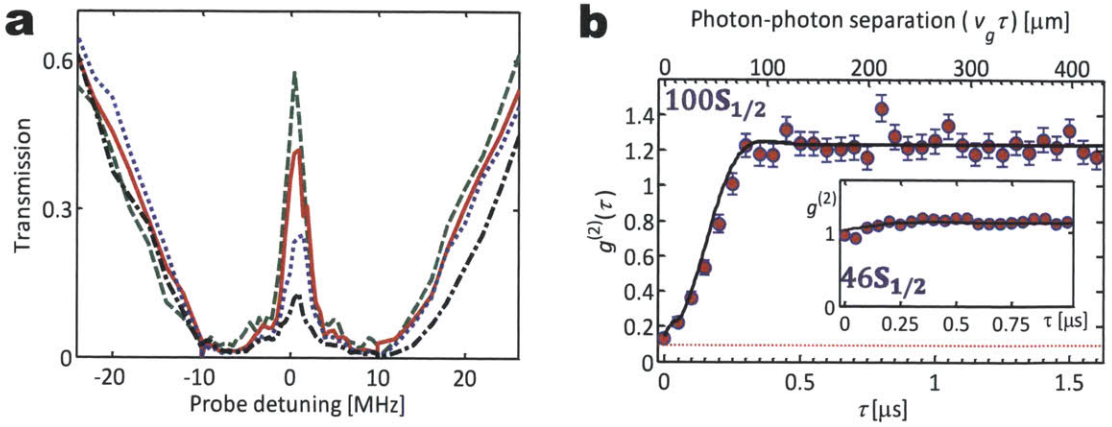

Figure 7-2: **Rydberg EIT nonlinearities. a,** Transmission spectra versus probe detuning at various incoming photon rates: $R_i = 1\mu s^{-1}, 2\mu s^{-1}, 4\mu s^{-1}, 6\mu s^{-1}$ (dashed green, solid red, dotted blue, and dot-dashed black, respectively) for $|100S_{1/2}\rangle$, optical depth $OD = 40$, and pulse delay time $\tau_d = 340$ ns. The system is nonlinear at a power as low as 0.25 pW. **b,** Photon-photon correlation function $g^{(2)}(\tau)$ at EIT resonance for the same parameters as in **a** with $R_i = 1.2\mu s^{-1}$. The top axis shows the separation $v_g\tau$ of polaritons with $v_g \approx 200$ m/s. The error bars indicate 1σ statistical uncertainty. Spurious detection events set a lower bound on $g^{(2)}$ of 0.09(3) (red dotted line). Inset shows $g^{(2)}(\tau)$ for the state $|46S_{1/2}\rangle$ with similar parameters. The solid lines are theoretical calculations as described in the text, with the probe waist fixed at $w_0 = 6$ μm. Values $g^{(2)} > 1$ are attributed to classical fluctuations (see Fig. 7-3 and Appendix C).

two-photon transition, we turn off the optical dipole trap before implementing the EIT scheme. The resonant optical depth of the cloud can be as large as $OD = 50$, with initial radial and axial rms cloud dimensions of $\sigma_\perp = 10$ μm and $\sigma_z = 36$ μm, respectively. The control light is filtered out from the transmitted light, and the photon-photon correlation function $g^{(2)}(\tau)$ of the probe beam can be measured by means of two photon counters.

7.2 Results

Probe transmission spectra are presented in Fig. 7-2a for large optical depth $OD = 40$ and the control laser tuned to the Rydberg state $|100S_{1/2}\rangle$. At very low incident photon rate $R_i \leq 1\mu s^{-1}$, the spectrum displays an EIT window with 60% transmission.

The extraordinary nonlinearity of the Rydberg EIT medium[63] becomes apparent as the incident photon rate is increased: the probe beam is strongly attenuated already at a photon flux of $R_i \sim 4\mu s^{-1}$. To demonstrate that we are operating in a quantum nonlinear regime, we show in Fig. 7-2b the correlation function $g^{(2)}(\tau)$ of the transmitted probe light, measured at $R_i = 1.2\ \mu s^{-1}$. For the most strongly interacting state $|100S_{1/2}\rangle$ with $r_b = 13\mu m \approx 5l_a \approx 2.9w_0$ we observe strong antibunching with $g^{(2)}(0) = 0.13(2)$, largely limited by background light. Spurious detection events (dark counts from the detector, imperfect polarization of probe light, residual control light) typically limit $g_2(\tau) \geq 0.1$. Subtraction of the independently measured background coincidence counts yields a corrected $g_c^{(2)}(0) = 0.04(2)$. These observations are in stark contrast to EIT transmission via a weakly interacting Rydberg state $|46S_{1/2}\rangle$ with $r_b = 3\ \mu m$, where the photon statistics of the transmitted light are similar to those of the incident coherent state (see inset). Interestingly, for $|100S_{1/2}\rangle$ the photons are anti-bunched over a length scale that exceeds the blockade radius (see top axis of Fig. 7-2b), indicating the influence of additional propagation effects beyond the simple picture outlined above.

At large atomic densities, the $g^{(2)}$ functions exhibit both a local super-Poissonian feature on a range of $\sim$20 μs and a global positive offset of 0.08 from the expected value 1 at large times (see Fig. 7-3 and Fig. 7-2). We attribute the local feature to the occasional population of metastable Rydberg levels not resonantly coupled by the control field to a fast decaying state. This process is relatively rare at the photon flux used in the $g^{(2)}$ measurements ($R_i < 2\ \mu s^{-1}$); however when it does occur, the medium becomes absorptive until the Rydberg atom has moved a distance larger than the blockade radius away from the probe beam area, or has decayed to a low-lying state. At high incoming probe rate ($R_i \geq 5\ \mu s^{-1}$), it results in a strong attenuation of the transmission over the course of the experiment (Fig. 7-3 inset). As the probe power increases, the attenuation happens on a shorter timescale and settles to a lower transmission rate. For R_i=100 μs^{-1}, the cloud becomes totally opaque in $\sim$ 1 μs. If the control field is turned off for a moment, the transmission progressively returns to its initial value in 20 μs. The decay shows no dependence on static electric fields up to 10 V/cm^{-1}, ruling out the presence of ions in the cloud. Black-body radiation is a possible source of excitation for atoms from the Rydberg state $|r\rangle$ to neighboring levels. For measurements at large rate, we restrict ourselves to

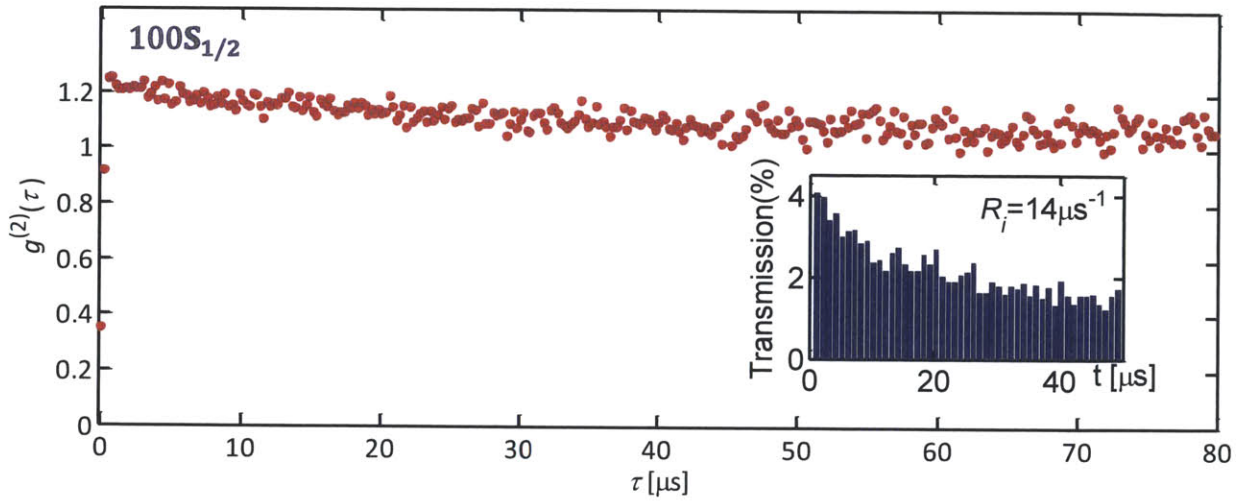

Figure 7-3: **Super-Poissonian features of the intensity correlation function.** Intensity correlation function $g^{(2)}(\tau)$ up to τ=80 μs for $|r\rangle$=100$S_{1/2}$. Outside the antibunching window, the light is super-Poissonian. We attribute this to the excitation of Rydberg atoms in the medium and, for very large τ, experimental drifts (see text). **Inset:** Transmission at high incoming probe photon rate (R_i = 14 μs^{-1}). It exhibits a decay of the transparency over the measurement time (not noticeable at low photon rate $R_i <$ 2 μs^{-1}), which is potentially a signature of the permanent blockade of the medium by a small Rydberg population.

the initial part of the signal shown in Fig. 7-3 inset. The global $g^{(2)}(\infty)$=1.08 feature is attributed to slow drifts and classical fluctuations in our system. These include *OD* fluctuations, frequency drifts of the spectroscopic reference for the transfer cavity lock and alterations of the alignment, resulting in slow variations of the observed transmission on the order of 20%.

In principle, we can compensate for the offset by modeling both mechanisms – the temporary local Rydberg blockades and the slow drift – as inhomogeneous fluctuations, and assume in general that, with probability p_i, the linear transmission of the medium changes to T_i. For an incoming photon rate R_i, the mean count rate at the output is $R_o = \sum_i p_i T_i R_i$. Under the assumption that the change in the transmission does not affect the dynamics of the photon-photon interaction, provided that both photons are eventually transmitted, the coincident count rate for photons separated by a small time

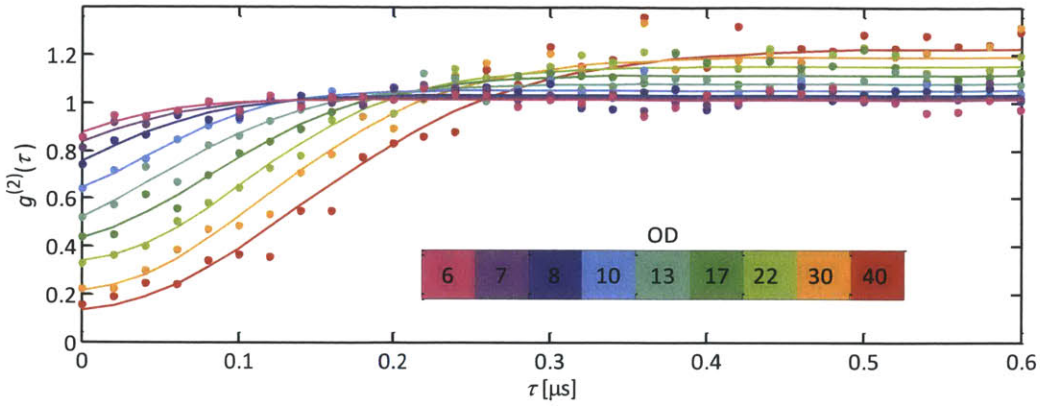

Figure 7-4: **Evolution of the correlation function with OD.** Measured $g^{(2)}(\tau)$ (colored dots) for $|r\rangle$=100$S_{1/2}$ and $\gamma_{\mathrm{EIT}} = 22$ MHz for different *OD*. The colored curves are visual guidelines. At low *OD*, the offset (attributed to the spontaneous population of neighboring Rydberg states and the depth are reduced because the increase in attenuation length weakens the blockade mechanism.

interval τ is $R_c = \sum_i p_i T_i^2 R_o^2 g^2(\tau)$ where $g^2(\tau)$ is the expected correlation function. The measured correlation function $R_c(\tau)/R_o^2$ is thus equal to the expected correlation function multiplied by a factor $\sum_i p_i T_i^2/(\sum_i p_i T_i)^2 > 1$, which correspond to the value of the offset at large τ (this normalization of the correlation function by its offset value is used in Chapter 8).

7.3 Scaling with OD

Two important features of the photon-photon blockade are the degree of two-photon suppression at equal times, $g^{(2)}(0)$, and the associated correlation time, *i.e.*, the half-width τ_c of the antibunching feature in $g^{(2)}(\tau)$. We study their dependance on the atomic density interaction dynamics for different optical depth using the following procedure: as the dipole trap is turned off, the mainly radial expansion of the elongated cloud continuously reduces the atomic density, allowing measurements of $g^{(2)}(\tau)$ at different *OD* (see Figure 7-4). Each curve is averaged over a 100 μs period in the cloud expansion, and we independently measure the average *OD* over this period. The attenuation length ranges from

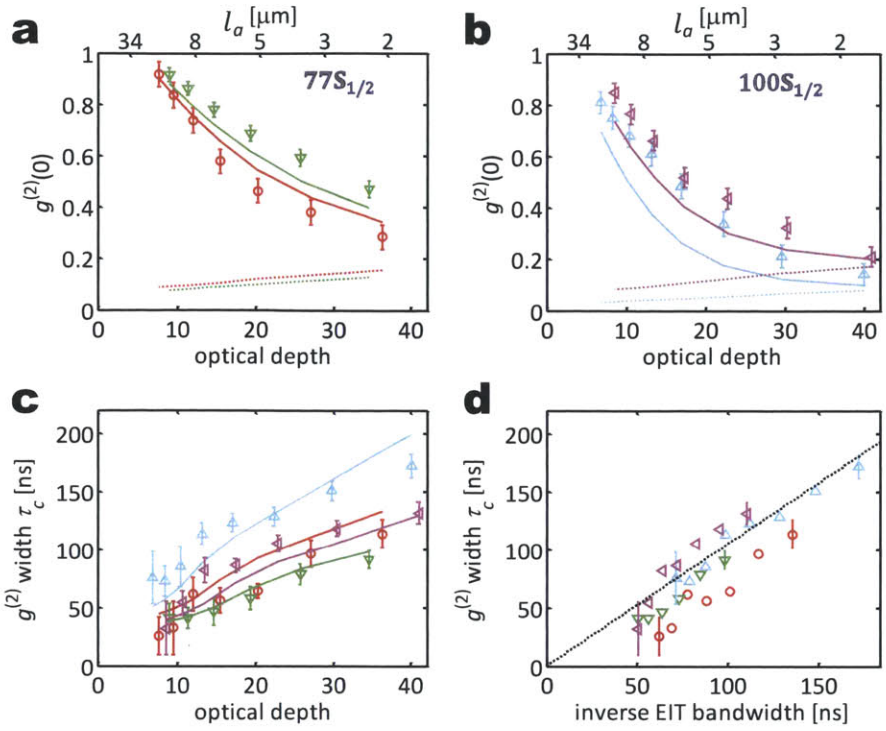

Figure 7-5: **Dependence of the correlation function on EIT parameters. a, b,** Equal-time photon-photon correlation $g^{(2)}(0)$ as a function of OD for $|77S_{1/2}\rangle$ (**a**) and $|100S_{1/2}\rangle$ (**b**), for a set of EIT widths $(\gamma_{EIT}^{\square}, \gamma_{EIT}^{\bigcirc}, \gamma_{EIT}^{\triangleleft}, \gamma_{EIT}^{\triangle}) = (20, 27, 16, 26)$ MHz. Solid lines are numerical solutions for a probe beam waist $w_0 = 6\mu$m including detection noise (dotted lines). **c, d,** Width τ_c of the anti-bunching feature in $g^{(2)}(\tau)$ as a function of optical depth (**c**) and EIT bandwidth (**d**) $B = \gamma_{EIT}/\sqrt{8OD}$, respectively. The black dashed line is $1.05/B$ and derives from an analytical solution of Equation (7.1) (see Appendix C). The error bars indicate 1σ statistical uncertainty.

2.3 μm (for $OD = 40$) to 19 μm (for $OD = 6$). The evolution of the correlation function with the atomic density is visualized in Fig. 7-4. The solid curves in the figure are fits to the experimental data, with the fit parameters being the depth at $\tau = 0$, the width of the anti-bunching feature, the constant offset value at large τ, and the slope (or "sharpness") at $\tau = 0$.

The summarized equal-time photon-photon correlation function $g^{(2)}(0)$ and the width τ_c of the anti-bunching feature are plotted in Fig. 7-5. The blockade mechanism is most effective if the optical depth per blockade radius $OD_b = r_b/l_a$ exceeds unity[62], and if the system is effectively one-dimensional, $r_b > w_0$. Since the blockade radius[146] increases

with the principal quantum number n as $r_b \propto n^{11/6}$, the combination of both effects results in a steep dependence of $g^{(2)}(0)$ upon n. A lower limit on the correlation time τ_c is set by the photon travel time r_b/v_g (~ 50 ns for $OD \sim 40$) through one blockade radius at the group velocity v_g ; an upper limit is set by the Rydberg decoherence rate, which for our system is dominated by Doppler broadening and laser linewidths, and amounts to $\gamma^{-1} = 500$ ns.

Figures 7-5a,b show that $g^{(2)}(0)$ improves with principal quantum number n of the Rydberg state and interaction strength r_b/l_a, resulting in a more than tenfold suppression of the two-photon transmission, limited by independently measured background light on the photon detector (dotted lines). At the same time, the observed width τ_c of the $g^{(2)}$ feature considerably exceeds the photon travel time r_b/v_g through the blockade radius (Figure 7-5c, d). Close examination (Fig. 7-5d) reveals that the correlation time is of the same order and scales proportionally with the inverse bandwidth of the EIT transparency window $B \propto \gamma_{\mathrm{EIT}}/\sqrt{OD}$, where $\gamma_{EIT} = \Omega_c^2/\Gamma$, Ω_c is the Rabi frequency of the control field and Γ is the decay rate constant of the state $|e\rangle$. This observation suggests that propagation effects play an important role in establishing the $g^{(2)}$ correlation time τ_c in a medium of large optical depth. Remarkably, we observe that, under appropriate conditions, two photon-events are suppressed inside the medium on a length scale that approaches the size $\sigma_z \sim 40$ μm of the entire atomic ensemble, and on a time scale that approaches the intrinsic coherence time γ^{-1}.

For direct comparisons with our experiments, we numerically solve the full set of propagation equations accounting for the Gaussian density profile of the trapped atomic cloud, the finite waist of the probe beam, and the linear photon absorption due to finite decoherence γ of the two-photon transition (see Appendix C). As shown in Figures 7-2 and 7-5, the theory captures the essential features of our measured correlation functions and, moreover, reproduces their dependence on the Rydberg states, control laser intensities and optical depths of the sample over a wide range of parameters.

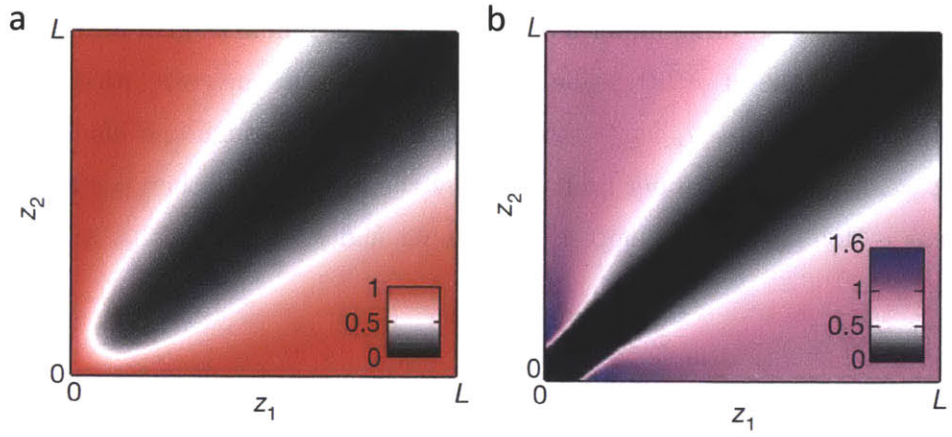

Figure 7-6: **Diffusion of the photon blockade. a, b,** Numerical simulations showing the spatial evolution of the probability distribution associated with two photons (**a**) and two Rydberg excitations (**b**) at positions (z_1,z_2) inside the medium, normalized by their values in the absence of blockade. Two Rydberg excitations are excluded from the blockaded range, resulting in the formation of an anti-bunching feature in the light field whose width increases during the propagation due to the finite EIT transmission bandwidth.

7.4 Two-photon interactions

To gain insights into these observations, we theoretically analyze the photon propagation dynamics in the weak-probe limit where the average number of photons inside the medium is much less than one. In this case, it suffices to consider two polaritons (Fig. 7-1b). The corresponding field component can be described[62] by the two-photon wavefunction $|\psi_2(t)\rangle = \frac{1}{2}\int d\mathbf{r}_1 d\mathbf{r}_2 EE(\mathbf{r}_1,\mathbf{r}_2,t)\hat{\mathcal{E}}^\dagger(\mathbf{r}_1)\hat{\mathcal{E}}^\dagger(\mathbf{r}_2)|0\rangle$, where $\hat{\mathcal{E}}(\mathbf{r})$ denotes the photon field operator and $|EE(\mathbf{r}_1,\mathbf{r}_2,t)|^2$ is the probability of finding two photons at locations $\mathbf{r}_1,\mathbf{r}_2$. This probability directly yields the spatially dependent photon-photon correlation function, and, via the group velocity v_g, the corresponding temporal correlation function $g^{(2)}(\tau)$. An intuitive picture emerges if we make the simplifications of a tightly focused probe beam (1D approximation) traveling through a homogeneous medium with perfect linear EIT transmission. In this case, the steady-state two-photon wavefunction in the medium obeys (see Appendix C):

$$\partial_R EE(z_1,z_2) = -\frac{\mathcal{V}(r)}{l_a} EE(z_1,z_2) + 4l_a\left[1+\mathcal{V}(r)\frac{\Omega^2}{\Gamma^2}\right]\partial_r^2 EE(z_1,z_2), \qquad (7.1)$$

where $R = (z_1 + z_2)/2, r = z_1 - z_2$ are the center-of-mass and relative coordinates of the two photons, respectively. The function $\mathcal{V}(r) = r_b^6/(r_b^6 - 2ir^6)$ can be regarded as an effective potential that describes the impact of Rydberg-Rydberg interactions[62]. For large photon-photon distances, $r \gg r_b$, the potential $\mathcal{V}$ vanishes, and equation (7.1) yields perfect transmission under EIT, while for distances $r \lesssim r_b$, the interaction $\mathcal{V}$ modifies the two-photon propagation. According to equation (7.1), photon correlations emerge from a combination of two processes as visualized in Fig. 7-6: The first term acts inside the blockade radius r_b and describes absorption with a coefficient l_a^{-1} as the interaction $\mathcal{V}$ tunes EIT out of resonance. This would create a sharp dip in the two-photon correlation function with a corresponding correlation time $\tau_b = r_b/v_g$. However, if the corresponding spectral width $\sim \tau_b^{-1}$ is too large, the second diffusion-like term acts to broaden the absorption dip (Fig. 7-6,a) to a width determined by the EIT bandwidth $\sim (\gamma_{\mathrm{EIT}}/\sqrt{OD})$, in agreement with experimental results (Fig. 7-6,b). To maintain strong two-photon suppression in the presence of diffusion, the loss term must exceed the diffusion on the length scale of the blockade radius, requiring $r_b > l_a$. Large optical depth $OD_b = r_b/l_a$ of the blockaded region is therefore the key experimental feature that allows us to extend earlier studies[63] into the quantum nonlinear regime.

7.5 Many-photon dynamics

To investigate the transmission characteristics of multiple photons through the medium, we plot in Fig. 7-7a the output photon rate R_o, scaled by the transmission measured at low probe power, as a function of incident photon rate R_i. At first, R_o increases linearly with R_i as expected, but then saturates abruptly to a constant value of $R_o = 1.3(3)\mu\mathrm{s}^{-1}$. Note that these observations deviate from the simplistic model of a multiphoton absorber that transmits only the one-photon component from the incoming coherent state (black dashed line). At the same time, the observed output flux corresponds to less than one photon per group delay $\tau_g = 300$ ns in the medium. Figure 7-7b shows the saturated output rate versus the ratio r_b/w_0 of blockade radius and probe beam waist for a wide range of principal quantum numbers, control field intensities, and optical depths. The approximate $R_o \propto (w_0/r_b)^2$ scaling indicates that the saturated rate for intermediate to

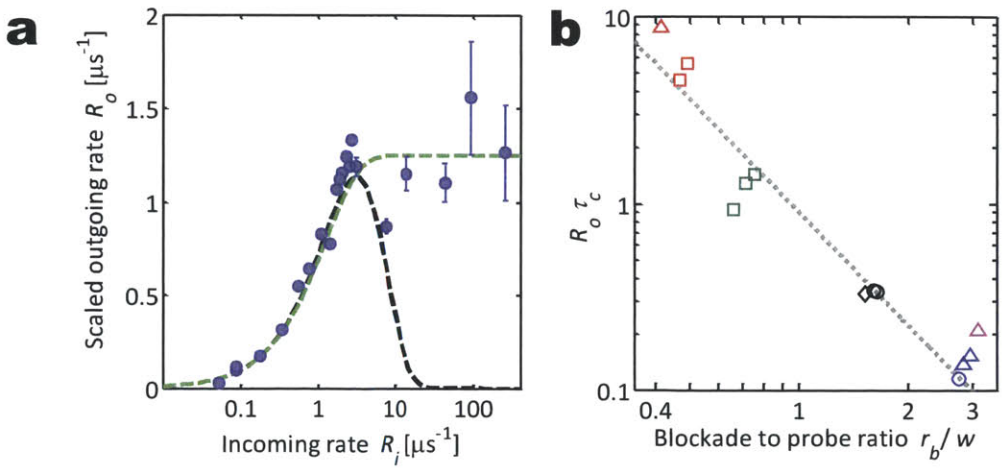

Figure 7-7: **Saturation behavior of the transmission. a,** Outgoing versus incoming photon rate for $|100S_{1/2}\rangle$, $\gamma_{EIT} = 2\pi \times 15$ MHz, $OD = 26$. All output rates are scaled by the transmission of 50% at low photon rate due to linear absorption. The dashed black curve outlines the expected rate if all multi-photon events within the anti-bunching time (τ_c=160 ns) are fully blocked, while the green dashed curve assumes that all multiphoton states are converted into an outgoing one-photon state, assuming $\tau_c = 800$ ns. **b,** Saturated rate of outgoing photons $R_o\tau_c$ per anti-bunching correlation time τ_c, scaled by the linear absorption, as a function of the ratio between the blockade radius r_b and the probe beam waist w_0. The Rydberg states are $|100S_{1/2}\rangle$ (blue, $w_0 = 4.5\mu$m, $OD_b \sim 8$; pink, $w_0 = 4.5\mu$m, $OD_b \sim 4$), $|77S_{1/2}\rangle$ (black, $w_0 = 4.5\mu$m, $OD_b \sim 3$), $|46S_{1/2}\rangle$ (green,$w_0 = 4.5\mu$m, $OD_b \sim 0.7$; red, $w_0 = 7\mu$m, $OD_b \sim 0.7$). The ranges for the EIT widths are: $(\gamma_{EIT}^{\square}, \gamma_{EIT}^{\triangle}, \gamma_{EIT}^{\circ}, \gamma_{EIT}^{\diamond}) = 2\pi\times$ (6-16,18-26,29-36,50) MHz. In the data plotted, the estimated τ_c varies from 60 to 330 ns. The dashed line corresponds to $0.9(r_b/w_0)^2$, indicating the expected scaling with transverse confinement.

strong interactions, $r_b \gtrsim l_a$, is largely determined by the transverse geometrical constraint, *i.e.* by the extent to which the Rydberg polaritons can propagate side by side. A more detailed analysis of the outgoing light in the presence of many-body interactions on the outcoming light has recently been carried out in [159].

7.6 Outlook

Our observations open intriguing prospects for ultimate quantum control of light quanta. At the same time, by using strong interactions in the dispersive regime, explored in

Chapter 8, the present approach can be used to implement deterministic quantum logic gates[190, 62], which would constitute a major advance towards all-optical quantum information processing[193]. Finally, our results may open the door for exploring quantum dynamics of strongly interacting photonic many-body systems. For example, it may be possible to create a crystalline state of strongly interacting polaritons[29].

Chapter 8

Attractive Photons in a Quantum Nonlinear Medium

8.1 Rydberg EIT in the dispersive regime

In Chapter 7, we demonstrated that Rydberg Electromagnetically Induced Transparency (EIT) in dense atomic cloud leads to strong dissipative interactions at the single photon level. In this chapter, we report on related experiments in the dispersive regime, where the photons coherently interact by imprinting on each other a mutual phase-shift. The passage from the dispersive to dissipative regime is obtained by introducing an intermediate detuning Δ of the control field from the short-lived intermediate state of the EIT level scheme. By operating away from the intermediate atomic resonance, the atomic absorption is low and only weakly nonlinear, as the transmission difference between the EIT in the 3-level atoms ensembles differs little from that of the same medium in the absence of control field, which corresponds to the idealized limit of the Rydberg blockade. In contrast, the index of refraction of the medium is largely modified by the presence on the control field. On two-photon resonance, the presence of the control field decouples the probe field from the atoms, which are rotated into a dark state. As a consequence, the probe experiences an index of refraction of unity and no phase-shift compared to a beam propagating in vacuum (see Appendix A). Similarly to the resonant case, the large change in index of refraction is still responsible for a large reduced group velocity. In the absence of control field, an off-resonant phase-shift $\phi \sim OD\Gamma/(4\Delta)$ is imprinted on the phase of

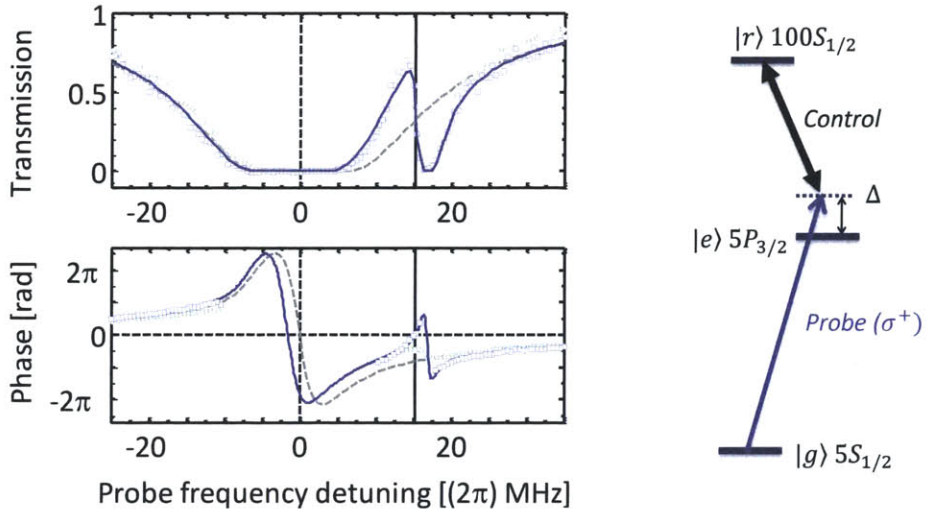

Figure 8-1: **Rydberg EIT in the dispersive regime.** A weak laser beam near the transition $|g\rangle \rightarrow |e\rangle$ at 780 nm is sent into a cold rubidium gas driven by a control laser near the transition $|e\rangle \rightarrow |r\rangle$ at 479 nm. Transmission spectra (top) and phase shift (bottom) for the probe photons with incoming rate of $R_i = 0.5\ \mu s^{-1}$ (blue squares) and $R_i = 5\ \mu s^{-1}$ (green circles), for a control field red-detuned by $\Delta = 15$ MHz (blue line is theory). The spectrum at high probe rate approaches that of the undriven two-level system, which is the idealized limit of a blockaded cloud (dashed gray). The solid vertical line corresponds to the EIT resonance.

the probe field by the atomic medium (where Γ is the lifetime of the intermediate state). In contrast to the dissipative interactions described in the previous chapter and several theoretical and experimental studies [63, 161, 155, 157], the Rydberg blockade primarily impacts the real part of the linear susceptibility of the medium [64, 62] and establishes coherent interactions between probe photons.

More quantitatively, the repulsive Van-der-Waals interaction between two Rydberg atoms $V(r) = \hbar C_6/r^6$ tunes the doubly excited Rydberg state far off EIT resonance for distances $|r| < r_B$, where $r_B = \sqrt[6]{C_6/\gamma_{EIT}}$ is the Rydberg blockade radius[62, 61, 152], C_6 the van der Waals coefficient, $\gamma_{EIT} = \Omega_c^2/|4\Delta|$ is the EIT linewidth at detuning $|\Delta| \gg \Gamma$, and Ω_c the Rabi frequency of the control field. While for photons with large separation in the medium $|r| > r_B$, the phase shift originating from the $|g\rangle \rightarrow |e\rangle$ probe transition is suppressed by EIT, for small photon separations $|r| \leq r_B$, the light experiences a phase shift originating from the index of refraction associated with the bare two-level

probe transition (see Fig. 8-1). This explicit dependence of the refractive index upon photon-photon separation can be modeled in one dimension as a potential well with a characteristic width of $2r_B$. Qualitatively, a substantial two-photon phase shift arises for $\frac{r_B}{l_a}\frac{\Gamma}{|\Delta|} \gtrsim 1$, where l_a is the resonant attenuation length in the medium, *i.e.* for sufficiently high atomic density. Furthermore, the probe field must also be transversally compressed to a waist size $w_0 < r_B$ to ensure interactions. For our parameters using the Rydberg state $100S_{1/2}$ and $\Omega_c = 10$ MHz, we have $r_B \cong 18\,\mu$m at detunings of a few Γ, $l_a = 4\,\mu$m at the peak density, and $w_0 = 4.5\,\mu$m, fulfilling the conditions for strong interactions for $|\Delta| \lesssim 5\Gamma$.

Our experiment makes use of an ultracold rubidium gas loaded into a dipole trap, as described previously in Chapter 6. The dipole trap is periodically switched off with a 5.5 μs half-period, and the measurements are performed during the dark time to avoid inhomogeneous broadening. Photons detected in the first 1.5 μs after the turn-off of the dipole trap are not included in the analysis, to guarantee steady-state EIT. For each experimental cycle, data is accumulated over 400 periods of the dipole-trap modulation. The trapped atomic cloud has a longitudinal r.m.s. length of $\sigma_z = 36$ μm and a peak density of $\mathcal{N} = 10^{12}$ atoms cm^{-3}. The average resonant optical depth is 22, with less than 20% variation over the measurement time. The probe and control beams are counter-propagating in order to reduce the residual Doppler broadening to 50 kHz. Linearly polarized probe laser light enters the medium at an average photon rate of 1.6 μs^{-1}. Here, we are interested in the σ^+-polarized component of the probe light, coupling the ground state $|g\rangle$ $(5S_{1/2}, F = 2, m_F = 2)$ to the Rydberg state $|r\rangle$ $(100S_{1/2}, J = 1/2, m_J = 1/2)$ via the intermediate state $|e\rangle$ $(5P_{3/2}, F = 3, m_F = 3)$ of linewidth $\Gamma = 6.1$ MHz by means of a control field that is detuned by Δ below the resonance frequency of the upper transition $|e\rangle \rightarrow |r\rangle$. Figure 8-1 shows the transmission and phase-shift spectra of the σ^+-polarized probe field at different probe incoming rates and in the absence of control field, which corresponds to the idealized limit of a fully blockaded medium. For a very weak probe field with mean incident photon rate $R_i = 0.5$ μs^{-1}, the EIT is established when the probe detuning matches that of the control field. This corresponds to a phase-shift of 0 and a transmission of $\sim$0.5. Note that the peak transmission is shifted to smaller probe detuning with respect to the two-photon resonance, due to the finite decoherence rate

between $|e\rangle$ and $|r\rangle$. As we can observe, the Rydberg medium is extremely nonlinear: a probe photon rate of $R_i = 5\ \mu s^{-1}$ already modifies the medium due to the Rydberg blockade [146], yielding a probe spectrum close to the bare two-level response. In most of the work described below, we perform our experiments on two-photon resonance, where the transmission is independent of the probe photon rate, yielding a purely dispersive nonlinearity. The linear dispersion at this point corresponds to a reduced probe group velocity of typically $v_g = 400$ m/s.

8.2 Conditional phase-shift measurement

The phase of the σ^+-polarized probe field presented in Fig. 8-1 is measured by interference with photons which interact only weakly with the atomic medium. More precisely, we prepare input photons in a linearly polarized state $|V\rangle = (|\sigma^+\rangle + |\sigma^-\rangle)/\sqrt{2}$, where the σ^- component serves as a phase reference. The full level-structure is precisely described in Fig. 8-2. The atoms are initially pumped into the ground state $|g\rangle = |5S_{1/2}, F = 2, m_F = 2\rangle$ magnetic sublevel. The σ^+ and σ^- components of the incoming linearly polarized probe light respectively couple to the $|e\rangle = |5P_{3/2}, F = 3, m_F = 3\rangle$ and $|e'\rangle = |5P_{3/2}, F = 3, m_F = 1\rangle$ excited states. For our magnetic field, the Zeeman splitting between these levels is 6 MHz, comparable to their inverse lifetime $\Gamma = 6.1$ MHz. The coupling dipole matrix element for the σ^+ transition is larger than for the σ^- transition by a factor of $\sqrt{15}$. The σ^- polarized control field couples the stretched state $|e\rangle$ to the Rydberg state with maximal projections of the nucleus spin (m_I) and total electronic angular momentum (m_J), $|r\rangle = |100S_{1/2}, m_I = 3/2, m_J = 1/2\rangle$. In addition, it couples $|e'\rangle$ to $|r'\rangle = |100S_{1/2}, m_I = -1/2, m_J = 1/2\rangle$ and $|r''\rangle = |100S_{1/2}, m_I = 1/2, m_J = -1/2\rangle$ with a $\sqrt{5}$-times weaker resonant Rabi frequency. Because the magnetic dipole moment of the nuclear spin is negligible compared to that of the electron, the energies of the levels $|r\rangle$ and $|r'\rangle$ are equally shifted by the magnetic field. As a consequence, both σ^+ and σ^- photons propagate under Rydberg EIT conditions. Nevertheless, the combined effect of the Zeeman shift of the intermediate level and the reduced dipole coupling $|g\rangle \rightarrow |e'\rangle$ suppresses the probability for σ^- photons to create or be affected by Rydberg blockade. As the σ^- probe photons interact only negligibly between themselves and weakly with

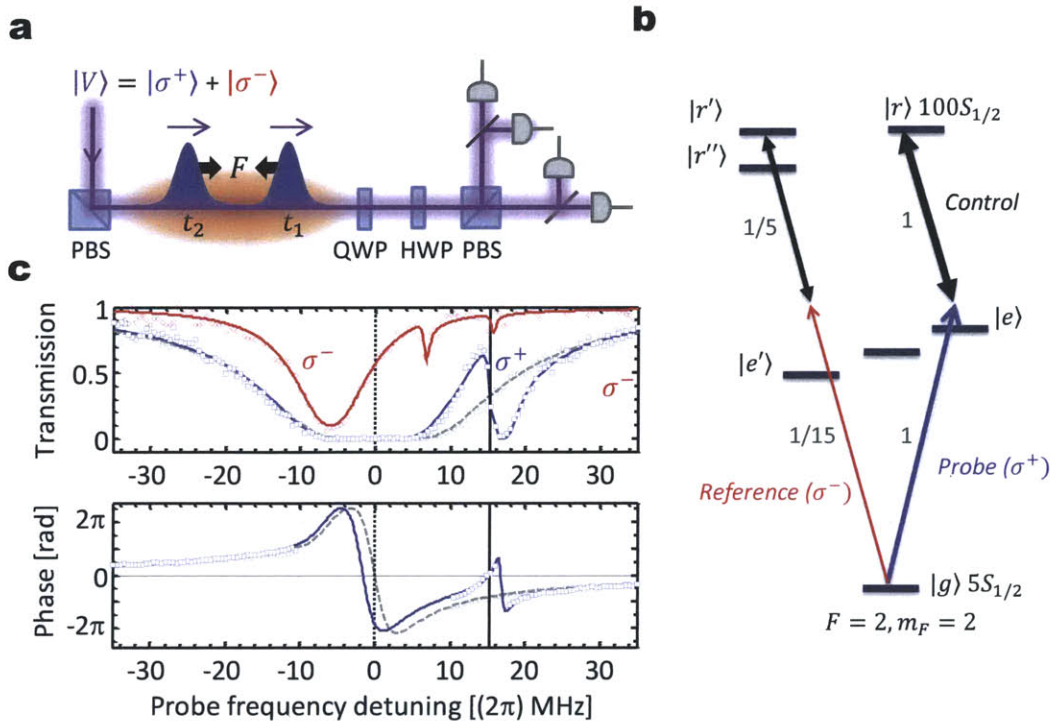

Figure 8-2: **Interferometric measurement of conditional phase-shifts.** **a,** A linearly polarized weak laser beam near the transition $|g\rangle \rightarrow |e\rangle$ at 780 nm is sent into a cold rubidium gas driven by a control laser near the transition $|e\rangle \rightarrow |r\rangle$ at 479 nm. Strong nonlinear interactions between σ^+-polarized photons are detected via photon-photon correlation functions of the transmitted light for a set of different polarization bases, as determined by a quarter-waveplate (QWP), a half-waveplate (HWP), and a polarizing beam-splitter (PBS). Here σ^- photons serve as a phase reference. **b,** Schematic representation of the atomic transitions. The levels are $|e\rangle = (5P_{3/2}, F = 3, m_F = 3)$, $|e'\rangle = |5P_{3/2}, F = 3, m_F = 1\rangle$, $|r\rangle = |100S_{1/2}, m_I = 3/2, m_J = 1/2\rangle$, $|r'\rangle = |100S_{1/2}, m_I = -1/2, m_J = 1/2\rangle$, $|r''\rangle = |100S_{1/2}, m_I = 1/2, m_J = -1/2\rangle$. **c,** Transmission (top) of the σ^+ polarization in the absence of control field ($\circ$, gray dashed line) and of the σ^+ ($\square$, blue line) and σ^- ($\diamond$, red line) with a control field red-detuned by $\Delta = 14$ MHz. The phase shift between the two circular polarizations (bottom) exhibits a difference of $\sim \pi \approx OD\Gamma/(4\Delta)$ at EIT resonance (solid vertical line).

σ^+ photons, they provide a reliable reference for measuring phase shifts of the σ^+ photons. Phase-shift and absorption of the σ^+ component result in polarization rotation and ellipticity of the probe field at the output of the medium. The outgoing polarization can be measured by Stokes analysis. For that purpose, a quarter waveplate, a half waveplate and a polarizing beamsplitter are inserted between the output of the vacuum chamber

and the single-photon detectors (see Fig. 8-2). By measuring the light in each arm of the polarizing beam splitter in three definite basis, we reconstruct the differential phase-shift between the σ_+ and σ_- components.

In addition to the angle and the ellipticity, the Stoke analysis yields the degree of polarization of the light. Interestingly, we observe that this degree is 1 for the entire spectra apart from a narrow window centered on two-photon resonance and of width ~ 1 MHz, for which the degree of polarization decreases to 0.5. We attribute the cause of this observation to the group velocity difference between the σ^+- and σ^--polarized photons. When the group delay difference (measured to be 300 ns) is not negligible compared to the the laser coherence time, the interference between the σ^+- and σ^--polarized photons is reduced and the polarization fluctuates randomly. Our laser linewidth is on the order of 200 kHz.

For a dense enough medium, the Rydberg blockade in the dispersive regime induces large conditional phase-shifts [46]. The mutual phase-shift between two interacting photons strongly modifies the propagation properties of photon pairs with respect to that of single photons. In order to explore these quantum dynamics, we perform a conditional polarization measurement dependent on the time interval between detection events. It consists in measuring the two-photon correlation functions $g^{(2)}_{\alpha\beta}$ of the transmitted light in different basis α, β. To clarify our approach, we first assume that the system is free of decoherence. In that case, the outgoing one-photon state, detected at time t, is a pure state:

$$|1\rangle_t = \left(\eta_+|\sigma^+\rangle_t + \eta_-|\sigma^-\rangle_t\right)/\sqrt{2}. \tag{8.1}$$

Here, η_+ and η_- characterize the linear susceptibility of the medium, accounting for absorption and phase shift leading to polarization rotation. For two photons arriving at times t_1 and t_2 on two single-photon detectors, the corresponding (unnormalized) outgoing state is:

$$\begin{aligned} |1,1\rangle_{t_1,t_2} \;=\; & \frac{1}{2}[\eta_+^2\,\psi(t_1,t_2)|\sigma^+\sigma^+\rangle_{t_1,t_2} + \eta_+\eta_-\,\chi(t_1,t_2)\left(|\sigma^+\sigma^-\rangle_{t_1,t_2} + |\sigma^-\sigma^+\rangle_{t_1,t_2}\right) \\ & +\eta_-^2\,\mu(t_1,t_2)|\sigma^-\sigma^-\rangle_{t_1,t_2}]. \end{aligned} \tag{8.2}$$

The photon-photon interactions are described by $\psi(t_1,t_2)$, $\chi(t_1,t_2)$, and $\mu(t_1,t_2)$, which

are chosen to be unity in the absence of nonlinear response. Here, the main quantity of interest characterizing the σ^+-photons interaction are the phase an amplitude of the two-photon temporal wavefunction $\psi(t_1, t_2)$. The squared amplitude of ψ_{t_1,t_2} is equal to the normalized second-order correlation function of σ^+ photons.

$$|\psi(t_1, t_2)|^2 = g^{(2)}_{++}(t_1, t_2) \tag{8.3}$$

After independent measurements of the linear transmission η_+ and the amplitude of ψ, the phase $\arg(\psi_{t_1,t_2})$ can be extracted by additional measurements of the two-photon correlation functions in different polarization bases . For example, assuming no interactions between the medium and σ^--polarized photons, $(\eta_- = \chi(t_1, t_2) = \mu(t_1, t_2) = 1)$, the correlation function for outgoing photons with the initial polarization is:

$$g^{(2)}_{VV}(t_1, t_2) = \left| \frac{\eta_+^2 + 2\eta_+ + \psi(t_1, t_2)}{(1 + \eta_+)^2} \right|^2 \tag{8.4}$$

In the presence of decoherence, the outgoing state of the photons must be described by density matrices, with $\rho^{(1)}(t)$ replacing $|1\rangle_t\langle 1|_t$, and $\rho(t_1, t_2)$ replacing $|1, 1\rangle_{t_1,t_2}\langle 1, 1|_{t_1,t_2}$. It is convenient to define the scaled matrix

$$\tilde{\rho}_{i,j}(t_1, t_2) = \frac{\rho_{i,j}(t_1, t_2)}{[\rho^{(1)}(t_1) \otimes \rho^{(1)}(t_2)]_{i,j}} \tag{8.5}$$

in the basis $\left\{ \left|\sigma_1^+\sigma_2^+\right\rangle, \left|\sigma_1^+\sigma_2^-\right\rangle, \left|\sigma_1^-\sigma_2^+\right\rangle, \left|\sigma_1^-\sigma_2^-\right\rangle \right\}$. By definition, all elements of $\tilde{\rho}$ are equal to 1 in the absence of nonlinearity. For a pure state, $\arg[\tilde{\rho}_{++,--}(t_1, t_2)] = \arg(\psi_{t_1,t_2}\mu^*_{t_1,t_2})$ is the nonlinear phase-shift of a $\sigma^+\sigma^+$ photon-pair with respect to that of the weakly interacting $\sigma^-\sigma^-$ pair.

The density matrices for the one-photon and two-photon states are measured by quantum state tomography via a maximum-likelihood estimation[195]. We numerically optimize a Hermitian, positive semidefinite, two-photon density-matrix,

$$\rho = \begin{pmatrix} \rho_{++,++} & \rho_{++,S} & \rho_{++,--} & 0 \\ \rho_{S,++} & \rho_{S,S} & \rho_{S,--} & 0 \\ \rho_{--,++} & \rho_{--,S} & \rho_{--,--} & 0 \\ 0 & 0 & 0 & \rho_{A,A} \end{pmatrix} \tag{8.6}$$

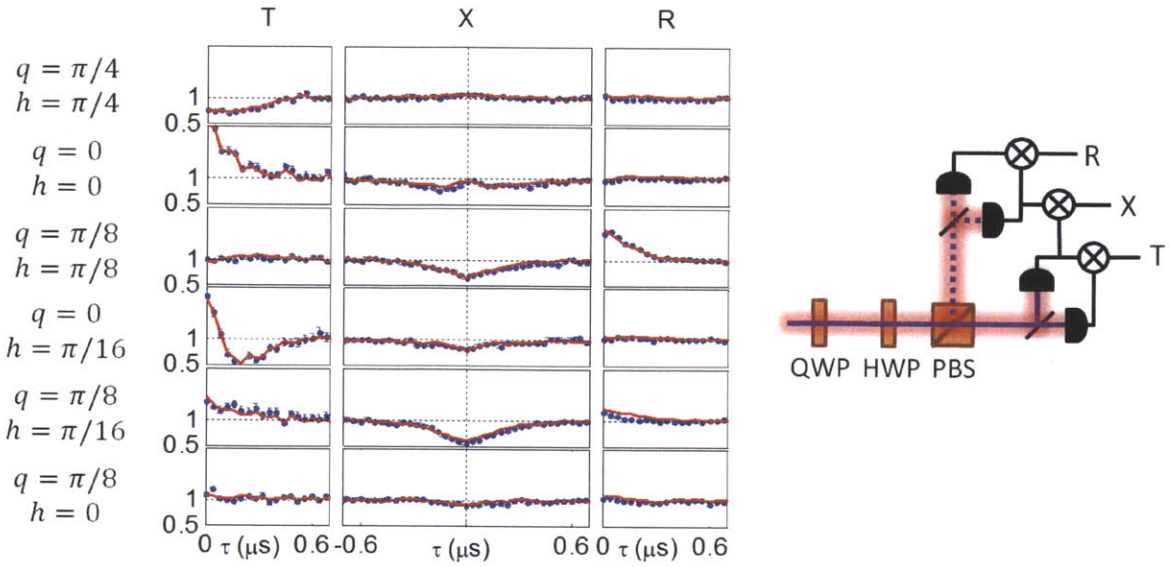

Figure 8-3: **Normalized photon-photon correlation functions in 6 polarization bases** (for $\Delta = 1.5\Gamma$). **a,** Each setting of the quarter wave-plate (QWP) at an angle q and the half wave-plate (HWP) at an angle h (angles specified on the left) followed by a polarizing beam splitter determines a polarization basis for three $g^{(2)}_{\alpha\beta}(\tau)$ measurements (blue points): for two transmitted photons (T), for two reflected photons (R), and for one-transmitted-one-reflected (X). The bases are equivalent to those proposed in Ref. [194]. The 18 pair counts from 6 different bases are used to tomographically reconstruct the two-photon density matrix using the maximum-likelihood estimation. Together with the reconstructed one-photon density matrix (obtained from the single counts), one can calculate the reconstructed $g^{(2)}_{\alpha\beta}(\tau)$ (red line).

in the two-qubit basis $\left\{\left|\sigma_1^+\sigma_2^+\right\rangle, |S\rangle, \left|\sigma_1^-\sigma_2^-\right\rangle, |A\rangle\right\}$, where $|S/A\rangle = (\left|\sigma_1^+\sigma_2^-\right\rangle \pm \left|\sigma_1^-\sigma_2^+\right\rangle)/\sqrt{2}$. Since the two photons share the same frequency and spatial mode, there is no coherence between the 3×3 symmetric and 1×1 anti-symmetric subspaces[194]. The photons have different temporal modes and are distinguishable by their arrival time. Nevertheless, because the interaction between the σ^+ and σ^--polarized photons is negligible, the $|\sigma^+\sigma^-\rangle$ component of the outgoing state is entirely in the symmetric subspace. We verified that all the measured $g^{(2)}_{\alpha\beta}(t_1, t_2)$ are symmetric with respect to $\tau = t_1 - t_2$, within our detection noise.

To set the 10 degrees of freedom in $\rho(t_1, t_2)$, we measure $g^{(2)}_{\alpha\beta}$ in six required polarization bases $\{q, h\} = \{\frac{\pi}{4}, \frac{\pi}{4}\}, \{0, 0\}, \{\frac{\pi}{8}, \frac{\pi}{8}\}, \{0, \frac{\pi}{16}\}, \{\frac{\pi}{8}, \frac{\pi}{16}\}, \{\frac{\pi}{8}, 0\}$, where q, respectively h, is the angle of the quarter-waveplate, respectively half-waveplate, using four single photon

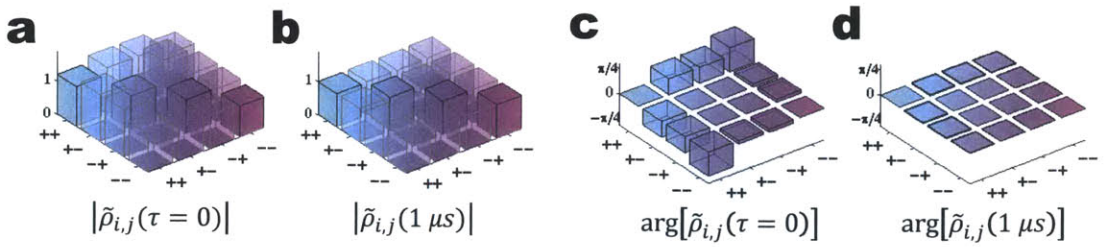

Figure 8-4: **Tomographic reconstruction of the scaled density matrix $\tilde{\rho}$.** Amplitude (**a,b**) and phase (**c,d**) of the scaled two-photon density matrix $\tilde{\rho}_{i,j}(\tau) = \rho_{i,j}(\tau)/[\rho^{(1)} \otimes \rho^{(1)}]_{i,j}$ for two photons with time separation $\tau = 0$ (**a,c**) and $\tau = 1\ \mu s$ (**b,d**) at a detuning of $\Delta = 2.3\Gamma$. All $\tilde{\rho}_{i,j}(1\,\mu s) = 1$, as expected in the absence of nonlinearity. The bunching is evident by $\tilde{\rho}_{++,++} > 1$ (**a**), while the nonlinear (conditional) phase shift is given by $\arg(\tilde{\rho}_{++,--}) \approx -\pi/4$ (**b**).

counters (see Fig. 8-3). The optimization follows the Maximum Likelihood Estimate[195], where all coincidence measurements are considered. The one-photon density matrix $\rho^{(1)}(t)$ is reconstructed using the same technique using the average transmission rates instead of the coincidence counts. Note that the correlation counts are rescaled to compensate for the offset at large τ (see discussion in chapter 7).

Figure 8-3 also presents a comparison between $g^{(2)}_{\alpha\beta}(\tau)$ curves measured in different polarization bases and those calculated from the reconstructed density matrices after maximum-likelihood estimation. The resulting scaled density matrices are plotted in Fig. 8-4 in the limits of proximal ($t_1 = t_2$) and distant (non-interacting) $|t_1 - t_2| = 1\ \mu s$ photons. As expected, at large time separation, the elements of the scaled matrix are all equal to unity. For photons exiting the medium simultaneously, we observe the existence of a large conditional phase-shift between $|\sigma^+\sigma^+\rangle$ and $|\sigma^-\sigma^-\rangle$. The small phase emerging between the $|\sigma^+\sigma^-\rangle$ and $|\sigma^-\sigma^-\rangle$ components underlines that photons with opposite polarizations interact very weakly.

8.3 Results

The component $g^{(2)}_{++}$ directly gives the probability density of the σ^+-polarized interacting photon pairs. Figure 8-5 shows $g^{(2)}_{++}$ for a control detuning $\Delta = 14$ MHz as a function of

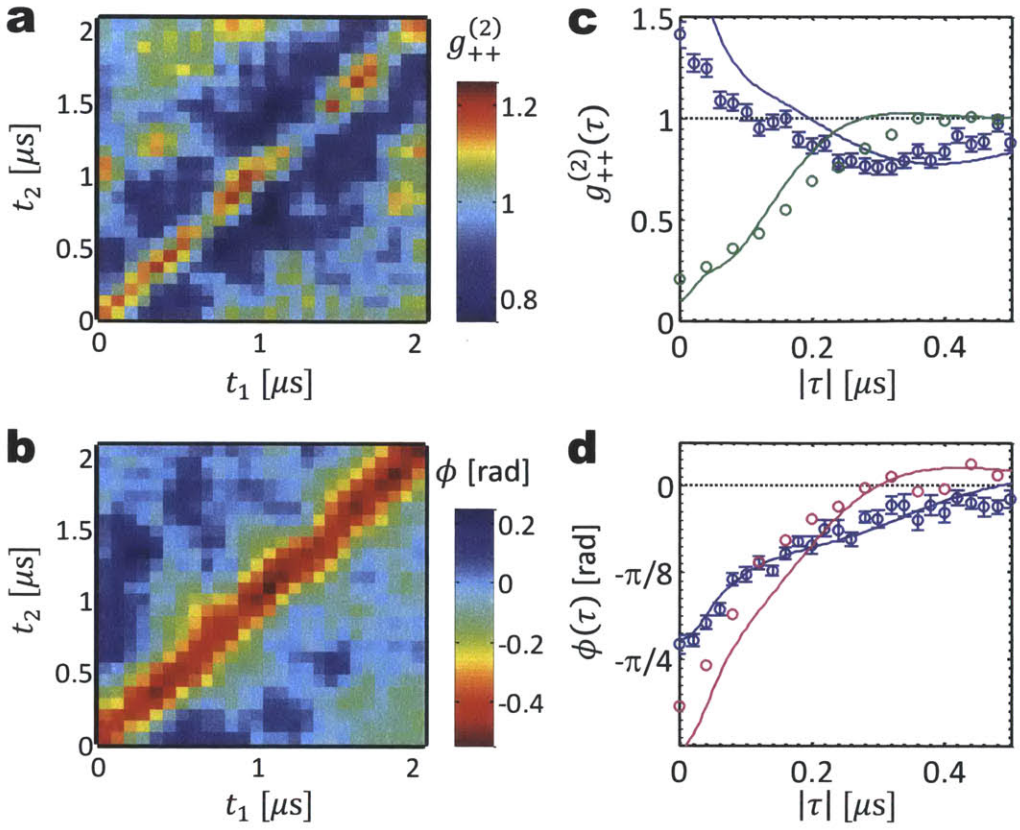

Figure 8-5: **Conditional phase-shift and photon bunching.** Measured second-order correlation function (**a**) and nonlinear phase shift (**b**) of interacting photon pairs at $\Delta = 2.3\Gamma$. The photons are detected at times t_1 and t_2. (**c**) Second-order correlation function displayed as a function of the time difference $|\tau| = |t_1 - t_2|$ between the photons, showing the transition from anti-bunching on resonance ($\Delta = 0$, green) to bunching at large detuning ($\Delta = 2.3\Gamma$, blue). Points are experimental data, lines are full numerical simulations. All $g^{(2)}_{++}$ measurements are rescaled by their value at $\tau > 1.5$ μs (See Chapter 7). (**d**) Nonlinear phase-shift versus $|\tau|$ for two different detunings ($\Delta = 1.5\Gamma$, purple, and $\Delta = 2.3\Gamma$, blue). The 1σ error is ± 30 mrad, dominated by photon shot noise.

the time separation $\tau = t_1 - t_2$ between the photons detected at times t_1, t_2, converted into a relative distance in the medium via the group velocity v_g. A prominent feature is the cusp at $r = v_g\tau = 0$, which is characteristic of a predicted two-photon bound state[34, 196], as discussed below.

The probability density of two interacting σ^+ photons, $g^{(2)}_{++}(t_1, t_2)$, and the nonlinear phase, acquired by the $\sigma^+\sigma^+$ pair relative to a non-interacting $\sigma^-\sigma^-$ pair, $\phi = \arg[\tilde{\rho}_{++,--}]$,

are shown in Figs. 8-5a,b for $\Delta = 14$ MHz. Clearly visible is the bunching of photons, *i.e.* an increased probability for photons to exit the medium simultaneously ($t_1 \approx t_2$), and a substantial nonlinear two-photon phase shift of -0.5 rad in that region. Here t_1 and t_2 belong to the central region of the 5 μs pulse, where the experiments is steady state. In that regime, the correlation function only depends on the detection time difference $\tau = t_2 - t_1$ and can be averaged along the diagonal lines. Figure 8-5,c shows the intensity correlation in the dissipation-dominated antibunching regime (see Chapter 7) at $\Delta = 0$ and in the dispersive regime at $|\Delta| > \Gamma$ and Fig. 8-5,d displays the nonlinear phase for two different detunings. The central result of this work is the large nonlinear Kerr phase-shift $> \pi/4$ at the single photon level for a medium with a large linear transmission of order 50%. The linear transmission is technically limited by the ground- to Rydberg-state decoherence, which arises from the probe and control field linewidth and the finite temperature of the atoms. This record conditional phase-shift outside the context of cavity QED is accompanied by the emergence of a visible bunching feature in the probability density of the two-photon wavefunction.

The transition from the dissipative to the dispersive regime with increasing $|\Delta|$ is summarized in Figs. 8-6,a,b. In the dispersive regime, the nonlinear phase shift $\phi(\tau = 0)$ can reach $(-0.32 \pm 0.02)\pi$, at a detuning $\Delta = 9$ MHz. Note that it is experimentally easier to access the amplitude of the wavefunction $\psi(t_1, t_2)$, which only requires the measurement of the correlation function $g^{(2)}_{++}(t_1, t_2)$ than to measure the phase $\phi(t_1, t_2)$ which we extract from the full tomographic process. As expected from the refractive index discrepancy between the 2-level and 3-level atomic ensemble, the blockade generates a large condition phase shift at $|\Delta| \gtrsim \Gamma$, which is ultimately limited by the absorption length l_a of the medium and the total optical depth OD. The absolute value of the nonlinear phase $|\phi|$ exhibits asymmetries under a sign change of the detuning Δ from the intermediate atomic $|e\rangle$ state. In particular, at negative values of Δ, corresponding to a blue-detuning of the control field, the phase-shift is strongly reduced and deviates from the predicted results given by our full theoretical simulations, plotted in blue. In theses simulations, we numerically solve the set of propagation equations for the light field and atomic coherences. The model incorporates the longitudinal atomic-density distribution and the decoherence of the Rydberg state (see Appendix D). In principle, the symmetry between

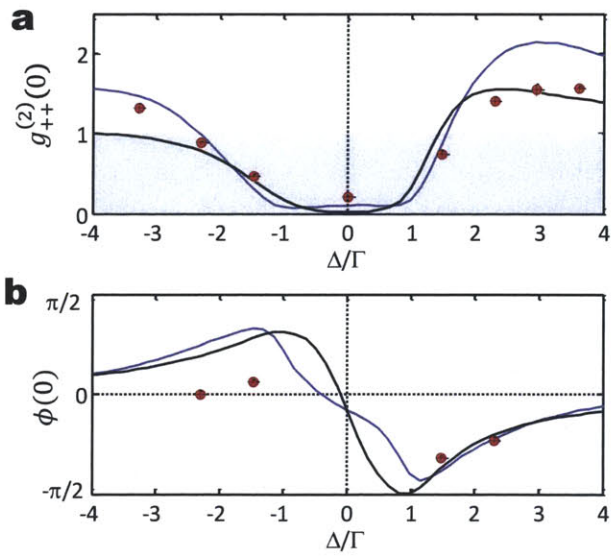

Figure 8-6: **Transition between the dissipative and dispersive regimes.** Equal-time two-photon correlation $g^{(2)}_{++}(0)$ (**a**) and nonlinear phase $\phi(0)$ (**b**) versus detuning Δ from the intermediate state $|e\rangle$. Blue lines are full theoretical simulations, while black lines are the result of the Schrodinger-equation approximation, assuming a simplified delta-function potential. Vertical error bars represent 1σ and horizontal error bars are ± 0.5 MHz.

positive and negative Δ is broken by the repulsive dipole interaction of the $100S_{1/2}$ states. For negative Δ, a positive energy shift of the Rydberg level of order $\Omega^2/|\Delta|$ tunes the two-photon Raman absorption dip in resonance with the probe field satisfying the two-photon resonance condition for unperturbed levels. On the contrary, for $\Delta > 0$, positive energy shifts of the Rydberg level detunes the two-photon absorption dip further away from the two-photon resonance. For negative Δ, this asymmetry introduces a dissipative interaction between photons at a distance equating the Van der Waals interaction and the control field Stark-shift, which is absent from the regime $\Delta > 0$.

8.4 Two-photon bound state.

We now turn to the explanation of the bunching feature, depicted in Figs. 8-5,c, 8-6,a. The propagation of σ^+-polarized photon pairs in such a medium can be understood by first considering an idealized situation with no decoherence between the Rydberg state and

the ground state. Then the steady-state in a one-dimensional homogenous medium can be described by a two-photon wavefunction $\psi(z_1, z_2)$, whose evolution is approximately governed by a simple equation (see Appendix D) in the center-of-mass $R = (z_1 + z_2)/2$ and relative $r = z_1 - z_2$ coordinates:

$$i\partial_R\psi = 4l_a\left[i + \frac{2\Delta}{\Gamma} - \mathcal{V}(r)\frac{\Omega_c^2}{\Gamma^2}\right]\partial_r^2\psi + \frac{\mathcal{V}(r)}{l_a}\psi. \tag{8.7}$$

Here the effective potential:

$$\mathcal{V}(r) = [i + 2\frac{\Delta}{\Gamma}(1 + 2r^6/r_B^6)]^{-1} \tag{8.8}$$

approaches $(i + 2\Delta/\Gamma)^{-1}$ inside the blockaded volume ($|r| < r_B$), and zero outside. The solution relates to the temporal wavefunction $\psi(\tau)$ defined in the previous section and to our measurements in time domain via:

$$\psi(R = L, r = v_g\tau) \sim \psi(\tau) = \sqrt{g_{++}^{(2)}(\tau)}e^{i\phi(\tau)} \tag{8.9}$$

This approximation only holds for small $|\tau|$ as discussed in Appendix D. Far off resonance ($|\Delta| \gg \Gamma, \Omega_c$), Eq.8.7 corresponds to a Schroedinger equation with the center-of-mass propagation distance R playing the role of effective time. The photons' effective mass $m \propto -\Gamma/(16l_a\Delta)$ can be positive or negative depending on the sign of the detuning Δ. The sign of the potential also changes with Δ and the potential is a well for $\Delta < 0$ and a barrier for $\Delta > 0$. Nevertheless, because the boundary condition $\psi(R = 0, r) = 1$ is unchanged under complex conjugation $\psi \rightarrow \psi^*$, the dynamics for positive Δ also correspond to a particle with positive mass in a potential well, as immediately derived by taking the complex conjugate of the Schroedinger equation, leading to an effective attractive force in both cases and opposite nonlinear phase-shifts. As mentioned earlier, the potential for $\Delta < 0$ also exhibits additional features near the edges of the well, corresponding to a Raman resonance $|g\rangle \rightarrow |r\rangle$ for the interaction-shifted Rydberg state at some interatomic distance near $|r| = r_B$ and these features are likely responsible for the deviation from (anti-)symmetry under the change of the sign of Δ displayed in Fig. 8-6.

In the experimentally relevant regime, the effective potential supports only one bound-

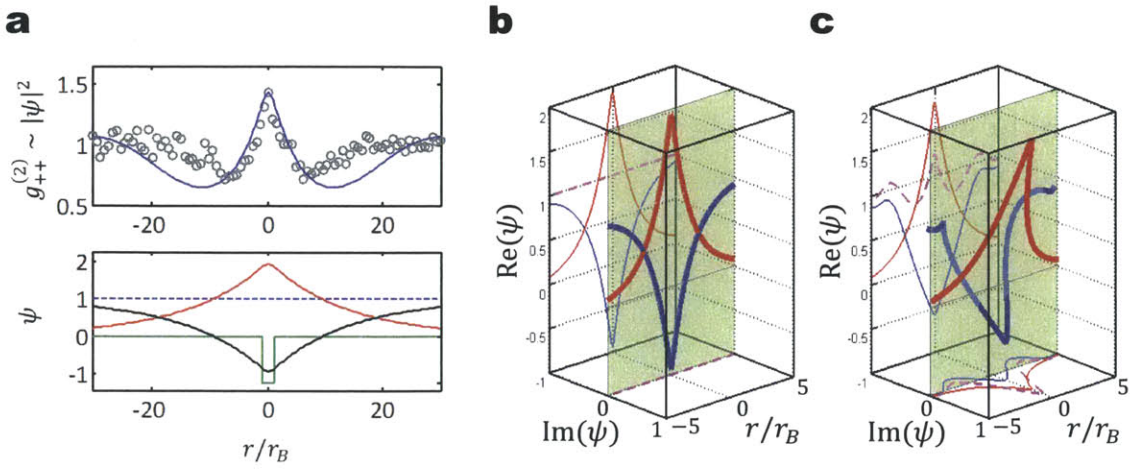

Figure 8-7: **Two-photon bound state evolution.** **a**, Photon bunching and two-photon bound state. Theoretically predicted photon-photon correlation function in the Schroedinger-equation approximation (top, blue line) for $\Delta = 14$ MHz, with a potential well of width $2r_B$ (bottom, green line). The bound state (bottom, red) and the superposition of scattering states (bottom, black) form the initial wave function $\psi = 1$ (bottom, dashed blue). The two-photon bound state results in the observed bunching in the correlation function $g^{(2)}_{++} \sim |\psi|^2$ (top, gray circles), where time has been converted into distance via the group velocity v_g. The boundary effects resulting from the finite extent of the atom cloud become important for $|r| \geq 5\ r_B$. **b,c,** Detailed visualization of the solution $\psi(R, r)$ to the Schroedinger Eq. 8.7 at the beginning ($R = 0$) and at the end ($R = L$) of the medium for $\Delta = 2.3\Gamma$ and $r_B = 0.15L$. ψ is a superposition of the unique bound eigenstate of the system (thick red) and a set scattering eigenstates (thick blue). For clearer visualization, the real and imaginary part of the bound (red) and scattering (blue) states, as well as the total wavefunction (dashed purple), are projected on the back and bottom planes of the tri-dimensional drawing. Initially, the bound state and the scattering states interfere to produce the boundary condition $\psi = 1$. On the short timescale corresponding to our parameters, the unitary evolution mainly rotates the bound state with respect to the scattering state, giving rise to a bunching peak on the real and imaginary part of ψ.

state $\psi_B(r)$ depicted in Fig. 8-7,a. The initial wavefunction $\psi(R = 0, r) = 1$ is a superposition of $\psi_B(r)$ and the continuum of scattering states. The accumulation of probability near $r = 0$ can then be understood as arising from the interference between the bound and scattering states that evolve at different frequencies. The exact evolution of the real and complex parts of the bound- and scattering states under Eq.8.7 is plotted in Figs. 8-7c,d. As shown in Fig. 8-7a, where the temporal wavefunction $\psi(\tau)$ has been rescaled by

the group velocity, the observed bunching feature in $g^{(2)}_{++}$ reflects the wavefunction of the two-photon bound state. The size of the two-photon bound state and correspondingly the width of the bunching feature $2\tau_b v_g \sim 70$ μm, exceed the width of the potential well of $2r_B \sim 35$ μm, as expected for a potential with one weakly bound state. As a consequence, the potential is well approximated by a simple δ-potential. Fig. 8-6 displays the solution of the Schroedinger-like equation 7.1 with a simplified delta-function potential (black curves), which agree well with our measurements and the theoretical predictions and capture the essential features of the nonlinear two-photon propagation.

8.5 Tuning of the interaction by two-photon detuning

Additional experimental evidence for the bound-state dynamics is obtained by tuning the probe field relative to the EIT resonance, thereby varying the strength of the two-photon interaction potential. As the probe detuning approaches the Raman resonance, $\delta \sim \Omega_c^2/(4\Delta)$, the difference in refractive indices inside and outside the blockade radius increases and the potential deepens (see Fig. 8-1). Consequently, the bound state becomes more localized and the bunching, quantified by $g^{(2)}_{++}(0)$, is enhanced, as evidenced in Fig. 8-8a. In that regime, the measured correlation function differs significantly from the prediction from our full theoretical model. At Raman resonance, the nonlinear interactions become mainly dissipative: single photons are strongly absorbed by the medium, with an opacity equal to the resonant OD in the absence of decoherence. Two-photon states are transmitted with large probability as the Rydberg blockade tunes the large absorption dip out of resonance. This strongly modifies the correlation-function: in the denominator, the transmission is dominated by multi-photon states, dark counts and polarization imperfections. The last two-effect strongly reduce the maximum observable correlation function, while the first effect requires the inclusion of higher many-body states in the theoretical model for our typical probe photon incoming rates. The numerator of the correlation function also possibly requires a many-body model to capture our experimental results. As shown in Fig. 8-8b, for measurements at very low probe power,

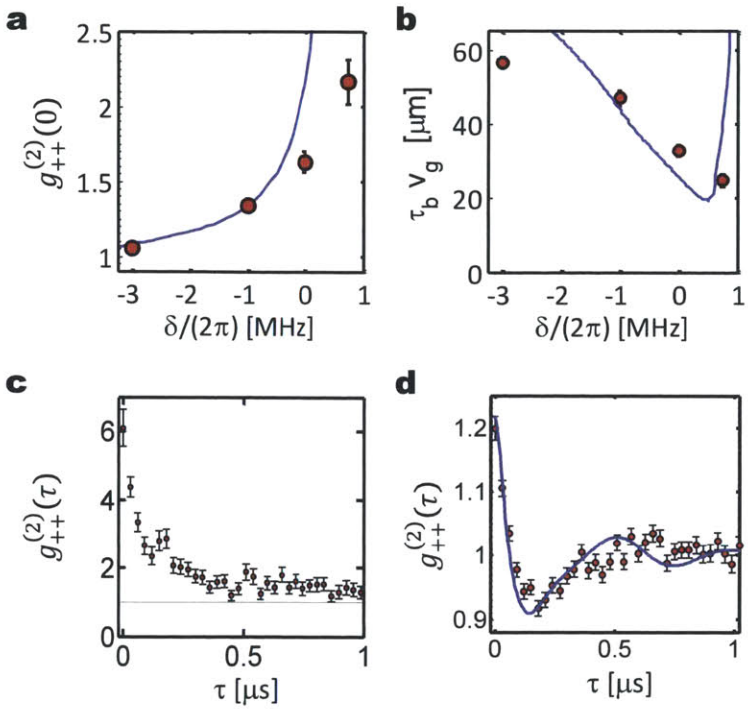

Figure 8-8: **Effect of the two-photon detuning.** Equal-time correlation function (**a**) and spatial extent of the bunching feature (**b**) versus Raman detuning δ from the EIT resonance $|g\rangle \rightarrow |r\rangle$ for $\Delta = 3\Gamma$, showing increased photon-photon attraction due to a deeper potential near Raman resonance (see Appendix D). The characteristic bunching-timescale τ_b is the half-width of the cusp feature of $g^{(2)}_{++}$, defined at half-height between the peak value at $\tau = 0$ and the local minimum closest to $\tau = 0$. Error bars correspond to $\pm 1\sigma$. The theoretical model (solid line) breaks down close to the Raman resonance at $\delta = 1.3$ MHz $\approx \Omega_c^2/(4\Delta)$, where the single-photon component of the probe field is strongly absorbed. **c,** Intensity correlation function for interacting photons $g^{(2)}_{++}(\tau)$ measured at the two-photon Raman absorption dip, for $\Delta = 1.5\Gamma$. The dissipative interactions lead to large bunching effects (the medium is strongly absorptive for single photons and transparent for multi-photon states). The value $g^{(2)}_{++}(0) \sim 6$ is limited by background noise and transmitted many-photon states, which dominate the average measured rates. **d,** Intensity correlation function for interacting photons $g^{(2)}_{++}(\tau)$ measured at the peak probe transmission for $\Delta = 3\Gamma$. The persistence of the bunching feature in a regime where dissipative interactions result in anti-bunching underlines the domination of dispersive interactions.

correlation function $g^{(2)}_{++}(0)$ up to 6 are observed. We stress that these large interactions are dissipative.

The opposite regime, $\Delta > 0, \delta < 0$, shifts the two-photon transitions towards the maximum of the transmission peak at $\delta \sim -\frac{\Delta}{\Gamma}\gamma$ where γ is the Rydberg- to ground-state decoherence rate. The potential depth is reduced (see Appendix D) and the transmission visibly higher than that of the 2-level medium. As shown in Fig. 8-8c, a clear bunching peak is still visible in the correlation function, followed by a wider sub-poissonian feature. The existence of the bunching feature in a regime where dissipative interactions lead to anti-bunching is a clear signature of the domination of the dispersive interaction for our experimental parameters. Note that is that regime, the theoretical simulations are in good agreement with our experimental results, confirming that the evolution of the two-photon wavepacket is dominated by the attractive force between the photons.

8.6 Entanglement

Finally, we study the quantum coherence and polarization properties of the transmitted photon pairs. Figure 8-9,a compares the purity of the two-photon density matrix $\rho(\tau)$, that includes photon interactions, to the purity of the product of one-photon matrices $\rho^{(1)} \otimes \rho^{(1)}$ for non-interacting photons. At large photon separation τ, the purity $P(\tau)$ of the two-photon density matrix is dominated by the one-photon decoherence due to partial depolarization of the transmitted light. This depolarization is attributed to the difference in group delay τ_d between the σ^+ and the faster σ^- photons ($\tau_d^{\sigma^+} - \tau_d^{\sigma^-} = 280$ ns) on the order of the coherence time of the probe laser (650 ns). A direct measurement of the Stokes degree of polarization gives $p_S = 0.8 \pm 0.05$, in good agreement with the purity of the reconstructed matrix $P[\rho(\tau)] = 0.62$ at large τ (we expect $P = (1 + p_S^2)^2/4$). At the same time, σ^+ photons bound to each other travel faster due to the reduction of the dispersion evidenced in Fig. 8-1 and are more robust against this decoherence mechanism, as evidenced by the greater purity at small τ. Even in the presence of this depolarization, the coherent nonlinear interaction in the dispersive medium produces entanglement in the outgoing polarization state of two photons. We quantify the degree of polarization entanglement by a time-dependent concurrence[197] $C(\tau)$ (see Fig. 8-9b). The obtained value $C(0) = 0.09 \pm 0.03$ clearly indicates deterministic entanglement of previously independent photons upon passage through the quantum nonlinear medium.

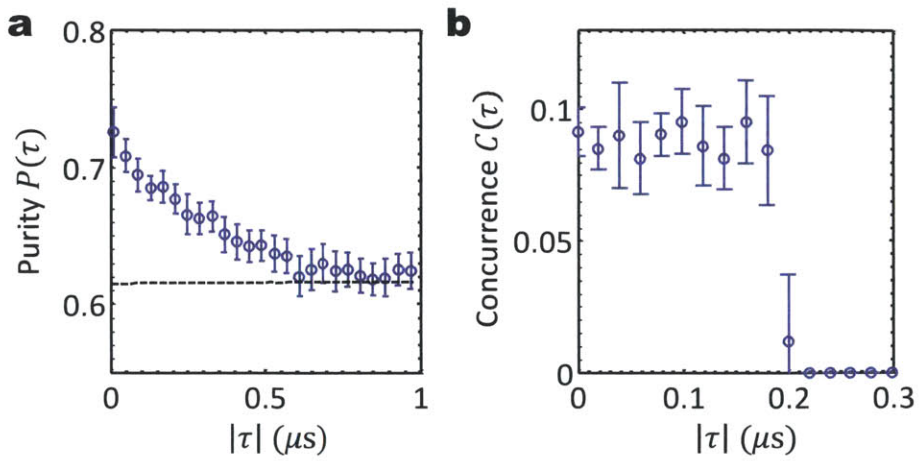

Figure 8-9: **Quantum coherence and entanglement.** **a,** Purity $P(\tau) = \mathrm{Tr}[\rho(\tau)^2]$ of the measured two-photon density-matrix for $\Delta = 2.3\Gamma$ (blue symbols), approaching at large photon separation the purity expected from the measured one-photon density-matrix $\mathrm{Tr}[(\rho^{(1)} \otimes \rho^{(1)})^2]$ (dotted black line). Interacting $\sigma^+\sigma^+$ photon pairs near $\tau = 0$ exhibit lower decoherence. Error bars (1σ) are derived from the uncertainty in the density matrix due to detection shot noise. **b,** Concurrence $C(t_1, t_2)$ calculated from the measured $\rho(t_1, t_2)$, indicating polarization entanglement of proximal photons upon transmission through the quantum nonlinear medium.

The measured value is in reasonable agreement with the theoretical prediction $C_{\mathrm{th}}(0) = 0.13$, calculated for a conditional phase $\phi(0) = \pi/4$, a purity $P(0) = 0.73$, and 50% σ^+ linear transmission.

The realization of coherent, dispersive photon-photon interactions opens up several new research directions. These include the exploration of a novel quantum matter composed from strongly interacting, massive photons[29]. Measurements of higher-order correlation functions may give direct experimental access to quantum solitons composed of a few interacting bosons[198], or to the detection of crystalline states of a photonic gas[29]. By colliding two counterpropagating photons, it may be possible to imprint a spatially homogeneous phase shift of π on the photon pair, corresponding to a deterministic quantum gate[62] for scalable optical quantum computation[10]. Finally, by accessing other Rydberg states via, *e.g.*, microwave transitions, it may become possible to control the state of multi-photon pulses with just one quantum of light, thereby realizing a single-photon

transistor[33] for applications in quantum networks, and the creation of multi-photon entangled states.

Appendix A

EIT

In this section, we briefly review the physics of Electromagnetically Induced Transparency (EIT), which is the building block of the work presented in this thesis. EIT originates from quantum interferences between excitation paths in multi-level atoms, resulting in the transparency of an otherwise opaque medium for a coherent light field. EIT was originally proposed by S. Harris and coworkers [199], building up on previous works about coherent optics in multi-level atoms, such as coherent population trapping and lasing without inversion [200]. Many singular effects of EIT, such as slow[185] and stopped [88] light, are best described by the propagation of part-matter part-light particles, called polaritons. Under specific circumstances, polaritons interact with an additional electric field or with other polaritons, effectively mediating interactions between photons. More extensive reviews on EIT can be found in [55, 201].

A.1 Dark states

We consider a medium composed of multi-level atoms with two long-lived states $|1\rangle$ and $|3\rangle$ (typically hyperfine or magnetic sub-levels of the ground state), with a non-zero dipole coupling to a short-lived state $|2\rangle$ (see Fig. A-1). For two coherent fields coupling the $|1\rangle \rightarrow |2\rangle$ and $|2\rangle \rightarrow |3\rangle$ levels with respective Rabi frequencies Ω_p and Ω_c and detunings Δ_p and Δ_c, the interaction Hamiltonian of the system is, in the rotating wave approximation and after transformation to the interaction picture:

$$\hat{H} = -\frac{\hbar}{2}\left(\Delta_p|2\rangle\langle 2| + \delta|3\rangle\langle 3| + \Omega_p|2\rangle\langle 1| + \Omega_c|3\rangle\langle 2|\right) + \text{h.c.} \tag{A.1}$$

For one- ($\Delta_p = 0$) and two-photon ($\delta = \Delta_p - \Delta_c = 0$) resonance, the atomic superposition

$$|D\rangle = \frac{1}{\sqrt{\Omega_p(t)^2 + \Omega_c(t)^2}}\left(\Omega_c(t)|1\rangle - \Omega_p(t)|3\rangle\right) \tag{A.2}$$

is an eigenstate with eigenvalue zero. $|D\rangle$ is called a dark state: its orthogonality to the excited state $|2\rangle$ prevents any decay from being observed by fluorescence once the atoms are pumped into $|D\rangle$. In contrast, the two-other eigenstates necessarily have a non-vanishing component of the excited state $|2\rangle$ (to satisfy the orthogonality of the eigenvalues) and are referred to as bright states.

If the fields are turned on abruptly, the atomic distribution is progressively and incoherently pumped into the dark state, which is decoupled from the other atomic states $|i\rangle$: $\langle i|\hat{H}|D\rangle = 0$. This process is known as coherent population trapping. It is also possible to adiabatically transfer the atoms from the ground state $|1\rangle$ into the dark state $|D\rangle$, which are equivalent in the absence of probe field. For a slow turn on of the probe field, the atomic population adiabatically follows the evolution of the eigenstate with $\Omega_p(t)$ and the atomic population is transferred in the dark state without ever populating the bright states. It is possible to extend this procedure to the final state $|3\rangle$ by adiabatically reducing the control field $\Omega_c(t)$. The so-called STIRAP (stimulated Raman adiabatic passage) completely transfers the atoms from state $|1\rangle$ to state $|3\rangle$ without populating the intermediate decaying state $|2\rangle$.

The coherent population transfer to the dark-state is the underlying mechanism governing EIT. For an atomic population initially pumped into $|1\rangle$ and in the presence of the control field, a slow varying pulse entering the medium rotates the population into a superposition of $|1\rangle$ and $|3\rangle$, with the largest mixing angle at the peak of the pulse. After the passing of the pulse peak, the population rotates back into $|1\rangle$, adiabatically following the dark state evolution. Throughout this evolution, the atomic population is constantly in the dark state and the light field is fully decoupled from the atoms, yielding a unity transparency and index of refraction.

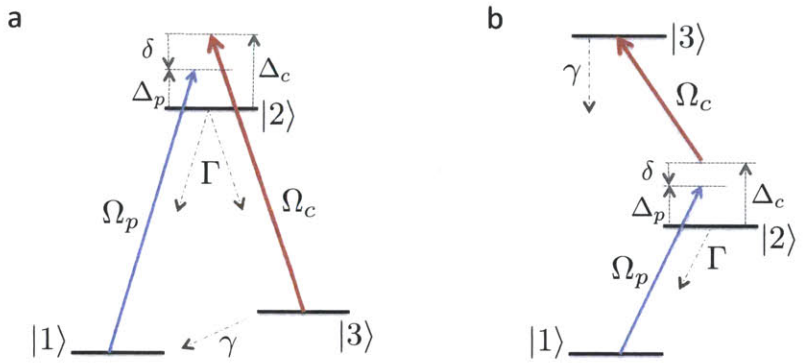

Figure A-1: **EIT level scheme. a**, Λ-type EIT. A control field with Rabi frequency Ω_c creates EIT conditions for a probe field (Ω_p). The detunings are defined as $\delta = \Delta_p - \Delta_c$, $\Delta_p = \omega_p - \omega_{21}$, $\Delta_c = \omega_c - \omega_{23}$, where ω_p, ω_c are the laser frequencies and ω_{21}, ω_{23} the corresponding atomic energy differences. Γ is the lifetime of the excited state and γ the ground states decoherence. (**b**) Ladder-type EIT where the ground state $|3\rangle$ has been replaced by a high lying metastable state.

A.2 Optical Bloch equations

Rigorously, the optical Bloch equations are the semi-classical limit of the Heisenberg-Langevin equations (introduced in the following section), where the operators are replaced by their average value. The Bloch equations govern the evolution of the density matrix, which fully describe the atomic states in the presence of decay and decoherence.

In the absence of atomic correlations, the density matrix for the individual atoms are replaced by a spatially averaged density matrix. The polarization density of the medium for the probe resonance is determined from the off-diagonal elements of the density matrix. The Bloch equations are particularly easy to solve for stationary fields, for which they reduce to a time-independent linear system. For illustration, we consider the specific example of EIT, but the method is very general. The master equation is:

$$\dot{\rho} = -\frac{i}{\hbar}\left[H(t), \rho\right] + \mathcal{L}[\rho] \tag{A.3}$$

The Lindblad operator $\mathcal{L}$ takes into account the lifetime and decoherence effects. The spontaneous decay of an excited level $|j\rangle$ to lower lying states $|i\rangle$ with rates Γ_{ji} is described by:

$$\mathcal{L}_j = \sum_i \frac{\Gamma_{ji}}{2} \left(2\sigma_{ij}\rho\sigma_{ji} - \rho\sigma_{jj} - \sigma_{jj}\rho\right) \tag{A.4}$$

where $\sigma_{ij} = |i\rangle\langle j|$. Additionaly, external dephasing processes can create decoherence between the atomic levels by introducing fluctuating energy shifts. These processes such as laser linewidth, atomic motion in inhomogeneous magnetic fields, Doppler broadening, are responsible for the decoherence of the off-diagonal elements of the density matrix. Provided that the fluctuations are fast with respect to the typical evolution time of the system, they can be modeled as:

$$\mathcal{L}_i^{deph} = \frac{\gamma_i}{2} \left(2\sigma_{ii}\rho\sigma_{ii} - \rho\sigma_{ii} - \sigma_{ii}\rho\right) \tag{A.5}$$

We consider an ensemble of three level atoms, as depicted in Fig. A-1,a. In the rotating wave approximation (RWA), the Hamiltonian of the system is, in the interaction picture ($e^{-E_i t/\hbar}|i\rangle \rightarrow |i\rangle$):

$$H_I(t) = -\frac{\hbar}{2}\left[\Omega_p e^{-i\Delta_p t}\sigma_{21} + \Omega_c e^{-i\Delta_c t}\sigma_{23}\right] + \text{h.c.} \tag{A.6}$$

where $\Delta_p = \omega_p - \omega_{21}$ and $\Delta_c = \omega_c - \omega_{23}$ (see Fig. A-1). The elements of the density matrix $\rho_{i,j} = \langle i|\rho|j\rangle$ obey the Bloch equations:

$$\dot{\rho}_{ij} = -\frac{\gamma_{ij}}{2}\rho_{ij} - \frac{i}{\hbar}\langle i|[H_I(t), \rho]|j\rangle \tag{A.7}$$

where $\gamma_{ii} = \sum_j \Gamma_{ij} = \Gamma_i$ is the lifetime of the excited state i and $\gamma_{ij} = \Gamma_i + \Gamma_j + \gamma_i + \gamma_j$ for $i \neq j$.

The time dependance of the Hamiltonian can be removed by passage to the rotating frame:

$$\rho_{21} \rightarrow e^{i\Delta_p t}\rho_{21},\ \rho_{23} \rightarrow e^{i\Delta_c t}\rho_{23},\ \rho_{31} \rightarrow e^{i\delta t}\rho_{31} \tag{A.8}$$

For the EIT Λ-system depicted in Fig. A-1, the optical Bloch equations are:

$$\dot{\rho}_{21} = -(\frac{\gamma_{21}}{2} - i\Delta_p)\rho_{21} + i\frac{\Omega_c}{2}\rho_{31} + i\frac{\Omega_p}{2}(\rho_{11} - \rho_{22}) \quad \text{(A.9)}$$

$$\dot{\rho}_{23} = -(\frac{\gamma_{23}}{2} - i\Delta_c)\rho_{23} + i\frac{\Omega_p}{2}\rho_{13} + i\frac{\Omega_c}{2}(\rho_{33} - \rho_{22}) \quad \text{(A.10)}$$

$$\dot{\rho}_{31} = -(\frac{\gamma_{31}}{2} - i\delta)\rho_{31} + i\frac{\Omega_c^*}{2}\rho_{21} - i\frac{\Omega_p}{2}\rho_{32} \quad \text{(A.11)}$$

They are further simplified by assuming that most atoms are in the ground state and substituting $\rho_{11} = 1$, $\rho_{22} = \rho_{33} = 0$ (which is exact to lowest order in Ω_p/Ω_c). In the low probe intensity limit, Eqs. A.9-A.11 are solved to first order in Ω_p and the term $-i\frac{\Omega_p}{2}\rho_{32}$ is neglected in A.11. In that case, for a constant control field, the system of Eqs. A.9-A.11 reduce to a linear system in the frequency domain:

$$\rho_{21} = \frac{i(\gamma - 2i\delta)}{(\Gamma - 2i\Delta_p)(\gamma - 2i\delta) + |\Omega_c|^2}\Omega_p \quad \text{(A.12)}$$

where we denoted $\gamma = \gamma_{31}$ and $\Gamma = \gamma_{21} = \Gamma_{31} + \Gamma_{32}$.

The polarization density of the medium is $P = \mathcal{N}\mu_{12}\mathrm{Tr}[\sigma_{12}\rho] = \mathcal{N}\mu_{12}\rho_{21}$ and the linear susceptibility $\chi^{(1)}$ (valid for $\Omega_p \ll \Omega_c$):

$$\tilde{\chi}^{(1)}(\Delta_p) = \frac{k_1}{2}\chi^{(1)}(\Delta_p) = \frac{1}{2l_a} \cdot \frac{i\Gamma(\gamma - 2i\delta)}{(\Gamma - 2i\Delta_p)(\gamma - 2i\delta) + |\Omega_c|^2} \quad \text{(A.13)}$$

in terms of absorption length $l_a = (\mathcal{N}\sigma_0)^{-1}$, related to the resonant atomic cross-section $\sigma_0 = \frac{2|\mu_{12}|^2\omega_p}{c\epsilon_0\Gamma\hbar}$.

A.3 EIT features.

A.3.1 Resonant control field

We first turn to the case of a resonant control field ($\Delta_c = 0$). The otherwise opaque medium characterized by its transmission $\mathrm{Exp}(-OD)$ is made transparent under EIT. The residual absorption $\mathrm{Exp}\left(-OD/\left(1 + \frac{\Omega_c^2}{\Gamma\gamma}\right)\right)$ is determined by the EIT linewidth $\gamma_{EIT} = \Omega_c^2/\Gamma$ and the decoherence γ and vanishes for $\gamma_{EIT} \gg \gamma$. The transparency window has an approximately Gaussian shape of variance $\Delta\omega_p \cong \gamma_{EIT}/\sqrt{8OD}$ (see Fig. A-2). For cold

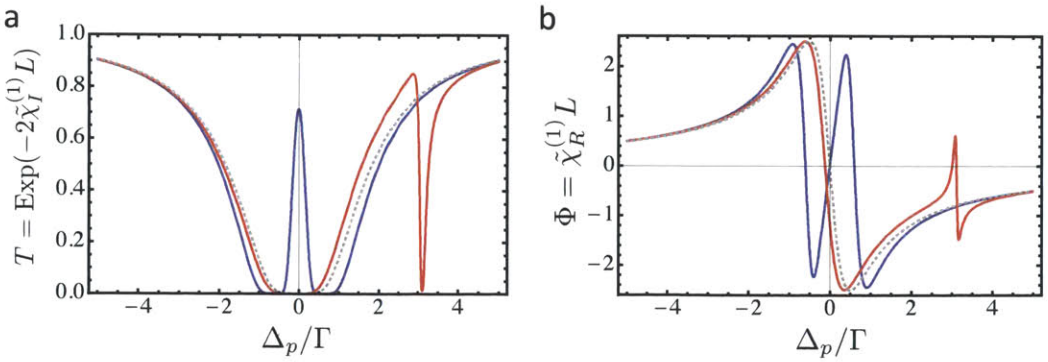

Figure A-2: **EIT spectra.** EIT intensity transmission spectrum (**a**) and corresponding phase-shift (**b**) for a control beam on resonance (blue line) and off resonance (red line) by $\Delta_c = 3\Gamma$, for $OD = 10$, $\Omega_c = 1.2\Gamma$, $\gamma = 0.05\Gamma$. The grey dashed line is the response of the medium in the absence of control field.

atomic systems, assuming a typical decoherence of 100 kHz and an optical transition of a few 10^{15} Hz, the quality factor of the EIT resonance can easily reach 10^{10}. The width of the transparency sets the bandwidth of the system: the shortest pulses which can propagate in the medium without absorption are of order $\tau_p \cong \Delta\omega_p^{-1}$. The narrow transmission linewidth is associated with a strong chromatic dispersion, enforcing a reduced group velocity:

$$v_g = \frac{c}{1 + c\partial_{\Delta_p}\tilde{\chi}_R^{(1)}(0)} = \left[\frac{1}{c} + \frac{1}{l_a}\frac{\Gamma}{\Gamma\gamma + |\Omega_c|^2}\right]^{-1} \approx l_a \gamma_{EIT} \tag{A.14}$$

In the large OD limit, the group delay $\tau_d = OD\gamma_{EIT}^{-1}$ is larger than the bandwidth limit $\tau_p \sim \sqrt{OD}\gamma_{EIT}^{-1}$, enabling the loss-free compression of a full pulse in the medium. The compression factor v_g/c results from the slowing down of the front end of the pulse with respect to the back end of the pulse still propagating at speed of light c outside the medium. The peak amplitude of the probe electric field in the medium is equal to that outside the medium for a bandwidth limited pulse in the absence of decoherence. As a consequence, the energy of the probe field inside the medium is reduced by a factor v_g/c and the energy difference is coherently stored by the stimulated Raman processes in the

control field and atomic energy difference between the ground states.

The propagation of the probe light in a medium under EIT conditions is given by (see Eq. 2.24):

$$\frac{\partial \mathcal{E}}{\partial z}(z,t) + \frac{1}{v_g}\frac{\partial \mathcal{E}}{\partial t}(z,t) = i\left(\tilde{\chi}^{(1)}(0)\right)\mathcal{E}(z,t) - \frac{i}{2}\left(\partial^2_{\Delta_p}\tilde{\chi}^{(1)}(0)\right)\frac{\partial^2 \mathcal{E}}{\partial t^2}(z,t) \tag{A.15}$$

On resonance the second derivative of the susceptibility is purely imaginary. In the coordinate system $Z = z - v_g t$ and $z = z$ the propagation equation for $\mathcal{E}(z,t)$ becomes a diffusion equation:

$$\frac{\partial \mathcal{E}}{\partial z} = \mathcal{D}\frac{\partial^2 \mathcal{E}}{\partial Z^2} \tag{A.16}$$

with a diffusion coefficient:

$$\mathcal{D} \cong \frac{1}{2}\left(\partial_{\Delta_p}\tilde{\chi}^{(1)}_R(0)\right)^{-2}\left(\partial^2_{\Delta_p}\tilde{\chi}^{(1)}_I(0)\right) \approx 2l_a \tag{A.17}$$

Eq. A.16 describes the broadening of the slow-propagating pulse due to the finite bandwidth, as described in Chapter 2.

A.3.2 Off-resonant control field

As illustrated in Fig. A-2, the response of the medium is modified when the control field is detuned from the corresponding atomic transition. In particular, when the detuning, Δ_c, is large with respect to the excited state linewidth Γ, the transmission spectrum of the probe field consists in a large central 1-photon absorption valley, a transmission peak equivalent to EIT on two-photon resonance, and a narrow two-photon (or Raman) absorption dip, shifted from the two-photon resonance by the Stark-shift $\Omega_c^2/(4\Delta_c)$. The transmission peak is unity at two-photon resonance in the absence of decoherence, and is effectively reduced and shifted by an amount $\Delta_c\gamma/\Gamma$ in the presence of dephasing. Similarly to the case of a resonant control field, the phase-shift cancels on two-photon resonance and the group velocity is equally reduced. A noticeable difference is the emergence of a non-zero group velocity dispersion, which dominates the bandwidth term in

	General	$\Delta_c = 0$	$\Delta_c \neq 0$
$\tilde{\chi}_I^{(1)}(0)$	$\frac{1}{2l_a}\frac{\gamma\Gamma\tilde{\Omega}_c^2}{4\gamma^2\Delta^2+\tilde{\Omega}_c^2}$	0	0
$\tilde{\chi}_R^{(1)}(0)$	$-\frac{1}{l_a}\frac{\gamma^2\Gamma\Delta}{4\gamma^2\Delta^2+\tilde{\Omega}_c^2}$	0	0
$\partial_{\Delta_p}\tilde{\chi}_I^{(1)}(0)$	–	0	0
$\partial_{\Delta_p}\tilde{\chi}_R^{(1)}(0)$	–	$\frac{1}{l_a}\frac{\Gamma}{\Omega_c^2}$	$\frac{1}{l_a}\frac{\Gamma}{\Omega_c^2}$
$\partial^2_{\Delta_p}\tilde{\chi}_I^{(1)}(0)$	–	$\frac{1}{l_a}\frac{4\Gamma^2}{\Omega_c^4}$	$\frac{1}{l_a}\frac{4\Gamma^2}{\Omega_c^4}$
$\partial^2_{\Delta_p}\tilde{\chi}_R^{(1)}(0)$	–	0	$\frac{1}{l_a}\frac{8\Gamma\Delta}{\Omega_c^4}$

Table A.1: EIT linear susceptibility: summary of the zero-,first- and second- order derivatives of $\tilde{\chi} = \frac{k_p}{2}\chi$ on two-photon resonance ($\delta = 0$) for an on-resonant ($\Delta_c = 0$) and off-resonance ($\Delta_c \neq 0$) control field, in the absence of decoherence ($\gamma = 0$)

Eq. A.15: the propagation equation now takes the form of a Schroedinger equation:

$$i\frac{\partial E_1}{\partial z} = -\frac{1}{2m^*}\frac{\partial^2 E_1}{\partial Z^2} \tag{A.18}$$

with an effective mass: $m^{*-1} = 8l_a$.

A.4 Heisenberg equations

In this section, we derive the Heisenberg-Langevin equations of motion corresponding to EIT in a ensemble of 3-level atoms where an excited state $|2\rangle$ is coherently coupled to two ground states $|1\rangle$ and $|3\rangle$. This approach allows for the quantification of the probe field, which is necessary to describe Rydberg EIT in the large density limit, where correlations are mapped onto the probe field. The evolution of an atom labelled j at position z_j is described in the Heisenberg picture by the atomic operators $\hat{\sigma}_{kl}^j(t)$. The interaction of the atoms with the (quantized) electric field E and the (classical) control field of slow varying

Rabi frequency $\Omega_c(z_j,t)$ is in the RWA: [186, 202]:

$$\hat{H}_I = -\sum_j \left[\mu_{12}\hat{E}^+(z_j,t)\hat{\sigma}^j_{21} + \frac{\hbar}{2}\Omega(z_j,t)e^{i(k_c z_j-\omega_c t)}\hat{\sigma}^j_{23}\right] + \text{h.c.} \tag{A.19}$$

where $\mu_{12} = -e\langle 1|\vec{r}\cdot\vec{\epsilon}|2\rangle$ and $\vec{\epsilon}$ is the polarization of the field. The quantized positive frequency field is given by a superposition of plane waves with wave vectors k_l:

$$\hat{E}^+(z,t) = \sum_l \sqrt{\frac{\hbar\omega_l}{2\epsilon_0 V}}\hat{a}_l e^{ik_l(z-ct)} \tag{A.20}$$

Here we take the modes l to be continuous, and we consider a slow varying electric field envelope $E(z,t)$ with the normalization $\int_{L_q} dz\,|E(z,t)|^2 = 1$ ($|E(z,t)|^2$ is equivalent to a probability density over the quantization length of the problem L_q). Its Fourier transform $\tilde{E}(k,t) = \int dz E(z,t)e^{-ikz}$ is non-zero over a small range $\delta k = k - k_p$ (k_p is the carrier wave vector). Making the substitution $\sum \hat{a}_l e^{ik_l z} \to \sqrt{L_q}\int dk\tilde{E}(k,t)\hat{a}_k e^{ikz}$, the quantized electric field is rewritten:

$$\hat{E}^+(z,t) = \sqrt{\frac{\hbar\omega_p}{2\epsilon_0 A}}\hat{\mathcal{E}}(z,t)e^{i(k_p z-\omega_p t)} \tag{A.21}$$

where $\omega_p = k_p c$. The field operator

$$\hat{\mathcal{E}}(z,t) = \int d(\delta k)\tilde{E}(\delta k,t)\hat{a}_{k_p+\delta k}e^{i\delta kz} \tag{A.22}$$

is the annihilation operator for a photon in mode $E(z,t)$ and obeys the bosonic commutation relations:

$$[\hat{\mathcal{E}}(z,t),\hat{\mathcal{E}}^\dagger(z',t)] = \delta(z-z') \tag{A.23}$$

The photon-atom interaction depends only of the tranverse area A of the field through the single photon-single atom coupling $\hbar g/2 = \mu_{12}\sqrt{\frac{\hbar\omega}{2\epsilon_0 A}}$ where g is related to the cooperativity $\eta = \sigma_0/A$ by $g^2 = \eta\Gamma c$. In the limit of a classical probe field, we can replace $g\hat{\mathcal{E}}(z,t)$ by the Rabi frequency of the probe field $\Omega_p(z,t)$.

For dense atomic media, we can defined coarse-grained continuous operators. The linear density is $\sum_{i=1}^N \delta(z-z_j)$ is replaced by the average atomic density $n(z)$ at position z ($n = N/L$ for N atoms constituting an homogeneous one-dimensional medium of length

L) and the continuous atomic operators, defined as

$$\hat{\sigma}_{m,n}(z,t) = \frac{1}{\sqrt{n(z)}} \sum_{j=1}^{N} \hat{\sigma}_{mn}^{j}(t)\delta(z - z_j), \tag{A.24}$$

replace the discrete operators (for any slow varying function or operator f):

$$\sum_j f(z_j,t)\hat{\sigma}_{mn}^{j}(t) \rightarrow \int dz f(z,t)\sqrt{n(z)}\hat{\sigma}_{mn}(z,t) \tag{A.25}$$

The $\sqrt{n}$ normalization imposes the commutation relations of a single particle annihilation operator (see at the end of this section):

$$[\hat{\sigma}_{k,l}(z,t), \hat{\sigma}_{m,n}(z',t)] = \frac{1}{\sqrt{n(z)}}(\delta_{lm}\hat{\sigma}_{kn}(z,t) - \delta_{nk}\hat{\sigma}_{ml}(z,t))\delta(z - z') \tag{A.26}$$

Finally, we can define slow-varying envelope operators for the "polarization", "spin-wave" and "control polarization" quantities:

$$\hat{\sigma}_{12}(z,t) = \hat{\mathcal{P}}(z,t)e^{-i\omega_p t} \tag{A.27}$$

$$\hat{\sigma}_{13}(z,t) = \hat{\mathcal{S}}(z,t)e^{-i(\omega_p - \omega_c)t} \tag{A.28}$$

$$\hat{\sigma}_{32}(z,t) = \hat{\mathcal{C}}(z,t)e^{-i\omega_c t} \tag{A.29}$$

The total Hamiltonian is: $\hat{H} = \hat{H}_0 + \hat{H}_I$ with:

$$\hat{H}_0 = \hbar \int dz \omega_p(\hat{\mathcal{E}}^\dagger\hat{\mathcal{E}}) + \hbar \int_L dz(\omega_{21}\hat{\mathcal{P}}^\dagger\hat{\mathcal{P}} + \omega_{31}\hat{\mathcal{S}}^\dagger\hat{\mathcal{S}}) \tag{A.30}$$

$$\hat{H}_I = -\frac{\hbar}{2}\int_L dz\sqrt{n(z)}\left[ge^{ik_p z}\hat{\mathcal{E}}(z,t)\hat{\mathcal{P}}^\dagger(z,t) + \Omega(z,t)e^{ik_c z}\hat{\mathcal{C}}^\dagger(z,t)\right] + \text{h.c.} \tag{A.31}$$

The Heisenberg equations for the atomic operators $\hat{\mathcal{O}}$:

$$i\hbar\frac{d\hat{\mathcal{O}}}{dt} = \left[\hat{H}_0 + \hat{H}_I, \hat{\mathcal{O}}\right] + i\hbar\frac{\partial\hat{\mathcal{O}}}{\partial t} \tag{A.32}$$

are calculated using the commutation relations in Eq. A.26:

$$\dot{\hat{\mathcal{P}}} = -\left(\frac{\gamma_{21}}{2} - i\Delta_p\right)\hat{\mathcal{P}} + i\frac{\Omega_c}{2}e^{ik_c z}\hat{\mathcal{S}} + i\frac{g}{2}e^{ik_p z}\hat{\mathcal{E}}(\hat{\sigma}_{11} - \hat{\sigma}_{22}) \tag{A.33}$$

$$\dot{\hat{\mathcal{C}}} = -\left(\frac{\gamma_{23}}{2} - i\Delta_c\right)\hat{\mathcal{C}} + i\frac{g}{2}e^{ik_p z}\hat{\mathcal{E}}\hat{\mathcal{S}}^\dagger + i\frac{\Omega_c}{2}e^{ik_c z}(\hat{\sigma}_{33} - \hat{\sigma}_{22}) \tag{A.34}$$

$$\dot{\hat{\mathcal{S}}} = -\left(\frac{\gamma_{31}}{2} - i\delta\right)\hat{\mathcal{S}} + i\frac{\Omega_c^*}{2}e^{-ik_c z}\hat{\mathcal{P}} - i\frac{g}{2}e^{ik_p z}\hat{\mathcal{E}}\hat{\mathcal{C}}^\dagger \tag{A.35}$$

The equations, are simplified in the low probe power limit, where the atoms are populating the ground state $|1\rangle$ with a close to unity probability. To first order in the probe field, the population operators reduce to $\hat{\sigma}_{11} = \sqrt{n}, \hat{\sigma}_{22} = 0, \hat{\sigma}_{33} = 0$. Furthermore, the explicit dependance on the wave vectors is removed by the substitutions $\hat{\mathcal{P}} \rightarrow \hat{\mathcal{P}}e^{ik_p z}, \hat{\mathcal{C}} \rightarrow \hat{\mathcal{C}}e^{ik_c z}$ and $\hat{\mathcal{S}} \rightarrow \hat{\mathcal{S}}e^{i(k_p - k_c)z}$.

$$\dot{\hat{\mathcal{P}}} = -\left(\frac{\gamma_{21}}{2} - i\Delta_p\right)\hat{\mathcal{P}} + i\frac{\Omega_c}{2}\hat{\mathcal{S}} + i\frac{g_p}{2}\hat{\mathcal{E}} \tag{A.36}$$

$$\dot{\hat{\mathcal{C}}} = -\left(\frac{\gamma_{23}}{2} - i\Delta_c\right)\hat{\mathcal{C}} + i\frac{g}{2}\hat{\mathcal{E}}\hat{\mathcal{S}}^\dagger \tag{A.37}$$

$$\dot{\hat{\mathcal{S}}} = -\left(\frac{\gamma_{31}}{2} - i\delta\right)\hat{\mathcal{S}} + i\frac{\Omega_c^*}{2}\hat{\mathcal{P}} - i\frac{g}{2}\hat{\mathcal{E}}\hat{\mathcal{C}}^\dagger \tag{A.38}$$

where g_p is the collectively enhanced cooperativity: $g_p = \sqrt{n}g$. To lowest order in the probe field, assuming all the population in the state $|1\rangle$, the commutation relation for the polarization and spin operators become:

$$\left[\hat{\mathcal{S}}(z,t), \hat{\mathcal{S}}^\dagger(z',t)\right] \cong \delta(z - z') \tag{A.39}$$

$$\left[\hat{\mathcal{P}}(z,t), \hat{\mathcal{P}}^\dagger(z',t)\right] \cong \delta(z - z') \tag{A.40}$$

The optical Bloch equations A.9-A.11 are the semi-classical limit of the above Heisenberg-Langevin equations, where the operators are replaced by their average value. The propagation of the probe electrical field is given by the slow varying envelope propagation equation:

$$\partial_t \hat{\mathcal{E}}(z,t) + c\partial_z \hat{\mathcal{E}}(z,t) = i\frac{g_p}{2}\hat{\mathcal{P}}(z,t) \tag{A.41}$$

A.5 Dark State Polariton

In the low probe limit, to first order, Eqs. A.36 -A.38 reduce to :

$$\dot{\hat{\mathcal{P}}} = -\left(\frac{\Gamma}{2} - i\Delta_p\right)\hat{\mathcal{P}} + i\frac{\Omega_c}{2}\hat{\mathcal{S}} + i\frac{g_p}{2}\hat{\mathcal{E}} \tag{A.42}$$

$$\dot{\hat{\mathcal{S}}} = -\left(\frac{\gamma}{2} - i\delta\right)\hat{\mathcal{S}} + i\frac{\Omega_c^*}{2}\hat{\mathcal{P}} \tag{A.43}$$

$$\tag{A.44}$$

where we used the same notations as in section A.2. We now turn to the response of the medium under EIT conditions, i.e. on two-photon resonance ($\delta = 0$) and in the absence of decoherence ($\gamma = 0$):

$$\hat{\mathcal{P}} = -\frac{2i}{\Omega^*}\dot{\hat{\mathcal{S}}} \tag{A.45}$$

$$\hat{\mathcal{S}} = -\frac{g_p}{\Omega}\hat{\mathcal{E}} - \frac{4(\Gamma - 2i\Delta_p)}{|\Omega|^2}\dot{\hat{\mathcal{S}}} - \frac{4}{|\Omega|^2}\left(\ddot{\hat{\mathcal{S}}} - \dot{\hat{\mathcal{S}}}\frac{\dot{\Omega}_c^*}{\Omega_c^*}\right) \tag{A.46}$$

The polarization $\hat{\mathcal{P}}$ can be adiabatically eliminated under the assumption that the slow varying envelopes of the spin-coherence and the control field have a characteristic variation time T significantly larger than the decay time of the excited state and the timescale of the EIT process: $1/T \ll \Gamma, \gamma_{EIT}$ for the generalized EIT linewidth $\gamma_{EIT} = \Omega^2/|\Gamma - 2i\Delta|$ [186, 202]. In that case, the higher derivatives of the spin operator $\ddot{\hat{\mathcal{S}}} \sim \dot{\hat{\mathcal{S}}}/T$ and $\dot{\hat{\mathcal{S}}} \sim \hat{\mathcal{S}}/T$ can be successively eliminated to yield:

$$\hat{\mathcal{S}}(t) = -\frac{g_p}{\Omega}\hat{\mathcal{E}}(z,t) \tag{A.47}$$

This relation establishes an exact equivalence between the spin coherence and the electric field, which characterizes the physics of EIT processes in the absence of decoherence. The propagation of the probe electric field is equivalent to the propagation of a spin coherence (so called spin-wave), whose envelope and group velocity are directly proportional to those

of the photon field. The propagation in the medium is governed by the equation:

$$\partial_t \hat{\mathcal{E}}(z,t) + c\partial_z \hat{\mathcal{E}}(z,t) = \frac{g_p}{\Omega^*}\partial_t \hat{\mathcal{S}}(z,t) = -\frac{g_p^2}{\Omega^*}\partial_t \frac{\hat{\mathcal{E}}(z,t)}{\Omega} \tag{A.48}$$

For a constant control field, it describes the pulse-preserving propagation of the field $\hat{\mathcal{E}}(z,t) = \hat{\mathcal{E}}(0, t - v_g^{-1}z)$ (or equivalently the spin-wave) at a strongly reduced group velocity $v_g = c(1 + g_p^2/|\Omega|^2)^{-1}$.

More generally, for a time-dependent control field, the excitation propagating at slow group velocity in the medium is described by a superposition of the electric field and the spin-wave, a so-called Dark-State polariton:

$$\hat{\Psi}(z,t) = \cos\theta(t)\hat{\mathcal{E}}(z,t) - \sin\theta(t)\hat{\mathcal{S}}(z,t) \tag{A.49}$$

$$\partial_t \hat{\Psi}(z,t) + v_g \partial_z \hat{\Psi}(z,t) = 0 \tag{A.50}$$

where the mixing angle $\tan^2\theta = g_p^2/|\Omega|^2$ determines the group velocity $v_g = c\cos^2\theta$. The group velocity now has a very simple interpretation: it is the weighted average speed between photons propagating at speed c and frozen atoms, the respective weights being determined by the mixing angle θ. Adiabatically reducing the control field intensity fully maps the polariton field onto its spin wave component, a building block for photon storage in quantum networks [88, 89, 203].

The polariton field operator $\hat{\Psi}(z,t)$ is a bosonic operator (see Eqs. A.39, A.40):

$$\left[\hat{\Psi}(z,t), \hat{\Psi}^\dagger(z',t)\right] \approx \delta(z - z') \tag{A.51}$$

creating and annihilating a polariton with the envelope of the compressed field $E(z,t)$ inside the medium. In the regime $g_p^2 \gg \Omega^2$, the polariton is essentially an atomic excitation in state $|3\rangle$, coherently shared by all the atoms overlapping with the compressed pulse envelope. The quantum state of a single polariton in the medium is:

$$\begin{aligned} |\psi\rangle = \int dz E(z,t)\hat{\Psi}^\dagger(z,t)|0\rangle \;\; &= \;\; \cos\theta(t)\int dz E(z,t)\hat{\mathcal{E}}^\dagger(z)|0\rangle \otimes |1_1, 1_2, ..., 1_N\rangle \\ &\quad - \sin\theta(t)\frac{1}{\sqrt{n}}\sum_{j=1}^{N} E(z_j,t)|0\rangle \otimes |1_1, 1_2, ..., 3_j ..., 1_N\rangle \end{aligned} \tag{A.52}$$

where the envelope satisfies the slow group velocity, pulse conserving condition $E(z,t) = E(z - \int dt v_g(t), 0)$.

Appendix B

Stationary Light Pulses in cold atoms.

B.1 Stationary Light Pulses

Building on the theoretical framework developped in Appendix A, we turn to the analytical treatment of stationary light pulses. Stationary light pulses are obtained when a standing wave control field is adiabatically ramped up to retrieve a spin-wave previously stored in the medium[85]. In that case, the light is trapped with a non-vanishing component of the electric field, and the medium can become highly nonlinear for the proper level scheme [60, 111]. We consider the general case of co- and-counterpopragating control fields in a 3-level Λ-system, detuned from the atomic resonance by $\Delta\pm = \Delta_c \pm \Delta$ where $\Delta_c = \omega_c - \omega_{21}$ is the average control field detuning, as depicted in Fig. B-1,a. Using the coarse-grain slow-varying polarization $\hat{\mathcal{P}}$ and spin $\hat{\mathcal{S}}$ operators defined in Eqs. A.27-A.29, the interaction Hamiltonian is given by (see Eq. A.31):

$$\hat{H}_I = -\frac{\hbar}{2}\int_L dz\sqrt{n}\left[g\left(e^{ik_pz}\hat{\mathcal{E}}_+(z,t) + e^{-ik_pz}\hat{\mathcal{E}}_-(z,t)\right)\hat{\mathcal{P}}^\dagger(z,t)\right] - \frac{\hbar}{2}\int_L dz\sqrt{n}\left[\left(\Omega_+ e^{i(k_c+\Delta k_+)z-i\Delta t} + \Omega_- e^{-i(k_c+\Delta k_-)z+i\Delta t}\right)\hat{\mathcal{C}}^\dagger(z,t)\right] + \text{h.c.} \tag{B.1}$$

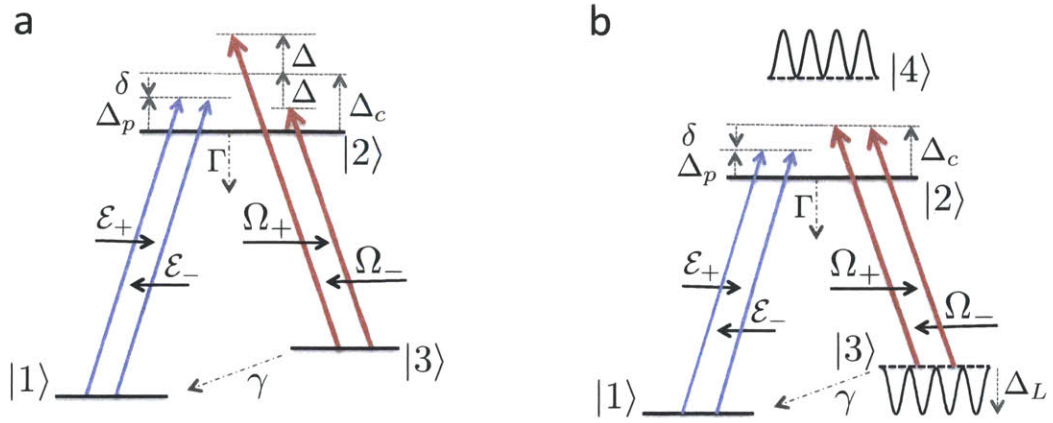

Figure B-1: **Level scheme for stationary light pulse techniques. a,** A running wave control field consisting of two counter-propagating fields with equal Rabi frequency creates mixing between the forward and backward propagating probe fields, resulting in an optical bandgap in the medium and reflection of the incoming probe light **b,** A Bragg-type reflection can also be achieved for a detuned standing wave control field creating a periodical levelshift of the ground state $|3\rangle$ by off-resonant coupling to a state $|4\rangle$.

where $\hat{\mathcal{E}}_+$ and $\hat{\mathcal{E}}_-$ are the field operators for the forward and backward propagating photons, $\Omega_\pm$ the Rabi frequencies of the control fields and $\Delta k_\pm = \pm\Delta/c$, as depicted in Fig. B-1,a. Over the length of our medium $L \sim 1$ cm, and for detunings of a few tens of MHz, $\Delta k_c L \ll 1$ and we set this term to zero in the rest of our anlysis. To first order in $\hat{\mathcal{E}}$ (see Eq. A.44) we obtain from the Heisenberg-Langevin equations:

$$\dot{\hat{\mathcal{P}}} = -\left(\frac{\Gamma}{2} - i\Delta_p\right)\hat{\mathcal{P}} + \frac{i}{2}\left(\Omega_+ e^{i(k_c z - \Delta t)} + \Omega_- e^{-i(k_c z - \Delta t)}\right)\hat{\mathcal{S}} + \frac{ig_p}{2}\left(e^{ik_p z}\hat{\mathcal{E}}_+ + e^{-ik_p z}\hat{\mathcal{E}}_-\right) \quad \text{(B.2)}$$

$$\dot{\hat{\mathcal{S}}} = -\left(\frac{\gamma}{2} - i\delta\right)\hat{\mathcal{S}} + \frac{i}{2}\left(\Omega_+^* e^{-i(k_c z - \Delta t)} + \Omega_-^* e^{i(k_c z - \Delta t)}\right)\hat{\mathcal{P}} \quad \text{(B.3)}$$

where $\delta = \Delta_p - \Delta_c$ is the two-photon detuning, and Δ_p the probe field detuning. The propagation of the probe fields is governed by the slow varying envelope Maxwell equation:

$$\partial_t \hat{\mathcal{E}}_\pm \pm c\partial_z \hat{\mathcal{E}}_\pm = i\frac{g_p}{2}\hat{\mathcal{P}}e^{\mp ik_p z} \tag{B.4}$$

The detuning of the control field introduces rotating term with frequencies $\pm\Delta$ and oscillating spatial dependancies $e^{\pm ik_c z}$. As a consequence, we can expand the atomic operators in harmonics of $i(k_c z - \Delta t)$:

$$\hat{\mathcal{P}} = \sum_m \hat{\mathcal{P}}^{(m)} e^{im(k_c z - \Delta t)} \tag{B.5}$$

$$\hat{\mathcal{S}} = \sum_m \hat{\mathcal{S}}^{(m)} e^{im(k_c z - \Delta t)} \tag{B.6}$$

The higher harmonics of the polarization create spatially oscillating terms $e^{imk_c z}$ for the probe fields. Nevertheless, for $|m| > 1$, these spatial oscillations are averaged out upon integration of Eq. B.4. Due to this phase-matching constraint, we ignore the higher harmonics of $\hat{\mathcal{E}}$. The system is now described by the following set of equations:

$$\begin{aligned}
\dot{\hat{\mathcal{P}}}^{(\pm 1)} &= \pm i\Delta\hat{\mathcal{P}}^{(\pm 1)} - \left(\frac{\Gamma}{2} - i\Delta_p\right)\hat{\mathcal{P}}^{(\pm 1)} + \frac{i}{2}\Omega_\pm \hat{\mathcal{S}}^{(0)} + \frac{i}{2}\Omega_\mp \hat{\mathcal{S}}^{(\pm 2)} \\
&\qquad + \frac{ig_p}{2}\hat{\mathcal{E}}_\pm e^{\pm i(k_p - k_c)z} e^{\pm i\Delta t}
\end{aligned} \tag{B.7}$$

$$\dot{\hat{\mathcal{P}}}^{(m)} = im\Delta\hat{\mathcal{P}}^{(m)} - \left(\frac{\Gamma}{2} - i\Delta_p\right)\hat{\mathcal{P}}^{(m)} + \frac{i}{2}\Omega_+ \hat{\mathcal{S}}^{(m-1)} + \frac{i}{2}\Omega_- \hat{\mathcal{S}}^{(m+1)} \tag{B.8}$$

$$\dot{\hat{\mathcal{S}}}^{(m)} = im\Delta\hat{\mathcal{S}}^{(m)} - \left(\frac{\gamma}{2} - i\delta\right)\hat{\mathcal{S}}^{(m)} + \frac{i}{2}\Omega_+^* \hat{\mathcal{P}}^{(m+1)} + \frac{i}{2}\Omega_-^* \hat{\mathcal{P}}^{(m-1)} \tag{B.9}$$

$$\partial_t \hat{\mathcal{E}}_\pm \pm c\partial_z \hat{\mathcal{E}}_\pm = i\frac{g_p}{2}\hat{\mathcal{P}}^{(\pm 1)} e^{\mp i\Delta t} e^{\pm i(k_c - k_p)z} \tag{B.10}$$

Due to phase-matching, terms oscillating faster than $\Delta k = k_p - k_c$ are ignored, as they average out upon spatial integration. The phase mismatch Δk can be factored away by the transformation: $\hat{\mathcal{E}}_\pm e^{i\pm\Delta k z} \rightarrow \hat{\mathcal{E}}_\pm$. The Maxwell equation is modified to:

$$\partial_t \hat{\mathcal{E}}_\pm \pm c\partial_z \hat{\mathcal{E}}_\pm = ic(\Delta k)\hat{\mathcal{E}}_\pm + i\frac{g_p}{2}\hat{\mathcal{P}}^{(\pm 1)}e^{\mp i\Delta t} \tag{B.11}$$

The polarization terms $\hat{\mathcal{P}}^{(\pm 1)}$ oscillate as $\hat{\mathcal{E}}_\pm e^{\pm i\Delta t}$, which in turn cancels the explicitly time-dependent terms in the propagation equation. This is reflected in the frequency domain by using the following Fourier transforms (where $\delta\omega$ is considered small with respect to the optical frequencies):

$$\hat{\mathcal{P}}(z,\delta\omega) = \int dt e^{i\delta\omega t}\hat{\mathcal{P}}(z,t), \tag{B.12}$$

$$\hat{\mathcal{E}}_\pm(z,\delta\omega \pm \Delta) = \int dt e^{i\delta\omega t}\hat{\mathcal{E}}_\pm(z,t)e^{\pm i\Delta t}, \tag{B.13}$$

yieding :

$$\begin{aligned} 0 = &-\left(\frac{\Gamma}{2} \mp i\Delta - i(\Delta_p + \delta\omega)\right)\hat{\mathcal{P}}^{(\pm 1)}(z,\delta\omega) + \frac{i}{2}\Omega_\pm \hat{\mathcal{S}}^{(0)}(z,\delta\omega) \\ &+\frac{i}{2}\Omega_\mp \hat{\mathcal{S}}^{(\pm 2)}(z,\delta\omega) + \frac{ig_p}{2}\hat{\mathcal{E}}_\pm(z,\delta\omega \pm \Delta) \end{aligned} \tag{B.14}$$

$$\begin{aligned} 0 = &-\left(\frac{\Gamma}{2} - im\Delta - i(\Delta_p + \delta\omega)\right)\hat{\mathcal{P}}^{(m)}(z,\delta\omega) \\ &+\frac{i}{2}\Omega_+ \hat{\mathcal{S}}^{(m-1)}(z,\delta\omega) + \frac{i}{2}\Omega_- \hat{\mathcal{S}}^{(m+1)}(z,\delta\omega) \end{aligned} \tag{B.15}$$

$$\begin{aligned} 0 = &-\left(\frac{\gamma}{2} - im\Delta - i(\delta + \delta\omega)\right)\hat{\mathcal{S}}^{(m)}(z,\delta\omega) \\ &+\frac{i}{2}\Omega_+^* \hat{\mathcal{P}}^{(m+1)}(z,\delta\omega) + \frac{i}{2}\Omega_-^* \hat{\mathcal{P}}^{(m-1)}(z,\delta\omega) \end{aligned} \tag{B.16}$$

$$-i\delta\omega\hat{\mathcal{E}}_\pm(z,\delta\omega) \pm c\partial_z\hat{\mathcal{E}}_\pm(z,\delta\omega) = ic(\Delta k)\hat{\mathcal{E}}_\pm(z,\delta\omega) + i\frac{g_p}{2}\hat{\mathcal{P}}^{(\pm 1)}(z,\delta\omega \mp \Delta) \tag{B.17}$$

By solving equations Eqs. B.14-B.16 (see section below for a discussion on how many orders to include in the calculation), we obtain the linear susceptibilities $\chi_{\pm\pm}$ and the mixing terms $\chi_{\pm\mp}$ defined as:

$$\hat{\mathcal{P}}^{(\pm 1)}(z,\delta\omega \mp \Delta) = \chi_{\pm\pm}(z,\delta\omega)\hat{\mathcal{E}}_\pm(z,\delta\omega) + \chi_{\pm\mp}(z,\delta\omega)\hat{\mathcal{E}}_\mp(z,\delta\omega) \tag{B.18}$$

The evolution of the forward and backward propagating fields is governed by a set of

coupled equations:

$$-i\delta\omega\hat{\mathcal{E}}_{\pm} \pm c\partial_z\hat{\mathcal{E}}_{\pm} = ic(\Delta k)\hat{\mathcal{E}}_{\pm} + i\frac{g_p}{2}\chi_{\pm\pm}\hat{\mathcal{E}}_{\pm} + i\frac{g_p}{2}\chi_{\pm\mp}\hat{\mathcal{E}}_{\mp} \tag{B.19}$$

The problem is simplified in the case of interest here, i.e. in the steady state regime ($\delta\omega = 0$) with a forward input control field corresponding to the boundary equations $\langle\hat{\mathcal{E}}_{+}(0, z = 0)\rangle \neq 0$ and $\langle\hat{\mathcal{E}}_{-}(0, z = L)\rangle = 0$ where L is the length of the medium, considered homegeneous. The transmission and reflection amplitude through the medium are given by $t = \frac{\langle\hat{\mathcal{E}}_{+}(0,L)\rangle}{\langle\hat{\mathcal{E}}_{+}(0,0)\rangle}$ and $r = \frac{\langle\hat{\mathcal{E}}_{-}(0,0)\rangle}{\langle\hat{\mathcal{E}}_{+}(0,0)\rangle}$ after integration over z of Eq. B.19.

B.2 Hot atoms versus cold atoms

To obtain the linear susceptibility $\chi_{\pm\pm}$ and coupling coefficients $\chi_{\mp\pm}$ from Eq. B.14 - B.16, it is necessary to solve a cascade of linear equations for higher harmonics of the spin coherence $\hat{\mathcal{S}}^{(2m)}$ and polarization density $\hat{\mathcal{P}}^{(2m+1)}$. Stationary light pulses and the associated bandgap were initially observed in room-temperature atomic vapors [85]. In that limit, the motion of the atoms leads to rapid dephasing of the fast spatial oscillations of the spin coherence. For EIT, the timescale of the process is governed by the EIT linewidth $\gamma_{EIT} = \Omega_c^2/|\Gamma - 2i\Delta|$ and is typically larger than 100 nanoseconds. During that time, for a room-temperature vapor, the atoms are displaced by a distance of ~ 15 μm. This displacement is much larger than the extent of the spatial oscillations of the m-th order spin coherence harmonics which are on the order of $(mk_c)^{-1}$. As a consequence, their contribution is nullified by setting $\hat{\mathcal{S}}^{(m)} = 0$ for $|m| \geq 1$, yielding a close set of equations for $\hat{\mathcal{S}}^{(0)}$, $\hat{\mathcal{P}}^{(\pm1)}$ and $\hat{\mathcal{E}}_{\pm}$. The integration of Eq. B.19 gives results in excellent agreement with the observations carried out in [85]. In particular, a large reflection peak and strong transmission suppression, characteristic of a Bragg-type bandgap, were observed on resonance ($\Delta_p = \Delta_c = 0, \Delta = 0$) and the possibility to store pulses was demonstrated in [85].

As pointed in several theoretical analysis [204, 105] and demonstrated experimentally in [105], this behavior is strongly altered for cold atoms. For a temperature of 40 μK, the motion of the atoms over the typical timescale of 100 nanoseconds is on the order

of λ, and the faster spatial oscillations of the spin coherence are partially preserved. The most striking consequence in the resonant case is the absence of photonic bandgap and of stationary light, reported in [105]. Stationary light pulses without Bragg grating have been discussed for double Λ-schemes with large energy splitting [105] or "diamond" configuration with orthogonal polarizations of the control fields [106, 95], for which the control fields do not form a standing-wave.

As described in Chapter 4.2, we probe the existence of a photonic bandgap in a three level system where the forward and backward control beams are symmetrically detuned by an amount $\Delta \sim 20$ MHz from the resonance. In that situation, the control fields form a moving standing wave. The running standing wave is shifted by a wavelength $\lambda_c = 2\pi/k_c$ in a time $1/\Delta$, and in the limit $|\Delta| > \gamma_{EIT} \sim \Omega_c^2/|\Delta|$, the effect of the higher order harmonics of the spin coherence $\hat{\mathcal{S}}^{(m\neq 0)}$ dephase and average out. In that case, we verify experimentally that the main features of the observed reflection are in good agreement with the 0-th order theory (see Section 4.2).

To 0-th order, the susceptibilities and coupling terms are given, for balanced control fields $\Omega_+ = \Omega_- = \Omega_c$, by:

$$\chi_{\pm\pm} = ig_p \frac{\tilde{\gamma}(\tilde{\Gamma} \pm i\Delta) + \Omega_c^2}{2\tilde{\Gamma}\Omega_c^2 + \tilde{\gamma}(\tilde{\Gamma}^2 + \Delta^2)}, \tag{B.20}$$

$$\chi_{\pm\mp} = -ig_p \frac{\Omega_c^2}{2\tilde{\Gamma}\Omega_c^2 + \tilde{\gamma}(\tilde{\Gamma}^2 + \Delta^2)}, \tag{B.21}$$

where $\tilde{\Gamma} = \Gamma - 2i\Delta_p$, $\tilde{\gamma} = \gamma - 2i\delta$.

B.3 Distributed Bragg Reflection in four-level atoms

We now consider the effect of an extra level $|4\rangle$, off-resonantly coupled to the ground state $|3\rangle$ by the co-and counter-propagating fields, as described in Fig. B-1,b. We here assume that the coupling only exists between the levels $|3\rangle$ and $|4\rangle$. The AC Stark shift induces a periodical modulation of the energy of the state $|3\rangle$, which affects the propagation of the probe fields. In the off-resonant regime, where the control fields are detuned from the $|3\rangle \rightarrow |2\rangle$ transitions, this is equivalent to a modulation of the index of refraction of the

medium, creating a distributed Bragg reflector. Here we assume that the Stark shift $\hbar\Delta_L$ at an antinode of the control field lattice (Δ_L is four times the level-shift generated by a single control field, due to constructive interference of the electric fields). In our case, the control fields are red-detuned from the $|3\rangle \rightarrow |4\rangle$ transition and $\Delta_L < 0$.

We model the effect of the fourth level by simply introducing a periodic modulation of the two-photon resonance:

$$\Delta_c \rightarrow \Delta_c + \frac{\Delta_L}{2}(1 + \cos(2k_c z - 2\Delta t)) \tag{B.22}$$

in Eq. B.3. Here we consider the general case of a running standing wave, with the same notations as in the previous section. In our experiment, we will only focus on the case of a still standing wave ($\Delta = 0$). Eq. B.9 becomes:

$$\begin{aligned}\dot{\hat{\mathcal{S}}}^{(m)} = &- i\frac{\Delta_L}{2}\hat{\mathcal{S}}^{(m)} - i\frac{\Delta_L}{4}\left(\hat{\mathcal{S}}^{(m+2)} + \hat{\mathcal{S}}^{(m-2)}\right) \\ &+ im\Delta\hat{\mathcal{S}}^{(m)} - \left(\frac{\gamma}{2} - i\delta\right)\hat{\mathcal{S}}^{(m)} + \frac{i}{2}\Omega_+^*\hat{\mathcal{P}}^{(m+1)} + \frac{i}{2}\Omega_-^*\hat{\mathcal{P}}^{(m-1)}\end{aligned} \tag{B.23}$$

The periodic Stark-shift adds an offset $\Delta_L/2$ to the two-photon resonance, resulting from the average level-shift, as well as additional direct coupling terms between the spin harmonics $\hat{\mathcal{S}}^{(m)}$ and $\hat{\mathcal{S}}^{(m\pm2)}$. For a three-level system,the harmonic terms of the spin-wave expansion were only indirectly coupled through the polarization density terms $\hat{\mathcal{P}}^{(2m\pm1)}$ for $\Delta \neq 0$. Here, the coupling survives even on two-photon resonance ($\delta = 0$) and for $\Delta = 0$. As done previously, we can now solve the Heisenberg equation to derive the susceptibilities $\chi_{\pm,\pm}$ and mixing terms $\chi_{\pm,\mp}$ and integrate the coupled propagation equations B.19. Experimental and analytical results are described in Section 4.2.

Appendix C

Rydberg EIT: Analytical model

C.1 Theoretical model

Here we present a theoretical model for Rydberg EIT, for a quantized probe field. For the conditions of the experiment, the beam width is smaller than the transverse extent of the medium, so that the atomic density can be assumed constant across the beam. To simplify this presentation, we will initially neglect the decay of the $|g\rangle$-$|r\rangle$ coherence, consider a beam waist that is much smaller than the blockade radius r_b, and assume that the medium has uniform density along the propagation direction z. However, for the numerical analysis used for comparison with experiments, we will lift these last three assumptions, as discussed below.

We define the collective atom-photon coupling constant g_p (which has units of frequency) via $g_p^2 = \Gamma c(OD/L)$, where c is the speed of light and L is the length of the medium, which extends from $z = 0$ to $z = L$. Let $\hat{\mathcal{E}}^\dagger(z)$, $\hat{\mathcal{P}}^\dagger(z)$, and $\hat{\mathcal{S}}^\dagger(z)$ be the slowly-varying operators for the creation of a photon, an intermediate-state excitation ($|e\rangle$), and a Rydberg excitation ($|r\rangle$), respectively, at position z. These satisfy the same-time commutation relations $[\hat{\mathcal{E}}(z), \hat{\mathcal{E}}^\dagger(z')] = [\hat{\mathcal{P}}(z), \hat{\mathcal{P}}^\dagger(z')] = [\hat{\mathcal{S}}(z), \hat{\mathcal{S}}^\dagger(z')] = \delta(z - z')$. Note that $\hat{\mathcal{P}}(z)$ and $\hat{\mathcal{S}}(z)$ are only defined inside the medium. The Heisenberg equation of motion for $z < 0$ and $z > L$ (*i.e.* outside the medium) is simply

$$\partial_t \hat{\mathcal{E}}(z,t) \;=\; -c\partial_z \hat{\mathcal{E}}(z,t), \tag{C.1}$$

while for $z \in [0, L]$ (*i.e.* inside the medium) the equations of motion are [62]

$$\partial_t \hat{\mathcal{E}}(z,t) = -c\partial_z \hat{\mathcal{E}}(z,t) + i\frac{g_p}{2}\hat{\mathcal{P}}(z,t), \tag{C.2}$$

$$\partial_t \hat{\mathcal{P}}(z,t) = -\frac{\Gamma}{2}\hat{\mathcal{P}} + i\frac{g_p}{2}\hat{\mathcal{E}}(z,t) + i\frac{\Omega_c}{2}\hat{\mathcal{S}}(z,t), \tag{C.3}$$

$$\partial_t \hat{\mathcal{S}}(z,t) = i\frac{\Omega_c}{2}\hat{\mathcal{P}}(z,t) - i\int dz' V(z-z')\hat{\mathcal{S}}^\dagger(z')\hat{\mathcal{S}}(z')\hat{\mathcal{S}}(z), \tag{C.4}$$

where $V(z-z') = C_6/(z-z')^6 = (r_b/(z-z'))^6\Omega_c^2/(2\Gamma)$. Langevin noise can be omitted as it does not affect our calculations [62, 159].

We take the input state as a weak coherent state with real amplitude β in a single mode with an envelope $h(t)$. Thus, before the pulse has entered the medium, it is described by a wavefunction [205]

$$|\psi(t)\rangle = \exp[\beta(\hat{a}^\dagger - \hat{a})]|0\rangle, \tag{C.5}$$

where

$$\hat{a}^\dagger = \int dz h(t - z/c)\mathcal{E}^\dagger(z) \tag{C.6}$$

is the creation operator for a photon in mode $h(t)$, normalized according to $\int dz|h(t - z/c)|^2 = 1$, so that $[\hat{a}, \hat{a}^\dagger] = 1$. We assume that $h(t)$ is a long flat pulse, such that, except for some short transient period, $h(t)$ can be assumed constant most of the time; during that time, we then define $\alpha = \beta h(t)$. For a very low input photon flux, *i.e.* small α, it is sufficient to keep track of at most two photons, so that the wavefunction can be written as

$$\begin{aligned}
|\psi(t)\rangle = \epsilon|0\rangle + \textstyle\int_{-\infty}^{\infty} \mathrm{d}z E(z,t)\hat{\mathcal{E}}^\dagger(z)|0\rangle + \int_0^L \mathrm{d}z P(z,t)\hat{\mathcal{P}}^\dagger(z)|0\rangle + \int_0^L \mathrm{d}z S(z,t)\hat{\mathcal{S}}^\dagger(z)|0\rangle \\
+\tfrac{1}{2}\textstyle\int_{-\infty}^{\infty}\mathrm{d}z\int_{-\infty}^{\infty}\mathrm{d}z' EE(z,z',t)\hat{\mathcal{E}}^\dagger(z)\hat{\mathcal{E}}^\dagger(z')|0\rangle + \int_{-\infty}^{\infty}\mathrm{d}z\int_0^L \mathrm{d}z' EP(z,z',t)\hat{\mathcal{E}}^\dagger(z)\hat{\mathcal{P}}^\dagger(z')|0\rangle \\
+\tfrac{1}{2}\textstyle\int_0^L\mathrm{d}z\int_0^L\mathrm{d}z' PP(z,z',t)\hat{\mathcal{P}}^\dagger(z)\hat{\mathcal{P}}^\dagger(z')|0\rangle + \int_{-\infty}^{\infty}\mathrm{d}z\int_0^L\mathrm{d}z' ES(z,z',t)\hat{\mathcal{E}}^\dagger(z)\hat{\mathcal{S}}^\dagger(z')|0\rangle \\
+\tfrac{1}{2}\textstyle\int_0^L\mathrm{d}z\int_0^L\mathrm{d}z' SS(z,z',t)\hat{\mathcal{S}}^\dagger(z)\hat{\mathcal{S}}^\dagger(z')|0\rangle + \int_0^L\mathrm{d}z\int_0^L\mathrm{d}z' PS(z,z',t)\hat{P}^\dagger(z)\hat{\mathcal{S}}^\dagger(z')|0\rangle
\end{aligned} \tag{C.7}$$

where the first line describes the vacuum and the single-excitation component, while the last three lines describe the double-excitation component. Without loss of generality, we take $EE(z,z') = EE(z',z)$, $PP(z,z') = PP(z',z)$, and $SS(z,z') = SS(z',z)$. Spontaneous emission, in general, requires a density matrix description. However, in the weak-field limit ($\alpha \ll 1$), the change of the single-excitation component due to the decay of the double-excitation component is negligible, so that the wavefunction treatment – as in the stochastic wavefunction formalism [206] – is sufficient. Similarly, in the weak-field limit, we can take $\epsilon = 1$ in Eq. (C.7).

The single-excitation component of $|\psi(t)\rangle$ is not subject to interactions and, thus, propagates through the EIT medium unperturbed. Since we took $h(t) \approx \alpha/\beta$, Eqs. (C.5,C.7), therefore, give a simple time-independent solution $E(z,t) = \alpha$. A time-dependent solution would give (in the limit $g_p \gg \Omega_c$) the EIT group velocity $v_g = \Omega_c^2 c/g_p^2$, EIT time delay $\tau_d = OD \cdot \Gamma/\Omega_c^2$, and EIT transparency window with width $B = \Omega_c^2/(\Gamma\sqrt{8 \cdot OD})$ (*i.e.* in frequency-space $|E(\omega, L)|^2 \propto \exp[-\omega^2/(2B^2)]$) [202] (see also Appendix A).

We now turn to the two-excitation component of $|\psi(t)\rangle$. Letting z and z' be the coordinates of the two excitations, we divide the z-z' plane into nine regions [see Fig. C-1]. To obtain the equations governing the two-particle amplitudes in these regions, we use Eqs. (C.2-C.4) and identities of the form $EE(z,z') = \langle 0|\hat{\mathcal{E}}(z)\hat{\mathcal{E}}(z')|\psi\rangle$ and $ES(z,z') = \langle 0|\hat{\mathcal{E}}(z)\hat{\mathcal{S}}(z')|\psi\rangle$.

In region 7, neither of the photons has entered the medium, and, $EE(z,z') = \alpha^2$, which follows from matching Eqs. (C.5) and (C.7). This gives a time-independent boundary condition

$$EE(z, z' = 0) = \alpha^2 \tag{C.8}$$

for region 4, where the equations of motion are

$$\partial_t EE(z,z') = -c(\partial_z + \partial_{z'})EE(z,z') + igEP(z,z'), \tag{C.9}$$

$$\partial_t EP(z,z') = -(c\partial_z + \Gamma/2)EP(z,z') + igEE(z,z') + i\Omega ES(z,z'), \tag{C.10}$$

$$\partial_t ES(z,z') = -c\partial_z ES(z,z') + i\Omega EP(z,z'), \tag{C.11}$$

where we have defined $\Omega = \Omega_c/2$, $g = g_p/2$ to simplify the notation. These equations

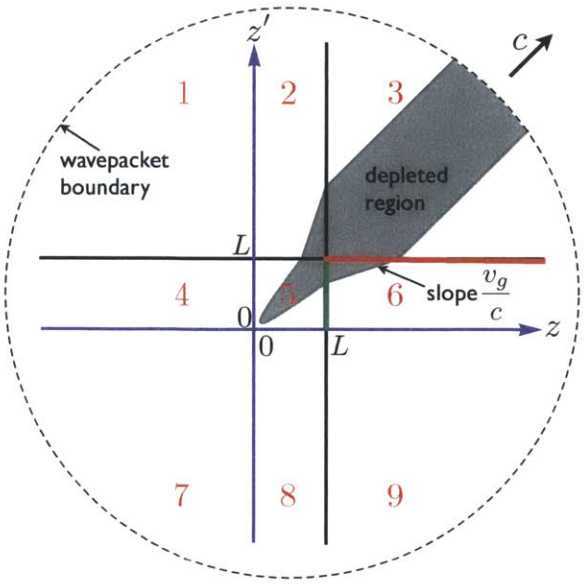

Figure C-1: **The schematic diagram of the two-particle wavefunction.** z and z' are the coordinates of the two particles, and the medium extends from 0 to L. In regions 1, 3, 7, and 9, both excitations are outside the medium. In regions 2, 4, 6, and 8, one excitation is inside the medium, while the other one is outside. Finally, in region 5, which is shown in Fig. 7-6, both excitations are inside the medium. We assume that the incident wavepacket is much longer than the extent of the medium (even after EIT compression). Therefore, the two-excitation wavepacket (boundary shown by the dashed line), which is moving in the top-right direction with c, is much larger than region 5. The distortion of the wavepacket's boundary due to EIT time delay is not shown. For the ease of presentation, the broadening of the depletion region in region 6 assumes $c/v_g = 3$ (in the experiment, c/v_g is 5 orders of magnitude larger).The diagram is symmetric across the line $z = z'$, and it is not necessary to define, for example, separate amplitudes for $\hat{\mathcal{E}}^\dagger(z)\hat{\mathcal{S}}^\dagger(z')$ and $\hat{\mathcal{E}}^\dagger(z')\hat{\mathcal{S}}^\dagger(z)$ (see Eq. C.7).

describe the propagation of the photon component at position z outside the medium at the speed of light and the propagation of the Rydberg polariton at position z' inside the EIT medium. The time-independent boundary condition Eq. (C.8) gives rise to a steady-state solution of Eqs. (C.9-C.11), which, together, with a symmetric solution in region 8,

gives boundary conditions for region 5:

$$EE(z=0,z') = EE(z,z'=0) = \alpha, \tag{C.12}$$

$$ES(z=0,z') = -\alpha g/\Omega, \tag{C.13}$$

$$EP(z=0,z') = 0. \tag{C.14}$$

Note that these boundary conditions satisfy the ideal dark-state polariton relationship [202]. In region 5, both excitations are inside the medium and are subject to interactions as described by the following propagation equations:

$$\partial_t EE(z,z') = -c(\partial_z + \partial_{z'})EE(z,z') + ig(EP(z,z') + EP(z',z)), \tag{C.15}$$

$$\partial_t EP(z,z') = -(c\partial_z + \frac{\Gamma}{2})EP(z,z') + ig(EE(z,z') + PP(z,z')) + i\Omega ES(z,z'), \tag{C.16}$$

$$\partial_t ES(z,z') = -c\partial_z ES(z,z') + igPS(z,z') + i\Omega EP(z,z'), \tag{C.17}$$

$$\partial_t PS(z,z') = -(\Gamma/2)PS(z,z') + igES(z,z') + i\Omega(PP(z,z') + SS(z,z')), \tag{C.18}$$

$$\partial_t PP(z,z') = -\Gamma PP(z,z') + ig(EP(z,z') + EP(z',z)) + i\Omega(PS(z,z') + PS(z',z)), \tag{C.19}$$

$$\partial_t SS(z,z') = i\Omega(PS(z,z') + PS(z',z)) - iV(z-z')SS(z,z'). \tag{C.20}$$

The time-independent boundary conditions [Eqs. (C.12-C.14)] allow us to solve Eqs. (C.15-C.20) in steady state. The resulting depletion of $|EE(z,z')|^2$ in region 5 is shown schematically in Fig. C-1 and is plotted in Fig. 7-6. This gives a boundary condition at $z = L$ to region 6, which, together with the boundary condition $EE(z > L, 0) = \alpha$, yields a steady-state solution in region 6, where Eqs. (C.9-C.11) hold. Finally, in region 3, both photons are outside the medium, so $EE(z,z')$ is constant along constant $(z - z')$, and $g^{(2)}(\tau)$ can be read out from the top boundary of region 6 [red line in Fig. C-1] using c as a conversion factor (and normalizing by $|E(z)|^4$) [205]:

$$g^{(2)}(\tau) = |EE(z = L + c\tau, z' = L)|^2/|\alpha|^4. \tag{C.21}$$

It is important to point out that, since EE is proportional to α^2, $g^{(2)}(\tau)$ does not depend

on α. It is also important to emphasize that the steady-state equations in region 6 [Eqs. (C.9-C.11) with left-hand-sides replaced with 0] are equivalent to the time-dependent propagation of a single-photon along z' with z/c playing the role of time. Therefore, the steady-state depletion feature in $EE(z, z')$ on the left boundary of region 6 [green line in Fig. C-1] is converted into $g^{(2)}(\tau)$ in two steps. First, ignoring the effects of finite EIT bandwidth, this feature is scaled up by c/v_g and is mapped onto the top boundary of region 6 [red line in Fig. C-1]. Second, it is converted to $g^{(2)}(\tau)$ using the speed of light via Eq. (C.21). Thus, to a good approximation,

$$g^{(2)}(\tau) \approx |EE(z = L, z' = L - v_g\tau)|^2/|\alpha|^4, \tag{C.22}$$

an expression we will use below for analytical calculations.

To compute $g^{(2)}(\tau)$ numerically for comparisons to the experiment, we extend the model to include several additional effects. First, we introduce the measured decay rate $\gamma/2 \approx 250$ kHz of the operator $\hat{\mathcal{S}}$ in Eq. (C.4). The effect of this spin-wave decoherence on $g^{(2)}(\tau)$ is, however, very weak. Second, we include the longitudinal variation in the density $\mathcal{N}(z)$ by replacing g^2 with $[\frac{\Gamma}{2}cOD/(2\sigma_z)]\exp(-z^2/(2\sigma_z^2))/\sqrt{2\pi}$, where σ_z is the longitudinal width of the Gaussian density profile. In this case, the entire z-z' plane is governed by the correspondingly generalized Eqs. (C.15-C.20). Finally, we take into account the transverse extent of the beam by writing $V(z - z') = C_6[(z - z')^2 + r_\perp^2]^{-3}$, where $r_\perp$ is the transverse distance between the two incoming photons whose probability distribution is determined by the Gaussian transverse profile of the probe beam. Neglecting probe-beam diffraction, this amounts to solving Eqs. (C.15-C.20) for different $r_\perp$; the numerator in $g^{(2)}(\tau)$ [Eq. (C.21)] is then computed by taking an average over the $r_\perp$ distribution. The results of these calculations are compared to the experimental measurements in Fig. C-2 and in Figs. 7-2,b, 7-5 and show very good agreement. We achieve best agreement for a beam waist of $w_0 = 6\mu$m, which is slightly larger than the measured value of 4.5 μm, possibly due to imperfect positioning of the cloud relative to the waist and due to finite diffraction of the beam along the length of the atomic cloud. In contrast to Fig. 7-5, where the experimental detection noise is included in both the theory and the experiment, in Fig. C-2, the detection noise is not included in the theory and is subtracted from the experimental data.

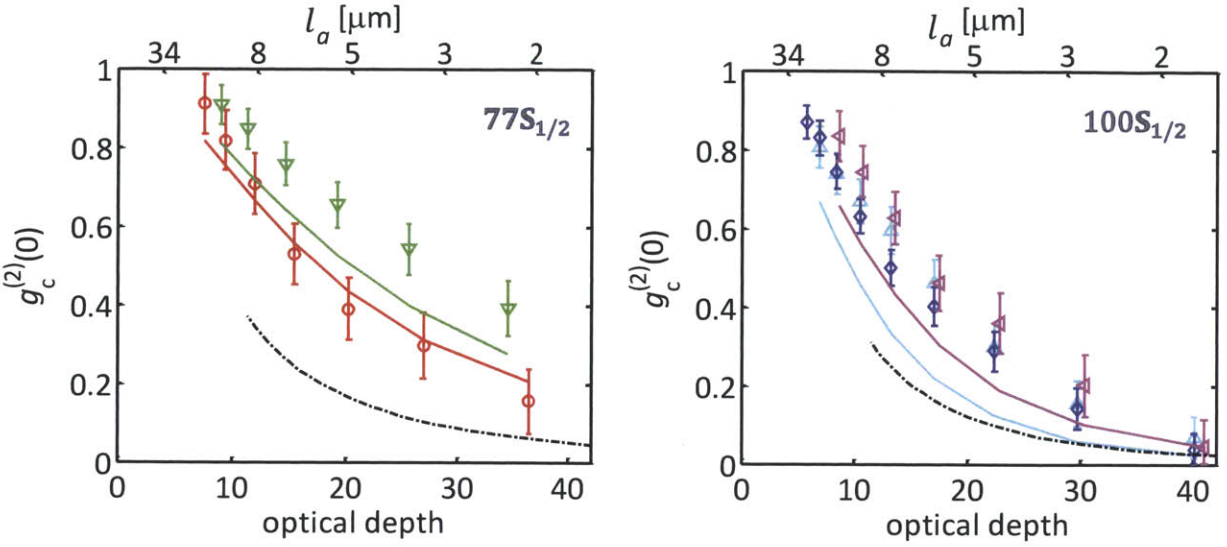

Figure C-2: **Comparison with numerical and analytical models.** Measured same-time photon-photon correlation function for $|r\rangle$=77S$_{1/2}$ (left) and 100S$_{1/2}$ (right) with EIT linewidths γ_{EIT}=20 ($\circ$), 27($\triangledown$), 16($\triangle$), 22,($\diamond$), 26($\triangleleft$) MHz. All curves are rescaled to compensate for background and noise detection events [hence the subscript c in $g_c^{(2)}(0)$]. The solid color curves correspond to numerical simulation, following Eqs. (C.15-C.20) in the steady state and taking into account the transverse Gaussian profile of the probe beam, the longitudinal density variation, and the decay of the $|g\rangle$-$|r\rangle$ coherence. The black dot-dash curve is the solution Eq. (C.42) to the one-dimensional diffusion equation (C.40) in the limit of large OD and assuming that $\mathcal{V}(r)$ is a step function of size $2r_b$, for γ_{EIT}=20 MHz and $L = 4.2\sigma_z$. For $|r\rangle$=100S$_{1/2}$, where $r_b/w_0 \sim 3$, the solution to the simple one-dimensional diffusion equation, the numerical simulation, and the measurements converge at high atomic density.

C.2 Approximate effective description: diffusion equation with local loss

In order to obtain an approximate single equation describing the steady-state behavior of the two-particle wavefunction, we now analyze the steady state of Eqs. (C.15-C.20). We define $ES_\pm(z,z') = (ES(z,z') \pm ES(z',z))/2$, $EP_\pm(z,z') = (EP(z,z') \pm EP(z',z))/2$, and $PS_\pm(z,z') = (PS(z,z') \pm PS(z',z))/2$, as well as center-of-mass and relative coordinates $R = (z+z')/2$ and $r = z-z'$ of the two excitations. To simplify the equations, we further define $U(r) = 2 \cdot V(r) \cdot \Gamma/\Omega_c^2$ (then $U(r_b) = 1$) and rescale time and all frequencies by

$\frac{\Gamma}{2}$, while spatial coordinates are rescaled by $2c/\Gamma$. In steady-state, Eqs. (C.15-C.20) then become

$$
\begin{aligned}
0 &= -\partial_R EE + i2gEP_+, && \text{(C.23)}\\
0 &= -\tfrac{1}{2}\partial_R EP_+ - \partial_r EP_- - EP_+ + ig(EE + PP) + i\Omega ES_+, && \text{(C.24)}\\
0 &= -\tfrac{1}{2}\partial_R EP_- - \partial_r EP_+ - EP_- + i\Omega ES_-, && \text{(C.25)}\\
0 &= -\tfrac{1}{2}\partial_R ES_+ - \partial_r ES_- + igPS_+ + i\Omega EP_+, && \text{(C.26)}\\
0 &= -\tfrac{1}{2}\partial_R ES_- - \partial_r ES_+ + igPS_- + i\Omega EP_-, && \text{(C.27)}\\
0 &= -PS_+ + igES_+ + i\Omega(PP + SS), && \text{(C.28)}\\
0 &= -PS_- + igES_-, && \text{(C.29)}\\
0 &= -2PP + i2gEP_+ + i2\Omega PS_+, && \text{(C.30)}\\
0 &= i2\Omega PS_+ - i\Omega^2 USS. && \text{(C.31)}
\end{aligned}
$$

We next simplify these equations using a number of approximations. For the parameters studied in this experiment, we checked numerically that the following are all excellent approximations (except near $R = 0$, the error in EE after all the approximations is at most a few percent). Here we simply list the steps leading to the effective equation, while the full derivation and analysis will be presented elsewhere. We solve Eqs. (C.29,C.30) for PS_- and EP_+, respectively, and insert the results into Eqs. (C.27,C.23), respectively. We neglect all but two terms that form the dominant balance in Eqs. (C.24,C.25,C.27) – this determines how variables adiabatically follow each other. We also neglect the last term in Eq. (C.26). Finally, we combine Eqs. (C.28,C.31) into an expression for PS_+ by eliminating SS. The result is

$$
\begin{aligned}
0 &= -\partial_R EE + 2PP - i2\Omega PS_+, && \text{(C.32)}\\
0 &= -\partial_r EP_- + igPP, && \text{(C.33)}\\
0 &= -EP_- + i\Omega ES_-, && \text{(C.34)}\\
0 &= -\tfrac{1}{2}\partial_R ES_+ - \partial_r ES_- + igPS_+, && \text{(C.35)}\\
0 &= -\partial_r ES_+ - g^2 ES_-, && \text{(C.36)}\\
PS_+ &= ig\mathcal{V}(r)ES_+ + i\Omega\mathcal{V}(r)PP, && \text{(C.37)}
\end{aligned}
$$

where

$$\mathcal{V}(r) = \frac{1}{1 - 2i(r/r_b)^6} \tag{C.38}$$

defines whether $|r|$ is larger or smaller than r_b [62]. Eliminating EP_- and PP from Eqs. (C.32-C.34), we find that $-(g/\Omega)EE$ obeys the same equation of motion as ES_+ in Eq. (C.35). Since $-(g/\Omega)EE$ also has the same boundary conditions as ES_+, $EE = -(\Omega/g)ES_+$ at all R and r. This means that ES_+ and EE obey the dark-state-polariton relationship for all R and r [202]. This is a surprising result, as one would not naively expect this relationship to hold within the blockaded region. Eliminating EP_-, PP, ES_-, and PS_+ from Eqs. (C.33-C.37), we find a closed diffusion equation for ES_+:

$$\partial_R ES_+ = -2g^2\mathcal{V}(r)ES_+ + \frac{2}{g^2}\left(1 + \Omega^2\mathcal{V}(r)\right)\partial_r^2 ES_+. \tag{C.39}$$

Since $EE = -(\Omega/g)ES_+$, EE obeys the same equation. Reverting to the original units, we obtain Eq. (7.1) (with $l_a = L/OD$):

$$\partial_R EE = -\frac{OD}{L}\mathcal{V}(r)EE + \frac{4L}{OD}\left(1 + \left(\frac{\Omega_c}{\Gamma}\right)^2\mathcal{V}(r)\right)\partial_r^2 EE. \tag{C.40}$$

$g^{(2)}(\tau)$ can be read out from the solution of this equation along the boundary $z = L$ [green line in Fig. C-1] via Eq. (C.22). It is remarkable that, for the full range of parameters considered in this experiment, the set of nine equations (C.23-C.31) is well-approximated by a single simple diffusion equation with a local loss term. The second term on the right-hand-side of Eq. (C.40) is the diffusion term, while the first term is the local loss term. Outside of the blockade radius ($\mathcal{V}(r) = 0$), we have a pure diffusion equation with a $4L/OD$ diffusion coefficient and no loss. Inside the blockade radius ($\mathcal{V}(r) = 1$), the diffusion coefficient is increased to $4(1 + (\Omega_c/\Gamma)^2)L/OD$. An increase in the diffusion coefficient increases $g^{(2)}(0)$ and increases the width at half-maximum τ_c of the dip in $g^{(2)}(\tau)$. In particular, a larger Ω_c gives a larger $g^{(2)}(0)$. The local loss term is nonzero on a strip of width $\approx 2r_b$ (or more precisely $\approx 2r_b/2^{1/6}$) where it has rate OD/L. This amplitude OD/L is consistent with physical intuition: $|EE|^2$ decays as $|EE(R = L)|^2 \propto |EE(R = 0)|^2 \exp(-2OD)$ – the factor of 2 accounts for the fact that either of the two

photons can be absorbed. The physics of this diffusion equation is as follows: the local loss term tries to deplete a narrow strip of width $\approx 2r_b$, while the diffusion term competes with the loss, preventing the depleted region from being too narrow. The diffusion term comes from the fact that the EIT medium cannot support without loss features narrower than the EIT bandwidth B [202]. Its effect is illustrated by the following simple situation. Suppose we had no loss term and an incoming boundary condition $EE(0,r) = \delta(r)$. Then $EE(L,r)$ will acquire a width $\sim L/\sqrt{OD}$. Converting to time using v_g, we would have a width $\sim L/(v_g\sqrt{OD}) = \tau_d/\sqrt{OD} \sim 1/B$ in agreement with the EIT bandwidth limit.

As we have already stated, this simple diffusion equation matches extremely well the solution of the full set of equations with a homogeneous density profile in the 1D-channel geometry (*i.e.* $r_\perp = 0$). When the longitudinal density variation $\mathcal{N}(z) \propto \exp[-z^2/(2\sigma_z^2)]$ is included, the solution to the diffusion equation also agrees well with the solution of the full set of equations provided we take $L \approx 4.2\sigma_z$.

Under the approximation that $\mathcal{V}(r)$ is a delta function or a step function and assuming the boundary conditions are along $R = 0$ and $r = \pm\infty$, Eq. (C.40) can be solved analytically using a Laplace transformation in R. The inverse Laplace transform can be taken exactly in certain limits.

Specifically, in the case of $\mathcal{V}(r) \approx 2r_b\delta(r)$, we find that $g^{(2)}(0)$ depends only on $x \equiv OD_b\sqrt{OD}$, where $OD_b = OD \cdot r_b/L$ is the blockaded optical depth [62]. In particular, for $x \ll 1$, $g^{(2)}(0) \approx 1 - x\sqrt{2/\pi}$, while for $x \gg 1$, $g^{(2)}(0) \approx 8/(\pi x^2)$. For $x \gg 1$, the width of the dip in $|EE(L - r/2, r)|^2$ is given by $\approx 4\text{InverseErfc}[1 - 2^{-1/2}]/\sqrt{OD} \approx 3/\sqrt{OD}$. To get to the time units, one has to multiply by the EIT time delay τ_d, so we get the correlation time

$$\tau_c \approx 1.05/B, \tag{C.41}$$

as expected from the physical intuition that the EIT medium cannot support without loss features wider in frequency space than B. Eq. (C.41) is shown as a dashed line in Fig. 7-5,d. It is remarkable that this simple formula derived by analytically solving the diffusion equation with delta-function loss term matches extremely well the experimental results.

In the case of $\mathcal{V}(r)$ being a unit step of length $2r_b$ [*i.e.* $f(|r| < r_b) = 1$ and $f(|r| >$

$r_b) = 0]$, in the limit of large OD, we find:

$$g^{(2)}(0) \approx \frac{4(1+(\Omega_c/\Gamma)^2)}{\pi OD} \exp\left[-\frac{OD_b}{\sqrt{1+(\Omega_c/\Gamma)^2}}\right]. \tag{C.42}$$

In Fig. C-2, we compare this analytical result to the full numerical solution and to the experimental data and find good agreement for the $100S_{1/2}$ Rydberg state (for which the propagation becomes nearly one-dimensional) in the limit of large OD. Eq. (C.42) expresses in a precise mathematical language the qualitative statements made in Chapter 7. Indeed, while $g^{(2)}(0)$ drops exponentially as one increases OD_b beyond unity, the reduction in $g^{(2)}(0)$ due to an increase in OD (for a fixed OD_b) is much slower ($\sim 1/OD$). We also see from Eq. (C.42), that the condition for the blockade to work used in Chapter 7 ($OD_b > 1$) can be stated more precisely as $OD_b^2 > 1 + (\Omega_c/\Gamma)^2$. This condition simply means that the loss term must exceed the diffusion (with $\mathcal{V} = 1$) on the length scale of the blockade radius, as stated in Chapter 7. One possible interpretation of this more precise condition is an effective renormalization of r_b when $\Omega_c \gtrsim \Gamma$. This interpretation is also supported by the fact that the blockade radius of SS can be shown to be determined by the same renormalized r_b.

Appendix D

Rydberg EIT in the dispersive regime: Schroedinger equation

D.1 Derivation of the Schroedinger equation

In this section, we present the theoretical framework describing photon interctions in the dispersive regime of Rydberg EIT, following the approach for the dissipative regime described in Appendix C. To a good approximation, the atomic density is constant across the probe beam, and all experiments are done in the regime where the blockade radius is larger than the beam waist. For these reasons, a one-dimensional approximation holds. Along the propagation direction z, we consider a Gaussian atomic density $\rho(z) = \exp[-z^2/(2\sigma_z^2)]$, normalized by the peak density ρ_0, with root-mean-square width σ_z. We define the peak atom-photon coupling constant g_p via $g_p^2/(\Gamma c) = \rho_0\sigma_0 = OD/(\sqrt{2\pi}\sigma_z)$, where σ_0 is the resonant atomic cross-section and OD the resonant optical depth of the medium. We consider the evolution of the slowly varying operators $\hat{\mathcal{E}}^\dagger(z)$, $\hat{\mathcal{P}}^\dagger(z)$, and $\hat{\mathcal{S}}^\dagger(z)$ corresponding to the creation of a photon, an intermediate-state excitation ($|e\rangle$), and a Rydberg excitation ($|r\rangle$), respectively, at position z. These satisfy the same-time commutation relations $[\hat{\mathcal{E}}(z), \hat{\mathcal{E}}^\dagger(z')] = [\hat{\mathcal{P}}(z), \hat{\mathcal{P}}^\dagger(z')] = [\hat{\mathcal{S}}(z), \hat{\mathcal{S}}^\dagger(z')] = \delta(z - z')$. The

Heisenberg equations of motion are then given by [62]

$$\partial_t \hat{\mathcal{E}}(z,t) = -c\partial_z \hat{\mathcal{E}}(z,t) + i\frac{g_p}{2}\sqrt{\rho(z)}\hat{\mathcal{P}}(z,t), \tag{D.1}$$

$$\partial_t \hat{\mathcal{P}}(z,t) = -\left(\frac{\Gamma}{2} - i(\Delta+\delta)\right)\hat{\mathcal{P}}(z,t) + i\frac{g_p}{2}\sqrt{\rho(z)}\hat{\mathcal{E}}(z,t) + i\frac{\Omega_c}{2}\hat{\mathcal{S}}(z,t), \tag{D.2}$$

$$\partial_t \hat{\mathcal{S}}(z,t) = -\left(\frac{\gamma}{2} - i\delta\right)\hat{\mathcal{S}}(z,t) + i\frac{\Omega_c}{2}\hat{\mathcal{P}}(z,t) - i\int dz' V(z-z')\hat{\mathcal{S}}^\dagger(z',t)\hat{\mathcal{S}}(z',t)\hat{\mathcal{S}}(z,t), \tag{D.3}$$

where $V(z) = C_6/z^6$, $\Delta = \omega_{re} - \omega_c$ and $\delta = \omega_p + \omega_c - \omega_{rg}$. Here ω_p and ω_c are the probe and control frequencies, while ω_{re} and ω_{rg} are the $|e\rangle \rightarrow |r\rangle$ and $|g\rangle \rightarrow |r\rangle$ transition frequencies, respectively. The Langevin noise is omitted since it does not affect our calculations. As in Appendix C, the input is assumed to be a weak coherent state of the form

$$\exp\left[\alpha\int dz(\hat{\mathcal{E}}^\dagger(z) - \hat{\mathcal{E}}(z))\right]|0\rangle, \tag{D.4}$$

where, for simplicity, α is assumed to be real. The single-photon and two-photon probability amplitudes are defined as $E(z) = \langle 0|\hat{\mathcal{E}}(z)|\Psi\rangle$ and $EE(z_1,z_2) = \langle 0|\hat{\mathcal{E}}(z_1)\hat{\mathcal{E}}(z_2)|\Psi\rangle$, respectively, where $|\Psi\rangle$ is the wavefunction of the system while $|0\rangle$ is the vacuum state. We define

$$\psi(z_1,z_2) = \frac{EE(z_1,z_2)}{E(z_1)E(z_2)}, \tag{D.5}$$

which is unity in the absence of interactions, and

$$\psi(\tau) = \psi(z_1 = z_0 + c\tau, z_2 = z_0), \tag{D.6}$$

where z_0 is chosen to be outside of the medium: $z_0 \gg \sigma_z$. Then $g^{(2)}(\tau) = |\psi(\tau)|^2$ and $\phi(\tau) = \arg\psi(\tau)$, provided that the single-photon component dominates the denominator of $g^{(2)}$. (This approximation may break down in the presence of strong linear absorption.)

In order to compute $\psi(\tau)$ numerically (solid lines in Figs. 8-5,c and 8-5d, and solid blue lines in Fig. 8-6), we follow the approach described in Appendix C. In particular, the

denominator in $\psi(\tau)$ can be easily found analytically using the EIT linear susceptibility:

$$E(z \geq z_0) = \alpha \exp\left[-\frac{\frac{\Gamma}{2}\left(\frac{\gamma}{2} - i\delta\right)\frac{OD}{2}}{\left(\frac{\Omega_c}{2}\right)^2 + \left(\frac{\Gamma}{2} - i(\Delta+\delta)\right)\left(\frac{\gamma}{2} - i\delta\right)}\right]. \tag{D.7}$$

This formula (divided by α) is used to obtain the blue and, for $\Omega_c = 0$, the gray dashed curves in Fig. 8-1 and in Fig. 8-2,a. It also shows that peak linear transmission is at $\delta = -\frac{\Delta\gamma}{\Gamma} + \mathcal{O}(\gamma^2)$, while peak (Raman) absorption is at $\delta = \frac{\Omega_c^2}{4\Delta}\left(1 - \frac{\gamma^2}{\Omega_c^2}\right)\left(1 + \frac{\Gamma\gamma}{\Omega_c^2}\right) + \mathcal{O}(\Delta^{-3})$.

To obtain analytical insight into the physics underlying the numerator of $\psi(\tau)$, we approximate the medium as a homogeneous slab with length $L = 4.2\sigma_z$ (see Appendix C), *i.e.* we re-define $\rho(z)$ to be 1 in $[0, L]$ and 0 otherwise and rescale g_p^2 by $\sqrt{2\pi}\sigma_z/L$. Furthermore, we take $\delta = \gamma = 0$, so that, in particular, $E(z) = \alpha$. Then for $z_1, z_2 \in [0, L]$, repeating the same approximations as in Appendix C, we obtain a Schroedinger-like equation for the two-photon probability amplitude

$$i\partial_R EE(R, r) = \left[-\frac{1}{2\tilde{m}(r)}\partial_r^2 + U(r)\right] EE(R, r), \tag{D.8}$$

where the spatially dependent mass $\tilde{m}(r)$ and potential $U(r)$ are given by

$$-\frac{1}{2\tilde{m}(r)} = \frac{4L}{OD}\left(\frac{2\Delta}{\Gamma} + i - \left(\frac{\Omega_c}{\Gamma}\right)^2 \mathcal{V}(r)\right), \tag{D.9}$$

$$U(r) = \frac{OD}{L}\mathcal{V}(r), \tag{D.10}$$

and

$$\mathcal{V}(r) = \frac{1}{\frac{2\Delta}{\Gamma} + i + 2\frac{r^6}{r_b^6}}. \tag{D.11}$$

Here $R = (z_1 + z_2)/2$, $r = z_1 - z_2$, and the resonant blockade radius is defined as $r_b = (2\Gamma C_6/\Omega_c^2)^{1/6}$. The initial condition is a uniform wavefunction $EE(z_1 = 0, z_2) = EE(z_1, z_2 = 0) = \alpha^2$.

By comparing the solutions of Eq. (D.8) with numerical simulations of the full dynamics, we find that for $\Delta \neq 0$, this equation does not approximate the full dynamics as well as it does for $\Delta = 0$, with the error in EE as large as $\sim 20\%$. However, we find that

it still captures the main qualitative features of the two-photon evolution. In the regime $|\Delta| \gg \Gamma, \Omega_c$, an excellent agreement with the full dynamics can be achieved by keeping higher-order derivatives in the effective equation.

In the presence of nonzero Δ, the blockade radius is increased to $\bar{r}_B = r_b \left(\left(\frac{2\Delta}{\Gamma}\right)^2 + 1 \right)^{1/12}$. In the limit of $|\Delta| \gg \Gamma$, it corresponds to the off-resonant blockade radius $r_B = (4\,|\Delta|\, C_6/\Omega_c^2)^{1/6}$, defined in Chapter 8. Outside the blockade region, $\tilde{m}(r > \bar{r}_B)$ stems directly from the effective mass of a single dark-state polariton, which, in the limit $|\Delta| \gg \Gamma$, is given by [207, 106, 95]

$$m = \frac{2\hbar}{v_g}\tilde{m} = -\frac{1}{16\pi}\frac{c}{v_g}\frac{\lambda}{l_a}\frac{\Gamma}{\Delta}\frac{\hbar\omega}{c^2}. \tag{D.12}$$

For our parameters, at the center of the medium, it corresponds to $|m| \approx 10^3 \frac{\hbar\omega}{c^2}$.

These considerations indicate that, for $\Delta > 0 (< 0)$ and $|\Delta| \gg \Gamma, \Omega_c$, we obtain a Schroedinger equation with negative (positive) mass and a potential barrier (dip) within the blockade radius. Note that, for the boundary value problem, the solution for a negative mass and a repulsive potential is formally equivalent to that for a positive mass and an attractive potential under the exchange $EE \rightarrow EE^*$. However, for $\Delta < 0$, $\mathcal{V}(r)$, and hence the potential, have a resonant Raman feature around the blockade radius, which breaks this symmetry.

To simplify the analysis, we make an additional approximation by assuming that the boundary conditions are $EE(R = 0, r) = EE(R, r = \pm\infty) = \alpha^2$. We find that this approximation is more forgiving than the approximations used in the derivation of Eq. (D.8). Dropping the r-dependent term in the effective mass (since it is typically small) and approximating the potential with a square well, we end up with a Schroedinger equation with a complex mass and a square-well potential with a complex amplitude, which can be solved directly (see, *e.g.*, the top theoretical curve in Fig. 1d of Chapter 8). The analytical solution is further simplified if one approximates the square-well potential with a δ function of the same area. This is a reasonable approximation because the variations in $EE(R, r)$ occur at a scale much larger than $\bar{r}_B$; for $|\Delta| \gg \Gamma$, when the mass and the potential are real, this follows from the fact that there is a single bound state and its extent is much larger than $\bar{r}_B$, as we will verify below. The mass and the potential then

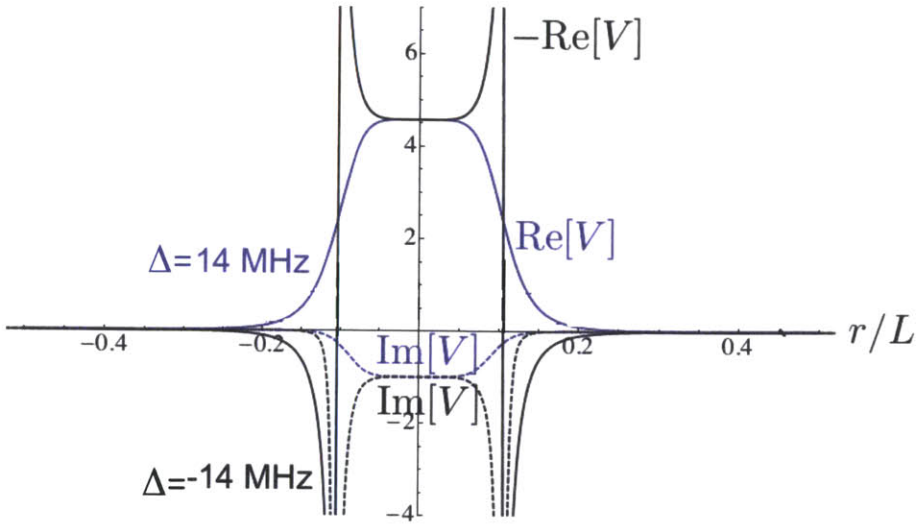

Figure D-1: **The shape of the effective potential well.** Effective potential V of the Schroedinger-like equation D.8 for a blue-detuned ($\Delta = 14$ MHz, blue lines, negative effective mass) and red-detuned ($\Delta = -14$ MHz, black lines, positive effective mass) probe field on two-photon resonance, for $\Omega_c = 10$ MHz. The real part of the potential (full lines) generally dominates over the imaginary part (dashed lines). For a blue-detuned probe, the potential displays additional feature at $r \sim r_B$ corresponding to the resonance with the two-photon Raman absorption.

simplify to

$$\begin{aligned} -\frac{1}{2\tilde{m}} &= \frac{4L}{OD}\left(\frac{2\Delta}{\Gamma}+i\right), \\ U(r) &= c_0 2OD_B \frac{1}{\frac{2\Delta}{\Gamma}+i}\delta(r), \end{aligned} \tag{D.13}$$

where $OD_B = OD \times \bar{r}_B/L$ is the optical depth within a blockade radius and $c_0 = \frac{\pi}{2^{1/6}3} e^{i \arg\left(\frac{2\Delta}{\Gamma}+i\right)^{1/6}}$ is chosen to keep $\int dr U(r)$ unchanged under the approximation. For $|\Delta| \gg \Gamma$, $\arg(c_0) = 0$ and $\pi/6$ for $\Delta > 0$ and $\Delta < 0$, respectively, accounting for non-negligible Raman absorption for $\Delta < 0$ and capturing the asymmetry between positive and negative Δ in Fig. 8-6. The resulting problem is equivalent to a free-particle Schroedinger equation on $R \in [0, L]$ and $r \in [0, \infty]$ with mixed boundary conditions at

$r = 0$. Using Laplace transformation in R, we find

$$\psi(\tau = 0) = \psi(R = L, r = 0) = e^{u^2}\mathrm{erfc}(u), \tag{D.14}$$

where erfc is the complementary error function and

$$u = \frac{c_0\sqrt{OD}OD_B}{2\left(1 - i\frac{2\Delta}{\Gamma}\right)^{3/2}}. \tag{D.15}$$

This formula was used to make the solid black curves in Figs. 8-6. At small u, we have $\psi(\tau = 0) - 1 = -\frac{2u}{\sqrt{\pi}} + O(u^2)$, which, for $|\Delta| \gg \Gamma$, gives $\arg[\psi(0) - 1] = \pm\pi/4 + \arg(c_0)$ for $\Delta \lessgtr 0$.

Within the δ-function approximation and by further assuming that $\Delta \gg \Gamma$, we obtain a real (negative) mass and a real (positive) potential. To get insight into the role of the bound state, we solve for the dynamics in this case analytically:

$$\psi(R, r) = \psi_b(R, r) + \psi_s(R, r), \tag{D.16}$$

where ψ_b and ψ_s are the contributions of the bound state and the scattering states, respectively,

$$\psi_b(R, r) = 2e^{-\kappa|r|}e^{-i8\kappa^2 RL\Delta/(OD\Gamma)}, \tag{D.17}$$

$$\psi_s(R, r) = \int_0^\infty dk \frac{i(b_k^{-1} - 1)}{2\pi k}\left(e^{ik|r|} + b_k e^{-ik|r|}\right)e^{i8k^2 RL\Delta/(OD\Gamma)}, \tag{D.18}$$

$\kappa = c_0(OD\Gamma/\Delta)^2\bar{r}_B/(16L^2)$ and $b_k = (ik + \kappa)/(ik - \kappa)$. Taking $OD = 22$, $\Delta = 14$ MHz, and $\Omega_c = 10$ MHz, the condition $\kappa\bar{r}_B \approx 1/14 \ll 1$ ensures that the extent of the bound state is indeed much wider than the blockade radius justifying the δ-function approximation. For the case of a square well, $\psi_b(0, r)$, $\psi_s(0, r)$, and $\psi_b(L, r)$, $\psi_s(L, r)$, $|\psi(L, r)|^2$ are shown in Fig. 8-7. Within this solution, the observed bunching can be understood as resulting from the relative phase evolution between the bound and the scattering states. For the parameters given above, both terms in Eq. (D.16) contribute to the superpoissonian feature $|\psi|^2 > 0$ at $r = 0$. The bound state ψ_b acquires a phase and becomes the dominant contribution to the imaginary part of ψ. The superposition of scattering

states ψ_s starts with a dip (because the bound-state contribution is subtracted), but its phase evolution "fills in" the dip associated with the real part of ψ, while contributing very little to the imaginary part, as visualized in Fig. 8-7. A combination of both the real and imaginary parts of ψ results in the bunching feature of $|\psi|^2$. Therefore, consistent with a simple intuition, the superpoissonian $g^{(2)}(0)$ is indeed driven by the bound-state formation.

D.2 Relation between measurements and the spatial Schroedinger equation

As in Appendix C, under the approximation of a homogeneous medium, the intuition we have just developed for the region of the z_1-z_2 plane where both photons are inside the medium is not sufficient for computing $\psi(\tau \neq 0)$. Indeed, one has to use this solution to obtain the boundary condition to the problem in the region where one photon is inside the medium while the other photon is already outside.The latter problem is equivalent to the retrieval from the medium of a spin-wave (defined along $z_1 = L$) corresponding to the second excitation (see, for example, Eq. (23) in Ref. [208]). While at $\Delta = 0$ and $OD \gg 1$, the retrieval can be described in terms of simple rescaling by the group velocity v_g (provided EIT bandwidth effects are ignored), at nonzero Δ the situation is more complicated [208]. At the same time, the theoretical prediction shown in Fig. 8-7 of the main text (obtained with $EE(R = L, v_g\tau)$ calculated from Eq. (D.8) using the boundary conditions $EE(R = 0, r) = EE(R, r = \pm\infty) = \alpha^2$) is in a good qualitative agreement with both the measured $\psi(\tau)$ and the full calculations described above. We emphasize that this comparison can only be interpreted qualitatively, especially at large photon separations, since it (1) assumes simple group velocity propagation and (2) corresponds to a read out of the second excitation along $R = L$ instead of $z_1 = L$. The comparison is, however, better than one might naively expect since the two approximations partially compensate for each other as they, respectively, underestimate and overestimate the mass-induced broadening of the second excitation.

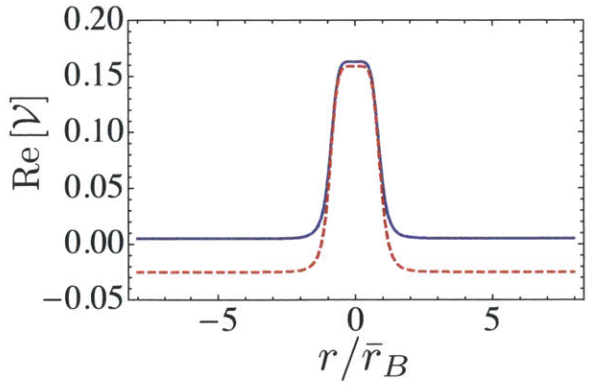

Figure D-2: **Variation of the potential well with two-photon detuning.** For $\Delta = 18$ MHz, $\Omega_c = 10$ MHz, $\gamma = 500$ kHz, $\delta = 0$ (solid blue) and $\delta = 250$ kHz (dashed red), we plot $\mathrm{Re}[\mathcal{V}(r)]$. Moving from $\delta = 0$ towards the Raman resonance at $\delta = 1.3$ MHz $\approx \Omega_c^2/(4\Delta)$ makes the potential well deeper by shifting the $r \gg \bar{r}_B$ baseline.

D.3 Engineering the two-photon potential with a non-zero Raman detuning

While we focused so far on the case of $\delta = \gamma = 0$, let us briefly consider the case of nonzero δ and γ. To get a qualitative insight, let us assume that δ and γ are small enough that the approximations leading to Eq. (D.8) still hold. Then Eqs. (D.9,D.11) are modified to

$$-\frac{1}{2\tilde{m}(r)} = \frac{4L}{OD}\left(\frac{2(\Delta+2\delta)}{\Gamma} + i\left(1+\frac{\gamma}{\Gamma}\right) - \left(\frac{\Omega_c}{\Gamma}\right)^2\left(1+\frac{2\delta+i\gamma}{2(\Delta+\delta)+i\Gamma}\right)\mathcal{V}(r)\right), \tag{D.19}$$

$$\mathcal{V}(r) = \left(\frac{2(\Delta+2\delta)}{\Gamma} + i(1+\frac{\gamma}{\Gamma}) + \frac{2i\Omega_c^2}{2\Gamma(\gamma-i2\delta)+i\Omega_c^2(r_b/r)^6}\right)^{-1}. \tag{D.20}$$

Since $|\delta|, \frac{1}{2}\Omega_c \ll |\Delta|$, the mass is affected by changes in δ only weakly. At the same time, the potential $U(r)$ is affected substantially by changes in δ. Specifically, we observe (Fig. D-2) that moving towards (away from) the Raman absorption peak at $\delta \approx \Omega_c^2/(4\Delta)$ makes the well deeper (shallower) by shifting the $r \gg \bar{r}_B$ baseline, which implies tighter (weaker) binding of photons, and resulting in more (less) bunching, consistent with the experimental observations in Fig. 8-8.

Bibliography

[1] Aspect, A., Grangier, P. & Roger, G. Experimental tests of realistic local theories via bell's theorem. *Phys. Rev. Lett.* **47**, 460–463 (1981).

[2] Aspect, A., Dalibard, J. & Roger, G. Experimental test of bell's inequalities using time- varying analyzers. *Phys. Rev. Lett.* **49**, 1804–1807 (1982).

[3] Nielsen, M. A. & Chuang, I. L. *Quantum Computation and Quantum Information* (Cambridge University Press, 2000).

[4] Cirac, J. I., Zoller, P., Kimble, H. J. & Mabuchi, H. Quantum state transfer and entanglement distribution among distant nodes in a quantum network. *Phys. Rev. Lett.* **78**, 3221–3224 (1997).

[5] Duan, L. M., Lukin, M. D., Cirac, J. I. & Zoller, P. Long-distance quantum communication with atomic ensembles and linear optics. *Nature* **414**, 413–418 (2001).

[6] Kimble, H. J. The quantum internet. *Nature* **453**, 1023–1030 (2008).

[7] Giovannetti, V., Lloyd, S. & Maccone, L. Quantum-enhanced measurements: Beating the standard quantum limit. *Science* **306**, 1330–1336 (2004).

[8] Monroe, C., Meekhof, D. M., King, B. E., Itano, W. M. & Wineland, D. J. Demonstration of a fundamental quantum logic gate. *Phys. Rev. Lett.* **75**, 4714–4717 (1995).

[9] Chuang, I. L., Vandersypen, L. M. K., Zhou, X., Leung, D. W. & Lloyd, S. Experimental realization of a quantum algorithm. *Nature* **393**, 143–146 (1998).

[10] Isenhower, L. *et al.* Demonstration of a neutral atom controlled-not quantum gate. *Phys. Rev. Lett.* **104**, 010503 (2010).

[11] Rauschenbeutel, A. *et al.* Coherent operation of a tunable quantum phase gate in cavity qed. *Phys. Rev. Lett.* **83**, 5166–5169 (1999).

[12] Plantenberg, J. H., de Groot, P. C., Harmans, C. J. P. M. & Mooij, J. E. Demonstration of controlled-not quantum gates on a pair of superconducting quantum bits. *Nature* **447**, 836–839 (2007).

[13] Bishop, L. S. *et al.* Nonlinear response of the vacuum rabi resonance. *Nat. Phys.* **5**, 105–109 (2009).

[14] Milburn, G. J. Quantum optical fredkin gate. *Phys. Rev. Lett.* **62**, 2124–2127 (1989).

[15] Chuang, I. L. & Yamamoto, Y. Simple quantum computer. *Phys. Rev. A* **52**, 3489–3496 (1995).

[16] Knill, E., Laflamme, R. & Milburn, G. J. A scheme for efficient quantum computation with linear optics. *Nature* **409**, 46–52 (2001).

[17] Gasparoni, S., Pan, J.-W., Walther, P., Rudolph, T. & Zeilinger, A. Realization of a photonic controlled-not gate sufficient for quantum computation. *Phys. Rev. Lett.* **93**, 020504 (2004).

[18] Imoto, N., Haus, H. A. & Yamamoto, Y. Quantum nondemolition measurement of the photon number via the optical kerr effect. *Phys. Rev. A* **32**, 2287–2292 (1985).

[19] Tonks, L. The complete equation of state of one, two and three-dimensional gases of hard elastic spheres. *Phys. Rev.* **50**, 955–963 (1936).

[20] Girardeau, M. Relationship between systems of impenetrable bosons and fermions in one dimension. *J. Math. Phys.* **1**, 516 –523 (1960).

[21] Kinoshita, T., Wenger, T. & Weiss, D. S. Observation of a one-dimensional tonks-girardeau gas. *Science* **305**, 1125–1128 (2004).

[22] Paredes, B. *et al.* Tonks-girardeau gas of ultracold atoms in an optical lattice. *Nature* **429**, 277–281 (2004).

[23] Greiner, M., Mandel, O., Esslinger, T., Hansch, T. W. & Bloch, I. Quantum phase transition from a superfluid to a mott insulator in a gas of ultracold atoms. *Nature* **415**, 39–44 (2002).

[24] Carusotto, I. & Ciuti, C. Quantum fluids of light. *Rev. Mod. Phys.* **85**, 299–366 (2013).

[25] Imamoglu, A., Schmidt, H., Woods, G. & Deutsch, M. Strongly interacting photons in a nonlinear cavity. *Phys. Rev. Lett.* **79**, 1467–1470 (1997).

[26] Hartmann, M. J., Brandao, F. G. S. L. & Plenio, M. B. Strongly interacting polaritons in coupled arrays of cavities. *Nat Phys* **2**, 849–855 (2006).

[27] Greentree, A. D., Tahan, C., Cole, J. H. & Hollenberg, L. C. L. Quantum phase transitions of light. *Nat Phys* **2**, 856–861 (2006).

[28] Hartmann, M. J. & Plenio, M. B. Strong photon nonlinearities and photonic mott insulators. *Phys. Rev. Lett.* **99**, 103601 (2007).

[29] Chang, D. E. *et al.* Crystallization of strongly interacting photons in a nonlinear optical fibre. *Nat Phys* **4**, 884–889 (2008).

[30] Hafezi, M., Chang, D. E., Gritsev, V., Demler, E. & Lukin, M. D. Quantum transport of strongly interacting photons in a one-dimensional nonlinear waveguide. *Phys. Rev. A* **85**, 013822 (2012).

[31] Dawkins, S. T., Mitsch, R., Reitz, D., Vetsch, E. & Rauschenbeutel, A. Dispersive optical interface based on nanofiber-trapped atoms. *Phys. Rev. Lett.* **107**, 243601 (2011).

[32] Hafezi, M., Chang, D. E., Gritsev, V., Demler, E. A. & Lukin, M. D. Photonic quantum transport in a nonlinear optical fiber. *EPL (Europhysics Letters)* **94**, 54006 (2011).

[33] Chang, D. E., Sorensen, A. S., Demler, E. A. & Lukin, M. D. A single-photon transistor using nanoscale surface plasmons. *Nat Phys* **3**, 807–812 (2007).

[34] Shen, J.-T. & Fan, S. Strongly correlated two-photon transport in a one-dimensional waveguide coupled to a two-level system. *Phys. Rev. Lett.* **98**, 153003 (2007).

[35] Drummond, P. D., Shelby, R. M., Friberg, S. R. & Yamamoto, Y. Quantum solitons in optical fibres. *Nature* **365**, 307–313 (1993).

[36] Pohl, T., Demler, E. & Lukin, M. D. Dynamical crystallization in the dipole blockade of ultracold atoms. *Phys. Rev. Lett.* **104**, 043002 (2010).

[37] Schau, P. *et al.* Observation of spatially ordered structures in a two-dimensional rydberg gas. *Nature* **491**, 87–91 (2012).

[38] Haroche, S. & Raimond, J. M. *Exploring the Quantum* (Oxford University Press, 2006).

[39] Harris, S. E., Field, J. E. & Imamoglu, A. Nonlinear optical processes using electromagnetically induced transparency. *Phys. Rev. Lett.* **64**, 1107–1110 (1990).

[40] Schmidt, H. & Imamoglu, A. Giant kerr nonlinearities obtained by electromagnetically induced transparency. *Opt. Lett.* **21**, 1936–1938 (1996).

[41] Birnbaum, K. M. *et al.* Photon blockade in an optical cavity with one trapped atom. *Nature* **436**, 87–90 (2005).

[42] Dayan, B. *et al.* A photon turnstile dynamically regulated by one atom. *Science* **319**, 1062–1065 (2008).

[43] Faraon, A. *et al.* Coherent generation of non-classical light on a chip via photon-induced tunnelling and blockade. *Nat Phys* **4**, 859–863 (2008).

[44] Reinhard, A. *et al.* Strongly correlated photons on a chip. *Nat Photon* **6**, 93–96 (2012).

[45] Lang, C. *et al.* Observation of resonant photon blockade at microwave frequencies using correlation function measurements. *Phys. Rev. Lett.* **106**, 243601 (2011).

[46] Turchette, Q. A., Hood, C. J., Lange, W., Mabuchi, H. & Kimble, H. J. Measurement of conditional phase shifts for quantum logic. *Phys. Rev. Lett.* **75**, 4710–4713 (1995).

[47] Fushman, I. *et al.* Controlled phase shifts with a single quantum dot. *Science* **320**, 769–772 (2008).

[48] Kirchmair, G. *et al.* Observation of quantum state collapse and revival due to the single-photon kerr effect. *Nature* **495**, 205–209 (2013).

[49] Boyd, R. W. *Nonlinear Optics* (Elsevier, 2008).

[50] Grynberg, G., Aspect, A. & Fabre, C. *Introduction to Quantum Optics: From the Semi-classical Approach to Quantized Light* (Cambridge University Press, 2010).

[51] Hasegawa, A. & Matsumoto, M. *Optical Solitons in Fibers* (Springer, 2002).

[52] Venkataraman, V., Saha, K. & Gaeta, A. L. Phase modulation at the few-photon level for weak-nonlinearity-based quantum computing. *Nature Photonics* **7**, 138–141 (2012).

[53] Harris, S. & Yamamoto, Y. Photon switching by quantum interference. *Phys. Rev. Lett.* **81**, 3611 (1998).

[54] Harris, S. & Hau, L. V. Nonlinear optics at low light levels. *Phys. Rev. Lett.* **82**, 4611(4) (1998).

[55] Fleischhauer, M., Imamoglu, A. & Marangos, J. P. Electromagnetically induced transparency: Optics in coherent media. *Rev. Mod. Phys.* **77**, 633–673 (2005).

[56] Braje, D., Balic, V., Yin, G. & Harris, S. Low-light-level nonlinear optics with slow light. *Phys. Rev. A* **68**, 041801(R) (2003).

[57] Dudin, Y. O., Li, L. & Kuzmich, A. Light storage on the time scale of a minute. *Phys. Rev. A* **87**, 031801 (2013).

[58] Lukin, M. & Imamoglu, A. Nonlinear optics and quantum entanglement of ultraslow single photons. *Phys. Rev. Lett.* **84**, 1419 (2000).

[59] Andre, A. & Lukin, M. Manipulating light pulses via dynamically controlled photonic band gas. *Phys. Rev. Lett.* **89**, 143602 (2002).

[60] André, A., Bajcsy, M., Zibrov, A. S. & Lukin, M. D. Nonlinear optics with stationary pulses of light. *Phys. Rev. Lett.* **94**, 063902 (2005).

[61] Sevinçli, S., Henkel, N., Ates, C. & Pohl, T. Nonlocal nonlinear optics in cold rydberg gases. *Phys. Rev. Lett.* **107**, 153001 (2011).

[62] Gorshkov, A. V., Otterbach, J., Fleischhauer, M., Pohl, T. & Lukin, M. D. Photon-photon interactions via rydberg blockade. *Phys. Rev. Lett.* **107**, 133602 (2011).

[63] Pritchard, J. D. *et al.* Cooperative atom-light interaction in a blockaded rydberg ensemble. *Phys. Rev. Lett.* **105**, 193603 (2010).

[64] Parigi, V. *et al.* Observation and measurement of interaction-induced dispersive optical nonlinearities in an ensemble of cold rydberg atoms. *Phys. Rev. Lett.* **109**, 233602 (2012).

[65] Schuster, I. *et al.* Nonlinear spectroscopy of photons bound to one atom. *Nature Phys.* **4**, 382–385 (2008).

[66] Beugnon, J. *et al.* Two-dimensional transport and transfer of a single atomic qubit in optical tweezers. *Nature Physics* **3**, 696 (2007).

[67] Cregan, R. *et al.* Single-mode photonic band gap guidance of light in air. *Science* **285**, 1537 – 1539 (1999).

[68] Yin, D., Schmidt, H., Barber, J. P. & Hawkins, A. R. Integrated arrow waveguides with hollow cores. *Optics Express* **12**, 2710 (2004).

[69] Tong, L. M. *et al.* Subwavelength-diameter silica wires for low-loss optical wave guiding. *Nature* **426**, 816 (2003).

[70] Thompson, J. D. *et al.* Coupling a single trapped atom to a nanoscale optical cavity. *Science* **340**, 1202–1205 (2013).

[71] Joannopoulos, J. D., Meade, R. D. & Winn, J. N. *Photonic Crystals: Molding the Flow of Light* (Princeton University Press, 1995).

[72] Saleh, B. E. A. & Teich, M. C. *Fundamentals of Photonics* (Wiley-Interscience, 1997), 2 edn.

[73] Benabid, F., Couny, F., Knight, J. C., Birks, T. A. & Russell, P. S. Compact, stable and efficient all-fibre gas cells using hollow-core photonic crystal fibres. *Nature* **434**, 488 (2005).

[74] Benabid, F., Knight, J., Antonopoulos, G. & Russell, P. Stimulated raman scattering in hydrogen-filled hollow-core photonic crystal fiber. *Science* **298**, 399–402 (2002).

[75] Konorov, S. O., Fedotov, A. B. & Zheltikov, A. M. Enhanced four-wave mixing in a hollow-core photonic-crystal fiber. *Opt. Lett.* **28**, 1448 – 1450 (2003).

[76] Ghosh, S. *et al.* Low-light-level optical interactions with rubidium vapor in a photonic band-gap fiber. *Phys. Rev. Lett.* **97**, 023603 (2006).

[77] Takekoshi, T. & Knize, R. J. Optical guiding of atoms through a hollow-core photonic band-gap fiber. *Phys. Rev. Lett.* **98**, 210404 (2007).

[78] Christensen, C. A. *et al.* Trapping of ultracold atoms in a hollow-core photonic crystal fiber. *Phys. Rev. A* **78**, 033429 (2008).

[79] Grimm, R., Weidemller, M. & Ovchinnikov, Y. B. Optical dipole traps for neutral atoms. *Phys. Rev. A* **62**, 013406 (2000).

[80] Vorrath, S., Moller, S. A., Windpassinger, P., Bongs, K. & Sengstock, K. Efficient guiding of cold atoms through a photonic band gap fiber. *New Journal of Physics* **12**, 123015 (2010).

[81] Yan, Z.-C., Dalgarno, A. & Babb, J. F. Long-range interactions of lithium atoms. *Phys. Rev. Lett.* **55**, 2882 (1997).

[82] Lin, Y., Teper, I., Chin, C. & Vuletic, V. Impact of the casimir-polder potential and johnson noise on bose- einstein condensate stability near surfaces. *Phys. Rev. Lett.* **92**, 050404 (2004).

[83] Yan, M., Rickey, E. & Zhu, Y. Observation of absorptive photon switching by quantum interference. *Phys. Rev. A* **64**, 041801(R) (2001).

[84] Chen, Y., Tsai, Z., Liu, Y. & Yu, I. Low-light-level photon switching by quantum interference. *Opt. Lett.* **30**, 3207 (2005).

[85] Bajcsy, M., Zibrov, A. S. & Lukin, M. D. Stationary pulses of light in an atomic medium. *Nature* **426**, 638–641 (2003).

[86] Imamoglu, A. High efficiency photon counting using stored light. *Phys. Rev. Lett.* **89**, 163602 (2002).

[87] James, D. & Kwiat, P. Atomic-vapor-based high efficiency optical detectors with photon number resolution. *Phys. Rev. Lett.* **89**, 183601 (2002).

[88] Phillips, D. F., Fleischhauer, A., Mair, A., Walsworth, R. L. & Lukin, M. D. Storage of light in atomic vapor. *Phys. Rev. Lett.* **86**, 783–786 (2001).

[89] Liu, C., Dutton, Z., Behroozi, C. H. & Hau, L. Observation of coherent optical information storage in an atomic medium using halted light pulses. *Nature* **409**, 490 – 493 (2001).

[90] Tanji-Suzuki, H. *et al.* Interaction between atomic ensembles and optical resonators: Classical description. *Adv. At. Mol. Opt. Phys.* **60**, 201 (2011).

[91] West, J., Smith, C., Borrelli, N., Allan, D. & Koch, K. Surface modes in air-core photonic band-gap fibers. *Opt. Express* **12**, 1485–1496 (2012).

[92] Wiederhecker, G. S. *et al.* Field enhancement within an optical fibre with a sub-wavelength air core. *Nature Photonics* **1**, 115 (2007).

[93] Bajcsy, M. *et al.* Efficient all-optical switching using slow light within a hollow fiber. *Phys. Rev. Lett.* **102**, 203902 (2009).

[94] Fleischhauer, M., Otterbach, J. & Unanyan, R. G. Bose-einstein condensation of stationary-light polaritons. *Phys. Rev. Lett.* **101**, 163601 (2008).

[95] Otterbach, J., Unanyan, R. G. & Fleischhauer, M. Confining stationary light: Dirac dynamics and klein tunneling. *Phys. Rev. Lett.* **102**, 063602 (2009).

[96] Otterbach, J., Ruseckas, J., Unanyan, R. G., Juzeliūnas, G. & Fleischhauer, M. Effective magnetic fields for stationary light. *Phys. Rev. Lett.* **104**, 033903 (2010).

[97] Yang, W. *et al.* Atomic spectroscopy on a chip. *Nature Photonics* **1**, 331 (2007).

[98] Quan, Q. M., Bulu, I. & Loncar, M. Broadband waveguide qed system on a chip. *Phys. Rev. A* **80**, 011810 (2009).

[99] Slepkov, A. D., Bhagwat, A. R., Venkataraman, V., Londero, P. & Gaeta, A. L. Generation of large alkali vapor densities inside bare hollow-core photonic band-gap fibers. *Opt. Express* **16**, 18976–18983 (2008).

[100] Lin, C.-C. *et al.* Enhanced all-optical switching with double slow light pulses. *Phys. Rev. A* **86**, 063836 (2012).

[101] Zimmer, F., Andre, A., Lukin, M. & Fleischhauer, M. Coherent control of stationary light pulses. *Opt. Comm.* **264**, 441453 (2006).

[102] Hansen, K. R. & Mlmer, K. Trapping of light pulses in ensembles of stationary lambda atoms. *Phys. Rev. A* **75**, 053802 (2007).

[103] Nikoghosyan, G. & Fleischhauer, M. Stationary light in cold-atomic gases. *Phys. Rev. A* **80**, 013818 (2009).

[104] Wu, J.-H., Artoni, M. & La Rocca, G. C. Decay of stationary light pulses in ultracold atoms. *Phys. Rev. A* **81**, 033822 (2010).

[105] Lin, Y.-W. *et al.* Stationary light pulses in cold atomic media and without bragg gratings. *Phys. Rev. Lett.* **102**, 213601 (2009).

[106] Zimmer, F. E., Otterbach, J., Unanyan, R. G., Shore, B. W. & Fleischhauer, M. Dark-state polaritons for multicomponent and stationary light fields. *Phys. Rev. A* **77**, 063823 (2008).

[107] Moiseev, S. A. & Ham, B. S. Quantum manipulation of two-color stationary light: Quantum wavelength conversion. *Phys. Rev. A* **73**, 033812 (2006).

[108] Wu, J.-H., Artoni, M. & La Rocca, G. C. All-optical light confinement in dynamic cavities in cold atoms. *Phys. Rev. Lett.* **103**, 133601 (2009).

[109] Horsley, S. A. R., Wu, J.-H., Artoni, M. & La Rocca, G. C. Optical nonreciprocity of cold atom bragg mirrors in motion. *Phys. Rev. Lett.* **110**, 223602 (2013).

[110] Gao, J.-W., Wu, J.-H., Ba, N., Cui, C.-L. & Tian, X.-X. Efficient all-optical routing using dynamically induced transparency windows and photonic band gaps. *Phys. Rev. A* **81**, 013804 (2010).

[111] Chen, Y.-H. *et al.* Demonstration of the interaction between two stopped light pulses. *Phys. Rev. Lett.* **108**, 173603 (2012).

[112] Freeman, R. R. & Kleppner, D. Core polarization and quantum defects in high-angular-momentum states of alkali atoms. *Phys. Rev. A* **14**, 1614–1619 (1976).

[113] Kleppner, D., Littman, M. G. & Zimmerman, M. L. Highly excited atoms. *Scientific American* **244**, 130 – 149 (1981).

[114] Gallas, J., Leuchs, G., Walther, H. & Figger, H. Rydberg atoms: high resolution spectroscopy and radiation interaction-rydberg molecules. *Advances in atomic and molecular physics* **Vol. 20**, 413–466 (1985).

[115] Li, W., Mourachko, I., Noel, M. W. & Gallagher, T. F. Millimeter-wave spectroscopy of cold rb rydberg atoms in a magneto-optical trap: Quantum defects of the ns, np, and nd series. *Phys. Rev. A* **67**, 052502 (2003).

[116] Stoicheff, B. P. & Weinberger, E. Doppler-free two-photon absorption spectrum of rubidium. *Canadian Journal of Physics* **57**, 2143–2154 (1979).

[117] Mack, M. *et al.* Measurement of absolute transition frequencies of ^{87}Rb to nS and nD rydberg states by means of electromagnetically induced transparency. *Phys. Rev. A* **83**, 052515 (2011).

[118] Zimmerman, M. L., Littman, M. G., Kash, M. M. & Kleppner, D. Stark structure of the rydberg states of alkali-metal atoms. *Phys. Rev. A* **20**, 2251–2275 (1979).

[119] Fabre, C. Etats tres excites des atomes alcalins. *Annales de Physique* **7**, 5–86 (1982).

[120] Saffman, M., Walker, T. G. & Mølmer, K. Quantum information with rydberg atoms. *Rev. Mod. Phys.* **82**, 2313–2363 (2010).

[121] Seaton, M. J. The quantum defect method. *Monthly Notices of the Royal Astronomical Society* **118**, 504 (1958).

[122] Marinescu, M., Sadeghpour, H. R. & Dalgarno, A. Dispersion coefficients for alkali-metal dimers. *Phys. Rev. A* **49**, 982–988 (1994).

[123] Haroche, S. & Raimond, J. M. Radiative properties of rydberg states in resonant cavities. *Advances in Atomic and Molecular Physics* **20**, 347 (1985).

[124] Edmonds, A. R., Picart, J., Minh, N. T. & Pullen, R. Tables for the computation of radial integrals in the coulomb approximation. *Journal of Physics B* **Vol. 12**, 2781–2787 (1979).

[125] Hulet, R. G. & Kleppner, D. Rydberg atoms in "circular" states. *Phys. Rev. Lett.* **51**, 1430–1433 (1983).

[126] Gounand, F. Calculation of radial matrix elements and radiative lifetimes for highly excited states of alkali atoms using the coulomb approximation. *J. Phys. France* **40**, 457–460 (1979).

[127] Oliveira, A. L. d., Mancini, M. W., Bagnato, V. S. & Marcassa, L. G. Measurement of rydberg-state lifetimes using cold trapped atoms. *Phys. Rev. A* **65**, 031401 (2002).

[128] Gallagher, T. F. & Cooke, W. E. Interactions of blackbody radiation with atoms. *Phys. Rev. Lett.* **42**, 835–839 (1979).

[129] Gallagher, T. *Rydberg Atoms* (Cambridge University Press, 1994).

[130] O'Sullivan, M. S. & Stoicheff, B. P. Scalar polarizabilities and avoided crossings of high rydberg states in rb. *Phys. Rev. A* **31**, 2718–2720 (1985).

[131] Meschede, D., Walther, H. & Müller, G. One-atom maser. *Phys. Rev. Lett.* **54**, 551–554 (1985).

[132] Brune, M. *et al.* Quantum rabi oscillation: A direct test of field quantization in a cavity. *Phys. Rev. Lett.* **76**, 1800–1803 (1996).

[133] Littman, M. G., Kash, M. M. & Kleppner, D. Field-ionization processes in excited atoms. *Phys. Rev. Lett.* **41**, 103–107 (1978).

[134] Saffman, M. & Walker, T. G. Analysis of a quantum logic device based on dipole-dipole interactions of optically trapped rydberg atoms. *Phys. Rev. A* **72**, 022347 (2005).

[135] Li, L., Dudin, Y. O. & Kuzmich, A. Entanglement between light and an optical atomic excitation. *Nature* **498**, 466–469 (2013).

[136] Dutta, S. K., Guest, J. R., Feldbaum, D., Walz-Flannigan, A. & Raithel, G. Ponderomotive optical lattice for rydberg atoms. *Phys. Rev. Lett.* **85**, 5551–5554 (2000).

[137] Anderson, S. E., Younge, K. C. & Raithel, G. Trapping rydberg atoms in an optical lattice. *Phys. Rev. Lett.* **107**, 263001 (2011).

[138] Anderson, S. E. & Raithel, G. Dependence of rydberg-atom optical lattices on the angular wave function. *Phys. Rev. Lett.* **109**, 023001 (2012).

[139] Potvliege, R. & Adams, C. Photo-ionization in far-off-resonance optical lattices. *New J. Phys.* **8**, 163 (2006).

[140] Marinescu, M. Dispersion coefficients for the nP-nP asymptote of homonuclear alkali-metal dimers. *Phys. Rev. A* **56**, 4764–4773 (1997).

[141] Singer, K., Stanojevic, J., Weidemüller, M. & Cote, R. Long-range interactions between alkali rydberg atom pairs correlated to the n s n s, n p n p and n d n d asymptotes. *Journal of Physics B: Atomic, Molecular and Optical Physics* **38**, S295 (2005).

[142] Reinhard, A., Liebisch, T. C., Knuffman, B. & Raithel, G. Level shifts of rubidium rydberg states due to binary interactions. *Phys. Rev. A* **75**, 032712 (2007).

[143] Walker, T. G. & Saffman, M. Consequences of zeeman degeneracy for the van der waals blockade between rydberg atoms. *Phys. Rev. A* **77**, 032723 (2008).

[144] Nipper, J. *et al.* Atomic pair-state interferometer: Controlling and measuring an interaction-induced phase shift in rydberg-atom pairs. *Phys. Rev. X* **2**, 031011 (2012).

[145] Jaksch, D. *et al.* Fast quantum gates for neutral atoms. *Phys. Rev. Lett.* **85**, 2208–2211 (2000).

[146] Lukin, M. D. *et al.* Dipole blockade and quantum information processing in mesoscopic atomic ensembles. *Phys. Rev. Lett.* **87**, 037901 (2001).

[147] Pritchard, J., Weatherill, K. & Adams, C. Non-linear optics using cold rydberg atoms. *arXiv:1205.4890v1* (2012).

[148] Gaetan, A. *et al.* Observation of collective excitation of two individual atoms in the rydberg blockade regime. *Nat Phys* **5**, 115–118 (2009).

[149] Urban, E. *et al.* Observation of rydberg blockade between two atoms. *Nat Phys* **5**, 110–114 (2009).

[150] Tong, D. *et al.* Local blockade of rydberg excitation in an ultracold gas. *Phys. Rev. Lett.* **93**, 063001 (2004).

[151] Singer, K., Reetz-Lamour, M., Amthor, T., Marcassa, L. G. & Weidemüller, M. Suppression of excitation and spectral broadening induced by interactions in a cold gas of rydberg atoms. *Phys. Rev. Lett.* **93**, 163001 (2004).

[152] Heidemann, R. *et al.* Evidence for coherent collective rydberg excitation in the strong blockade regime. *Phys. Rev. Lett.* **99**, 163601 (2007).

[153] Heidemann, R. *et al.* Rydberg excitation of bose-einstein condensates. *Phys. Rev. Lett.* **100**, 033601 (2008).

[154] Dudin, Y. O., Li, L., Bariani, F. & Kuzmich, A. Observation of coherent many-body rabi oscillations. *Nature Physics* **8**, 790–794 (2012).

[155] Dudin, Y. O. & Kuzmich, A. Strongly interacting rydberg excitations of a cold atomic gas. *Science* **336**, 887–889 (2012).

[156] Friedler, I., Petrosyan, D., Fleischhauer, M. & Kurizki, G. Long-range interactions and entanglement of slow single-photon pulses. *Phys. Rev. A* **72**, 043803 (2005).

[157] Petrosyan, D., Otterbach, J. & Fleischhauer, M. Electromagnetically induced transparency with rydberg atoms. *Phys. Rev. Lett.* **107**, 213601 (2011).

[158] Low, R. *et al.* An experimental and theoretical guide to strongly interacting rydberg gases. *J. Phys. B: At. Mol. Opt. Phys.* **45**, 113001 (2012).

[159] Gorshkov, A. V., Nath, R. & Pohl, T. Dissipative many-body quantum optics in rydberg media. *Phys. Rev. Lett.* **110**, 153601 (2013).

[160] Dudin, Y. O., Bariani, F. & Kuzmich, A. Emergence of spatial spin-wave correlations in a cold atomic gas. *Phys. Rev. Lett.* **109**, 133602 (2012).

[161] Maxwell, D. *et al.* Storage and control of optical photons using rydberg polaritons. *Phys. Rev. Lett.* **110**, 103001 (2013).

[162] Birnbaum, K. & Group, T. Q. O. Ultra-high vacuum chambers. *Caltech* (2005).

[163] Bguin, L., Vernier, A., Chicireanu, R., Lahaye, T. & Browaeys, A. Direct measurement of the van der waals interaction between two single atoms. *arXiv:1302.4262* (2013).

[164] Winoto, S. L., DePue, M. T., Bramall, N. E. & Weiss, D. S. Laser cooling at high density in deep far-detuned optical lattices. *Phys. Rev. A* **59**, R19–R22 (1999).

[165] Vuletić, V., Chin, C., Kerman, A. J. & Chu, S. Degenerate raman sideband cooling of trapped cesium atoms at very high atomic densities. *Phys. Rev. Lett.* **81**, 5768–5771 (1998).

[166] Boiron, D., Triché, C., Meacher, D. R., Verkerk, P. & Grynberg, G. Three-dimensional cooling of cesium atoms in four-beam gray optical molasses. *Phys. Rev. A* **52**, R3425–R3428 (1995).

[167] Adams, C. S., Lee, H. J., Davidson, N., Kasevich, M. & Chu, S. Evaporative cooling in a crossed dipole trap. *Phys. Rev. Lett.* **74**, 3577–3580 (1995).

[168] Barrett, M. D., Sauer, J. A. & Chapman, M. S. All-optical formation of an atomic bose-einstein condensate. *Phys. Rev. Lett.* **87**, 010404 (2001).

[169] Cennini, G., Ritt, G., Geckeler, C. & Weitz, M. All-optical realization of an atom laser. *Phys. Rev. Lett.* **91**, 240408 (2003).

[170] Granade, S. R., Gehm, M. E., O'Hara, K. M. & Thomas, J. E. All-optical production of a degenerate fermi gas. *Phys. Rev. Lett.* **88**, 120405 (2002).

[171] Friebel, S., D'Andrea, C., Walz, J., Weitz, M. & Hänsch, T. W. co_2-laser optical lattice with cold rubidium atoms. *Phys. Rev. A* **57**, R20–R23 (1998).

[172] Petrich, W., Anderson, M. H., Ensher, J. R. & Cornell, E. A. Behavior of atoms in a compressed magneto-optical trap. *J. Opt. Soc. Am. B* **11**, 1332–1335 (1994).

[173] Walhout, M., Sterr, U. & Rolston, S. L. Magnetic inhibition of polarization-gradient laser cooling in σ_+-σ_- optical molasses. *Phys. Rev. A* **54**, 2275–2279 (1996).

[174] Kuppens, S. J. M., Corwin, K. L., Miller, K. W., Chupp, T. E. & Wieman, C. E. Loading an optical dipole trap. *Phys. Rev. A* **62**, 013406 (2000).

[175] Ketterle, W., Davis, K. B., Joffe, M. A., Martin, A. & Pritchard, D. E. High densities of cold atoms in a *dark* spontaneous-force optical trap. *Phys. Rev. Lett.* **70**, 2253–2256 (1993).

[176] Gallagher, A. & Pritchard, D. E. Exoergic collisions of cold na*-na. *Phys. Rev. Lett.* **63**, 957–960 (1989).

[177] Schwarzkopf, A., Sapiro, R. E. & Raithel, G. Imaging spatial correlations of rydberg excitations in cold atom clouds. *Phys. Rev. Lett.* **107**, 103001 (2011).

[178] Kuhnle, E. Apparatus for excitation and detection of rydberg atoms in quantum gases. *Thesis, T.Pfau's group, Stuttgart University* (2006).

[179] Olmos, B., Li, W., Hofferberth, S. & Lesanovsky, I. Amplifying single impurities immersed in a gas of ultracold atoms. *Phys. Rev. A* **84**, 041607 (2011).

[180] Gunter, G. *et al.* Interaction enhanced imaging of individual rydberg atoms in dense gases. *Phys. Rev. Lett.* **108**, 013002 (2012).

[181] Mazurenko, A. Optical imaging of rydberg atoms. *Undergraduate Thesis, V.Vuletic's group, MIT* (2012).

[182] Black, E. D. An introduction to pound-driver -hall laser frequency stabilization. *Am. J. Phys.* **69**, 79 (2011).

[183] Bendkowsky, V. *et al.* Observation of ultralong-range rydberg molecules. *Nature* **458**, 1005–1008 (2009).

[184] Steck, D. Rubidium 87 d line data. *http://steck.us/alkalidata/* (2010).

[185] Hau, L. V., Harris, S. E., Dutton, Z. & Behroozi, C. H. Light speed reduction to 17 metres per second in an ultracold atomic gas. *Nature* **397**, 594–598 (1999).

[186] Fleischhauer, M. & Lukin, M. D. Dark-state polaritons in electromagnetically induced transparency. *Phys. Rev. Lett.* **84**, 5094–5097 (2000).

[187] Liebisch, T. C., Reinhard, A., Berman, P. R. & Raithel, G. Atom counting statistics in ensembles of interacting rydberg atoms. *Phys. Rev. Lett.* **95**, 253002 (2005).

[188] Johnson, T. A. *et al.* Rabi oscillations between ground and rydberg states with dipole-dipole atomic interactions. *Phys. Rev. Lett.* **100**, 113003– (2008).

[189] Tanji-Suzuki, H., Chen, W., Landig, R., Simon, J. & Vuletić, V. Vacuum-induced transparency. *Science* **333**, 1266–1269 (2011).

[190] Shahmoon, E., Kurizki, G., Fleischhauer, M. & Petrosyan, D. Strongly interacting photons in hollow-core waveguides. *Phys. Rev. A* **83**, 033806 (2011).

[191] Møller, D., Madsen, L. B. & Mølmer, K. Quantum gates and multiparticle entanglement by rydberg excitation blockade and adiabatic passage. *Phys. Rev. Lett.* **100**, 170504 (2008).

[192] Müller, M., Lesanovsky, I., Weimer, H., Büchler, H. P. & Zoller, P. Mesoscopic rydberg gate based on electromagnetically induced transparency. *Phys. Rev. Lett.* **102**, 170502 (2009).

[193] Han, Y., He, B., Heshami, K., Li, C.-Z. & Simon, C. Quantum repeaters based on rydberg-blockade-coupled atomic ensembles. *Phys. Rev. A* **81**, 052311 (2010).

[194] Adamson, R. B. A., Shalm, L. K., Mitchell, M. W. & Steinberg, A. M. Multiparticle state tomography: Hidden differences. *Phys. Rev. Lett.* **98**, 043601 (2007).

[195] James, D. F. V., Kwiat, P. G., Munro, W. J. & White, A. G. Measurement of qubits. *Phys. Rev. A* **64**, 052312 (2001).

[196] Cheng, Z. & Kurizki, G. Optical "multiexcitons": Quantum gap solitons in nonlinear bragg reflectors. *Phys. Rev. Lett.* **75**, 3430–3433 (1995).

[197] Wootters, W. K. Entanglement of formation of an arbitrary state of two qubits. *Phys. Rev. Lett.* **80**, 2245–2248 (1998).

[198] Drummond, P. D. & He, H. Optical mesons. *Phys. Rev. A* **56**, R1107–R1109 (1997).

[199] Boller, K.-J., Imamolu, A. & Harris, S. E. Observation of electromagnetically induced transparency. *Phys. Rev. Lett.* **66**, 2593–2596 (1991).

[200] Harris, S. E. Lasers without inversion: Interference of lifetime-broadened resonances. *Phys. Rev. Lett.* **62**, 1033–1036 (1989).

[201] Marangos, J. P. Electromagnetically induced transparency. *Journal of Modern Optics* **45**, 471–503 (1998).

[202] Fleischhauer, M. & Lukin, M. D. Quantum memory for photons: Dark-state polaritons. *Phys. Rev. A* **65**, 022314 (2002).

[203] Chanelire, T. *et al.* Storage and retrieval of single photons transmitted between remote quantum memories. *Nature* **438**, 833–836 (2005).

[204] Nikoghosyan, G. & Fleischhauer, M. Stationary light in cold-atomic gases. *Phys. Rev. A* **80**, 013818 (2009).

[205] Loudon, R. *Quantum Theory of Light* (Oxford University Press, New York, 2000).

[206] Yamamoto, Y. & Imamoglu, A. *Mesoscopic Quantum Optics* (John Wiley & Sons, Inc., New York, 1999).

[207] Zimmer, F. E., André, A., Lukin, M. D. & Fleischhauer, M. Coherent control of stationary light pulses. *Opt. Comm.* **264**, 441 (2006).

[208] Gorshkov, A. V., Andre, A., Lukin, M. D. & Sorensen, A. S. Photon storage in λ-type optically dense atomic media. ii. free-space model. *Phys. Rev. A* **76**, 033805 (2007).